# High bandwidth detection of mechanical stress in optical fibre using coherent detection of Rayleigh scattering

Sterenn Guerrier

INSTITUT POLYTECHNIQUE DE PARIS

NNT : 2022IPPAT004

Thèse de doctorat

# High bandwidth detection of mechanical stress in optical fibre using coherent detection of Rayleigh scattering

Thèse de doctorat de l'Institut Polytechnique de Paris
préparée à Télécom Paris

École doctorale n°626 École doctorale de l'Institut Polytechnique de Paris (EDIPP)
Spécialité de doctorat : Electronique et Optoélectronique

Thèse présentée et soutenue à Palaiseau, le 03 Février 2022, par

**MME STERENN GUERRIER**

Composition du Jury :

| | |
|---|---|
| Pierre Duhamel<br>Professeur, Centrale Supélec (L2S Paris-Saclay) | Rapporteur, Président |
| Luca Palmieri<br>Professor, University of Padova (Photonics and Electromagnetic Group, PEG) | Rapporteur |
| Nicolas Dubreuil<br>Professeur, Institut d'Optique Graduate School (LP2N) | Examinateur |
| Arthur H. Hartog<br>Expert, Worthy Photonics | Examinateur |
| Renaud Gabet<br>Maître de Conférence, HDR, Télécom Paris (LTCI) | Directeur de thèse |
| Elie Awwad<br>Maître de Conférence, Télécom Paris (LTCI) | Co-Encadrant de thèse |

Invité :

| | |
|---|---|
| Christian Dorize<br>Ingénieur de Recherche, Nokia Bell Labs (OSDR lab) | Encadrant de thèse |

# Captation de perturbations mécaniques large bande par détection cohérente de la rétrodiffusion Rayleigh dans les fibres optiques

–

# High bandwidth detection of mechanical stress in optical fibre using coherent detection of Rayleigh scattering

Sterenn Guerrier

Février 2022

# Acknowledgements

*My first thanks go to the members of the jury, who kindly accepted the invitation to review this work. I am grateful for the variety of skills and approaches that you brought to the table, in your comments, your reviews, and your questions during the defence. Thank you also for the remarks and discussions before and after the defence, such that the manuscript is hopefully in better shape now that after the first submission.*

*I would like also to express my warmest thanks to my supervisors, thesis directors.*
Christian et Elie, merci d'avoir proposé ce sujet de thèse, et de l'avoir suivi avec brio. Vous avez su me transmettre votre passion pour la recherche qu'il s'agisse du traitement de signal ou du labo d'optique, votre complémentarité et votre pédagogie m'ont permis d'apprendre une quantité improbable d'informations – quantité tout à fait raisonnable quand il s'agit d'appréhender les capteurs sur fibre optique dans le contexte des télécom, j'admets que le défi était grand. Merci à Renaud (et Yves) pour le suivi régulier du travail de thèse, le regard extérieur bien utile, merci surtout pour la relecture attentive du manuscrit qui aura permis de donner une dimension plus "académique" à ce travail !

*Big thanks also to my colleagues, fellow students on their PhD or master thesis, who made the work more instructive and the coffee breaks more enjoyable.*
A mes collègues, qu'ils soient les autres doctorants, le "groupe des jeunes", les stagiaires de passage, les personnes qui étaient déjà là avant que ce soit Alcatel, merci pour les conversations passionnantes, et aussi pour les discussions stupides. Merci à ceux dont "le sensing" n'était pas le sujet et qui sont venus s'y intéresser, donner de précieux conseils et coups de main, qui ont su propager leur motivation.

*I am grateful to my teachers, from engineering school and ROSP master, who introduced me to the researcher mindset.*
Merci aussi aux enseignants qui ont su me donner le goût de la recherche, en école d'ingénieur puis lors du master ROSP : de la curiosité est née la passion. Aussi, merci aux organisateurs de formations doctorales et autres conférences, ainsi qu'aux élèves comme moi, vous avez su construire et entretenir cette communauté de chercheurs et chercheuses de l'optique. On s'y sent utiles, inclus, et on s'y fait parfois des amis.

Je tiens à remercier[1] ma grand-mère, ma mère, mon père, et mes sœurs pour leur soutien, leur attention, leurs sages conseils, et pour leur confiance surtout. Vous êtes des points fixes dans ma vie, et ce malgré vos chemins personnels possiblement mouvementés. Vous êtes fortes et fort, vous êtes des modèles. Merci également à mon neveu qui se fiche probablement de ce que je fais, ce qui importe est qui je suis ; merci à mes oncles, tantes, cousins et cousines qui auront pensé à moi, pris des nouvelles, tendu la main, envoyé des petits mots.

Trugarez d'am eil familh, pa vefec'h o chom e tu all ar straed pe e penn all ar bed, evit ar predoù asambles, ar valeadennoù, an dibennoù-sizhun, ar skype-où. Kaozeal en ur

[1] A tous les suivants et à toutes les suivantes, sachez que cette page de la thèse est un prétexte, car ces remerciements sont surtout pour tout le reste.

predti pe dañsal er pradoù, da lidañ ar bloaz nevez, un deiz ha bloaz pe ar blijadur da vezañ asambles, atav eo bet ur banne frankiz, ur barrad aer fresk. Adarre, an dezenn a zo un abeg hepken, o drugarekaat a ran evit ar vuhez.

Merci aux amis et amies, au(x) coloc(s), qui ont pu ouvrir de grands yeux disant “tu vas vraiment faire de *l'optique* ?”, merci d'avoir rendu le défi plus grand. A celles et ceux que j'ai perdus de vue, à celles et ceux que l'on retrouve pour le nouvel-an ou des vacances, ou pour un verre entre deux trains, merci d'avoir été et d'être là, merci pour les paris stupides et les sages conseils.

Ma reconnaissance à Tanguy, toi qui as droit à ton prénom dans cette liste où les autres doivent jouer à se reconnaître, pour beaucoup de choses, y compris pour ces trois dernières années de thèse – ensemble.

Enfin merci, merci aux relecteurs et relectrices, que j'ai sûrement déjà remerciés par ailleurs. Qu'il se soit agi du manuscrit ou des planches de présentation pour la soutenance, votre implication fut le gâteau sous la cerise.

# Abstract


## Résumé

Répondant à une demande croissante de connectivité entre les individus, entre les pays et par conséquent entre les continents, les fibres optiques de télécommunications sont déployées dans le monde entier. Les continents commes les océans sont désormais quadrillés par ces réseaux dont l'importance stratégique n'est plus à démontrer. Aussi convient-il de surveiller cette infrastructure avec précision, au-delà de la simple détection de coupures de câbles. De manière plus générale, les fibres optiques sont une alternative aux capteurs électrodynamiques de vibrations, avec un atout majeur : la possibilité de détecter et localiser des phénomènes indépendants tout au long de la fibre.

Ainsi, les millions de kilomètres de fibres optiques actuellement déployées à travers le monde (réseaux d'opérateurs telecom ou bien réseaux locaux) constituent une énorme base potentielle de capteurs. Si des solutions commerciales telles que l'OTDR (*Optical Time Domain Reflectometer*) permettent déjà la détection de défauts ou de coupures le long d'une fibre optique, le potentiel des capteurs de vibration distribués est bien plus grand, allant jusqu'à la reconnaissance de multiples signatures audio voire de la parole. Au-delà des applications de type "Ville Intelligente" (*Smart City*) où l'usage des capteurs distribués pour la surveillance des infrastructures présente un grand intérêt, ou encore des applications de captation sous-marine pour la détection des séismes, la surveillance fine des fibres optiques télécom déployées par capteurs distribués est la base de la télémétrie pour la sécurisation et la résilience des réseaux télécom.

Cette thèse a pour but d'étudier finement la rétro-diffusion Rayleigh dans les fibres optiques, qui permet de capter de l'information induite par des perturbations mécaniques tout le long d'une fibre. Nous étudions le potentiel des fibres optiques en tant que microphones distribués, en terme de bande passante mécanique et de sensibilité. Nous décrivons le système d'interrogation des capteurs à fibre distribués, et proposons la modélisation d'un tel interrogateur en tenant compte du multiplexage des signaux sur deux axes orthogonaux de polarisation lors de la propagation dans la fibre. Nous étudions la problématique de l'évanouissement dans la fibre : à la fois l'évanouissement de polarisation que nous parvenons à annuler grâce à la méthode d'interrogation *Coherent-MIMO* (*Multiple In, Multiple Out*), et l'évanouissement cohérent (ou scintillement) que nous proposons de diminuer en recourant à une interrogation multi-porteuses électronique. Différents résultats de mesure sont également présentés dans cette thèse : tout d'abord, des mesures fines sur de faibles longueurs de fibre (quelques kilomètres) permettent de valider le seuil de distinction du système d'interrogation sur fibre monomodes de télécommunications. Ensuite, des mesures sur plusieurs dizaines de kilomètres de fibre monomode et coexistant avec la transmission de données à haut débit permettent de valider la pertinence d'un système de captation par segment de fibres dans les réseaux télécom, ouvrant ainsi la voie à des systèmes de télémétrie évoluée dédiés aux réseaux optiques de demain.

# Abstract

Telecommunication fibres are being deployed all over the world, connecting distant people, institutions, companies with an outstanding quality of service in terms of data rate and latency. Their strategic value in terms of global economy and daily life is now undeniable. Monitoring such an infrastructure is now mandatory, and that far beyond the standard case of breaks localization. From a broader standpoint, optical fibres are an alternative to electro-dynamic point sensors, with a strong asset: the capability to detect and localize multiple independent phenomena all along a fibre.

Thus, the millions of kilometers of currently deployed optical fibre around the world (networks of telecom operators or local networks) constitute a huge potential grid of sensors. While existing commercial solutions such as OTDR (Optical Time Domain Reflectometer) allow for the mere detection of losses and breaks, distributed vibration sensors have a strong potential regarding sensing of dynamic events, detecting of multiple acoustic signatures up to speech signals. Beyond applications such as "Smart city" or detection of earthquakes where the use of distributed sensors is a major stake for infrastructure monitoring, the in-depth monitoring of deployed telecommunication optical fibres is a basis for safety and resilience of today's and future telecommunication networks.

In this thesis, we show how distributed optical fibre sensors can be designed on top of telecommunication fibres, namely standard single mode fibres, and we explore their potential in terms of reach, detection threshold, and sensing bandwidth. We present the interrogator systems for distributed fibre sensing and build a dual-polarization numerical model of such an interrogation system and fibre sensor. We investigate the advantage of Coherent-MIMO-OTDR (Multiple In, Multiple Out), namely interrogating the fibre sensor jointly onto two input polarization axes and retrieving the backscattered light on two polarization axes: the technique enables to fully mitigate polarization fading issues. We derive a reliability metric to be associated with Coherent-MIMO measurements, aimed at further classification of the detected events. Secondly, we tackle the coherent fading issue which is another major concern in coherent-OTDR sensing technology. In the literature, most solutions to mitigate coherent fading rely on optically generated frequency diversity interrogation. Our interrogation system performs frequency diversity in the digital domain, i.e. directly applicable at the modulation of the interrogation sequences, before entering the optical domain. We developed MIMO-OFDM (Orthogonal Frequency Division Multiplexing) which retrieves independent channel estimations from a single fibre segment; the estimations are further combined, and the obtained estimations are assessed with regards to the reliability metric. Throughout this thesis journey, many experimental measurements were conducted, assessing the capabilities of the Coherent-MIMO interrogator on single-mode-fibre sensors in terms of reach, bandwidth, sensitivity, and detection of dynamic events. A study involving sensing of acoustic events on a fibre cable propagating live data was finally performed. We show how Coherent-MIMO sensing can co-propagate along full C-band high data rate channels, within a frequency slot as narrow as 4GHz, without any impact on the transmitted data, paving the way to the enhanced monitoring and telemetry in deployed telecommunication networks.

# Contents

# List of Acronyms

| | |
|---|---|
| AOM | Acousto-Optic Modulator |
| ASE | Amplified Spontaneous Emission |
| AWGN | Additive White Gaussian Noise |
| BPD | Balanced PhotoDiodes |
| b-SOP | Backscattered State Of Polarization |
| BPSK | Binary Phase Shift Keying |
| CUT | Channel Under Test |
| DAS | Distributed Acoustic Sensor |
| DFB | Distributed FeedBack (laser) |
| DOFS | Distributed Optical Fibre Sensor |
| DP | Dual Polarization |
| DVS | Distributed Vibration Sensor |
| DWDM | Dense Wavelength Division Multiplexing |
| EDFA | Erbium Doped Fibre Amplifier |
| EOM | Electro Optic Modulator |
| FBG | Fibre Bragg Grating |
| FFT | Fast Fourier Transform |
| FUT | Fibre Under Test |
| IQ | In-phase and Quadrature |
| LO | Local Oscillator |
| MIMO | Multiple Input Multiple Output |
| MZM | Mach-Zehnder Modulator |
| OFDM | Orthogonal Frequency Division Multiplexing |
| OFDR | Optical Frequency Domain Reflectometer |
| OTDR | Optical Time Domain Reflectometer |
| PBL | Polarization Beat Length |
| PDF | Probability Density Function |
| PDL | Polarization Dependent Loss |
| PDM | Polarization Division Multiplexing |
| PEA | Piezo-Electric Actuator |
| PMD | Polarization Mode Dispersion |
| PSD | Power Spectral Density |
| RBS | Rayleigh BackScattering |
| RMS | Root Mean Square |
| RVS | Rotated Vector Sum |
| RX | Receiver |
| SIMO | Single Input Multiple Output |
| SISO | Single Input Single Output |
| SNR | Signal-to-Noise Ratio |
| SOP | State of Polarization |
| SPL | Sound Pressure Level |
| SSMF | Standard Single Mode Fibre |
| TX | Transmitter |
| WDM | Wavelength Division Multiplexing |

# List of Symbols

| | | |
|---|---|---|
| $\alpha$ | Linear attenuation | [km$^{-1}$] |
| $\alpha_{dB}$ | Attenuation | [dB/km] |
| $\eta$ | Polarization transfer coefficient | [none] |
| $\epsilon$ | Strain | [nm/m] or [n$\varepsilon$] |
| $\lambda$ | Wavelength | [nm] |
| $\phi$ | Phase | [rad] |
| $\Delta\phi$ | Differential Phase | [rad] |
| $\sigma_\varphi$ | Differential phase standard deviation | [rad] |
| $\sigma_\varepsilon$ | Strain standard deviation | [n$\varepsilon$] |
| $\nu$ or $f$ | Frequency | [Hz] |
| $\Delta\nu$ | Laser linewidth | [Hz] |
| $\xi$ | Photo-elastic coefficient for silica | [none] |
| $B_{elec}$ | Electrical bandwidth | [MHz] |
| $B_{meca}$ | Mechanical bandwidth | Hz |
| $c$ | Celerity of light in vacuum | [m/s] |
| $c_{fibre}$ | $c_{fibre} = c/n_g$, speed of light in a fibre with index $n_g$ | [m/s] |
| $\mathbf{D}$ | Unitary diagonal $2 \times 2$ matrix: usually phase retarder | |
| $E$ | Optical field | [$2 \times 1$ vector, V/m] |
| $f_{Symb}$ | Baud rate | [MBaud] |
| $f_{Symb,carr}$ | Baud rate per carrier | [MBaud] |
| $G$ | Gauge length | [m] |
| $h$ | Planck constant | |
| $\mathbf{H}$ | Round-trip $2 \times 2$ Jones matrix | |
| $L_{coh}$ | (Laser) coherence length | [m] |
| $L_f$ | Fibre length | [m] |
| $L_{pb}$ | Polarization beat length | [m] |
| $L_s$ | Segment length: spatial sampling resolution | [m] |
| $\mathbf{M}$ | Mirror/reflection $2 \times 2$ Jones matrix | |
| $n_g$ | Refractive group index (usually in a single-mode fibre) | [none] |
| $N_{code}$ | Number of symbols that compose the code | |
| $N_{sc}$ | Number of sub-carriers | |
| $\mathbf{R}$ | Unitary rotation $2 \times 2$ matrix | |
| $R_d$ | Photodiode responisivity (chap. 1) | [none] |
| $R_{t,d,n}$ | Reliability metric (chap. 3 to 6) | [none] |
| $T_{code}$ | For coded interrogation, code duration | [s] |
| $T_S$ | Symbol duration | [s] |
| $\mathbf{U}$ | Unitary unidirectional $2 \times 2$ matrix | |

# List of Figures

# Résumé en français

Un capteur est un dispositif qui va transformer l'état d'une grandeur physique en un signal, une information manipulable. Ainsi, la thermomètre est un capteur qui va fournir une hauteur de mercure en fonction de la température ambiante, la photodiode et un capteur qui va transformer une intensité lumineuse en signal électrique. Qu'il s'agisse d'applications de sécurité traditionnelles, de la réalisation de systèmes complexes tels que les Villes Intelligentes (*Smart Cities*) ou du suivi de la performance dans les réseaux optiques (télémétrie), les capteurs sont des éléments clés de ces développements.

Il existe désormais de nombreuses méthodes de captation, parmi elles les Capteurs à Fibre Optique (CFO). Développée initialement dans les années 1980, cette famille de technologies de capteurs se distingue par son caractère distribué et s'applique dans différentes configurations, y compris celle que nous verrons dans ce travail de thèse. Les capteurs à fibre optique distribués permettent entre autres la surveillance de perturbations mécaniques (pression, étirement, déplacement) et de variations de température de façon continûment distribuée, sans la contrainte de l'alimentation énergétique que pourrait avoir un réseau de capteurs ponctuels. De plus, les fibres optiques sont un matériau résistant qui rend ainsi possible des mesures dans des environnements extrêmes ou hostiles (hautes températures, hautes pressions, interférence électro-magnétique).

La technologie des CFO repose sur la capacité qu'a la lumière de transporter de l'information, y compris l'information qui doit être captée. Plus précisément, les CFO distribués exploitent les effets de rétro-diffusion de la lumière dans la fibre optique: le principe général est celui de l'OTDR (*Optical Time Domain Reflectometer*) où des impulsions lumineuses sont envoyées dans la fibre optique, dont une fraction est rétro-diffusée par le matériau (en l'occurrence, la silice) puis est récupérée par un récepteur du même côté de la fibre optique. La rétro-diffusion se produisant en tout point de la fibre, la différence de temps de trajet des contributions rétro-diffusées donne l'information de localisation (la lumière réfléchie en début de fibre atteindra le récepteur plus tôt que celle réfléchie en fin de fibre). Une fonction de l'OTDR est de détecter des pertes, réflexions et coupures dans une fibre optique: la quantité lumineuse rétro-diffusée sera plus faible après une perte, plus importante en présence d'une réflexion, et nulle après une coupure.

La rétro-diffusion peut être "élastique", c'est-à-dire que l'émission et la réception se font à la même longueur d'onde : le phénomène exploité dans ce cas est celui de la rétro-diffusion Rayleigh, dû aux fluctuations d'indice de réfraction le long de la fibre. C'est cet

effet qui sera exploité dans la thèse. Il existe néanmoins des effets “inélastiques”, les effets Raman et Brillouin : il s'agit d'effet non-linéaires où, en réaction à une forte puissance optique envoyée dans la fibre, il se crée un réseau de fluctuations d'indice de réfraction mobile en présence de phonons optiques ou acoustiques. De la même façon que pour le Rayleigh, les fluctuations d'indice vont rétro-diffuser une partie de l'intensité lumineuse, mais cette fois-ci avec une longueur d'onde différente de la lumière incidente.

L'utilisation de la rétro-diffusion Rayleigh plutôt que d'un effet inélastique répond aux exigences du réseau de télécommunications, où chaque ressource en longueur d'onde est précieuse : le double défi est d'utiliser une faible bande passante, avec une faible puissance optique (comparable à la puissance optique des autres canaux de communication) pour éviter la création des effets inélastiques.

## La rétro-diffusion Rayleigh dans les fibres optiques

L'objectif de ce travail de thèse est d'utiliser le phénomène de rétro-diffusion de Rayleigh dans la fibre optique pour aller au-delà de l'OTDR d'intensité, et par là dépasser la simple détection des événements statiques tels que les coupures ou les réflexions.

Dans un contexte où les réseaux de télécommunications transportent des données de plus en plus stratégiques (économie, commerce, sécurité...), le coût de l'interruption de service est croissant. Il est donc nécessaire de surveiller l'infrastructure Télécom sur une échelle plus fine que la localisation des coupures, de sorte à récolter de l'information dynamique et distribuée tout au long du réseau : déplacements, vibrations, déformations... Cette surveillance n'étant pas possible sur la base de la seule captation de l'intensité rétro-diffusée, on s'intéresse à la phase. Pour permettre la captation de variations de phase le long de la fibre optique, l'utilisation d'une source laser à faible largeur spectrale (ou grande longueur de cohérence) est une condition nécessaire. On parle alors de solution de type $\phi$-OTDR ou $\Delta\phi$-OTDR ($\Delta\phi$ pour “phase différentielle”).

Les vibrations au voisinage de fibres optiques sont de nature très variée, allant d'événements fortement énergétiques et de faible fréquence comme les tremblements de terre à des événements peu énergétiques avec des fréquences élevées comme de la voix. Ainsi, les systèmes d'interrogations de capteurs à fibre optique doivent être développés de sorte à s'adapter à leur cible, et ce dans des conditions de déploiement particulières (fibres enterrées ou aériennes, fibres avec revêtement plus ou moins épais) qui peuvent agir sur le capteur comme des filtres de fréquences acoustiques (en l'occurrence, des filtres passe-bas).

La première grande partie de cette thèse s'intéresse à l'architecture du système d'interrogation du capteur à fibre optique, dont un schéma global est présenté dans la figure ci-dessous. On y étudie la pertinence de la diversité de polarisation, à la fois à l'émission et à la réception, de sorte à optimiser le seuil de détection du système de captation. En découle la présentation du système “Coherent-MIMO”, inspiré des technologies de la transmission optique à très haut débit, qui permet d'interroger la fibre optique à l'aide de codes envoyés sur deux axes de polarisation orthogonaux et de récupérer le signal rétro-diffusé à l'aide

d'un récepteur cohérent.

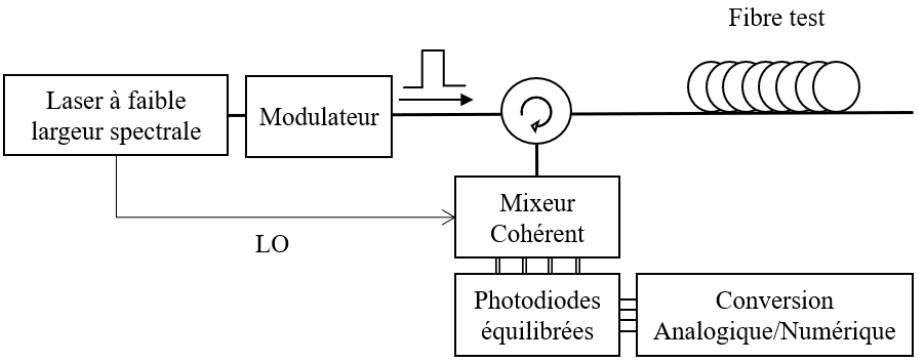


*Schéma de principe d'un $\Delta\phi$ OTDR avec détection cohérente, LO: Oscillateur Local*

Les performances du système d'interrogation Coherent-MIMO sont étudiées à la fois par simulations numériques et expérimentalement. Il apparaît que l'implémentation Coherent-MIMO permet de s'affranchir des effets d'évanouissement dûs à la polarisation dans les capteurs. D'autres expériences montrent également la possibilité qu'a l'interrogateur Coherent-MIMO de capter différents types de signaux acoustiques, dont des signaux de parole.

## Fiabilité et effets de polarisation

Comme les effets d'évanouissement dûs à la polarisation sont évités grâce à l'usage de l'interrogateur Cohérent-MIMO, il reste à aborder le sujet de l'évanouissement Cohérent, ou "bruit de scintillement" (*speckle*). Cet effet est dû aux interférences destructives qui peuvent arriver lors de l'interrogation du capteur distribué. En effet, au sein d'une même impulsion et sur une section donnée de la fibre, les contributions rétro-diffusées peuvent interférer entre elles et résulter en une intensité nulle au récepteur, créant ainsi une zone "aveugle" sur le capteur. On définit une métrique de fiabilité à partir de l'intensité rétro-diffusée mesurée au récepteur pour quantifier l'évanouissement des différentes estimations.

Une solution face à l'évanouissement cohérent est d'utiliser la diversité de fréquences, sachant que le motif Rayleigh rétro-diffusé dépend de la longueur d'onde d'interrogation. En interrogeant la fibre simultanément avec plusieurs longueurs d'ondes (ou fréquences), on peut obtenir des estimations différentes pour de mêmes segments de fibre.

Dans cette thèse, un schéma d'interrogation multi-fréquentiel est proposé sous la forme d'une interrogation OFDM (*Orthogonal Frequency Division Multiplexing*). Cette technique permet d'introduire une diversité fréquentielle numérique, sans apporter de modification au schéma optique de l'interrogateur : en envoyant plusieurs signaux d'interrogations en parallèle sur des sous-porteuses fréquentielles orthogonales entre elles. A la réception, on récupère les plusieurs estimations par segment de fibre et par instant. Ces estimations sont ensuite combinées constructivement de sorte à maximiser la fiabilité de l'estimation.

On montre une amélioration de la fiabilité des mesures grâce à l'interrogation OFDM (2 ou 4 sous-porteuses), et par conséquent une diminution des fausses alarmes sur la

phase. Des mesures ont été faites le long d'un câble télécom déployé sous une route (figure ci-dessous), les fausses alarmes (en rouge) disparaissent dès l'utilisation de deux sous-porteuses pour l'interrogation.

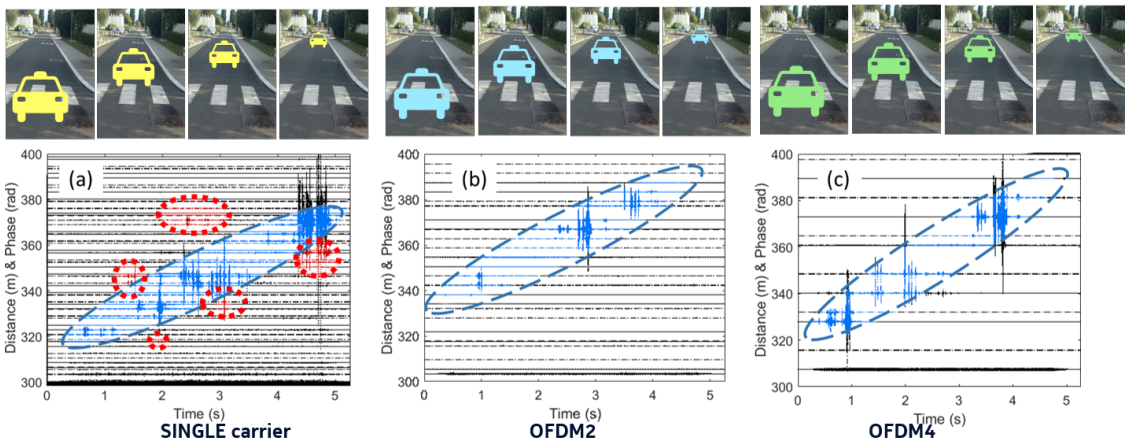


*Interrogations d'une fibre déployée sous une route avec 1, 2 et 4 sous-porteuses OFDM, détection de trajectoires d'une automobile*

L'interrogation MIMO-OFDM propose un compromis entre résolution spatiale, occupation spectrale et fiabilité de la mesure de phase, pour affronter la problématique du bruit de scintillement. Le compromis, ainsi que la recherche du nombre optimal de sous-porteuses OFDM, sont étudiés dans le manuscrit.

## Co-existence dans une liaison télécom

Une fois les outils d'interrogation présentés, cette thèse s'intéresse à des implémentations plus réalistes en terme de CFO à interroger. Le premier aspect commun aux fibres de télécommunications déployées est la distance : il est rare que les réseaux déployés soient constitués de sections de fibre inférieurs au kilomètre, à part dans les réseaux d'accès ou les centres de données. En s'aidant de résultats de modélisation et avec une interrogation Cohérent-MIMO, on étudie dans un premier temps le comportement de la phase rétro-diffusée le long d'une section de 50km de fibre.

Le deuxième aspect est le caractère déployé de la fibre, pour lequel on s'intéresse à des configurations comme mentionnées précédemment pour la détection de trajectoire en utilisant le MIMO-OFDM. Contrairement aux fibres en laboratoire où il est possible d'appliquer des contraintes localement, les fibres déployées sont soumises à des perturbations soit ponctuellement soit dans toute une zone, certaines perturbations sont permanentes (e.g. une pompe en bout de canalisation) et d'autres sont dynamiques (e.g. un véhicule). Toutes ces contraintes et perturbations sont autant de sollicitations pour le multi-microphone qu'est la fibre optique.

Le troisième aspect, enfin, est la nécessaire co-existence des signaux de télécommunications avec le signal d'interrogation : une dernière expérience montre la possibilité d'utiliser le système d'interrogation Coherent-MIMO en présence de données en transmission dans des canaux adjacents, et ce avec un coût minimal en bande passante. En effet, non

seulement l'expérience montre la capacité de capter un phénomène acoustique après plus de 80km de fibre optique, elle montre aussi qu'il est possible de le faire avec un espacement de moins de 4GHz entre les canaux de télécommunication et le canal dédié à la captation $\Delta\phi$-OTDR (figure ci-dessous), et ce sans impact sur la qualité de transmission des données dans les canaux adjacents.

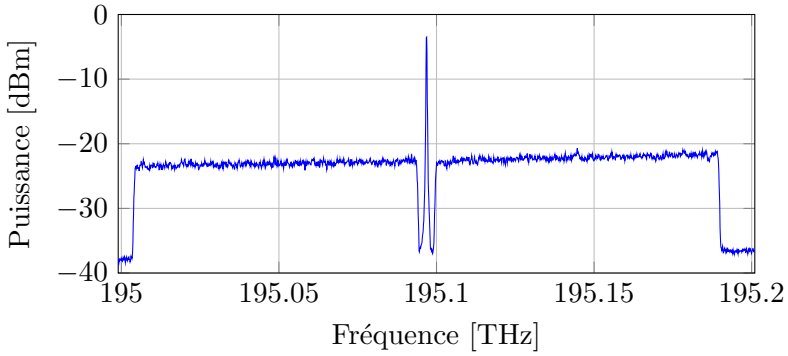


*Spectre optique de deux canaux télécom espacés chacun de 2GHz du signal d'interrogation*

## Perspectives

Cette thèse aura permis d'aborder les problèmes les plus courants de la captation distribuée sur fibre optique, à savoir l'évanouissement (en polarisation ainsi qu'en intensité : le bruit de scintillement), et aura été l'occasion de chercher les limites de l'interrogation de fibre à la fois en distance (jusqu'à 82km) et en bande passante mécanique (détection de signaux de parole dans une bande passante de 6.1kHz).

Il aura été montré que l'interrogation Coherent-MIMO, et plus généralement l'introduction des technologies en provenance des télécommunications optiques à haut débit, sont un ajout considérable à l'écosystème des CFO distribués.

Les prochaines étapes de ce sujet d'étude seront assez diverses, allant de la problématique de la collecte et du traitement de grande quantités de données, de l'acquisition en temps réel, à la question du dépliement de la phase dans des conditions de fortes perturbations, ou du traitement de l'état de polarisation rétro-diffusé.

# Introduction

## Sensors and fibre optics

A sensor is a device that reacts to changes in its environment, such as movement, pressure or heat, converting the measurands into electronic signals that can be read, processed and collected. Be it for traditional security applications such as infrastructure monitoring and intrusion detection or supporting the development of complex systems such as smart cities, sensors are key agents in the development of modern societies. Nowadays, a wide variety of point sensors and sensing technologies are available, namely electronic, piezoelectric or micro-electro-mechanical systems (MEMS) sensing devices. In the 1980s, a technology of distributed sensors was suggested (as opposed to point sensors): Distributed Optical Fibre Sensors (DOFS) technology, which is the shared foundation for diverse sensor types including those which will be discussed in this thesis. The use of distributed sensors allows to monitor mechanical perturbations and temperature variations in a spatially continuous manner, without any constraints such as remote energy supply that would occur for point sensors. Besides, optical fibres allow sensing in extreme environments (high pressure or temperature conditions, electro-magnetic interference), therefore solving new issues in hostile environments [1].

The distributed optical fibre sensor technology relies on the capacity of the light to convey the information, including the information which is sensed. More precisely, DOFS rely on the backscattering effect of light inside the fibres. The general principle is that of Optical Time Domain Reflectometry (OTDR), where the interrogating instrument launches a series of light pulses into an optical fibre. As the probe pulses travel along the fibre, a small fraction is scattered by the propagation medium and returns to the launching end of the fibre, where it is captured by a detector. Light which is reflected near the launching end of the fibre will reach the detector faster than light that reflected at the end of the fibre, hence localization information can be accessed. One main application of OTDR is to allow the detection of breaks, losses and attenuation in the fibre.

OTDR relies on the Rayleigh scattering effect, which is due to refractive index inhomogeneities in the fibre, with a scale smaller than the interrogation wavelength (small-scale). The effect is "elastic" as the energy of the scattered photons is preserved, as pictured in Figure 1. Rayleigh backscattering in optical fibres is mainly strain-sensitive in addition to be useful for losses and breaks detection, though the refractive index fluctuations are also temperature-dependent. It allows to measure with a fine spatial resolution up to the

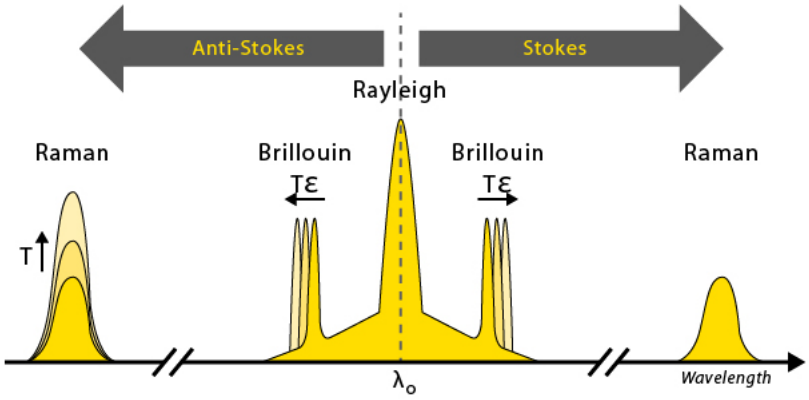


Figure 1: Illustrative spectra of backscattering mechanisms in optical fibres, after interrogation with a $\lambda_0$ light source. Source: febus-optics.com

centimetre scale [2] and ranges up to several tens of kilometres [3].

Other scattering effects coexist with Rayleigh scattering in optical fibres: Brillouin scattering is due to small scale refractive index fluctuation as well, however the fluctuations are driven by phonons after interaction of light and acoustic waves. This yields a frequency shift of the backscattered spectra (the effect is inelastic), with Stokes and anti-Stokes components, of the order of 11GHz in silica for $\lambda_0 = 1550$nm, as pictured in Figure 1. Brillouin effect results in the creation of a dynamic refractive index grating in the fibre, linearly dependent on both temperature and strain. Brillouin sensors range up to hundreds of kilometres and can reach spatial resolutions of the order of the meter [4].

Raman effect finally, is an inelastic scattering effect resulting from light-matter interaction. As light interacts with the transmission medium, optical phonons are absorbed and released, thus creating Stokes and anti-Stokes frequency components, typically of the order of few THz to tens of THz, 13THz away from the excitation wavelength in silica. The anti-Stokes component is temperature-sensitive, with a precision of the order of $0.1°C$ [5]. Raman-based temperature sensors have a range from several kilometres up to several tens of kilometres [6].

## Rayleigh backscattering in optical fibres

In the context of the deployment of the Internet of Things (IoT) and the development of smart cities, the telecommunication infrastructure is more than relevant. Indeed, telecommunication fibres are already being deployed all over the globe, telecommunication equipment is being produced and deployed at a global scale, thus reducing the costs and facilitating the transfer of technologies to other fields of application. Standard Single Mode Fibre (SSMF) is at the basis of long haul and metropolitan fibre networks. Similarly to all other types of optical fibre, it can be used as a distributed sensor. While dedicated fibres are used for public and industrial infrastructure monitoring (bridges, power plants) [7], sensing through deployed telecom fibres enable network management and monitoring for

operators, road or train traffic monitoring (as fibre cables of the terrestrial links are deployed along these routes), or even intrusion detection around and inside buildings.

Rayleigh scattering is especially suited for sensing over telecommunication infrastructure applications, which will use telecommunication wavelengths and thus existing telecommunication equipment. Indeed, it does not require to stimulate scattering onto different frequencies (i.e. wavelengths, in this particular case of Wavelength Division Multiplexing (WDM) in optical transmission) unlike for stimulated Brillouin scattering-type sensors. Besides, Raman scattering is far outside the telecommunications equipments' bandwidth.

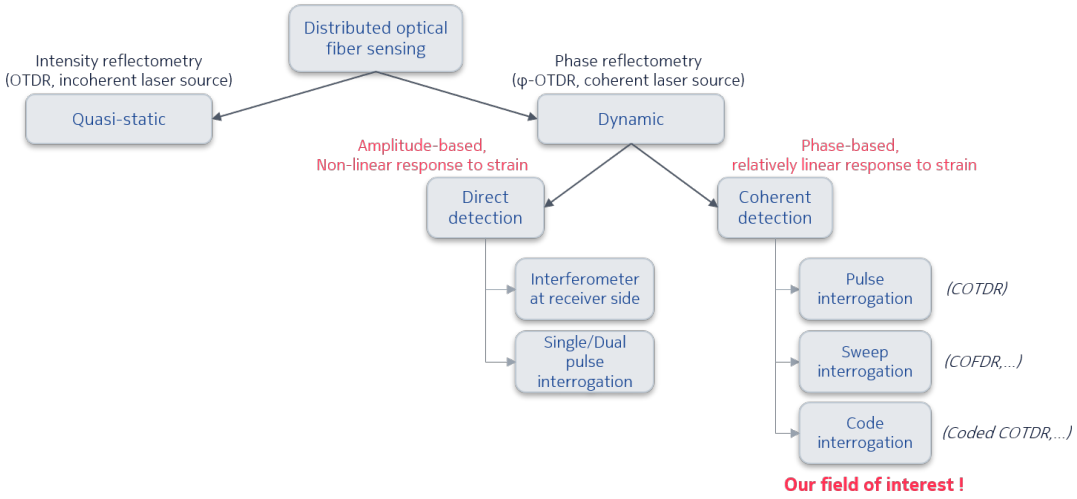


Figure 2: Distributed Rayleigh sensing tree of technologies

Figure 2 displays the main sensing techniques deriving from Rayleigh scattering. Besides the already mentioned OTDR technique which is used for the detection of static impairments or breaks and which trace is represented as the upper black line on Figure 3, techniques based on coherent laser sources such as $\phi$-OTDR or $\Delta\phi$-OTDR allow to monitor dynamic events along the fibre sensor by capturing the phase variations of backscattered light, therefore allowing for Distributed Acoustic Sensing (DAS). A typical coherent $\phi$-OTDR trace is given in Figure 3 as the red trace. DAS will focus on mechanical events, namely small displacements consequently to the occurrence of a mechanical wave, sound or strain.

Very diverse acoustic disturbances occur in the neighbourhood of deployed telecommunication fibres, from very low frequency events with high energy such as earthquakes, to higher frequency events with large mechanical bandwidth and lower energy such as speech. In addition, the environment and properties of these deployed fibres is diverse too, be it the depth of burial and the nature of the ground in case the fibre is buried, the length of the fibre, its coating... The development of a sensing interrogator in that context is challenging as it must consider sensitivity, reach, spatial resolution and mechanical bandwidth as an ensemble of parameters to be jointly optimized.

Recent works [8, 9] demonstrated sensing capability for low frequency events on trans-oceanic fibre distance, and [10] reported the longest range DAS measurements using low-

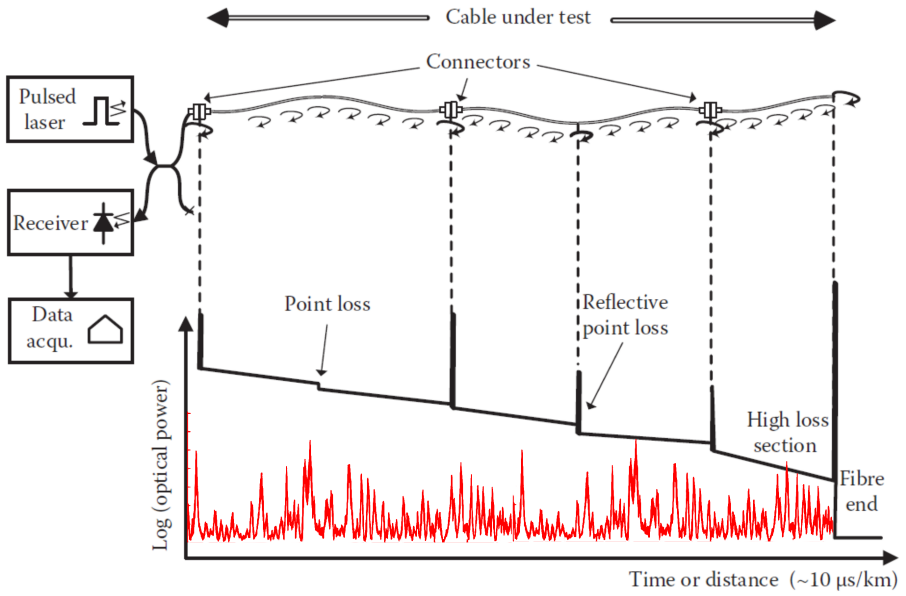


Figure 3: Intensity OTDR (black) compared to speckle pattern (red), adapted from [1]

loss fibre using their own commercial solution. Meanwhile, [11] investigated the methods for reducing the noise floor for precise DAS measurements over shorter fibre distances. On the other hand, [12, 13] included the telecom network aspect to their work, therefore introducing new concerns such as the spectral occupancy of a DAS interrogation signal, the network configurations that are not necessarily a single fibre span or the coexistence of a sensing channel with WDM data channels over multi-span systems containing a diversity of components: amplifiers, multiplexers... Acknowledging the multitude of aspects that DAS addresses, and concious of the need for lightweight solutions, this work aims at the development of a flexible fibre interrogator, adapting to network architectures as well as reaching longer distance and measuring with a high dynamic range, without bringing much complexity to its optical hardware implementation.

## Thesis outline

In this thesis, we show how distributed optical fibre sensors can be designed on top of telecommunication fibres, namely standard single mode fibres, and explore their potential in terms of reach, sensitivity, and sensing bandwidth.

The first chapter is titled “Interrogation, estimation, and processing. Adapting to the context” as it addresses the general concepts of sensors, the usual hardware set-ups used for distributed fibre sensing, and the different categories of fibre sensor interrogation. A brief overview of the diverse use-cases is done as well. Then, chapter 2 dives into some theory as a dual-polarization backscattering model is built to begin with the study of distributed optical fibre sensors (DOFS): the fibre sensor is modelled, the transmitter and receiver noise are studied, a dynamic version of the model is briefly investigated. Chapter 3: “Polarization effects and reliability” first explores the polarization fading mechanism in fibre sensors as a function of the interrogation method, and suggests a method which is immune to polarization fading. Then, the detection threshold of $\Delta\phi$-OTDR measurements

is further investigated as a specific reliability metric is developed. Taking advantage of the polarization fading immune interrogation method and reliability metric, some experiments are conducted in chapter 4. The investigated parameters are mostly the detection threshold and bandwidth of the fibre sensor, as the fibres under test in this chapter are rather short (no more than 2km). Chapter 5 investigates the second main issue in DOFS: coherent fading (the first being polarization fading). A digital frequency diversity interrogation method is developed, and experienced to cope with this issue. Finally, some more experimental studies are conducted in chapter 6 to validate the techniques proposed throughout the manuscript, investigating the range of the proposed distributed fibre interrogator.

# Chapter 1

# Interrogation, estimation, and processing. Adapting to the context

Telecommunication fibres are being deployed all over the world, from town to cities to oceans. Monitoring such an infrastructure has become mandatory, and that beyond the sole localization of breaks. Also, the use of distributed sensors over deployed cables can help detect natural hazards such as earthquakes and thus protect populations. At the same time, the deployment of the internet of things and the development of smart cities is requiring a huge amount of sensors, whose cost and complexity could skyrocket if aggregated solutions (as opposed to point sensors) are not considered. We will see that distributed optical fibre sensors (especially when designed on top of deployed telecommunication fibres) offer such aggregated sensing solutions.

This chapter addresses the general concepts of fibre-optic sensing, from the sensor to the interrogation unit. Metrology concepts are given, before diving into the specifics of Rayleigh distributed sensors. The first section: "Description of a distributed vibration sensor", discusses the properties of the sensor and interrogation systems as we introduce the accurate vocabulary for the following of our study. Metrology notions are introduced, followed by elements on the Rayleigh scattering effect and on the reflectometry-based optical sensors. Then, in the second section: "Measurement of the phase, state of polarization, and intensity", we draw more attention to the interrogator system and address the main methods that can be used to probe an optical fibre sensor. Depending on the type of measure it is supposed to capture, the sensor will be probed differently. As a consequence, specific constraints will apply in terms of reach, bandwidth and sensitivity. The interrogation set-up that is used in the following chapters will be described and different use cases will be discussed.

## 1.1 Description of a distributed vibration sensor

Optical fibre sensors are a promising technique to meet telecommunications operators expectations in terms of network monitoring and maintenance, and more generally to address the needs of industrial users in terms of deployment, volume, maintenance. In this section and after the general definition of a sensor, we give an overview of the principles of distributed vibration sensors, mainly those which exploit the Rayleigh backscattering effect for sake of interoperability with telecommunication networks.

### 1.1.1 Metrology tools

A sensor is a device which transforms a physical phenomenon into any object a user can handle, such as physical metrics. The stakes for developing a reliable sensor are bound up with metrology concepts, and the main elements are recalled below.

**General notions of measurement** The quantity to be measured is called a **measurand**. The objective of a measurement is to determine the value of the measurand [14], in general in the form of an estimate accompanied by an uncertainty of that estimate. Also in many cases, the result of a measurement is determined on the basis of series of observations obtained under **repeatability** conditions. Figure 1.1 illustrates the terms which are introduced below.

- **Uncertainty** characterizes the dispersion of the values that could reasonably be attributed to the measurand, the underlying idea being that the measurement result is a random variable, therefore uncertainty is somehow defined to characterize the width of a statistical distribution [15]. It can be expressed in terms of standard deviation, or confidence interval for example.
- **Repeatability** is defined as closeness of the agreement between the results of successive measurements of the same measurand carried out under the same conditions of measurement [14]. It may be expressed in terms of the spread, or dispersion of the result. Repeatability is supposed to characterize the measurement instrument alone, having excluded all external influence (operator, object, time delay between measurements...).
- **Reproducibility** is the closeness of the agreement between the results of measurements of the same measurand carried out under changed conditions of measurement, i.e. including all external influences, as well as the method of measurement, etc. The reproducibility is commonly referred to as “Precision”.
- **Error** (or absolute error of measurement) is the result of a measurement minus the true value of the measurand [14]. It is typically constituted of a random component and a systematic component. The systematic error is commonly referred to as “Accuracy”. Even if the true value is never known, practically an estimation can be obtained using a second measurement system whose error is known and lower than the one for the measurement system we wish to characterize.

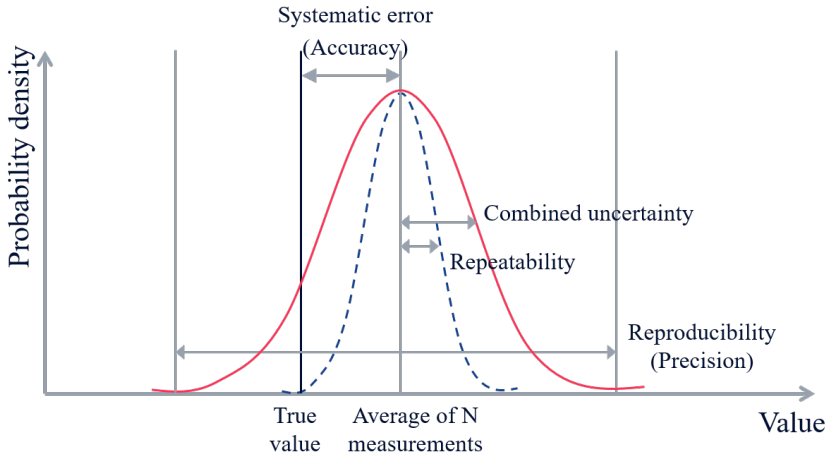


Figure 1.1: Main metrology terms, for a probability density distribution of N measurements

**Measurement instrument** One should differentiate between the sensor and the measurement instrument or system. A measurement instrument (or system) is characterized in particular through the characteristics of the sensor, namely its measurand(s), its error (or accuracy) and reproducibility (or precision). Other important parameters to characterize the measurement system are: the **sensitivity**, the **distinction threshold**, the (mechanical) **bandwidth**, the **range**, and the **linearity**. The response time and dynamic range can be considered as well.

- The **sensitivity** is defined as the variation of output signal as a function of a variation of the measurand at the input
- The **distinction threshold** is defined as the smallest measurand variation the system can detect, or conversely the highest variation of the measurand which doesn't change the sensor response.
- The **mechanical bandwidth** is the frequency range in which a mechanical event (eg. vibration, acoustic signal in our case) is captured and rendered by the system.
- The **range** is the interval over which the instrument can measure the measurand, for distributed sensors we extend the definition to the maximum distance over which the measurement instrument can operate.
- **Linearity** is the capability of the signal to give a linear response as an output when a linear variation of the measurand is done at the input
- The **dynamic range** is the range over which a measurand is detected with reasonable accuracy, defined as the difference between the highest measurable measurand quantity (before saturation) and the distinction threshold.

**Sensor array** In case of distributed sensors, a notion of multiple sensors is introduced, as the sensor is actually an array of sensors, as pictured in Figure 1.2: a measure $m$ will be given not only as a function of time $m(t)$ but also as a function of distance $m(t, d)$. Therefore, we introduce the notion of **spatial resolution**, which is the resolution with

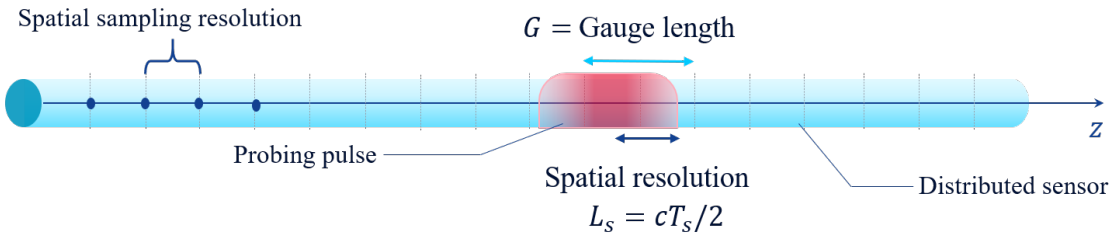


Figure 1.2: Spatial resolution, spatial sampling and gauge length examples for a distributed sensing system

which the backscattered light is measured ; it is the smallest distance along the sensor array for which two distinct measurand values can be retrieved [16], or conversely the largest distance along the sensor for which a measurand difference will not be reported by the system.

The configuration of the measurement instrument comprises an interrogation frequency and a sampling frequency at the receiver side, which in turn defines a **spatial sampling resolution**, that can be very different from the true spatial resolution of the sensor. Finally, the **gauge length** of the system is defined consequently: is the spatial resolution with which the measurand is measured by the system, it is a distance as well. It is defined by the manufacturer [16], likely as a multiple of the spatial sampling resolution, namely the closest to the true spatial resolution (e.g. $G = \lceil L_s \rceil$).

In this work, spatial sampling resolution will refer equally to the resolution at the receiver after analogue to digital conversion, and to the spatial sampling resolution after possible downsampling at the digital signal processing stage in which case the downsampling factor will be given.

### 1.1.2 General principles for Rayleigh distributed sensing

Optical fibre is mainly composed of silica glass, and manufactured in order to have a refractive index difference between the silica glass of the core (in the general case the refractive index is $n_1 = n_1(r)$ where $r$ is the radius of the fibre, in single mode step-index fibres $n_1$ is constant) and the silica glass of the cladding (index $n_2 < n_1$) such that the light injected in the core stays confined due to total internal reflection effect at the core-cladding interface. Figure 1.3 gives an illustration of a step-index single mode fibre.

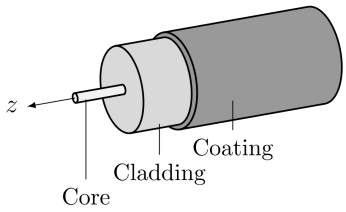


Figure 1.3: Typical step-index Single Mode Fibre composition

In a Single-Mode Fibre (SMF), the cladding diameter is usually of 125$\mu$m and the core radius below 10$\mu$m.

During the manufacturing process of an optical fibre, namely the preform construction and drawing of the fibre, the material of the core may not have uniform properties: the distribution of density is frozen during the fast cooling of the fibre after drawing [17]. Therefore the refractive index will slightly fluctuate along the fibre, on a small scale compared to the light wavelength.

When these fluctuations are illuminated by an incident wavelength which is larger than the scattering centres, they are responsible for the Rayleigh scattering effect, which is the main loss mechanism in SMF nowadays. Indeed, the density fluctuations scatter the incident light in all directions, at the same wavelength since Rayleigh scattering mechanism is an elastic scattering: energy, thus frequency of the scattered photons is the same as that of incident photons. Although the light backscattered in the backward direction can be retrieved, the remaining scattered light ends into cladding modes of the optical fibre and is lost. In the following, the regions where the refractive index is different from the mean value may be referred to as "**scatterers**" [17].

Silica is especially interesting as a material to transmit light since it presents an attenuation (mainly due to Rayleigh scattering effect) below 0.4dB/km for wavelengths around $\lambda = 1300$nm and about 0.2dB/km around $\lambda = 1550$nm. The Rayleigh scattering coefficient is proportional to the inverse fourth power of wavelength; in pure silica, it is of $0.7\,\mathrm{dB\,km^{-1}}\mu\mathrm{m}^{-4}$ [17]. Note that the Rayleigh scattering effect is stronger in case of smaller wavelengths [18].

**Polarization beat length** One other consequence of inhomogeneities in the fibre due to the manufacturing process is the random evolution of birefringence in the fibre, leading to variations of the polarization of a lightwave propagating in the fibre. The birefringence in optical fibres is often presented as a difference of the refractive index $\Delta n$ between the two axes along which the electromagnetic field oscillates (namely $x$ and $y$ as light propagates in the $z$ direction), or two polarization modes. The "speed" at which the polarization changes can be characterized by the polarization beat length $L_{pb}$, which depends on $\Delta n$ as follows: $L_{pb} = \lambda_0/\Delta n$, where $\lambda_0$ is the vacuum wavelength (not the wavelength in the medium) [19]. If two waves propagating in the birefringent fibre with different polarizations were originally in phase at $L = 0$, then their phase delay will be maximum after $L = L_{pb}/2$ and they will go back in phase after $L = L_{pb}$.

Note that apart from manufacturing imperfections, polarization variations are also related to random mechanical stress and twists applied over the deployed fibre.

**Distance-resolved measurements** It was already indicated that the Rayleigh scattering mechanism scatters the incident light in all directions, at the same wavelength. Only a fraction of the incident light is scattered (scattering intensity proportional to $1/\lambda^4$ where $\lambda$ is the wavelength of the propagating optical signal), and in turn only a fraction of the scattered light is backscattered towards the launching end of the fibre (the remaining scattered light vanishes into cladding modes, as stated above). However, when probing the fibre with sufficient input power, the backscattered light can be measured. The tech-

nique consisting in probing an optical fibre by means of light pulses and retrieving the backscattered light is called Optical Time Domain Reflectometry [20] (OTDR). A notion of distance from the reflection location $d$ is obtained as a function of the time delay $\Delta t$ as follows:

$$d = \frac{c\Delta t}{2n_g} \tag{1.1}$$

with $n_g$ being the group refraction index, $c$ the celerity of light in vacuum, the factor '2' stands for the round-trip in the fibre.
Now, the use of fibre as a sensor is interesting because of several properties in addition to the low loss along distance as mentioned above, namely:

- Optical fibre is compact and lightweight, so it can be shaped to match different types of spaces or environmental constraints
- Optical fibre sensors can convey the information (in optical form) from a hostile environment such as very-high temperature or pressure environment (namely borehole, oil-and gas applications)
- Optical fibres can be immune to electro-magnetic effects and thus be installed alongside energy cables, yet they can be used as current or voltage sensors using Faraday effect
- The high bandwidth of optical fibres allows to multiplex different optical signals, therefore multiple sensors could be multiplexed, for example.

Moreover, the literature shows that optical fibre can be used as a sensor for a wide variety of measurands, such as displacement, pressure, electrical current, radiation, temperature and strain.

Finally, we call "interrogator" the transmitter and receiver unit which come together with the fibre sensor to form the full measurement device. Transmitter elements are mostly a laser source and a modulator, sometimes completed by an amplifier, whereas receiver elements consist in a detector, and further signal analysis material. In the next subsection, we explore the main set-ups for measurements devices based on Rayleigh backscattering or similar.

### 1.1.3 Hardware of a sensing system

Outside the conventional optical time domain reflectometer (OTDR) which we describe below, optical fibre sensing principles are based on interferometry either using heterodyne detection at the receiver (beating of reference signal and received signal) or with a coherent source where intra-pulse interference occurs, giving rise to 1-D speckle.

**Interferometric sensors** The most intuitive fibre sensors are the following class of interferometric sensors, based on homodyne or heterodyne detection [21]. Figure 1.4 presents an interferometric fibre optic sensor based on a fibre optic Mach-Zehnder configuration where the signal arm is used as a sensor: for sensing pressure, strain, electric and magnetic fields.

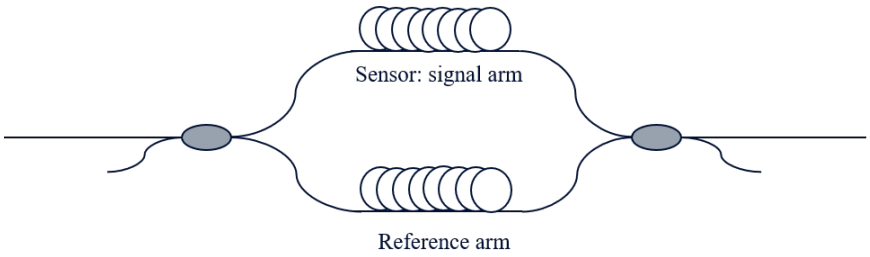


Figure 1.4: Interferometric fibre optic sensor, Mach-Zehnder configuration, adapted from [22]

Other interferometric sensors implementations were studied, including Michelson, fibre Fabry-Perot, Sagnac, and ring-resonator configurations [23]. Such sensors are mostly used for quasi-distributed fibre sensing, where many of them are multiplexed along a single mode fibre, for example.

Such sensors have a limited size due to the need for keeping a non-disturbed reference arm. Therefore, the usage of interferometric sensors is rather punctual or quasi-distributed (when several small interferometric sensors deployed along a longer optical fibre). Applications such as long distance distributed sensing, single-ended sensing are not well suited for interferometric sensors.

**Optical Time Domain Reflectometer (OTDR)** Figure 1.5 gives the most common OTDR arrangement, where light pulses are delivered by a laser and sent into a sensor fibre. This fibre sensor configuration was initially referred to as "amplitude sensors" as opposed to interferometric sensors [21].

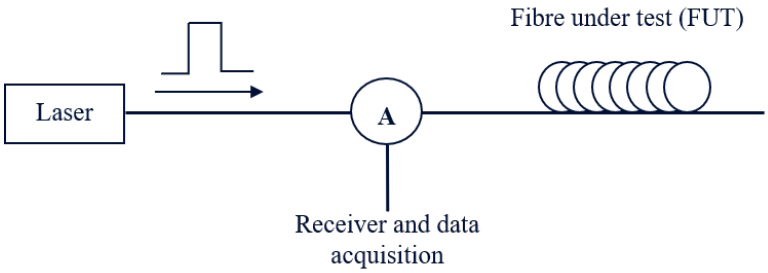


Figure 1.5: Optical Time Domain Reflectometer set-up, where element **A** is either a coupler, a fast switch [**Nakazawa˙fastswitch˙1981**], or a three-port circulator

The returning backscattered light is redirected towards the receiver thanks to either a directional coupler (passive directional coupler to avoid reflections from within the device [1]) or a three-port circulator (more efficient solution). The receiver generally consists of a photodetector and an electrical pre-amplifier (direct detection), similarly to low-cost optical telecommunication systems.

Overall, the backscattered intensity is monitored [24] to track possible losses or breaks along the fibre sensor. Since the spectral width of the laser used for OTDR interrogation is usually broad (gigahertz range, yielding coherence length[1] shorter than pulse width), the

[1]Coherence length is further developed in section 2.2.

fluctuations of the return signal due to interference is avoided (light adds incoherently).

Conversely, in case the coherence length of the source is larger that the pulse width, the source is called *coherent*. In that case, backscattered light interfere within the probing pulse width (intra-pulse interference), yielding a fluctuating return signal. Such fluctuations are considered an undesirable source of noise in conventional OTDR. Figure 1.6 illustrates the difference between the OTDR intensity traces resulting from coherent and incoherent sources.

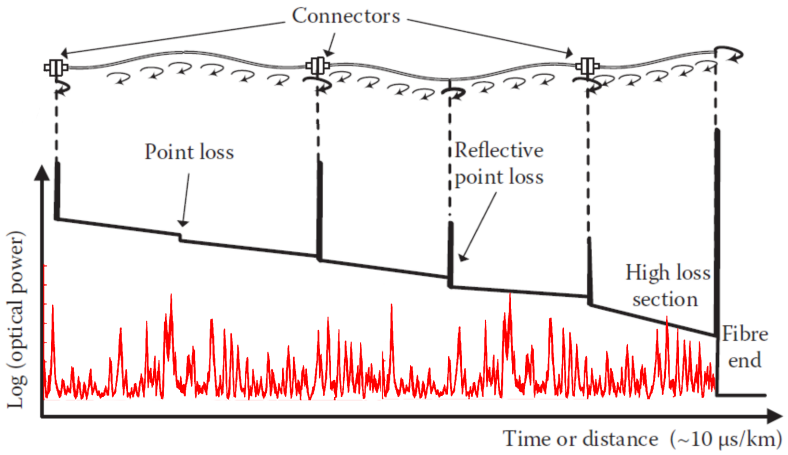


Figure 1.6: OTDR intensity trace from coherent (red, below) and incoherent (black, above) source interrogations, adapted from [1]

**Polarization OTDR** Polarization-OTDR (POTDR) is a special OTDR case where polarization analysis is performed at the reception of the backscattered light, which was developed in the wake of the conventional OTDR [25, 26].

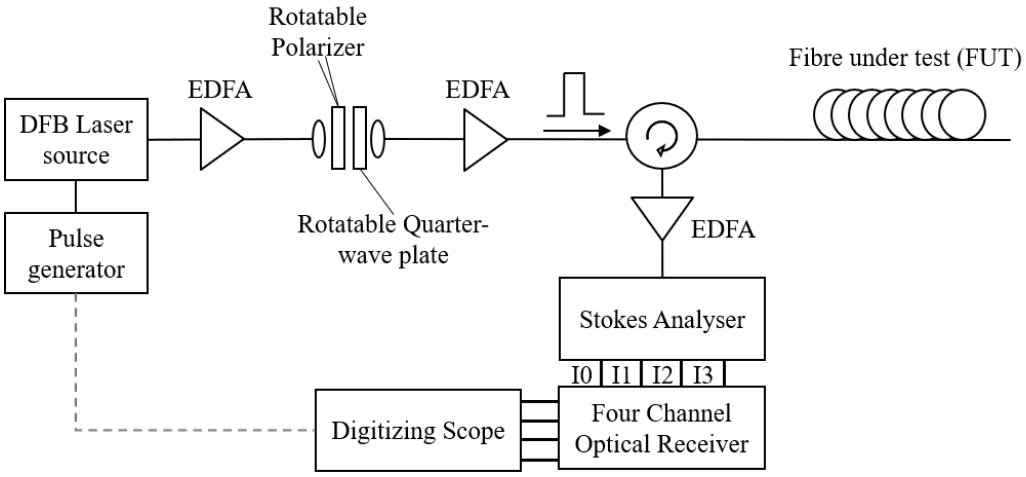


Figure 1.7: Set-up of a polarimetric OTDR system, adapted from [27]. DFB: Distributed FeedBack laser, EDFA: Erbium-Doper Fibre Amplifier, I1 to I3 are the Stokes parameters

Rayleigh scattering and a fortiori Rayleigh backscattering effect preserves the State Of Polarization (SOP) of the probe pulse. The idea of POTDR is to measure the backscattered light on two polarization axes: the one parallel to the probe pulse and the orthogonal state. The total backscattered power is the sum of both measurements and returns an

OTDR trace which is more accurate than that of a conventional OTDR. In the first implementations, a polarizer is included at the emission and polarization analyzer at the reception to read the backscattered polarization information in the form of S parameters, as pictured in Figure 1.7.

The other advantage is to effectively track the SOP evolution along the fibre. However, because of the two-way propagation of light in the fibre sensor, some circular birefringence contributions are cancelled by the round-trip and thus cannot be analysed using usual Jones calculus[2]. Simultaneous acquisition of Stokes parameters allowed to increase the acquisition rate of the SOP [28]. Since polarization is affected by twists or bending of the fibre sensor, POTDR was applied to distributed pressure sensing and to the localization of fibre coils [29]. Another application of P-OTDR are fully polarimetric OTDRs. They were developed for the study of fibre birefringence during fibre manufacturing stage and spooling process [27].

**Phase-OTDR** Coherent-OTDR (COTDR), or phase-OTDR ($\phi$-OTDR) takes advantage from the speckled intensity pattern obtained when a coherent source is used (see Figure 1.6 above). In order to achieve $\phi$-OTDR, the basic OTDR scheme from Figure 1.5 requires some adjustments: the laser is replaced by a very narrow linewidth, continuous wave (CW) laser source [30], which is modulated into a probing signal that is sent to the fibre sensor. The linewidth is considered narrow from 10kHz [30] to below the Hz [8] depending on the fibre sensor distance to span and to the sensitivity requirements of the system. Practically, we get from OTDR to $\phi$-OTDR from the point where backscattered light comes in a jagged or speckled pattern [31, 32]: coherent backscattered light interferes within the interrogating pulse which results in 1-dimensional speckle at the receiver [33] (intra-pulse interference). Moreover, the speckle pattern is dependent on the probing wavelength, for the same reason that makes the Rayleigh scattering dependent on the wavelength.

Several receiver implementations allow to recover the phase information from coherent backscatter. Using direct detection, we obtain "phase-sensitive OTDR" or $\phi$-OTDR, whose traces are a plot of returned optical power versus time [34], such as for conventional OTDR. However, subtracting successive $\phi$-OTDR intensity traces allows to retrieve the effect of phase change resulting from strain, pressure or temperature change.
Then, detection is possible with balanced detectors and heterodyne detection to enhance the dynamic range and spatial resolution [35], one possible implementation is depicted in Figure 1.8. The different reception schemes will be addressed later in section 1.2.

Overall, COTDR and $\phi$-OTDR appellations are alternatively used to describe an OTDR device which source satisfies intra-pulse interferences, allowing to get speckled power-versus-time traces, from which phase information can be extracted.

**$\Delta\phi$-OTDR** An outline schematic of a $\Delta\phi$-OTDR set-up with coherent detection is presented in Figure 1.9. To recover the phase using coherent detection, the narrow-linewidth

[2]Jones calculus is described in the following chapter.

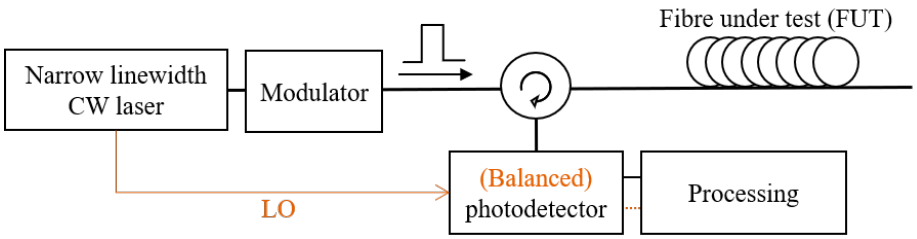


Figure 1.8: Outline schematic of a $\phi$-OTDR set-up, possibly (in orange) using heterodyne detection and balanced photodetection

source will be used both as the probing signal and as the local oscillator (LO) from homodyne or heterodyne reception at the receiver side, therefore it is split into two paths. At the receiver side, either a balanced photodetector [36] or a polarization-diversity coherent mixer (made of two $90^o$ hybrids) followed by balanced photodiodes is used. The detectors are fed by both the LO from the narrow linewidth source and the backscattered signal from the circulator. They are followed by analog-to-digital conversion. A more detailed overview or optical receivers is given later in subsection 1.2.2.

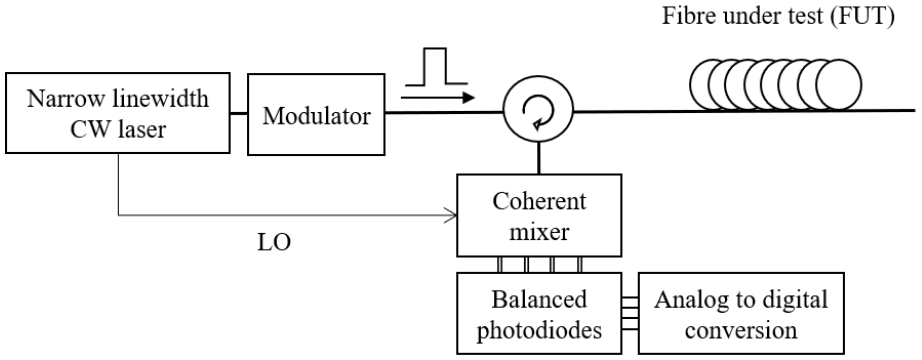


Figure 1.9: Outline schematic of a $\Delta\phi$ OTDR set-up with coherent detection

Note that the coherent mixer and photodiodes in Figure 1.9 are displayed with 4 outputs, illustrating the in-phase and in-quadrature outputs for both polarizations: therefore the coherent mixer here is a dual-polarization coherent mixer. In some implementations, a single-polarization coherent receiver is used, such that Figure 1.8 with heterodyne balanced photodetection can be used as a $\Delta\phi$-OTDR setup. Such an interrogator allows to directly recover the phase of the backscattered light, therefore the detection of multiple disturbances along the fibre sensor is done by processing the differential phases between spatial fibre segments.

**Coherent-MIMO** Willing to make the most of all optical parameters, the Coherent-MIMO set-up, where MIMO stands for Multiple Input, Multiple Output, is displayed in Figure 1.10. Inputs and outputs correspond to two orthogonal polarization states of light at the TX and RX respectively.
Coherent-MIMO extends the possibilities of polarization diversity to the transmitter side in addition to keeping a dual-polarization coherent mixer at the receiver side. The received data are further processed in the digital domain, either on-chip or via a computer. The

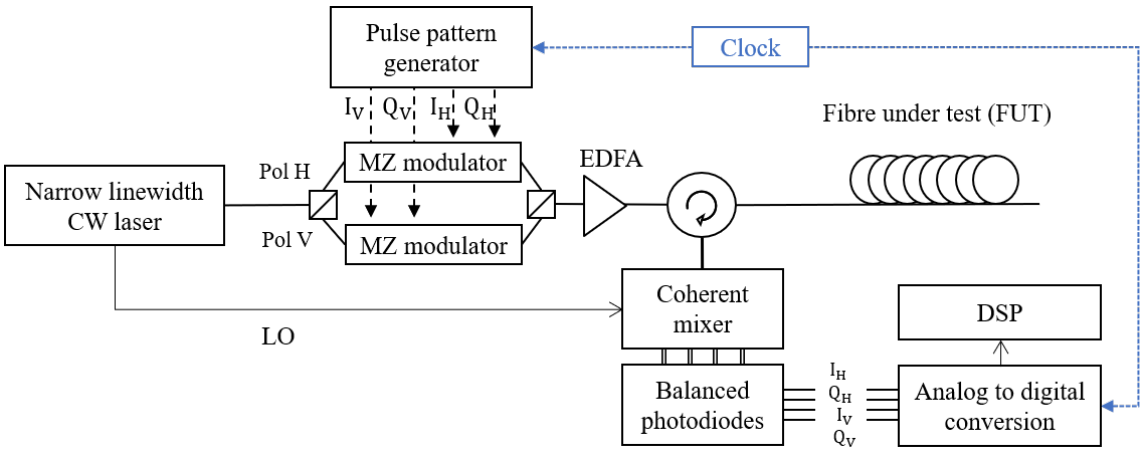


Figure 1.10: Outline schematic of a coherent-MIMO set-up. DSP: Digital Signal Processing; CW: Continuous Wave; LO: Local Oscillator; MIMO: Multiple In, Multiple Out; MZ: Mach-Zehnder

principles and advantages of Coherent-MIMO sensing will be discussed in the following chapters.

Yet, note that over the years of the development of the OTDR, from simple OTDR setups Figure 1.5 to the Coherent-MIMO interrogator Figure 1.10, the influence of modern optical telecommunications is significant.

#### 1.1.3.1 Signal generation and processing

Now that we have described the main OTDR-related implementations, we further detail the probing signal and phase retrieval.

**Probing signal generation** To modulate the probing light, one option is to use an acousto-optic modulator (AOM) which is driven by an electrical signal. The AOM performs both modulation and frequency shifting operations, possibly[3] leading to heterodyne detection at the receiver since the LO and signal frequencies will differ. Since AOMs can modulate up to the nanosecond speed, analogue filtering methods are used to obtain narrower pulses. Successive modulators can be used, for example the AOM can be followed by an Electro-Optic modulator (EOM) to generate narrower pulses. In that case, the AOM mainly serves to shift the probing signal frequency while the EOM shapes the probing signal [11]. Conversely, the EOM can be used for frequency modulation prior to the AOM, which eventually shapes the probing signal into pulses [3].

Electro-refraction based Mach-Zehnder interferometer (called MZM) with synchronous arms are an example of an EOM that can be used to perform phase and intensity modulations to shape the probe signal without inducing any frequency shift [37], possibly leading to homodyne detection at the receiver side [38].

**Phase estimation** With $\Delta\phi$-OTDR, a local phase information is processed as a differentiation between the phase estimated at a given fibre segment and that estimated at one

[3]In case of balanced or coherent detection

previous location. The very first fibre segment serves as a reference. Repeating this phase estimation process in time allows to capture and localize mechanical perturbations that may affect the fibre.

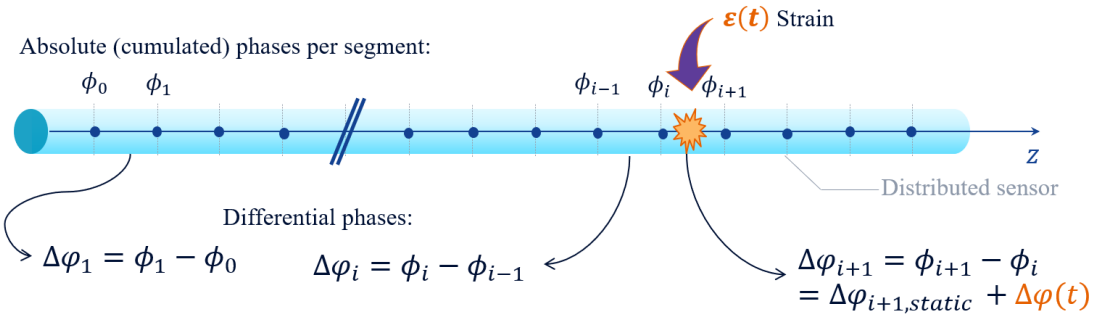


Figure 1.11: Outline schematic: Differential phase processing in $\Delta\phi$-OTDR

The phase retrieval is detailed below and further illustrated in Figure 1.11:
In static mode, for two given segments indices $i$ and $j$ with $j > i$, the measured differential phase is constant over time and given by $\Delta\varphi_{static} = \phi_j - \phi_i$, $\phi_i$ being the absolute, or "cumulated" phase backscattered from segment index $i$. Note that $j - i$ stays constant: usually consecutive segments are processed such that $j - i = 1$ (therefore $j = i + 1$ in Figure 1.11). Cases when $j - i > 1$ are referred to as "low sampling resolution" in the manuscript and addressed in subsection 3.3.4.

In dynamic mode, assuming a strain $\varepsilon$ is applied locally at segment position $i$, the phase is linearly disturbed relatively to the perturbation, following:

$$\Delta\varphi_{single-pass}(t) = n\xi G\varepsilon(t)\frac{2\pi}{\lambda} \tag{1.2}$$

where $n$ is the refraction index, $\xi$ photo-elasticity coefficient ($= 0.79$ ratio for silica [39]), $\varepsilon \cdot G$ the fibre elongation where $G$ is the gauge length, or segment length. So if segment $i$ is disturbed, the measured phase is $\Delta\varphi_{dyn} = \phi_j - \phi_i + 2\Delta\varphi_{single-pass}(t) = \Delta\varphi_{static} + \Delta\varphi_{dual-pass}(t)$, and $\Delta\varphi_{dual-pass}(t) = 2\Delta\varphi_{single-pass}(t)$. The phase delay is applied twice since the light does a round-trip in the segment (way faster than the mechanical disturbance action, so the measurement of mechanical perturbations is considered instantaneous).

For the detection of a dynamic event, we choose to monitor the standard deviation of the differential phase over time, along the fibre distance (denoted $\sigma_\varphi$). When an event occurs along the sensor, phase variations appear in time, thus increasing the phase standard deviation locally.

### 1.1.4 Other sensing methods ; non exhaustive

Solutions based on reflectometry for accurate vibration sensing or based on interferometry on transoceanic distances exist to complement DAS solutions where DAS lacks sensitivity or reach.

**Fibre Bragg Gratings:** FBG sensors are a convenient tool to design distributed fibre sensors based on light backscattering. Instead of relying on the weak reflections from density fluctuations of a SMF, the fibre sensor is periodically inscribed with a stronger reflector [40, 41]. For permanent gratings, the modulation of the refraction index is done by damaging the fibre, namely by exposing it to patterns of intense UV light [42].

When exposed to a large bandwidth light source, the grating will reflect a single wavelength (or few nm wavelength interval) called the "Bragg wavelength". Thus FBGs are of great interest because of their filtering properties, such that they are used for example as narrow-bandpass filters or as dispersion compensation devices. Regarding sensor use, the wavelength reflected by FBGs is sensitive to temperature and strain. Quasi-distributed sensor arrays can be designed as successive FBGs with low reflectivity (for example, $10^{-3}$ which is still much higher than Rayleigh scattering) [43]. Such sensor setups can reach considerable distance, namely over 100km with seven FBGs [44].

Of course, this is not compatible with sensing on deployed fibre since such inscription of a reflectors array would degrade the data transmission capability of a telecommunication fibre.

**Forward, phase sensing:** Phase sensing consists here in measuring the phase difference between a reference signal and transmitted light which travelled inside an optical fibre along some distance, or over two fibres in the same cable. On the one hand, in the absence of perturbation along the optical fibre route, the phase difference will remain constant. On the other hand, the presence of a mechanical event along the fibre will yield a change in the measured phase difference. This method is similar to phase-OTDR since a differential phase is obtained after processing. However, the phase difference is derived over the full sensor length as depicted in Figure 1.12, such that no localization can be retrieved from the sole interferometric measurement.

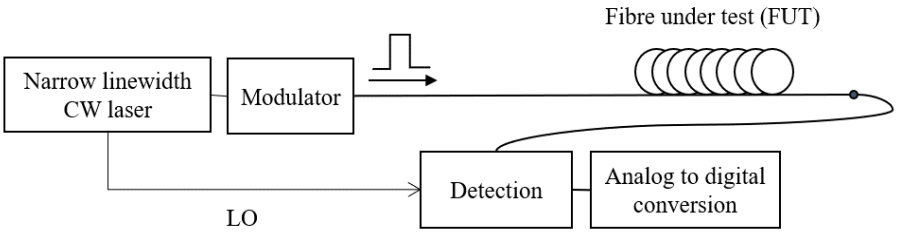


Figure 1.12: Outline schematic of a forward phase sensing setup. CW: Continuous wave, LO: Local Oscillator

This fibre sensing technique is used on very long distances such as transoceanic cables [8] for which the Rayleigh scattering would be too low, among other issues. Indeed, conventional (intensity-based) OTDR solutions exist for transoceanic cables (over 10.000km), enabling the detection and localization of major losses and breaks [45]. However it requires several hours of averaging, therefore the capture of the phase by means of Distributed Acoustic Sensors (DAS) is yet impossible to perform.
Phase sensing allows to get dynamic information from deployed long distance cables. The

main drawback with such a sensing technique is that the localization information is not straightforward (unlike DAS or OTDR), and requires triangulation techniques to retrieve the position of a detected event [46] (provided that a series of fibres spread in the environment are simultaneously sensed).

Some research groups are working on the localization aspect as they introduce frequency shifts at the halfway point of the fibre-optic link to differentiate between the detection of an event in both directions [47]. Another method would rely on retrieving the phase on two contra-propagative channels (fibres) is a same cable and provided a fine synchronization of the network nodes, the localization information would be retrieved [48].

## 1.2 Measurement of the phase, state of polarization, and intensity

Optical fibre vibrations and strain sensing is possible because of the disturbances slightly and locally changing the shape of the fibre sensor, thus transferring their information to the light conveyed by the fibre. In subsection 1.1.2, we summarized the interests of using optical fibre as a sensor, and recalled the different measurands ("disturbances") that can be captured. Now, the various measurands can be encoded onto many attributes of the propagating light, including intensity, polarization, phase, propagation time, optical spectrum, coherence...

Since we are interested in capturing dynamic variations of the measurands, the conventional techniques such as intensity-based OTDR will not meet our conditions here. Therefore we consider the use of a coherent laser source that allows to capture the phase from the backscattered signal (Coherent-OTDR, $\phi$-OTDR, $\Delta\phi$-OTDR). Yet, this does not mean that phase is the only relevant parameter, so all parameters will still be considered in the following.

Intensity of the backscattered light will depend on local losses and attenuation, but will not have a linear response to strain in most cases, whereas **dynamic phase variations depend linearly on the vibrations applied to the fibre sensor** (see Equation 1.2), allowing for quantitative vibration measurements. Now backscattered intensity, polarization and phase can be captured either jointly or separately using different probing techniques, some of them are presented below.

### 1.2.1 Pulse interrogation

Single light pulses or pulse trains are the most straightforward probe signals in terms of optical generation, and they allow to directly retrieve the backscattered response of the fibre sensor along distance, with single-ended measurements. Light pulses are generally generated by acousto-optic modulators (AOM) in pulsed mode [30, 36]. There are other means for pulse generation such as fibre lasers [34] or semiconductor optical amplifiers [49].

When one temporally narrow (in terms of duration $\tau_p$, of $\mu$s to ns range usually) light pulse is sent into the fibre sensor, it is backscattered from all successive scattering centres

in the fibre, resulting in a continuous signal at the receiver and yielding a notion of distance following equation (1.1) in the previous section. The spatial resolution $\delta z$ of the system is therefore tuned by adjusting the pulse duration $\tau_p$, following $\delta z = c\tau_p/2n$ where $n$ is the refractive index in the fibre and $c$ the speed of light in vacuum. When pulses are repeatedly sent to probe the fibre sensor, the measurement is time resolved at the pulse rate. The repetition rate must verify at least $\tau_r \geq \frac{2nL_f}{c}$ ($n$ mean refractive index along the fibre, $L_f$ fibre length) such that the current pulse backscattered responses do not superimpose with the previous ones in the absence of specific processing. The rate $\tau_r$ conditions the mechanical bandwidth of the sensor, defined as $B_{meca} = 1/\tau_r$. As a consequence, a fundamental limit in optical backscatter time reflectometry is $B_{meca} \leq \frac{c}{2nL_f}$.

Similarly to light which is transmitted from one fibre end to the other, the probing pulses experience attenuation along distance, and so does the backscattered light as well. The sensing system is therefore limited by the detector sensitivity on the one hand, and by the maximum launchable power on the other hand, as there are indeed possible issues when sending too much power to the fibre sensor, such as non-linearities in the fibre [49]. To avoid high peak powers levels, the interrogation pulse can be widened, but this consequently degrades the spatial resolution $dz$ of the sensor.

Therefore, spread-pulse or spread-spectrum techniques were developed in order to send higher power probing signals to the fibre and to relax the conditions on the maximum peak power and detector sensitivity. These techniques are detailed later in this section.

### 1.2.2 Reception of sensing signals

In subsection 1.1.3, we referred to the different methods available for the detection of backscattered signals, namely direct detection and coherent detection. The detection step is crucial, since the distributed sensing information is enclosed in very low-power backscattered light. In this subsection, we give some more details about the optical receivers.

**Direct detection** Direct detection requires a single photodetector and captures the backscattered optical power in OTDR and phase-OTDR.

The role of a detector is to convert light into electrical signals. Semiconductor photodiodes meet the requirement: absorption of incident photons results in the generation of an electrical current (photocurrent). The photocurrent is directly proportional to the rate of photon absorption, and the probability of photon absorption is defined as the quantum efficiency $Q$. A detector also features a **responsivity** $R_d$ [A/W] as the ratio of the photocurrent to the incident optical power. Therefore:

$$R_d = \frac{q}{E_{photon}}.Q = \frac{qQ}{h\nu} \tag{1.3}$$

where $q$ is the electron charge, $h$ the Planck constant, $\nu$ the frequency of light [17]. Finally the generated current $I(t)$ verifies, if illuminated by a source with power $P_0$:

$$I(t) = R_d P_0 \tag{1.4}$$

Avalanche photodetectors (APD) are semiconductor-based photodiodes with internal signal amplification, making them more sensitive than usual PIN photodetectors (high $Q$) and thus well-suited for the detection of low power signals. They are the most commonly used direct detectors in OTDR [17].

**Balanced detection: differential receiver** Yet, Rayleigh backscattering power is several orders of magnitude below the transmitted signal power, hence an interest for methods to increase the output current of the receiver or decrease the noise contributions.

Balanced photodetection, whose general principle is given in Figure 1.13, uses two photodetectors to capture optical power from the signal and from a local oscillator (LO). It allows to gain 3dB compared with direct detection due to the multiple sources, to DC component suppression and minimization of possible laser relative intensity noise (RIN) [50].

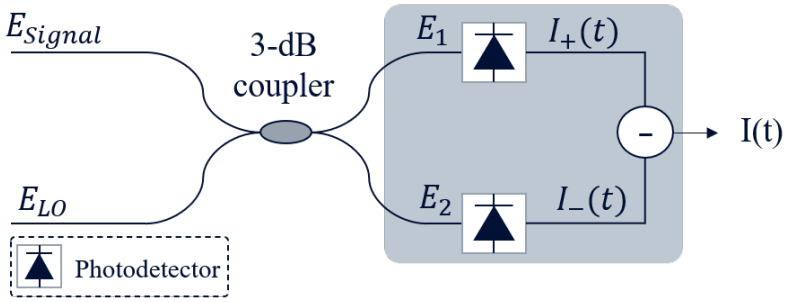


Figure 1.13: Balanced photodetector, adapted from [50]. Balanced detection is used to remove the DC component of the interference signal and increase the sensitivity by 3dB

For a signal optical field $E_{Signal} = E_s = A_s exp(\omega_s t + j\phi_s)$ and a LO optical field $E_{LO} = A_{LO} exp(\omega_{LO} t + j\phi_{LO})$ ($\phi$ stands for the phase, $\omega$ is the angular optical frequency with THz range), we get an output current $I(t)$:

$$I(t) = I_+(t) - I_-(t) = 2R_d\sqrt{P_s P_{LO}}\, cos(\omega_{IF}\, t + \phi_s - \phi_{LO}) \tag{1.5}$$

where $\omega_{IF} = \omega_s - \omega_{LO}$, the intermediate frequency.

**Coherent detection and digital signal processing** Coherent detection relies on detecting a signal through the beating with a reference frequency carrier. The general idea in case of sensors applications is to increase the spectral efficiency of the receiver using phase, amplitude, and polarization of an optical carrier to enclose information (instead of the sole optical power).

It has firstly attracted a strong interest from the research community in the 1980's as a mean to enhance the receiver sensitivity, but was set aside as erbium doped fibre amplifiers (EDFA) allowed to increase the transmission systems performance more easily. Coherent technologies regained interest in the 2010's since it allowed to use specific Digital Signal Processing (DSP) algorithms to compensate for chromatic dispersion, to use large modulation formats, and therefore allowed to enhance the capacity of long haul optical communication systems to reach record capacity transmissions [51].

In case of DOFS, the introduction of coherent detection is first motivated by the perspective of improving the receiver sensitivity, as for the first introduction of coherent detection in telecommunications. In some cases, the introduction of balanced photodetectors as described above was already satisfactory [52], sometimes coupled with polarization diversity [53, 54] which demonstrated higher Signal-to-Noise Ratio (SNR) than traditional direct detection $\phi$-OTDR.

Moreover, $\Delta\phi$-OTDR technology also stems from the second motivation in transmission: having the possibility to retrieve amplitude and phase, to develop powerful DSP.

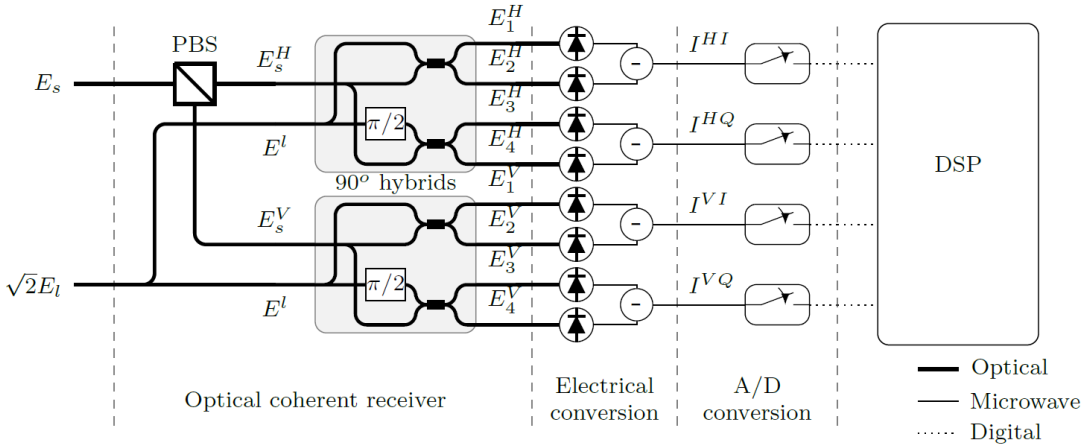


Figure 1.14: Schematic of a polarization diversity coherent receiver, sampling and offline DSP, from [55]. PBS: Polarization Beam Splitter, A/D: Analog to Digital, DSP: Digital Signal Processing

A coherent detector is depicted in Figure 1.14. The coherent detector is constituted of four balanced photodetectors as described above, preceded by:

- a polarization beam splitter that splits the received signal into two (random) orthogonal polarization components $E_s^H$ and $E_s^V$
- two $90^o$ hybrids (or coherent mixers), one per polarization: the purpose of the four output ports of the $90^o$ optical hybrid is to generate a $90^o$ phase shift for I and Q components, and $180^o$ phase shift for balanced detection
- in an ideal $90^o$ hybrid, a 3dB coupler adds a $180^o$ phase shift between the two output ports.
  The signal is also mixed with a $\pi/2$ ($90^o$) phase shifted version of the LO field [56]
- as a result, 8 optical fields are generated and fed into photodetectors, which are all possible combinations of $E_s^H$ and $E_s^V$ signal components.

Finally, four photocurrent outputs are generated by the dual-polarization coherent receiver, verifying:

$$\begin{bmatrix} I^{HI} \\ I^{HQ} \\ I^{VI} \\ I^{VQ} \end{bmatrix} = R_d \begin{bmatrix} \Re(E_s^H E_{LO}^*) \\ \Im(E_s^H E_{LO}^*) \\ \Re(E_s^V E_{LO}^*) \\ \Im(E_s^V E_{LO}^*) \end{bmatrix} \tag{1.6}$$

where $R_d$ is the photodiode responsivity and $*$ denotes the complex conjugate. Coherent reception allows to retrieve the real and imaginary parts of both polarization components after balanced photodetection.

Coherent receivers are used in $\Delta\phi$-OTDRs in case of complex coded probing sequences relying on phase and intensity modulation formats (Golay BPSK, random PSK) [38, 57, 58], or time-gated OFDR [59]. Many recent research results in $\phi$- and $\Delta\phi$-OTDR did report the use of balanced detection, referring to it as "coherent reception" [60, 61], here used for fading noise and frequency drift mitigation purposes.

### 1.2.3 Spread-spectrum pulse and continuous signal interrogation techniques

We mentioned that pulsed interrogation is limited by non-linearities issues due to the required high pulse power as soon as the operator wishes to increase the range of the measurement instrument, or increase the spatial sampling resolution thus concentrating the pulse power in even shorter time.
Optical Frequency Domain Reflectometry (OFDR) or frequency sweeps [62], multi-frequency interrogation [11], linear frequency modulation [3], as well as coded interrogation [38, 58, 63] address the issue of increasing the range of Rayleigh-based fibre sensors by spreading the probe power in time.

**Optical Frequency Domain Reflectometry** (OFDR) consists in sending continuous, frequency-swept probing signals to the fibre sensor, as the amplitude is kept constant. At the receiver side, the backscattered signal beats with a single frequency or with the reference sweeped signal [62]. The tuning of the system is such that each received frequency corresponds to a specific location in the fibre. The frequency range will define the spatial resolution of the system, thus allowing for very precise spatial resolutions (below the metre) even though the sweep modulation doesn't exceed the MHz range. For such an application, frequency linearity of the sweep and detector are required, therefore it is mostly used on short distances. Despite that, long distance OFDR sensing with detection of a Fresnel reflection over 100km fibre was also demonstrated [64].

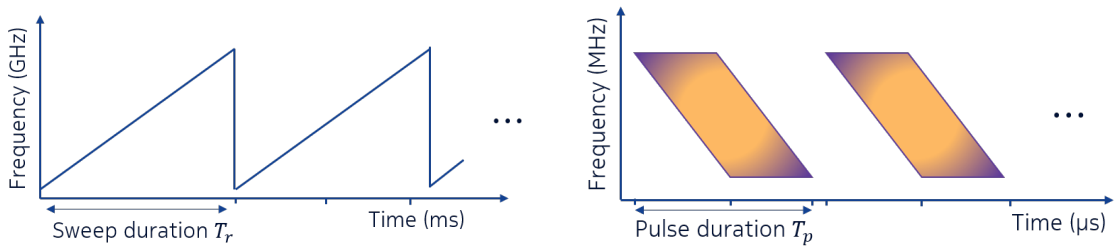


(a) OFDR (b) Chirped pulse

Figure 1.15: OFDR and chirped pulse: outline schematic of probing signals

**Chirped pulse** Chirped pulse OTDR was introduced in [52] and [65]. It allows to perform distributed measurements with precise spatial resolution without the need of fre-

quency sweeps, thus avoiding frequency linearity issues over long distances. The principle of chirped-pulse OTDR is to send optical pulses with rectangular intensity profile but linearly shifted phase profile, which corresponds to frequency changes in a much shorter magnitude as depicted in Figure 1.15. The strain or temperature profiles are recovered at the receiver side by correlation of successive traces. Chirped pulse interrogation is further used for Time-Gated Digital OFDR (TGD-OFDR) where a long chirped pulse is compressed [59], which also overcomes the effects of laser phase noise in classic OFDR and enables precise sensing over 40km. The technique was pushed forward by further pulse-shaping and spectral occupancy management to achieve distributed sensing over 80km [3] with over 49dB dynamic range. On the other hand, interrogation using pulse trains that are shifted in frequency, somehow relating to a discrete chirp, did show very low noise floor and thus very high sensitivity [11] with up to 80dB dynamic range at 1kHz.

**Coded interrogation** Chirped pulse methods are still sensitive to phase noise issues if the generated pulses differ from each other along the sensing duration. An alternative to OFDR that still spreads the energy of the probing signal is to use coded sequences. Coded sequences are either specific binary sequences [63] or data which is coded over a constant modulus thanks to optical communication modulators [57], with correlation properties that allow to recover the system impulse response at the receiver side. Moreover, coded interrogation is interesting regarding avoidance of frequency distortion effects as it is generally coded over a finite alphabet, and sent with a constant symbol rate. Sequences with autocorrelation properties are of different kinds, either periodic or aperiodic. In early versions of commercial intensity OTDR, pseudorandom sequences were used in replacement of pulsed interrogation [66]. Complementary Golay sequences were used in direct-detection OTDR [67] provided a coding method managing unipolar codes, as well as Hadamard-based S-codes [68] which do not need a correlation operation at the receiver side. Later, thanks to coherent detection, it was possible to send bipolar codes on PSK (Phase-Shift Keying) constellations [57]. Legendre codes demonstrated good results for distributed dynamic strain sensing [38], and Golay complementary codes could be used in their bipolar form [69].

### 1.2.4 Dual-polarization interrogation and Jones estimates

The above presented probing methods retrieve intensity, and/or phase of the disturbance (strain, vibration, temperature change). It is also possible to retrieve polarization, either with a polarimeter at the receiver side or using a polarization splitter and two receivers. However, in interrogator set-ups that enclose a coherent receiver, a fortiori a dual-polarization coherent receiver (similarly to optical communication systems), phase, intensity and polarization are retrieved simultaneously. Yet, complexity remains in the polarization and phase rotations along the sensor fibre: how to capture strain and vibration information while avoiding crosstalk in distributed measurements?

#### 1.2.4.1 Jones calculus

The Jones notation allows to represent the effect of a retardation plate or a partial polarizer on the intensity and polarization of incoming light as matrix operators $\mathbf{M} = \begin{bmatrix} m_1 & m_2 \\ m_3 & m_4 \end{bmatrix}$ that operate on the incoming light vector $E_{in} = \begin{bmatrix} E_{x0} & E_{y0} \end{bmatrix}^T$ [70]. Such operators modify the state of polarization and sometimes the intensity of the light. The output light is then described by $E_{out} = \mathbf{M}E_{in}$.

When light crosses a multi-elements system, the $n$ superposed optical elements will correspond to a new element $\mathbf{M}^{(n)} = \mathbf{M}_n\mathbf{M}_{n-1}...\mathbf{M}_2\mathbf{M}_1$ assuming the light crosses element with matrix description $\mathbf{M}_1$ first, then $\mathbf{M}_2$ ... and finally $\mathbf{M}_n$.

An optical system can be described as such a succession of optical elements, namely retardation plates and partial polarizers. Such a notation will therefore be used in the following to characterize polarization properties of the optical fibre sensor. In the paragraphs below, Jones calculus is used for the description of dual-polarization interrogation of a fibre sensor.

#### 1.2.4.2 Dual-polarization Golay coded interrogation

On the one hand, distributed optical fibre sensing tends to consider the optical fibre as a single channel which is interrogated. On the other hand, modern optical communications tend to consider the optical fibre as a medium for transmitting over multiple channels, be it through wavelength division multiplexing (WDM) or polarization division multiplexing (PDM). Now, we consider the fibre sensor as a dual-polarization channel, which can be successively or simultaneously interrogated (modulation of one or two polarization states). For simultaneous interrogation, one has to design specific sequences per polarization.

The proposed method is a single wavelength, multiple-input multiple-output (MIMO) approach through polarization multiplexing at the transmitter and polarization-diversity detection at the receiver side [58]. It allows to retrieve not only the phase and amplitude along the fibre sensor but also the backscattered state of polarization in the form of $2 \times 2$ Jones matrices denoted $\mathbf{H}$, following:

$$E_{out} = \mathbf{H}E_{in} + \mathbf{N} \tag{1.7}$$

where $E_{in}$ is the $2 \times 1$ probing signal (on two polarization axes) $E_{in} = \begin{bmatrix} E_{x0} & E_{y0} \end{bmatrix}^T$, $\mathbf{H}$ the $2 \times 2$ description of polarization and phase transformations in the fibre sensor, $E_{out}$ the $2 \times 1$ backscattered signal and $\mathbf{N}$ the noise contribution of the interrogation system, also on both polarization axes.

The Golay-based probing sequences consist of two mutually orthogonal complementary pairs $\{G_{a1}, G_{b1}\}$ and $\{G_{a2}, G_{b2}\}$ derived from Golay codes, mapped to binary-phase-shift-keying (BPSK) symbols that jointly and continuously modulate two orthogonal polarization states of a narrow-linewidth laser source. The complementary property gives that for

each polarization axis ($i = 1, 2$), $\{G_{ai}, G_{bi}\}$ verifies:

$$G_{ai}(n) \otimes G_{ai}(n) + G_{bi}(n) \otimes G_{bi}(n) = \delta(n) \tag{1.8}$$

where $\otimes$ denotes the correlation operator, $\delta(\cdot)$ stands for the delta function and $n$ is a time index. The mutually orthogonal property adds the fact that:

$$\begin{aligned} G_{a1}(n) \otimes G_{a2}(n) + G_{b1}(n) \otimes G_{b2}(n) = 0 \\ G_{a1}(n) \otimes G_{b1}(n) + G_{a2}(n) \otimes G_{b2}(n) = 0 \end{aligned} \tag{1.9}$$

On a single polarization axis, we call "Golay code" the two successive sequences of a complementary Golay pair $\{G_{ai}, G_{bi}\}$, constituted of $N_{code} = 2^{K+3}$ symbols, where $K$ is an integer. A basic example of mutually orthogonal complementary pairs of length $N_{code} = 8$ is $G_{a1}$= [1,-1,-1,-1], $G_{b1}$= [-1,1,-1,-1], $G_{a2}$= [-1,-1,1,-1], $G_{b2}$= [-1,-1,-1,1], from which longer sequences can be obtained recursively to get the desirable probing length [58, 67].

The probing sequences are generated at the transmitter side at symbol rate $f_{Symb}$, such that the code duration is $T_{code} = N_{code}/f_{Symb}$, as pictured in Figure 1.16. The fibre sensor is continuously probed by polarization-division-multiplexed (PDM) BPSK sequences with a period $T_{code}$ yielding a mechanical bandwidth $B_{meca} = 1/_{2T_{code}}$. The spatial resolution $L_s$ is equal to $L_s = c_{fibre}/2f_{Symb}$, where $c_{fibre} = c/n$ is the velocity of light in the SMF core.

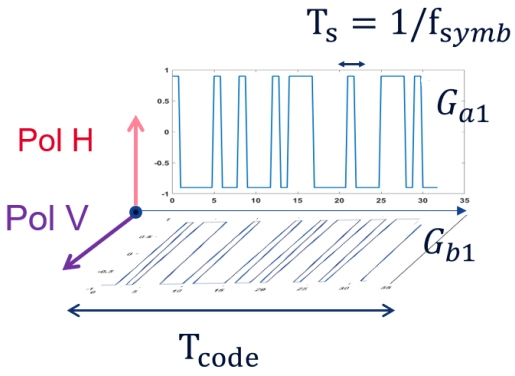


Figure 1.16: Overview of dual-polarization probing sequences

At the receiver side, the channel response is extracted through a correlation process between the two received symbol-vectors and the two emitted symbol-vectors. The specific orthogonality properties between the designed sequences guarantee the perfect channel estimation provided that a suitable sequence length is chosen: $T_{code}$ must verify $4.T_{ir} < T_{code} < T_{coh}$ where $T_{ir} = 2L/c_{fibre}$ stands for the time spreading of the channel response for a fibre of length $L$ and $T_{coh}$ is the coherence time of the narrow-linewidth laser source. To ensure that the channel remains stationary, $T_{code} < T_{coh}$ guarantees that the reference phase is almost constant over the duration of a single code, and the condition $4.T_{ir} < T_{code}$ is necessary to avoid the overlapping of successive fibre estimations (channel impulse responses) after correlation at the reception [58].

Selecting $T_{code}$ close to the lower duration limit $T_{ir}$ will maximize the sensing mechanical bandwidth $B_{meca}$. In case of low frequency sensing, namely on underwater or buried cables, $T_{code}$ can be increased to restrict the mechanical bandwidth, and a spatial resolution of the order of $L_s = 10$m is sufficient since the lower frequencies spatially spread over large areas. Else, in the case of smart-city applications, a spatial resolution around $L_s = 1$m is preferred for accurate localization [71]. To cope with 1m spatial resolution, the symbol rate of the interrogator should be $f_{Symb} = c_{fibre}/_{2L_s} = 100$MHz. Considering that commercial WDM (wavelength division multiplexing) systems enclose 100GHz frequency transport wavelength slots [72], there is no risk of overlapping if a sensing signal spreading in $B_{elec} = 100$MHz is affected to one WDM channel next to the telecom data, assuming it has comparable launching power. Moreover, increasing the sensing electrical bandwidth $B_{elec}$ by ten times in order to have a finer resolution, is still supported by a commercial transmission system (as demonstrated later in chapter 6).

Note that other coded interrogation methods exist to retrieve the full Jones matrices $\mathbf{H}$ of a fibre sensor, with relaxed orthogonality conditions, such as with pseudorandom sequences [57, 66] as mentioned in the previous section. In such cases however, the estimation will include noise due to flawed autocorrelation of the sequences (not equal to a dirac).

#### 1.2.4.3 CAZAC and sweeps

The dual-polarization (or "MIMO") interrogation presented above is powerful, yet limited in terms of mechanical sensing bandwidth, i.e. in terms of sensing high frequency vibrations and acoustic signals. Indeed, since $T_{code} > 4L/c_{fibre}$, then the mechanical bandwidth is limited to $B_{meca} \leq \frac{c_{fibre}}{8L}$, which is 4 times smaller than the theoretical limit for pulse interrogation given in subsection 1.2.1.

**CAZAC** As an alternative to the above-mentioned probing technique, we consider phase-modulated CAZAC (Constant Amplitude Zero-Autocorrelation Code) sequences usually used in the telecommunication domain to perform channel estimation of a transmission link [73]. The symbols from a class of perfect-squares minimum-phase CAZAC sequences are defined as

$$c_n = exp\left(j\frac{2\pi}{\sqrt{N}} \times \left(mod\left(n-1, \sqrt{N}\right)+1\right) \times \left(\left\lfloor \frac{n-1}{\sqrt{N}} \right\rfloor + 1\right)\right) \tag{1.10}$$

where $n = \{1, \ldots, N\}$ denotes the time index of the symbol with $N = 4^M$, $M$ is a non-zero positive integer. Formally, the CAZAC sequences can be considered as a (discrete) phase sweep since the modulus of the symbols is kept constant.

The alphabet is composed of $2^M$ complex symbols having the same module and distributed over the unit circle, leading to a $2^M$-symbol Phase Shift Keying ($2^M$-PSK) constellation.
Similarly to dual polarization coded interrogation, the CAZAC sequences sent on each orthogonal polarization axis should verify mutual orthogonality. Exploiting the properties

of CAZAC sequences, we apply a circular shift of $N/2$ symbols onto the initial N-symbol CAZAC sequence **c** which leads to a sequence **c'**, as pictured in Figure 1.17. Sending **c** and **c'** simultaneously over two polarization states offers mutual orthogonality [73] and achieves perfect channel estimation as for the above codes derived from Golay, however with a less-stringent constraint on the length of the probing sequence: when estimating a fibre Rayleigh backscattering over a round-trip duration of $T_{ir}$, the perfect estimation is now obtained under the condition $T_{cazac} > 2T_{ir}$ [74].

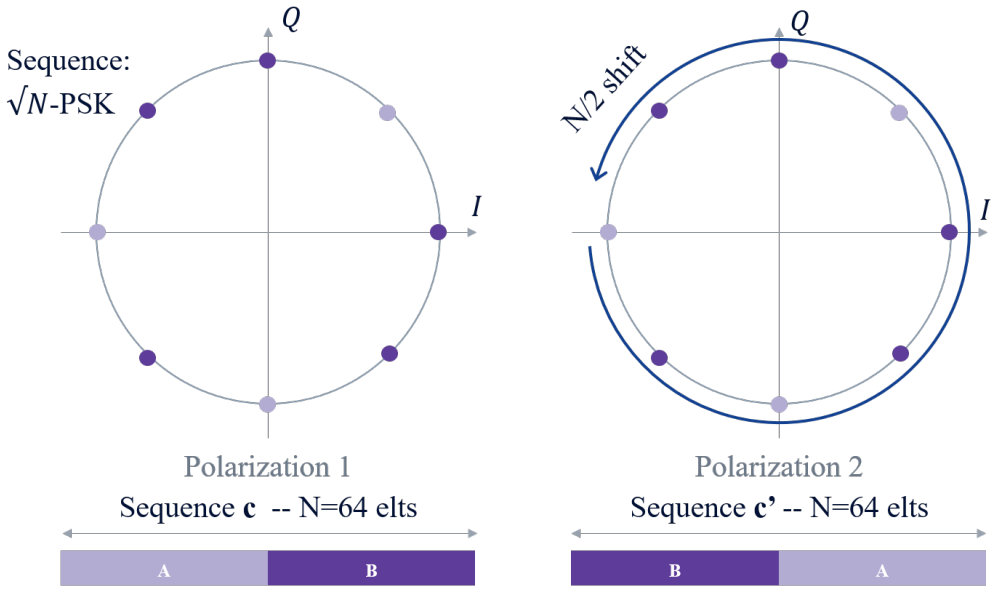


Figure 1.17: Overview of dual-polarization CAZAC probing sequences on unit circle, for a sequence with $N_{cazac} = 64$ elements.

**Frequency sweep** The frequency sweep interrogation is worth considering as an alternative, somehow more intuitive, way to generate a dual-polarization frequency sweep as it is achieved with the CAZAC method. A first amplitude modulated real-valued sweep signal is used to linearly and uniformly cover the $[0 : f_{symb}/2]$ bandwidth over a period $T_{sweep} = T_{cazac}$ over the first polarization and a second identical signal, but delayed by half the sweep period, modulates simultaneously the second polarization. The two continuously repeated signals are, for a practical use case example, digitally generated and then converted by two Digital to Analog Converters (DACs) prior to modulating the laser light onto the two polarization axes. Similarly to CAZAC sequences, the perfect estimation with dual-polarization frequency sweeps is obtained under the condition $T_{cazac} > 2T_{ir}$ [74].

**Relative performance of dual-polarization interrogations** The relative error on intensity and phase estimation for Coded, CAZAC and frequency sweep interrogations was investigated through simulations displayed in Figure 1.18 using a dual-polarization Rayleigh backscatter model [75].
Golay codes (PDM-BPSK), digital sweeps and CAZAC sequences are generated with a duration $T = 328\mu$s (corresponding to $N_{code} = N_{cazac} = 2^{14}$ elements and a symbol rate $f_{Symb} = 50$MHz) while simulations are run for fibre length ranging from 1km to 20km. The fibre interrogation is such that a native spatial resolution of 2m is obtained. In Figure 1.18,

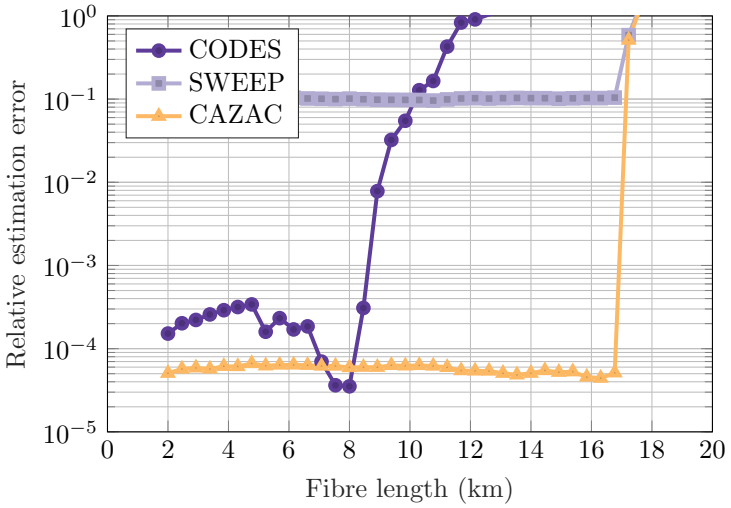


(a) Error on intensity estimation, no noise

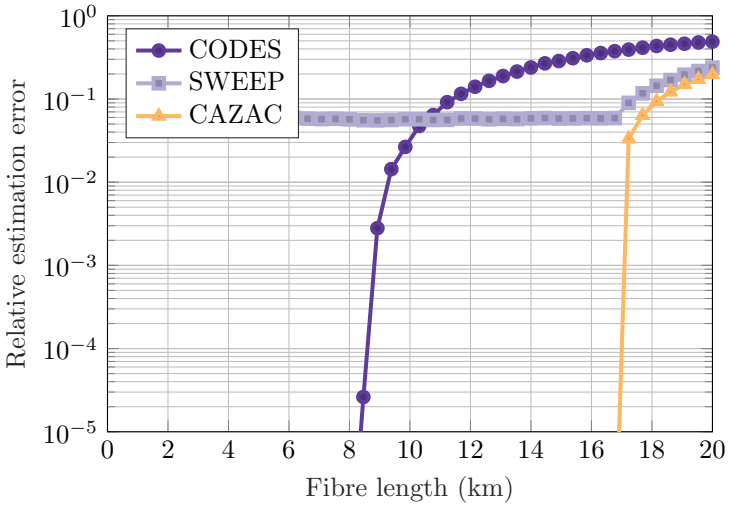


(b) Error on phase estimation, no noise

Figure 1.18: Simulation of relative error on intensity and phase estimation depending on the interrogation method, as a function of fibre distance

the mean relative error between the simulated segments and estimated segments is derived, both in phase Figure 1.18(b) and intensity Figure 1.18(a). The maximal fibre length to be probed with PDM-BPSK codes to achieve perfect estimation is $L_{Code}^{Max} = \frac{1}{4} \cdot \frac{N_{Code}.c_{fibre}}{2.f_{Symb}}$, which yields 8.2km here, whereas the maximal length $L_{cazac}^{Max} = \frac{1}{2} \cdot \frac{N_{cazac}.c_{fibre}}{2.f_{Symb}}$ is twice larger when using CAZAC and sweep sequences.

Results in Figure 1.18 highlight the perfect channel estimation provided by the initial code interrogation technique up to the 8.2km limit. As expected, the error starts increasing beyond 8.2km whereas CAZAC codes keep providing a low estimation error until 16.4km. Note also that the maximal achievable bandwidth is $BW_{Code}^{Max} = \frac{1}{4} \cdot \frac{c_{fibre}}{4.L} = 3\text{kHz}$ with BPSK whereas CAZAC sequences allow for $BW_{Code}^{Max} = \frac{1}{2} \cdot \frac{c_{fibre}}{4.L} = 6\text{kHz}$ for a given fibre length $L = 8.2\text{km}$.

However, frequency sweeps do not provide perfect estimation from the smallest fibre

lengths: they keep an intensity estimation and phase estimation error around $10^{-1}$. This is mainly due to a loss of orthogonality in the transition period between two successive sweep sequences. Similarly to the CAZAC interrogation method, their error starts increasing from 16.4km vs. 8.2km for PDM-BPSK. In practical cases where system noises are present, sweeps and CAZAC can show very similar performances to PDM-BPSK coded sequences, which makes them evenly interesting as an alternative to PDM-BPSK coded sequences [74].

Also, CAZAC sequences are sensitive to phase noise which can degrade the quality of the probing for high cardinality sequences. As the number of CAZAC symbols increases, the distance between successive symbols $d_H$ decreases so much that the channel estimation is not possible in the presence of noise. CAZAC interrogation would therefore require a fine tuning of the modulator and a very low-noise receiver, which is not achievable in current systems for high cardinality sequences.

Dual-polarization digital sweep and CAZAC interrogations allow to relax conditions on the reach of the sensor (or conversely, on the mechanical bandwidth) in theory with regards to dual-polarization BPSK coded interrogation, with a tradeoff regarding the channel estimation accuracy, therefore the sensitivity of the system for practical use cases.

## 1.3 Context and use cases

In this part, we will be describing a few Coherent-OTDR use cases and their orders of magnitude, keeping in mind that Brillouin and Raman distributed sensing remain the preferred methods in some fields. As discussed in the opening, the applications of distributed fibre sensing are more and more attractive, for instance in replacement of electronic point sensors which can be more energy-consuming or bulky, or because of price and robustness advantages of optical fibre.

**Medicine** In biomedical applications, fibre optics is used for spectrometry, velocimetry, and of course vibration and temperature sensing since several decades [76]. Fibre optic sensors are of interest in the biomedical field in order to capture parameters such as pressure, temperature, strain at specific points, sometimes inside living organisms [77]. The sensor needs to have high sensitivity and fine spatial resolution (gauge length). Besides, dedicated sensors are used, allowing to decide on the type of glass (silica or not), to inscribe periodic gratings in order to enhance the backscattered signal. Fibre lengths are of the order of the centimetre up to tens of meters, with gauge lengths sometimes of the millimetre scale [78]. These fibre sensors can be probed by OTDR-like interrogators, to recover the intensity, phase or polarization variations which will better convey the strain or temperature information. OFDR and frequency sweeps are preferred because of their high spatial resolution.

**Infrastructure monitoring** Structural health monitoring as well as borehole measurement (oil and gas namely) applications also require optical fibre sensors, which are dedicated fibres most of the time, therefore there are no associated constraints of data trans-

mission other than transmitting the sensor data back to the interrogator. Also, the mechanical frequency range is pre-determined by the application, therefore the fibre sensor can be manufactured accordingly (enhanced sensitivity in some range).
Brillouin sensors are particularly interesting for structure monitoring over long periods of time, such as building and bridge structures monitoring, as Brillouin sensing provides a stable reference in time - absolute measurement in contrast with Rayleigh OTDR which is a relative measurement. Yet, measuring the Rayleigh scattering can be of great interest for the discrimination between strain and temperature information in Brillouin scattering-based sensors [79].

Companies such as Febus-optics [80], Luna [81] currently develop and maintain commercial systems for infrastructure monitoring. Moreover, specific monitoring is developed by the companies that develop the infrastructure themselves, e.g. in case of radiations monitoring using DOFS for nuclear plants safety [82].

**Submarine sensing** Transoceanic distances are not yet covered by phase-OTDR solutions [8], only by intensity DAS. Solutions that rely on interferometry, or "phase sensing", were mentioned in subsection 1.1.4 above. However, distributed vibration sensing can be of interest on "small", namely below 200km, portions of fibre that are deployed on the marine ground. Indeed, seismic activity can be monitored such as in [83] where earthquakes in Fidji were detected over a 40km fibre deployed in the North sea from a location in Belgium. Another phase-sensitive DAS solution over a 41.5km long fibre deployed offshore was used to explore the seafloor of the Mediterranean sea [84], with 20m gauge length. It captured microseisms with peak ground velocity of $2\mu$m/s (measured with a seismometer) over a $[0, 15]$Hz frequency range, and observed interactions between ocean and solid earth through "oceanic surface gravity waves" in a $[0.1, 0.25]$Hz frequency range thus getting some insights on the energy of coastal waves.

**Aerial telecom cables** Telecommunications networks can be very heterogeneous, especially in the access part. Beyond the different types of fibre (single mode, multi-mode...), the coatings of deployed fibre cables can vary, and most importantly the environment where the fibre is deployed varies: for buried fibres, the burial depth can change, thus modifying the pressure conditions and the sensitivity to mechanical vibrations (the ground acts as a low-pass filter). Fibre sections can be deployed as aerial cable, supported by utility poles. In this configuration, they are much more sensitive to environmental disturbances as already noticed in [85]. In a recent work, [86] proposed to use the fibre optic deployed in aerial cables to detect the presence of static weight on the cable in between two utility poles. They notice frequency shifts in the cross-spectral-density matrices obtained from their monitored fibre segments when static weights are applied to the fibre.

**Crack and intrusion detection** Intrusion detection is a broader term used since the 90's to introduce the principle of coherent-OTDR [87] as a patent: from prior art intensity-OTDR, Taylor and Lee describe an OTDR system which would rely on the backscatter of coherent light pulses. If an intruder steps over the fibre sensor, a change in the backscat-

tered intensity would allow to detect and localize the intruder. Although the sensitivity threshold for phase OTDR was not yet enough to capture acoustic vibrations, the detection of a 80kg person stepping over a 44m long buried (20cm depth) optical fibre was reported [34], yielding phase variations over $8\pi$rad in the $\phi$-OTDR trace at the intrusion location.

Pencil-crack detection [36] goes a step further in intrusion detection applications. The proposed system relies on $\Delta\phi$-OTDR with heterodyne detection. This experiment consisted in breaking a pencil lead near the fibre sensor to emulate typical crack in civil structures. Since it is not broken on the fibre but nearby, the fibre sensor detects an acoustic vibration. It is detected and localized with a 5m accuracy and within a 1kHz bandwidth, demonstrating a better sensitivity threshold than previous $\phi$-OTDR intrusion detection. More recently, intrusion detection was improved by enlarging the sensing range to over 130km, with a gauge length of 8m [88], for pipelines monitoring applications in the low-frequency range ($< 5$Hz). Commercial solutions for intrusion detection, border and perimeter security that rely on DAS are currently developed by companies such as Fotech [89], Febus or OptaSense.

## Summary on the probing methods for distributed fibre sensors

Several probing methods were presented, together with the possible implementations of such systems. Although each probing method is tunable either in terms of spatial resolution, mechanical bandwidth, sensitivity or reach (distance), it is important to notice that each method will have one or several preferred domains of application. The measured metrics are of variable interest, since the phase will be preferred to monitor small disturbances in the surroundings of the fibre sensor whereas the intensity or polarization are more suited to capture strong mechanical events. Also, some parameters are not relevant in some applications, such as large mechanical bandwidth on buried cables, since the ground and cable coating act as low pass filters. Therefore, choosing the correct probing method is one of the firsts concerns when designing a sensor. Then, it is necessary to identify the remaining weaknesses and limitations of the chosen method, either to adapt the optical setup or to aim at the most efficient signal processing techniques.

The next chapter is dedicated to system modelling, in order to understand and quantify the limitations of a sensor and interrogator.

# Chapter 2

# Dual-polarization backscattering model

Distributed optical fibre sensors (DOFS) belong to the category of "active" sensors, as they require that an interrogator system sends a signal into the sensor to get information on the measurand (strain, temperature, vibration...). Also, DOFS are intrinsic sensors meaning that the sensor is the fibre itself, as opposed to extrinsic sensors where the sensor would be connected to the fibre but outside the fibre. Therefore to understand the DOFS in full, exploration of both the fibre sensor and the active interrogator is needed.

In this chapter, a distributed acoustic sensor is modelled from the fibre model to the interrogator transmitter and receiver noise contributions. The considered fibre is (telecom) Standard Single Mode Fibre (SSMF), for which a two-dimensional model is given, taking two polarization axes into account for the study of transmission and backscattering in the fibre. The definitions and notations that are given here will serve as a base for the following of this thesis.

## 2.1 Fibre model

Several existing models investigated the backscattered phase and amplitude from optical fibres. The first step is to consider the fibre under static conditions [90], the second is to add perturbations to the simulated fibre [91]. We first restrict ourselves to the static approach and introduce the polarization dimension to the model: the channel is seen as N successive fibre segments of length $L_s$ resulting from the spatial width of the probe pulse, and each of these segments will be associated not only to the returned phase and amplitude (complex scalar), but to its complete Jones $2 \times 2$ matrix [92], denoted $\mathbf{H}$, to also cover the polarization state dimension. The polarization state dimension was already studied in many ways in case of transmitted light [93], and also introduced to present the polarization-OTDR [27]. Our scope is SSMF, usually of several kilometres length, with a highly coherent source (fibre length $L_f$ small compared to source coherence length $L_{coh}$).

We are interested in the profile of coherent light backscattered from an SSMF, probed

by a signal which is assumed to be quasi-monochromatic with optical carrier frequency $\omega_0$. The backscattered signal is a summation of the contributions of the backscattered light from the probing signal $E_{in}$ all along the fibre sensor. Figure 2.1 gives a schematic view of the backscattering process. Therefore, when $E_{in}$ consists of a rectangular pulse rect() ($\mathsf{rect}(x) = 1$ if $x \in [-\frac{1}{2}, \frac{1}{2}]$, $\mathsf{rect}(x) = 0$ else) with an amplitude $E_0$ and a duration $T_s$, the complex optical field of the scalar optical field at the receiver side $E_{rx}$ can be expressed as:

$$E_{rx}(t) = \sum_{m=0}^{M} A_m e^{j\phi_m} e^{-2\alpha z_m + j[\omega_0(t-t_m) - 2\beta z_m]} E_0 \mathrm{rect}(\frac{t-t_m}{T_s}) \tag{2.1}$$

where $M$ is the number of fibre segments defined by the probe symbol duration $T_s$ and the fibre length, $A_m$ and $\phi_m$ are respectively the Rayleigh-distributed backscattered amplitude and the backscattered phase from the $m^{\text{th}}$ fibre segment [90, 91]. $\alpha$ denotes the attenuation coefficient along the fibre and $\beta$ is the propagation constant. $z_m$ is the distance of segment $m$ from the fibre start, therefore the round-trip time of the pulse travelling up to the $m^{\text{th}}$ segment is $t_m = \frac{2z_m c}{n_g}$ where and $c/n_g$ is the speed of light in the fibre and $n_g$ is the refractive group index.

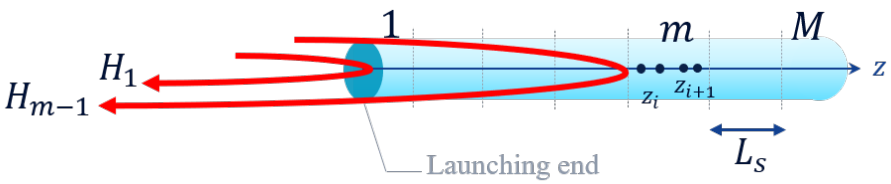


Figure 2.1: Backscattering model: $M$ segments with $N_{scat}$ scatterers within each segment. Segment index is $m$, scatterer index within segment $m$ is $i$. $\mathbf{H}_m$ is the $2 \times 2$ Jones matrix describing the SOP evolution up to segment $m$.

Each $A_m e^{j\phi_m}$ term in (2.1) results from the sum of elementary contributions within the $m^{\text{th}}$ segment:

$$A_m e^{j\phi_m} = \sum_{i=0}^{N_{scat}} a(z_i) e^{j\varphi(z_i)} \tag{2.2}$$

where $N_{scat}$ is the number of elementary scatterers within segment $m$. Each scatterer is located at a distance $z_i$ from the fibre start, as displayed in Figure 2.1, backscatters an amplitude $a(z_i)$ and rotates the phase of incident light by $\varphi(z_i)$. The Rayleigh backscattering is wavelength-dependent, such that $a(z_i) = a_i = a_i(\lambda)$ and $\varphi(z_i) = \varphi_i = \varphi_i(\lambda)$, however we will operate in a spectral interval $\Delta\lambda$ such that $\Delta\lambda \ll \lambda$ if not specified otherwise. Therefore, $a_i$ and $\varphi_i$ are assumed constant. Note that any change in the $m^{\text{th}}$ segment (length, relative position of scatterers...) could change the value $N_{scat}$ and therefore change the resulting interference of $a(z_i)e^{j\varphi(z_i)}$ elements in (2.2), without $a_i$ and $\varphi_i$ changing.

The model can be extended to a vector-format (for dual-polarization) using the Jones formalism, where the backscattered phase and amplitude are distributed over a $2 \times 2$ Jones matrix $\mathbf{H}_m$ describing the evolution of the State Of Polarization (SOP) of the transmitted probe [92], as depicted in Figure 2.1. For the following, we define a phasor per segment

$m$ from (2.1) as follows:

$$p_m = A_m e^{j\phi_m} e^{-2\alpha z_m + j[\omega_0(t-t_m) - 2\beta z_m]} \tag{2.3}$$

$p_m$ gives the dual-pass attenuation in the fibre together with the Rayleigh backscattered amplitude and phase from segment $m$. $|p_m|$ follows a Rayleigh distribution [90].

A fibre of length $L_f$ probed with symbol rate $f_{symb} = 1/T_s$ is sampled into M segments of length $L_s = \dfrac{c}{2nf_{symb}}$ following equation (1.1), such that $L_f = \dfrac{\mathrm{M}c}{2nf_{symb}}$. To each segment $m \in [1, \mathrm{M}]$, a single-pass, unitary Jones matrix $\mathbf{U}_m$ is associated. It comprises the random polarization effects encountered by the light travelling through the fibre segment (forward transmission). To model these polarization effects, three random unitary matrices are generated: $\mathbf{D}_{\beta_m} = \mathrm{diag}(e^{j\beta_m}; e^{-j\beta_m})$ and $\mathbf{D}_{\gamma_m} = \mathrm{diag}(e^{j\gamma_m}; e^{-j\gamma_m})$, diagonal phase retarders with $\gamma_m$ and $\beta_m$ uniformly drawn in $[-\pi, \pi]$ ($x \mapsto e^x$ is the exponential function), and $\mathbf{R}_{\Theta_m} = \begin{bmatrix} \cos\Theta_m & -\sin\Theta_m \\ \sin\Theta_m & \cos\Theta_m \end{bmatrix}$ a polarization rotation real matrix, with $\Theta_m = \arcsin\sqrt{\xi_m}$ and $\xi_m$ uniformly drawn in $[0, 1]$ [94]. $\mathbf{U}_i$ is the following product:

$$\mathbf{U}_m = e^{j\phi}\mathbf{D}_{\beta_m}\mathbf{R}_{\Theta_m}\mathbf{D}_{\gamma_m} \tag{2.4}$$

where $\phi$ is the common phase term to cover all possible unitary matrices. It results from Eq. (2.4) that $\mathbf{U}_m$ is a random unitary matrix, which is accurate to describe the polarization state of any static fibre segment [95].

In the following, as the interest is on the differential phase between segments, the common phase $\phi$ won't be considered in the expression of $\mathbf{U}$. Generated this way, Jones matrices cover all possible SOPs. For verification, it is possible to switch from Jones space to Stokes space and project the simulated SOP on the Poincaré sphere: for a significant number of random drawings, the full unit-radius sphere is covered, as shown in Figure 2.2.

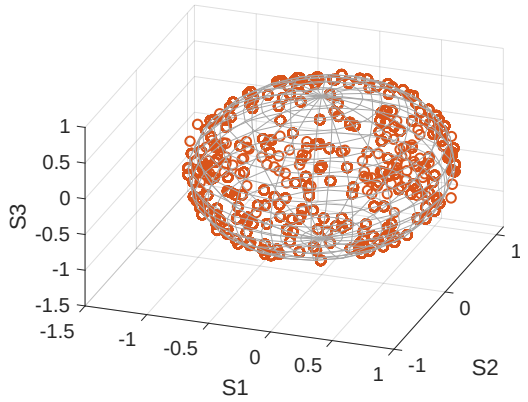


Figure 2.2: Poincaré sphere of a simulation of $\mathbf{U}$ matrices over 500m SSMF : SOP of all 2m fibre segments (coloured circles), unit sphere (grey, plain lines)

As we are interested in the backscattered light, the forward and reflection paths are modelled for each fibre segment. The reflection is placed at the end of each fibre segment, as pictured in Figure 2.1: the contributions of the scatterers along the $m^{th}$ segment are

aggregated into a reflection placed at a distance $m \times L_s$ from the fibre launching end. The reflection can be modelled either as a perfect reflection $\mathbf{M} = \begin{bmatrix} 1 & 0 \\ 0 & 1 \end{bmatrix}$, or considering polarization transfers at the reflection, introducing a transfer coefficient $\eta \in [0, 0.05]$: $\mathbf{M}_\eta = \begin{bmatrix} \sqrt{1-\eta} & -\sqrt{\eta} \\ \sqrt{\eta} & \sqrt{1-\eta} \end{bmatrix}$[1]. The value of this polarization transfer coefficient has to be measured and verified. The existence of such a transfer coefficient was considered for physical properties of silica [96], independently of optical fibre transmission. It could result in slight polarization changes of the Rayleigh backscattered light [17], which we estimate below 5% of light transferred from one polarization state to its orthogonal state. As it is not considered in most studies on Rayleigh backscatter, $\eta = 0$ is set in the following, if not specified otherwise.

The optical fibre is reciprocal from a propagation point of view, which translates into $\mathbf{U}_{backward} = \mathbf{U}_{forward}^T$, with $T$ standing for the transpose operator. Assuming that $\mathbf{U}_m$ can be the forward matrix of segment $m$ as well as the product of all forward matrices from segment 1 to segment $m$ (since a product of random unitary matrices is a random unitary matrix), the full dual-pass Jones matrix from the initial segment up to fibre segment $m$ is then:

$$\mathbf{H}_m = p_m \mathbf{U}_m^T \mathbf{M} \mathbf{U}_m \tag{2.5}$$

where $p_m$ is the phasor defined in (2.3).

Polarization Dependent Loss (PDL) and Polarization Mode Dispersion (PMD) are considered negligible in the fibre sensor. The general shape of the Jones backscatter matrix is computed as follows for all spatial segments $m$:

$$\mathbf{H}_m = p_m \begin{bmatrix} e^{j2\gamma_m}(\cos 2\beta_m + j \sin 2\beta_m \cos 2\Theta_m) & -j \sin 2\beta_m \sin 2\Theta_m \\ -j \sin 2\beta_m \sin 2\Theta_m & e^{-j2\gamma_m}(\cos 2\beta_m - j \sin 2\beta_m \cos 2\Theta_m) \end{bmatrix} \tag{2.6}$$

As the SOP of the emitted signal at the transmitter and the incident signal at the receiver side are not perfectly aligned, a misalignment parameter $\theta$ will be considered. It is reported as an additional rotation, for example at the entrance of the system $\mathbf{R}_\theta = \begin{bmatrix} \cos\theta & -\sin\theta \\ \sin\theta & \cos\theta \end{bmatrix}$, resulting in $\mathbf{H}_m = p_m \mathbf{U}_m^T \mathbf{M} \mathbf{U}_m \mathbf{R}_\theta$. No phase retarder is added as the considered fibre portions at the transmitter and receiver are small compared to the fibre sensor length $L_f$.

**Polarization beat length** Finally, the polarization beat length $L_{pb}$ of the simulated fibre is considered. This way, the speed of polarization variations from one fibre segment to the other is controlled. For single mode fibres, $L_{pb}$ is of the order of magnitude of 10m [97]. By definition if $L_s/L_{pb} \geq 1$, then the SOP in two successive segments is uncorrelated: polarization parameters are randomly drawn from one segment to the other, the SOP of light returning from segment $m+1$ is independent from the SOP of light returning from

[1] We assume that the forward SOP is expressed in an $(x, y, z)$ coordinate system where the $z$ axis points towards the propagation axis and the backward SOP is expressed in the $(x, y, -z)$ coordinate system.

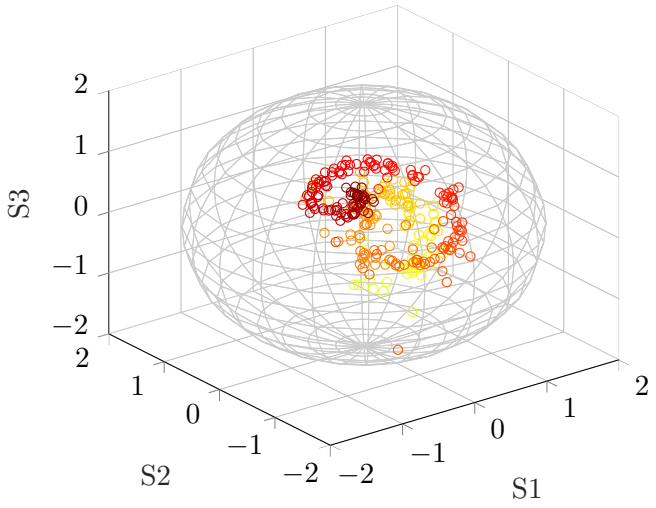


(a) $L_s/L_{pb}$= 1.4.10$^{-2}$

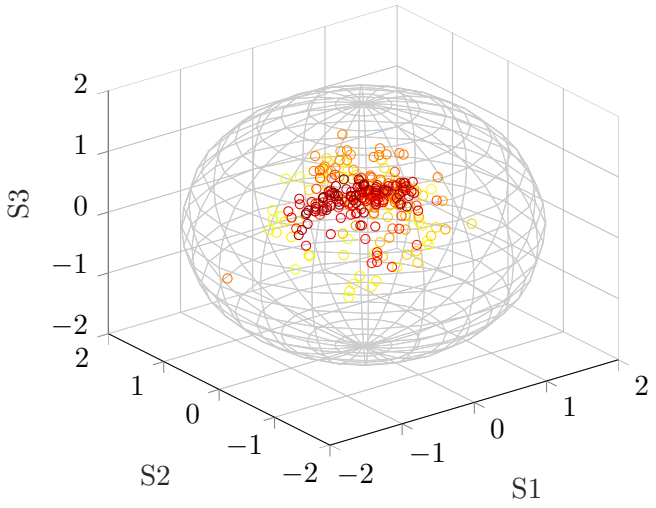


(b) $L_s/L_{pb}$= 6.8.10$^{-2}$

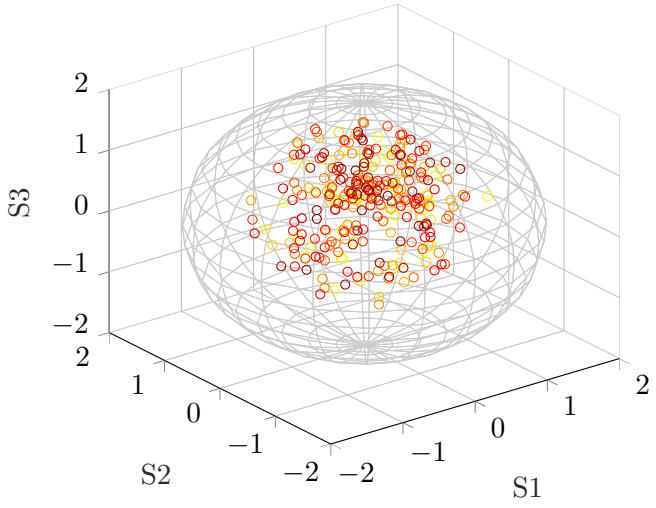


(c) $L_s/L_{pb}$= 3.4.10$^{-1}$

Figure 2.3: Poincaré sphere of polarization evolution along the fibre (forward transmission), for different spatial resolutions $L_s$. Color changes with distance to fibre start.

segment $m$ ; else if $L_s/L_{pb} \to 0$, then there is almost no SOP change from one fibre segment to the next ; for values of $L_s/L_{pb}$ comprised in $]0, 1[$, the change in the SOP will be proportional to the ratio $L_s/L_{pb}$, with the polarization parameters $\rho$ (referring to $\beta$, $\gamma$ or $\Theta$) verifying $\rho_{m+1} = \rho_m + \frac{L_s}{L_{pb}} \times \rho_{new}$, with $m$ the segment index. $\rho_{new}$ is randomly drawn as described in the beginning of this section and independent from $\rho_m$.

Simulations for different $L_s/L_{pb}$ ratios are shown in Figure 2.3, where it appears that the larger $L_s/L_{pb}$, the more random the trajectory of the SOP of light in the fibre (including attenuation $\alpha$, thus not of constant modulus on the sphere).

We observe in Figure 2.3(c) that from $L_s/L_{pb} > 10^{-1}$, the distribution of the SOP over the Poincaré sphere is already random. When targeting sensing applications over telecom fibres, the spatial resolution $L_s$ is typically in the range of 1m to 10m (specific fields such as medicine are out of the scope here). **Therefore, and for sake of simplicity, the simulation study below is conducted with uncorrelated SOP from one segment to the next** ($L_s/L_{pb} \geq 1$ case). Notice that additional simulations performed with $L_s/L_{pb} \simeq 10^{-1}$ and $L_s/L_{pb} > 1$ in the sensor, which are not displayed here, lead to similar results.

## 2.2 Extrinsic noise contributions

Once the fibre model is defined, the probing method and the receiver parameters are introduced. Many waveforms can be used for the interrogation of such a fibre model, from simple pulse trains to frequency sweeps or specific coded sequences (including those presented in chapter 1) which can be integrated to the expression (2.1).

Figure 2.4 gives a schematic view of a $\Delta\phi$-OTDR and the elements of the set-up are associated to their main noise contributions. We call "extrinsic noise" the noises which come from other sources than the sensor itself, namely instrumentation-related noises. The propagation medium is the fibre, the model of which is described in the previous section.

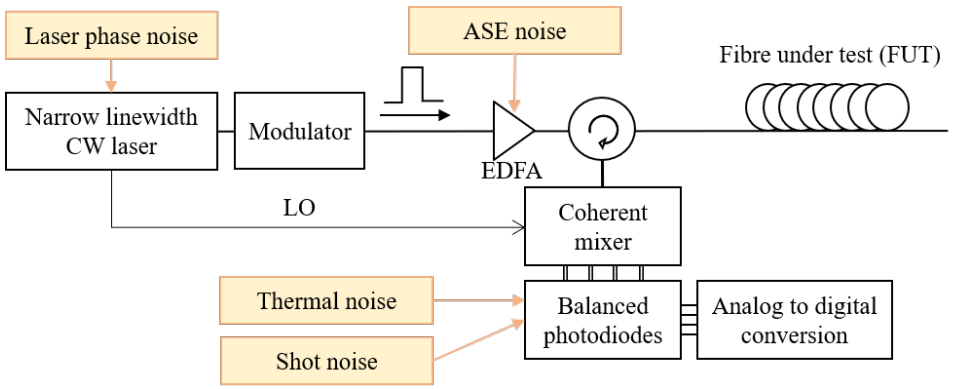


Figure 2.4: Schematic view of a coherent differential phase OTDR system (white boxes) and associated noise contributions (orange boxes). CW: Continuous Wave, LO: Local Oscillator, ASE: Amplified Spontaneous Emisssion, EDFA: Erbium Doped Fibre Amplifier

**Laser phase noise** The transmitter encloses a narrow linewidth laser, modulated by a specific pattern. The laser is not ideal, therefore its linewidth $\Delta\nu$ is not zero (phase noise) and its frequency can fluctuate (frequency noise). Yet, since differential phase OTDRs measure phase variations, they require a certain stability of the probe laser, which guarantees that the measured variations are from the fibre sensor and not from the probe. The accurate term is "coherence" condition: the laser *coherence length* is defined as the propagation length over which the phase of the transmitted light can still coherently add with the output light of the laser.
In coherent-OTDR, the least condition is to have intra-pulse coherence [33] which ensures coherent interference of the probe pulse at the fibre segment level. Another condition applies to spread-pulse techniques which require stationarity of the channel response, along with coherence state, during the full duration of a code [58]. Therefore, any degradation of the laser coherence leads to specific noise which we refer to as "laser phase noise" since it implies source phase fluctuations.

Laser phase noise here is modelled as a Wiener process of variance $\sigma^2 = 2\pi\Delta\nu T_s$ where $\Delta\nu$ is the laser linewidth, $T_s$ is the symbol period. Therefore, the coherence length $L_{coh}$ is defined as

$$L_{coh} = \frac{c}{\pi n \Delta\nu} \tag{2.7}$$

where $c$ is the celerity of light and $n$ the average refractive index in the fibre [33]. Although this does not perfectly match the physical reality, for which laser frequency noise increases in $1/f^d$, $d \geq 1$ [98], this enables to predict the general evolution of the error on phase estimation over distance [99].

Simulations where the phase noise variations in time are displayed along fibre distance, in Figure 2.5, did demonstrate how the laser linewidth in its first approximation (white part, no $1/f^d$ contribution) impacts the distinction threshold over long distances of fibre[2].

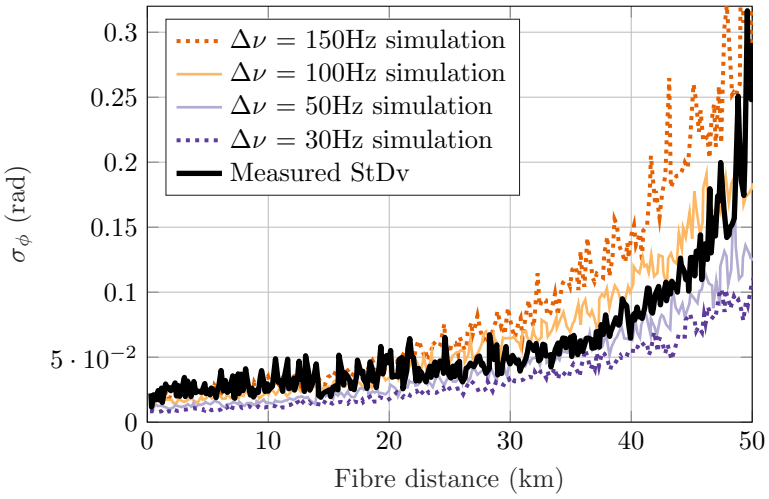


Figure 2.5: Optical phase standard deviation along fibre distance, for several laser linewidths, compared to experimental data

[2]Of course, other noise contributions impact the distinction threshold, such as attenuation, coherent fading...

In addition, a measurement of phase noise variations along fibre distance was performed over 50km static (insulated from any mechanical noise[3]) SSMF and is displayed in black thick line in Figure 2.5, which allowed to estimate the laser linewidth of the source that is used in the following of the study. Indeed, a laser source is often given an instantaneous linewidth value but it is very difficult to measure the linewidth in long time frames (of the millisecond order).

Beyond the Lorentzian model, a typical laser frequency noise spectral density is also composed of flicker noise at low frequencies, which is commonly referred to as "$1/f$ noise" [100]. A method was reported by University of Neuchâtel [101, 102] to estimate the laser linewidth from the frequency noise spectral density to separate the contributions of flicker and white noise to the linewidth. However the $1/f$ noise contribution did not appear as a main contribution to the noises for distances below 50km, as demonstrated in Figure 2.5 above where an experimental measurement is well approached by simulation including first order phase noise only. Such a $1/f$ noise model might come useful in case of longer simulated fibre distances, i.e. 100km and beyond.

Other research groups in the distributed sensing domain investigated the impact of laser phase noise. They show how narrower laser linewidths allow an increase of the Signal-to-Noise Ratio (SNR) for distributed acoustic sensors [103], and different groups investigated laser phase noise immunity of their interrogation technique to relax the coherence conditions [33, 104].

**White noise** An interrogator system encloses electronic and optic devices, among which active elements that all introduce Additive White Gaussian Noise (AWGN). Passive elements will generally introduce losses, such as insertion losses.

At the transmission stage, an Erbium Doper Fibre Amplifier (EDFA) is used to amplify the signal at the output of the modulator before sending the probing signal towards the fibre sensor. White noise is generated here in the form of Amplified Spontaneous Emission noise (ASE), due to the amplifications mechanisms of Erbium. Also, fluctuations of the source output power can cause Relative Intensity Noise (RIN).

Secondly, the backscattered light from the fibre enters the reception stage through the circulator. The reception block encloses a dual-polarization coherent receiver prior to analog-to-digital conversion and post-processing. The balanced photodiodes are subject to shot noise or quantum noise mainly from the photodetectors, and thermal noise mainly from their trans-impedance amplifiers (TIA). The circulator and coherent mixer are included in the model as losses whereas the photodiodes are considered as a source of AWGN. The white noise of the receiver is considered as $\sigma^2_{AWGN} = \sigma^2_{th} + \sigma^2_s + \sigma^2_{RIN}$, where the contributions of the shot noise $\sigma^2_s$ and thermal noise $\sigma^2_{th}$ are dominant compared to the RIN in our case, due to low backscattered power level.

At the receiver side, analogue-to-digital conversion is performed after photodetection.

[3]Soundproofing or "mechanical insulation" of a box means that foam-like materials have been placed on the inside of the box such that external environmental perturbations are sufficiently damped to avoid affecting the fibre.

Since the Rayleigh backscattered signals can be very low-power, a fine quantification is necessary at this stage. Coarse quantification by the Analogue-to-Digital Converters (ADCs) can be a source of imperfections and thus of noise at the receiver. A thorough study of the quantification requirements enabling the determination of the minimal Effective Number Of Bits (ENOB) is outside the scope of that manuscript.

## 2.3 Dynamic model ; limitations

Once the full dual-polarization backscatter model is set up, it is of interest to introduce small variations to the model, to emulate external perturbations. While the backscattered State Of Polarization (b-SOP) is impacted by strong disturbances such as bending the fibre or strain directly applied to the fibre, the backscattered phase is rather impacted by acoustic perturbation in the surroundings (that mainly impacts the phase as it induces small longitudinal strain).

We develop a small disturbance perturbation model for the fibre model. We now consider a single segment location in Figure 2.6. A low frequency excitation is applied point-wise at the center of a selected fibre segment to emulate a periodic longitudinal extension, and the segment extremities are assumed to be fixed points. Therefore, the system behaves such that the full segment is excited, and this segment only. The excitation changes the geometric coordinates of the elementary scatterers in the segment according to the instantaneous amplitude and to a time varying term $p_m$ (defined in Eq. (2.3)). The rest of the equation, that is the polarization and the reflection terms, is left unchanged, which is an acceptable assumption in case of a low energy perturbation.

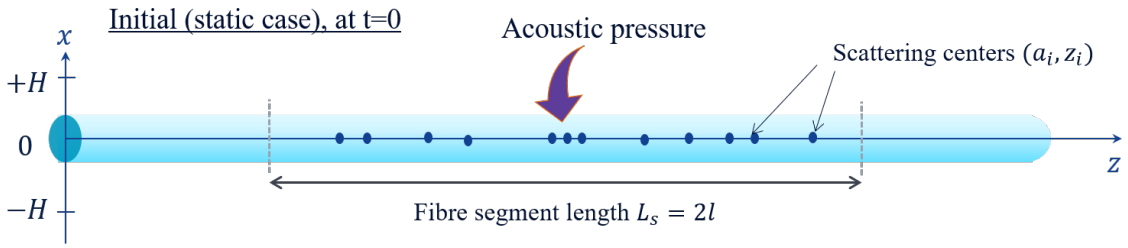


(a) Fibre model

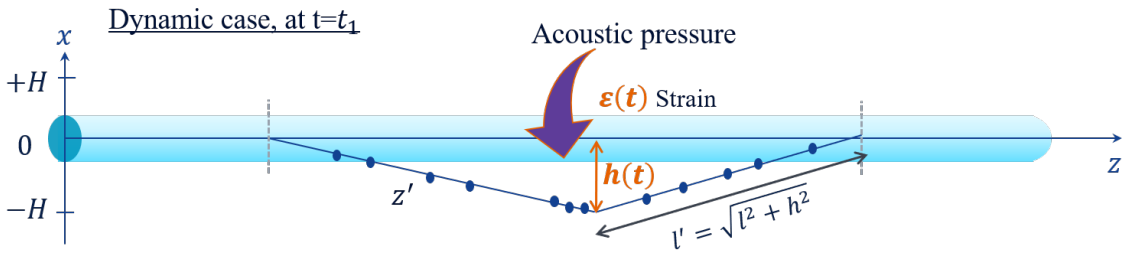


(b) Deformation

Figure 2.6: Dynamic model: local perturbation geometry

Figure 2.6(a) displays a schematic view of the modelled fibre segment of length $L = 2l$ which experiences strain. The strain will be such that the middle of the segment moves along axis $x$ of a distance $h(t)$ comprised between $-H$ and $+H$, orthogonal to the fibre axis

$z$. Consequently, the distance between the virtual scattering centres is modified following Figure 2.6(b): the fibre elongates such that the half fibre segments verify $l' = \sqrt{l^2 + h(t)^2}$, shifting the scattering centres along the new fibre segment length. Finally, the fibre segment stretch is modelled as a longitudinal stretch (along axis $z$ only) as pictured in Figure 2.7. The strain applied to the fibre segment is expressed as $\varepsilon(t) = \frac{l'(t)-l}{L_s}$.

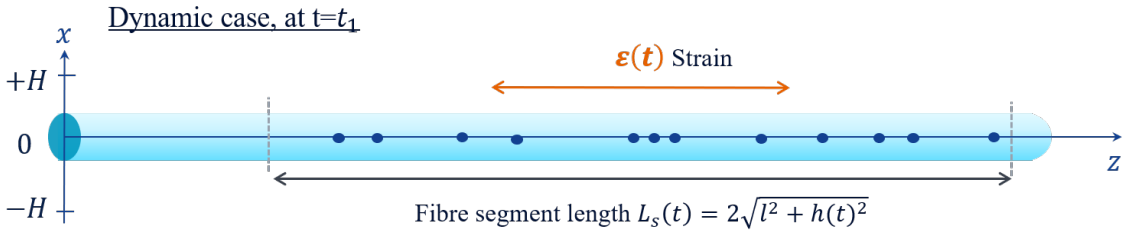


Figure 2.7: Dynamic model: equivalent longitudinal strain

The dynamic simulation runs similarly to the static simulation defined in the previous sections, with the sole difference that, for a given segment $m$, the $p_m$ common phasor varies in time.

A dynamic simulation result is displayed in Figure 2.8. A 1km long fibre is simulated and the segment located 410m from the fibre start is excited with an increasing extension $h(t)$ (see Figure 2.8(a)) such that the extension of the segments ranges from 0 to 100 $n\varepsilon$, at $f_{strain} = 200$Hz frequency. Laser phase noise is added to the simulation ($\Delta\nu = 75$Hz), codes are used for the interrogation which verifies $f_{Symb} = 50$MBaud, $B_{meca} = 760$Hz. The time versus distance phase map of the simulated fibre between 406m and 416m is displayed in Figure 2.8(b). The excited segment is clearly noticeable as we see its phase being modulated in time, with growing amplitude as the simulated strain increases. The optical amplitude (expressed as the modulus of the determinant of backscattered Jones matrices $|\det|$) and phase backscattered from the excited segment and its neighbours are displayed in Figure 2.9.

The difference in the mean values of backscattered amplitude in time are due to coherent fading, namely the random drawing of $p_m$ values during the modelling process of the fibre. We notice in Figure 2.9(a) that the backscattered amplitude is also modulated by the strain, although not in the same proportions as for the phase. In both the amplitude and phase figures in Figure 2.9, the adjacent segments are also affected by the disturbance as we notice a small modulation of amplitude and phase around 412m. Other segments are simply affected by laser phase noise. This is mainly due to the noise which degrades the differential phase process, which in turns propagates residual phase variations to static segments. Such artefacts are observed on experimental measurements as well. Working on the mitigation of such artefacts is more convenient with a simulation model where each noise contribution is monitored, hence the interest of such a dynamic model.

Yet, the "small disturbance" model rapidly meets its limit as the observed behaviour of light backscattered from an excited segment includes a modulation of the determinant of backscattered Jones matrices [105] even at small strain values, and that in most observed

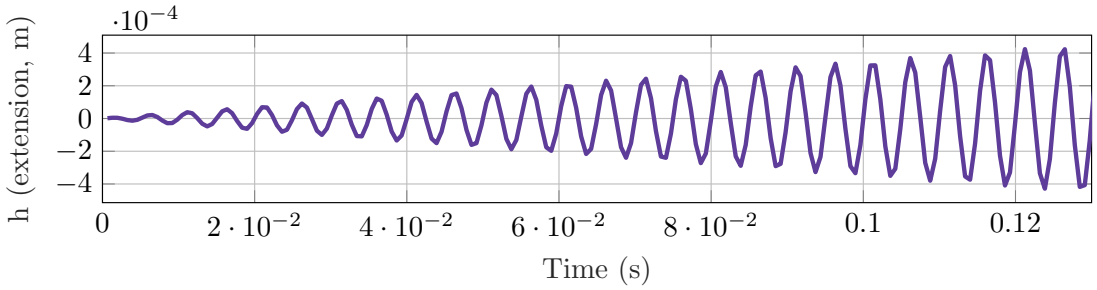


(a) Excitation $h(t)$ of the fibre segment

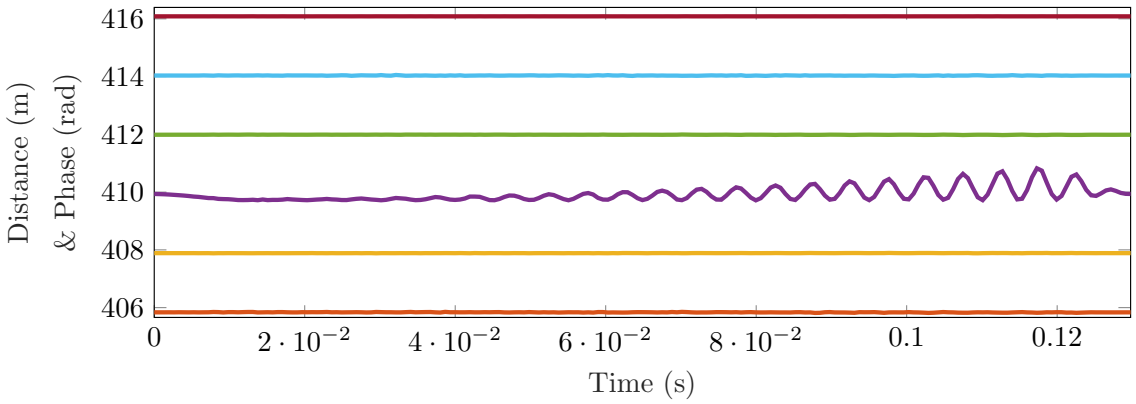


(b) Time/Distance map around the excited segment location

Figure 2.8: Dynamic model: fibre extension yielding strain from 0 to 100n$\varepsilon$, at $f_{strain}$ = 200Hz and on $200T_{code}$ duration (0.13s) and corresponding Time/Distance map of phase for a simulated fibre where the segment around 410m (segment size is 2m) is exposed to strain

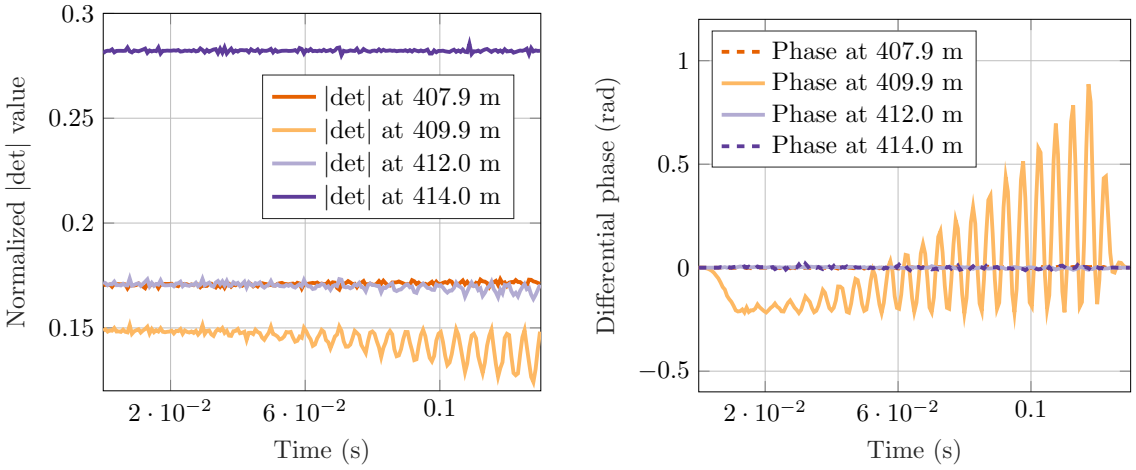


(a) Backscattered amplitude in time at perturbation location

(b) Phase at perturbation location

Figure 2.9: 0 to 100n$\varepsilon$ simulated strain perturbation around 410m (segment size is 2m) on 200$T_{code}$ duration (0.13s)

real-life situation the b-SOP is modulated as well. Moreover, this dynamic model did not include variations of the SOP (at the perturbation location: $\mathbf{D}_{\beta_m}, \mathbf{R}_{\Theta_m}, \mathbf{D}_{\gamma_m}$) which would allow to fully characterize the polarization variations induced by a disturbance near the fibre sensor. Therefore, a close understanding of the b-SOP is needed to further develop a comprehensive dynamic dual-polarization backscatter model, which is outside the scope of this study.

## Summary on the use of a dual polarization backscatter model

The development of a dual-polarization backscatter model first allowed to compare the roles of the different noises and attenuations occurring in the fibre, therefore giving an evaluation of the contributions of each block of the interrogator system. The laser linewidth was identified as a major contributor to the increase of phase noise at long fibre distances for example, in addition to the usual attenuation in optical fibres.

Also, all random polarization effects were modelled along the fibre, allowing to change parameters that are usually constant in optical fibres such as polarization beat length. In the following, the polarization dimension will be exploited to compare different phase-OTDR interrogation methods of the fibre sensor.

# Chapter 3

# Polarization effects and reliability

A comprehensive model for dual-polarization Distributed Optical Fibre Sensors (DOFS) was developed in the former chapter. Different aspects of light transmission and backscattering in fibres were defined, such as intra pulse interference for backscattered light and polarization effects. Moreover, the main noise contributions to a $\Delta\phi$-OTDR were mentioned.

Now that the fibre and interrogator system are defined, we aim at understanding the interrogation (or probing) process which was first described in chapter 1. Mainly, Rayleigh scattering is known to be polarization-dependent [106], so the role of polarization in fibre sensor interrogation is investigated in this chapter. Eventually, we aim at quantifying the advantage of polarization diversity, be it at the receiver side or at the transmitter side of a coherent $\Delta\phi$-OTDR. A robust interrogation method is proposed as we reach a better understanding of DOFS.

## 3.1 Input and output polarization states: on the mitigation of polarization fading

In this first section, we define the phase estimators according to the interrogation scheme. The input and output states of polarization are considered such that we can compare single and dual polarization interrogation schemes, considering Single polarization Input - Single polarization Output (SISO), Single Input - Multiple Output ($1 \times 2$ SIMO) and Multiple Input - Multiple Output ($2 \times 2$ MIMO) probing techniques, and investigate the issues related to each of them.

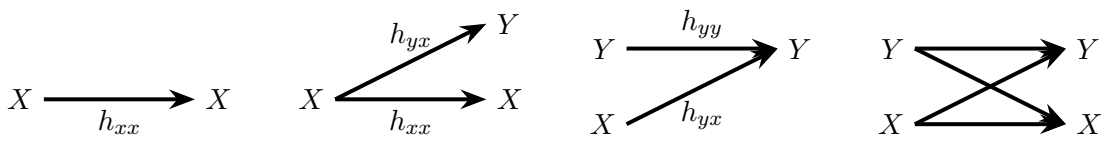


(a) SISO (b) SIMO (c) MISO (d) MIMO

Figure 3.1: Schematic of different transmission configurations, with two projection axes at the receiver and transmitter.

In Figure 3.1, we illustrate the different possible interrogation schemes from a general telecommunications point of view, with projections on arbitrary orthogonal polarization axes $X$ and $Y$.

### 3.1.1 Phase estimators and polarization diversity

The Jones notation [70] was briefly described in subsection 1.2.4, and used for system modelling in chapter 2. It allows to represent optical elements that can modify polarization state, phase or intensity of light as $2\times2$ matrix operators. Then it allows to further express the optical field $E_{out}$ at the output of an optical system as a function of the input field $E_{in}$ and of the optical elements $\mathbf{H}$ as follows: $E_{out} = \mathbf{H}E_{in}$.

Therefore, the Jones matrices allow to express the contributions of optical elements to the polarization state of the light. In our case, the optical elements are the successive fibre segments described in chapter 2. We denote $x$ and $y$ the orthogonal polarization axes, for example in Jones notation $x = \begin{bmatrix}1\\0\end{bmatrix}$ and $y = \begin{bmatrix}0\\1\end{bmatrix}$. The subscript $xy$ means "received on $x$ axis, sent on $y$ axis", as depicted in Figure 3.2.

$$\mathbf{H} = \begin{pmatrix} h_{xx} & h_{xy} \\ h_{yx} & h_{yy} \end{pmatrix}$$

Figure 3.2: Convention on Jones matrices terms: in thin blue is what was sent on polarization axis $x$ (to $x$ and $y$), in thick red is what was received on polarization $x$ (from $x$ and $y$)

**SISO interrogation:** SISO also consists in sending light on one polarization axis. It recovers information on one polarization only ($h_{xx}$ for example), such that the estimated phase is $\hat{\phi}_{SISO} = \angle(h_{xx})$.

A SISO interrogator is displayed in Figure 3.3(a), it is an implementation of $\Delta\phi$-OTDR where only one polarization is modulated at the transmitter side and one polarization is recovered at the receiver.

**SIMO interrogation:** SIMO probes a single polarization. For a recovered signal on both polarizations, if the probing is done over the $x$ polarization, then we get a channel estimation $\mathbf{H'} = [\,h_{xx}\;\; h_{yx}\,]^T$, and the common phase can be estimated as:

$$\hat{\phi}_{SIMO} = \angle(h_{xx} + h_{yx}) \tag{3.1}$$

Note that in Eq. (3.1) we also have $\hat{\phi}_{SIMO} = \arctan\left(\frac{\Im_{xx} + \Im_{yx}}{\Re_{xx} + \Re_{yx}}\right)$ with $\Re$, $\Im$ the real and imaginary parts of $h_{xx}$ and $h_{yx}$ data [107].

The SIMO interrogator set-up is depicted in Figure 3.3(b) as as a $\Delta\phi$-OTDR setup where only one polarization is modulated at the transmitter side, it is as a usual implementation of $\Delta\phi$-OTDR in the recent literature.

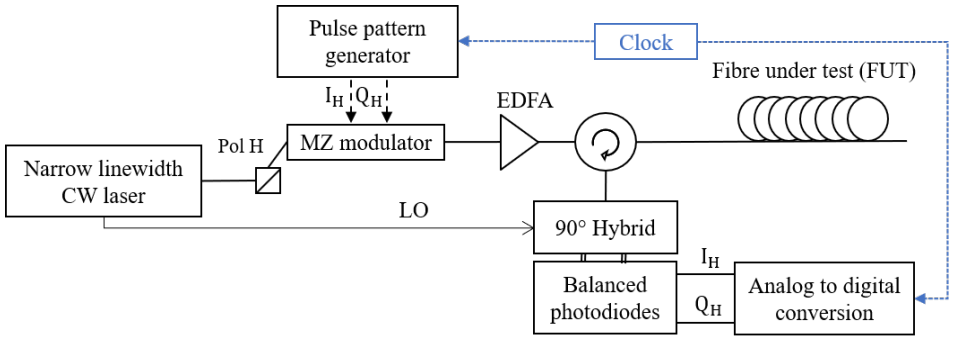


(a) SISO interrogator set-up

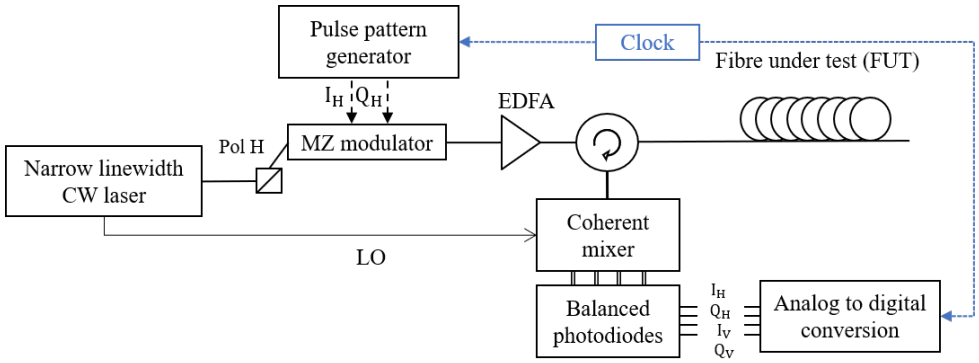


(b) SIMO interrogator set-up

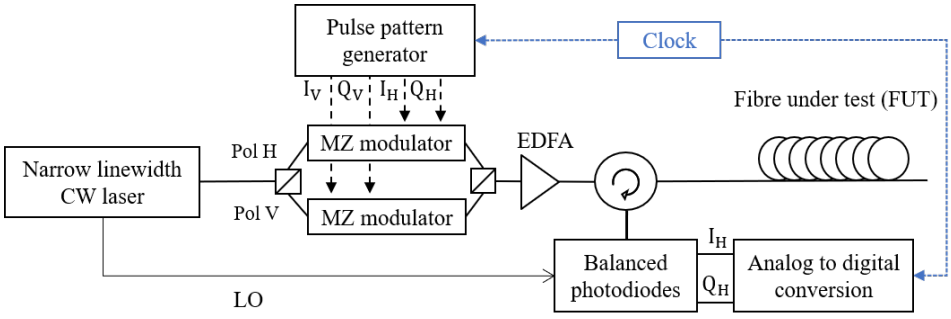


(c) MISO interrogator set-up

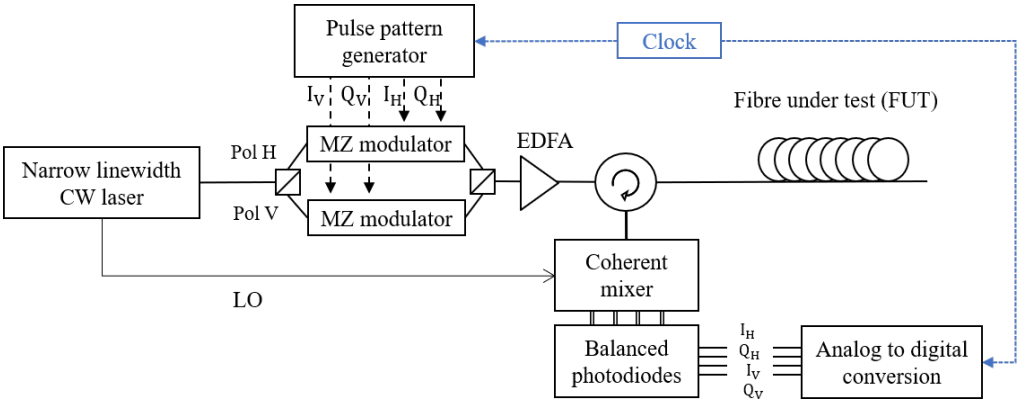


(d) Coherent-MIMO interrogator set-up

Figure 3.3: Interrogator set-ups, according to the number of polarizations at the transmitter and receiver. MIMO: Multiple In, Multiple Out; CW: Continuous Wave; EDFA: Erbium Doped Fibre Amplifier; LO: Local Oscillator; MZ: Mach-Zehnder, Pol.: Polarization

**MISO interrogation:** MISO proceeds the same way as SISO at the receiver side: only one polarization is recovered, therefore we get $h_{xx} + h_{xy}$ with no additional information to differentiate both polarization components. Two components are recovered because the MISO interrogation probes two polarization axes at the transmitter side. Estimated MISO phase is then $\hat{\phi}_{MISO} = \angle(h_{xx} + h_{xy})$.

The MISO interrogator depicted in Figure 3.3(c) is an unusual but possible implementation of $\Delta\phi$-OTDR where two polarization are modulated at the transmitted side but without polarization diversity at the receiver.

**MIMO interrogation:** MIMO relies on specific interrogation sequences or sweeps that are simultaneously sent onto two orthogonal polarization axes, as detailed in subsection 1.2.4. The sequences sent on one polarization axis are orthogonal to the sequences sent on the second axis, or at least show a satisfying extinction ratio, such that the full $2 \times 2$ Jones matrix $\mathbf{H}$ of the channel is recovered.

For $\mathbf{H}$ which general expression was given in (2.6), we assume $\mathbf{H}$ has a common backscattered phase $\phi$ such that $\mathbf{H} = e^{j\phi}\left[\begin{smallmatrix} h'_{xx} & h'_{xy} \\ h'_{yx} & h'_{yy} \end{smallmatrix}\right]$, where $\left[\begin{smallmatrix} h'_{xx} & h'_{xy} \\ h'_{yx} & h'_{yy} \end{smallmatrix}\right]$ is unitary. With $\mathbf{H}$ being the dual-pass matrix of the channel, $\phi$ is the dual-pass phase. Hence the use of the following phase estimator:

$$\hat{\phi}_{MIMO} = 0.5\angle(\det \mathbf{H}) \tag{3.2}$$

where $\det \mathbf{H}$ is the determinant of $\mathbf{H}$ (yielding $\det \mathbf{H} = h_{xx}h_{yy} - h_{yx}h_{xy}$)[1] and $\angle$ denotes the *angle* function. We recall below the $\Delta\phi$-OTDR set-up associated with MIMO which was presented in subsection 1.1.3 as Figure 3.3(d).

### 3.1.2 Polarization intensity fading

We consider the backscattered field $\vec{E}_m$ from a fibre segment $m$. $\vec{E}_m$ results from the summation of $N_{scat}$ elementary fields reflected in segment $m$. In Equation 2.2, we considered that all contributions were aligned, so that a scalar summation was realized. Yet in the general case, each elementary field is with a specific polarization $\vec{\mathbf{e}}$. Therefore:

$$\vec{E}_m = \sum_{i=0}^{N_{scat}} a(z_i)e^{j\varphi(z_i)}\vec{\mathbf{e}}_i \tag{3.3}$$

Similarly to coherent fading which occurs if the $a(z_i)e^{j\varphi(z_i)}$ interfere destructively in case of aligned contributions, polarization fading occurs in case the $\vec{\mathbf{e}}_i$ are orthogonal.

For example, with $N_{scat} = 2$, the resulting intensity $I_m$ of $\vec{E}_m$ is:

$$I_m = 2(\vec{\mathbf{e}}_1 \cdot \vec{\mathbf{e}}_2)\,\Re\Big(a(z_1)a(z_2)e^{-j(\varphi(z_1)-\varphi(z_2))}\Big) \tag{3.4}$$

therefore if $\vec{\mathbf{e}}_1 \perp \vec{\mathbf{e}}_2$, then $I_m = 0$. Moreover, polarization fading occurs at the receiver side

[1] The 0.5 factor in the expression of $\hat{\phi}_{MIMO}$ is due to the derivation of $\det(\mathbf{H})$ where each $h_{ij}$ holds the phase information, therefore $\det(\mathbf{H})$ holds $2 \times \hat{\phi}_{MIMO}$.

of the sensor system when the incident SOP $\vec{\mathbf{e}}_m$ and the SOP of the Local Oscillator (LO) $\vec{\mathbf{e}}_{LO}$ at the receiver become orthogonal, as follows[2]:

$$I_{RX} = 2(\vec{\mathbf{e}}_m \cdot \vec{\mathbf{e}}_{LO})\,\Re\Big(A_m A_{LO} e^{-j(\varphi_m - \varphi_{LO})}\Big) = 0 \times \Re\Big(A_m A_{LO} e^{-j(\varphi_m - \varphi_{LO})}\Big)$$

Polarization fading was identified in interferometric sensors [22, 108], and remains an issue in coherent detection DAS. In more recent fibre sensors with coherent detection, polarization effects can prevent detection of the strength of perturbations [36].

Existing SISO and MISO configurations do not necessarily include a coherent receiver with polarization diversity but rather a single polarization or single 90° hybrid direct detection receiver, and use all-optical techniques to recover the phase such as delay lines, dual pulses, chirped pulses... Using direct detection, there is no sensitivity to SOP variations of the incoming light: the full intensity of the signal is received [56]. We recall that the difference between $\phi$-OTDR and $\Delta\phi$-OTDR was given in subsection 1.1.2: in direct detection and coherent source scheme (namely phase OTDR), it is possible to have a rather stable $\phi$-OTDR trace from comparisons of successive power-versus-time traces [34]. Further trace-averaging can be performed if a speckle pattern is still noticeable [63]. Also, it was noticed that considering polarizations separately could bring a better accuracy to the system [109].

Referring to the notations in subsection 3.1.1, polarization fading strongly impacts SISO configuration: when detecting $h_{xx}$, an intensity fading will occur for periodic $(\Theta, \beta)$ pairs corresponding to orthogonality between the emitted $x$-polarization and the received $x$-polarization, resulting in no reliable phase estimation.

To overcome this polarization intensity fading effect, recent work focus on the receiver design and uses a dual-polarization coherent receiver [57, 107] so that the overall received optical power is kept constant independently from the state of polarization of the incident signal at the receiver side.

### 3.1.3 Polarization induced phase noise

A widespread assumption is that polarization-diversity receivers are the key to mitigate polarization fading [54], yet polarization-diversity reception can be improved [110]. What's more, the dual-polarization receiver setup is not sufficient to provide a perfect channel estimation. It would be more accurate to mention "polarization fadings" as several mechanisms are involved. The transmitter setup must as well be taken into account for fully achieving a polarization insensitive sensor as polarization induced phase noise is actually transmitter-dependent. This effect was observed in [111] and further analysed in [112], it depends on the input state of polarization (SOP).

**SIMO resilience to polarization in $\Delta\phi$-OTDR** Here, we use $\Delta\phi$-OTDR, namely coherent detection based phase-OTDR with a coherent laser source. Coherent receivers

[2]See the coherent detection equations in subsection 1.2.2

are sensitive to the SOP of incoming light. To recover the full signal, we need to use a polarization diversity scheme, where each polarization component is detected by projecting the incident signal over two orthogonal polarization states and beating each projection with the same LO [56]. Since the polarization information is fully recovered with SIMO and MIMO, there is no polarization intensity fading in these systems. In other words, SIMO and MIMO modes are supposed to be resilient to polarization fading, meaning there will always be a phase estimation that is stable in time for a given segment $m$:

$$\phi_{SIMO} = \angle\Big(p_m \cdot \Big(e^{j2\gamma_m}\cos 2\beta_m - j\sin 2\beta_m(e^{j2\gamma_m}\cos 2\Theta_m + \sin 2\Theta_m)\Big)\Big) \tag{3.5}$$

here, Eq. (3.1) is applied to $\mathbf{H}$ defined in chapter 2 with polarization transfer coefficient $\eta = 0$ as $\mathbf{H} = p_m \mathbf{U}_m^T \mathbf{M} \mathbf{U}_m$. We recall $\mathbf{U}$ is defined in equation (2.4) as a function of phase retarders $\mathbf{D}_{\beta_m}$, $\mathbf{D}_{\gamma_m}$ and a rotator $\mathbf{R}_{\Theta_m}$. The MIMO phase estimation is $\phi_{MIMO} = \angle(p_m)$.

Yet, without considering coherent fading effect that could lead to $\angle(p_i) \to 0$ and therefore (3.5)$\to$ *undetermined*[3], it appears that phase-OTDR systems in SIMO configuration encounter unexpected fading effects that their authors report as "polarization-related issues", such as in [53, 113]. When [22] first reported input polarization phase noise in interferometric sensors in the form of visibility fluctuations, they mitigated the effect using a depolarized signal at the sensor input. In recent phase-OTDR systems, we expect input polarization phase noise to stay present in case the probing signal comes from a single laser without further processing (no depolarization).

It is worth noticing that MISO also allows to recover a phase estimation as its expression is similar to that of SIMO using Eq. (3.1): even if the receiver SOP is orthogonal to polarization $y$, polarization $x$ will be recovered, and vice-versa. Of course, MISO- and SIMO- estimated absolute phases differ from the real common phase due to polarization effects (SOP transformation parameters $\Theta, \gamma, \beta$ appear in their expression) but when sensing dynamic events, we are only interested in phase variations compared to a stable reference. Therefore, polarization diversity at the transmitter side would in theory allow to mitigate some of the polarization-related noise, even without polarization diversity at the detector.

## 3.2 Impact of polarization effects on phase estimation

Recent and older results, together with our definitions of SISO and SIMO, agree on the need for multiple receivers, should it be in direct detection [114] or by employing polarization diversity system in coherent OTDR [53, 54]. However, some impairments referred to as "polarization effects" are still reported, which we relate here to input polarization phase noise. Meanwhile, MISO case is not considered in the literature for optical systems, even though it is of great interest for radiocommunications. Yet, it seems interesting from a theoretical point of view to investigate the impact of diversity at the transmitter. In fibre interferometers, using depolarized light at the transmitter was reported to limit the

[3]More precisely, $\angle(p_i) \to \angle(0 + \mathsf{noise})$, therefore $\phi_{SIMO}$ will tend towards the phase of $\mathsf{noise}$, which is a random phase.

polarization fading effects [112]. The polarization beat length was also mentioned, as it could play a role in the quality of the received signal when confronted to polarization fading [91].

For the detection of an event, we chose to monitor the standard deviation of the differential phase over time, along the fibre distance, denoted $\sigma_\varphi$: when an event occurs along the sensor, phase variations appear in time, thus increasing the phase standard deviation locally; conversely, in the absence of an event no phase variations should occur and $\sigma_\varphi$ should remain close to zero (ideally zero). Therefore, $\sigma_\varphi$ in the absence of events is used as a distinction threshold metric of the system. We will show later how it is translated to a strain ($\varepsilon$) noise floor.

The displayed traces in this section are simulations of a $\Delta\phi$-OTDR, where the phase is recovered according to the estimators defined in subsection 3.1.1. All simulations are static, e.g. with no strain variation applied to the sensor. Therefore, this study focuses on the false alarm issue, not onto the non-detection case (from a statistical point of view): the main requirement for phase sensors is that no variation or "false alarm" occurs when the fibre is not disturbed, which is also the condition to achieve the lowest distinction threshold.

### 3.2.1 Accuracy and false alarms

Firstly, the global behaviour of the $\sigma_\varphi$ along sensor distance is considered in order to highlight the difference between the given phase estimators. Secondly, paying attention to the $\sigma_\varphi$ peaks, we show how they relate to the polarization rotation and birefringence in the fibre segments.
Figure 3.4 gives the phase standard deviation $\sigma_\varphi$, integrated on a given duration (here, 2s), along fibre distance for static simulations along 50km SSMF, where Figure 3.4(a) is a zoom on 1.4km at the beginning of one simulated fibre, with a spatial step of 20m. We use the polarization multiplexed BPSK codes presented in subsubsection 1.2.4.2. The interrogation duration is 5.24ms with a symbol rate $f_{symb}$ = 25Mbaud, at a constant power of 7dBm at the entrance of the fibre sensor, and a power density of Additive White Gaussian Noise (AWGN) $\sigma_{AWGN} = 1.7\text{mV}_{RMS}$ at the receiver. The spatial resolution, corresponding here to the gauge length of the system (see definitions in subsection 1.1.1), is 4m.

Figure 3.4(b) displays the $\sigma_\varphi$ averaged over 50 independent fibre simulations for SISO, SIMO (MISO similar to SIMO, not displayed) and MIMO phase estimators, and for a theoretical case with no polarization effects along the fibre with a spatial step of 200m, along 50km SSMF. This theoretical case is derived by taking only coherent noise into account, i.e. $\mathbf{U}_i$ in Eq. (2.4) becomes the identity matrix for all fibre segments. Averaging of fibre simulations is performed in Figure 3.4(b) to evaluate the global impact of polarization effects on estimations, while avoiding the local false alarms induced by coherent fading. Figure 3.4 shows a clear hierarchy between no polarization diversity (Dual Polarization, DP) at all, DP at one side, and DP at both TX (transmitter) and RX (receiver) sides.

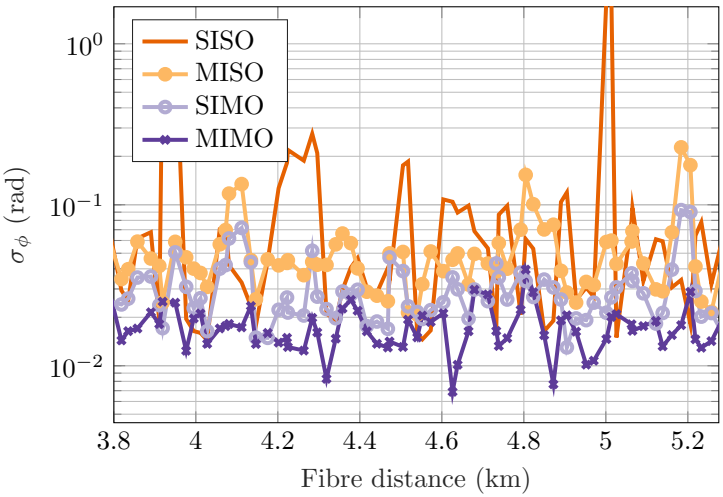


(a) Zoom on one simulated fibre section, log scale, 20m spatial sampling resolution

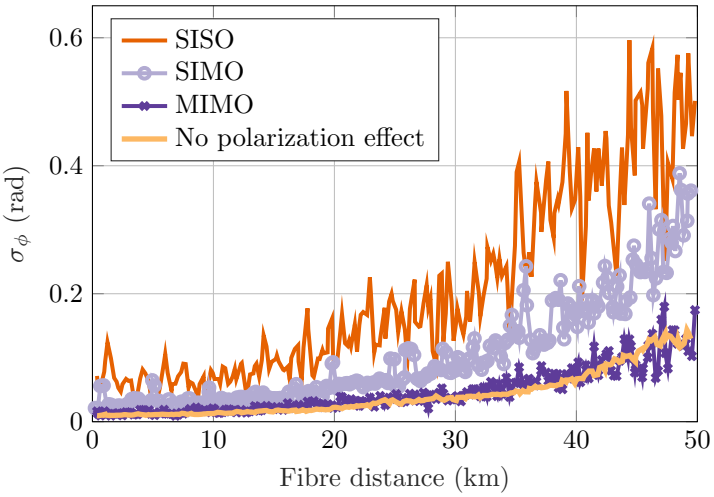


(b) Mean $\sigma_\varphi$ over 50 fibre simulations, 200m spatial sampling resolution, MISO case not displayed as it is comparable to SIMO

Figure 3.4: Phase $\sigma_\varphi$ along distance, laser linewidth $\Delta\nu = 75$Hz, 50km fibre simulations. Zoom on the beginning of one fibre with 20m resolution and averaged simulations along 50km with coarser resolution.

As depicted in Figure 3.4(b), the general trend of the $\sigma_\varphi$ over long distance is to grow exponentially with distance, with a slope depending on the laser linewidth $\Delta\nu$ [75, 99]. The value $\Delta\nu = 75$Hz is used in the simulations since it corresponds to the laser used in the experiments. What differentiates the phase $\sigma_\varphi$ traces of the different phase estimators is the amount and dynamic of $\sigma_\varphi$ peaks, or false alarms, as shown in the single fibre simulation from Figure 3.4(a) (e.g. SISO $\sigma_\varphi$ peaks are almost two orders of magnitude higher than MIMO $\sigma_\varphi$ peaks). Deriving the mean value over several simulations as displayed in Figure 3.4(b) shows how variable the phase estimation tends to be according to the chosen estimator. We also demonstrate in Figure 3.4(b) that considering no polarization effects or using MIMO probing will lead to the same phase $\sigma_\varphi$ values. On average, MIMO is matching the theoretical fading-free phase $\sigma_\varphi$ profile: it is polarization-independent.

**Relative performance of the estimators** What comes out is that MIMO estimated phases are the most stable, with no $\sigma_\varphi$ value above $5.10^{-2}$rad over the first 5km. It

corresponds to a strain distinction threshold of 1.31n$\varepsilon$ in a 190Hz bandwidth, over the given 200m gauge length, which is lower than 100p$\varepsilon/\sqrt{\text{Hz}}$. Meanwhile SISO can vary a lot locally and quite often over fibre distance with 6 peaks above $10^{-1}$rad (above 190p$\varepsilon/\sqrt{\text{Hz}}$) within one km in Figure 3.4(a) for example. SIMO and MISO show an intermediate behaviour with randomly distributed $\sigma_\varphi$ peaks, here 1 to 3 $\sigma_\varphi$ peaks above $10^{-1}$rad within 1km. Figure 3.4(b) shows that after 50km of fibre sensor, the $\sigma_\varphi$ decreases by a factor of 5 and 2 when going from SISO to MIMO and SIMO to MIMO respectively. Therefore, for sake of clarity, the rest of the study concentrates on the comparison between SIMO and MIMO cases only.

**Polarization-dependent false alarms** Regardless of the phase estimation method, the evolution of the state of polarization in the fibre is described mainly by $\Theta$, $\beta$, $\gamma$ and $\theta$ defined in chapter 2 provided that the Rayleigh scattering is an ideal reflector (no polarization transfer $\eta$ at reflection stage). In Figure 3.5(a), a 3-D view involving the evolution of angles $\Theta$ and $\theta$ for fixed randomly drawn values of $\gamma$ and $\beta$ together at a single segment location with a fixed reflected intensity is used to track the $\sigma_\varphi$ behaviour. It shows that the occurrence of sudden phase variations (errors on the phase estimation, or "false alarms") in SIMO is not random, but rather concentrated at some specific polarization parameters.

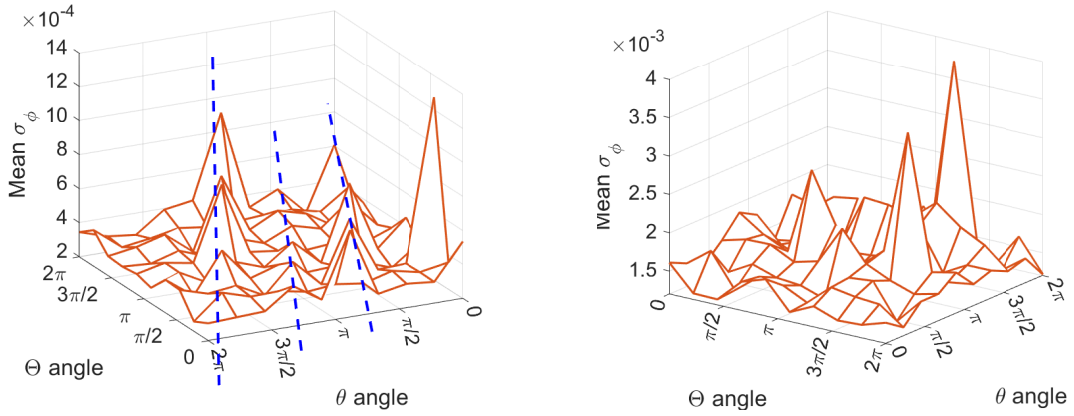


(a) SIMO, $\eta = 0$, dashed lines to show alignment of false alarms

(b) SIMO, $\eta = 5\%$

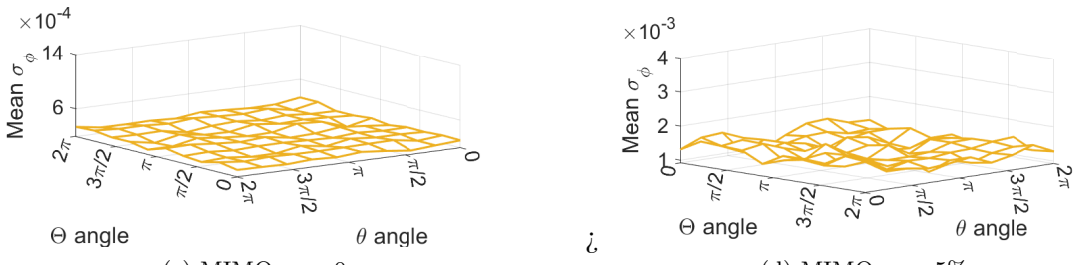


(c) MIMO, $\eta = 0$

¿

(d) MIMO, $\eta = 5\%$

Figure 3.5: Phase standard deviation in one fibre segment as a function of rotations in the fibre, $\Delta\nu = 75$Hz with and without $\eta$.

Specific $(\Theta, \theta)$ pairs at fixed random $\gamma$ and $\beta$ trigger $\sigma_\varphi$ peaks in SIMO, which is quite clear in Figure 3.5(a) and (b) (with dashed lines that show alignment of the false alarms in (a)). On the same fibre simulations, the corresponding MIMO estimation is

performed in Figure 3.5(c): the estimated phase is stable for all possible $(\Theta, \theta)$ pairs. If $\eta \neq 0$ where $\eta$ is the polarization transfer coefficient defined in section 2.1 (i.e. $\mathbf{M}$ is not an ideal reflector and introduces some crosstalk), then the locations of $\sigma_\varphi$ peaks change as shown in Figure 3.5(b): the false alarms peaks occur for different $(\Theta, \theta)$ locations, and the level of $\sigma_\varphi$ increases of $10^{-3}$ to $3.10^{-3}$ rad. The noise floor also slightly rises in MIMO in Figure 3.5(d) compared to $\eta = 0$. The laser phase noise $\Delta\nu$ impacts the height of the $\sigma_\varphi$ peaks and $\sigma_\varphi$ values and not the general shape (position of the $\sigma_\varphi$ peaks in the $(\Theta, \theta)$ plane), so the case $\Delta\nu = 0$Hz is not displayed. From Figure 3.5, we may suspect the phase estimation to be modulated by some $(\Theta, \theta)$ "pathological" pairs which degrade the backscattered information. This assumption is further investigated below.

**SIMO phase-fading coefficient** Back to subsection 3.1.1, the SIMO phase estimator for segment index $m$ was defined as:

$$\begin{aligned}\phi_{SIMO} &= \angle\Big(p_m \times \Big(e^{j2\gamma_m}\cos 2\beta_m - j\sin 2\beta_m(e^{j2\gamma_m}\cos 2\Theta_i + \sin 2\Theta_i)\Big)\Big) \\ &= \angle\big(\, p_m \times c_{mult,\mathrm{SIMO}} \,\big)\end{aligned}$$

if $\eta$ and $\theta$ are dismissed. It is recalled that $\Theta$ stands for the random polarization rotation in the fibre segment, and $\beta, \gamma$ are phase retarder coefficients, defined in section 2.1. This estimator is declared immune to intensity fading issues as it allows to get a phase estimation at all locations in the fibre, regardless of the state of polarization.

However, the phase $\angle(p_i)$ is modulated by the coefficient $c_{mult,\mathrm{SIMO}}$. This coefficient is plotted in Figure 3.6(a) (for a given input angle $\theta$ and a randomly chosen $\gamma$). Some $(\Theta, \beta)$ pairs lead to extremely low values for that coefficient, which highly attenuate or "fade" the received phase value. For $\eta \neq 0$, this phase-fading coefficient $c_{mult,\mathrm{SIMO}}$ becomes a function of $\gamma, \beta, \Theta, \eta$ and produces a similar, still less regular pattern than in Figure 3.6(a). This is illustrated in Figure 3.6(b), where a constant $\gamma$ is chosen in $[-\pi, \pi]$, and $\eta$ is set to 0.15. This configuration also has fading combinations of $\gamma, \beta, \Theta$, shown here for $\Theta, \beta$ varying in $[-\pi, \pi]$. It is possible to predict the values of the polarization parameters for which they cause such phase-fading.
Note that there is no phase fading with MIMO phase estimation since the equivalent coefficient for MIMO is $c_{mult,\mathrm{MIMO}} = \mathrm{abs}(\det \mathbf{H}) = 1$ since $\mathbf{H}$ is a unitary $2 \times 2$ matrix.

| |
|---|
| Overall, we were able to confirm the existence of input polarization induced phase noise in $\Delta\phi$-OTDR as we demonstrated how the phase coefficient can be modulated by $c_{mult,\mathrm{SIMO}}$, a "phase-fading" coefficient. $c_{mult,\mathrm{SIMO}}$ depends on polarization parameters and can get close to a null value even using a polarization-diversity detector. |

### 3.2.2 Sensitivity expectations

The $\sigma_\varphi$ was previously introduced as a distinction threshold metric in the absence of a perturbation ("static" configuration). Indeed, the variations of the differential phase captured from the sensor in static configuration are due to detector Additive White Gaussian Noise (AWGN) including thermal noises, laser source phase noise, attenuation and fading.

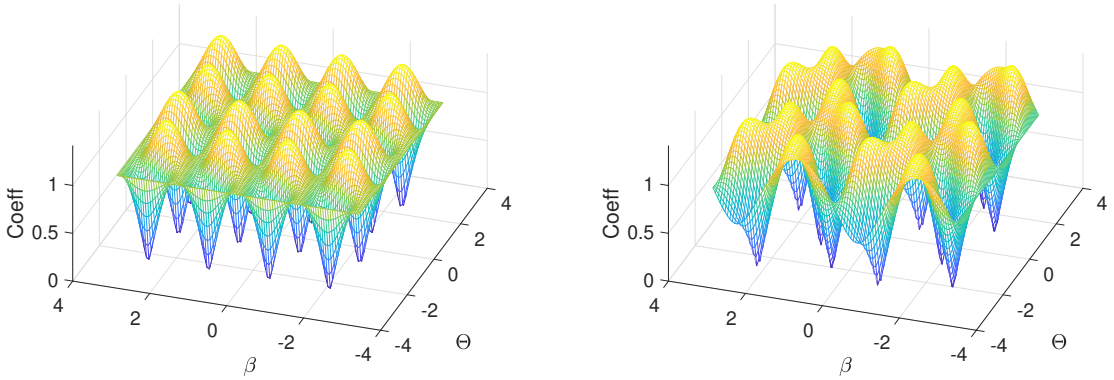


(a) Function of $\Theta$ and $\beta$, random constant $\gamma$ between $-\pi$ and $\pi$, $\eta = 0$

(b) Function of $\Theta$ and $\beta$, random constant $\gamma$ between $-\pi$ and $\pi$, $\eta = 0.15$

Figure 3.6: Phase-fading coefficient $c_{mult,\text{SIMO}}$ as function of polarization rotation parameters : SIMO phase modulation for a single fibre segment

This static level of $\sigma_\varphi$ defines the level below which perturbations are not going to be detected, namely the distinction threshold. $\sigma_\varphi$ is also used as a metric for the detection of events in dynamic configuration, which will be addressed in the next chapters.

We have seen in subsection 3.2.1 how SIMO and MIMO detection thresholds differ, especially on long distance. To further quantify the performance increase brought by MIMO probing and its associated phase estimation compared to SIMO, a study is conducted by means of simulations. Here again, the fibres are probed using complementary codes described in subsubsection 1.2.4.2 on either one or two polarizations.

**SNR definitions for phase and strain** We introduce two metrics to help fairly compare the sensing performance as a function of the interrogation method. The intensity metric $\text{Intensity}_{dB}$ and the distinction threshold metrics $\text{SNR}_{\varphi,dB}$ and $\text{SNR}_{\varepsilon,dB}$ are derived as follows:

$$\text{Intensity}_{dB} = 10\log_{10}(|\det(\mathbf{H})|) \tag{3.6}$$

$$\begin{aligned} \text{SNR}_{\varphi,\text{dB}} &= 10\log_{10}\left(1/\sigma_\varphi^2\right) \\ \text{SNR}_{\varepsilon,\text{dB}} = 10\log_{10}\left(1/\sigma_\varepsilon^2\right) &= 20\log_{10}\left(\frac{4\pi n\xi G}{\lambda\sigma_\varphi}\right) \end{aligned} \tag{3.7}$$

with $n$ the refractive index of the fibre, $\xi$ the photo-elastic scaling factor in isotropic material, $\lambda$ the laser wavelength of the interrogator expressed in nm, $G$ the gauge length is the system, in m. The gauge length $G$ definition is based on the receiver characteristics which define the performance of the interrogation system, see subsection 1.1.1, therefore $G = cT_S/2n$ with $1/T_S$ the symbol rate of the system, here $T_S = 20$ns therefore $G = 2.05$m. We remind that these parameters were already defined for the expression of equation (1.2) which gave an expression of the measured differential phase in $\Delta\phi$-OTDR.

The $\text{Intensity}_{dB}$ in (3.6) is the intensity estimated from $|\det(\mathbf{H})|$ which, as emphasized in the following (see section 3.3), informs about the ability to reliably derive a phase estimate from $\mathbf{H}$.

The $\text{SNR}_{\varepsilon,dB}$ in (3.7) expresses the strain sensitivity following the relation $\sigma_\varepsilon = \dfrac{\lambda\sigma_\varphi}{4\pi n\xi G}$

(see [16] and (1.2)) in n$\varepsilon$, where the standard deviation of phase in time $\sigma_\varphi$ expresses the noise floor of the system (in radians). Therefore $N_\varepsilon = \frac{\sigma_\varepsilon^2}{B_{meca}}$ is the strain noise power density as the phase estimation at each segment is refreshed each $T_{code} = (2B_{meca})^{-1}$. We define $\text{SNR}_{\varepsilon,dB} = 10\log_{10}(1/\sigma_\varepsilon^2)$ to express the strain noise in the absence of signal (assuming a reference strain signal of power $1n\varepsilon^2$). The maximum value of $\sigma_\varepsilon$ (or equivalently minimum value of $\text{SNR}_\varepsilon$) in a static measurement will be considered to be the strain distinction threshold of the interrogator. $\text{SNR}_\varepsilon = 0$dB corresponds to a 1n$\epsilon$ strain sensitivity in a given mechanical bandwidth $B_{meca}$.

**Statistical comparison of SIMO and MIMO estimators** The statistical study is conducted on a high number of simulations ($\text{N} = 10^6$ simulated points, corresponding to 2000 fibre generations for 340m length, 40 fibres for 25km and 20 for 50km), with $f_{symb} =$ 50Mbaud, corresponding to a gauge length $G = 2$m. MIMO and SIMO probing simulations are run on randomly generated fibres, and the $\sigma_\varphi$ is derived for every fibre segment. The polarization beat length $L_{pb}$ is selected such that $L_{pb} \leq L_s$, assuming independent polarization state between consecutive segments (see section 2.1). $L_s$ is defined as $L_s = \frac{c_{fibre}}{2f_{symb}}$, here $G = L_s$.

Three different fibre lengths are simulated to investigate the influence of distance on the $\sigma_\varphi$ distribution, and therefore on the $\text{SNR}_\varepsilon$ according to the phase estimation method, so to compare the relative robustness of the SIMO and MIMO estimators over distance. The MIMO values in $\sigma_\varphi$ are highly concentrated around low values (yielding high $\text{SNR}_{\varepsilon,dB}$) and spread with an exponential decrease, whereas SIMO values are less concentrated and spread further. This is translated into values of $\text{SNR}_{\varepsilon,dB}$ in Figure 3.7, where the probability density function of $\text{SNR}_{\varepsilon,dB}$ is displayed for 340m fibre, 25km and 50km respectively.

The distributions shapes change with distance, however the same differences are observed between SIMO and MIMO cases: MIMO allows to get a lower $\sigma_\varepsilon$ noise floor than SIMO, consequently a higher $\text{SNR}_{\varepsilon,dB}$: Figure 3.7(a) displays a 10dB difference in the lower $\text{SNR}_{\varepsilon,dB}$ values for MIMO and SIMO after a short fibre distance, and so does Figure 3.7(b) for lower SNR values with probability density below $5.10^{-3}$. SIMO distributions have a lower $\text{SNR}_{\varepsilon,dB}$ mean value than MIMO.

From 25km and beyond, a concentration of low SNR values appear at the left tail of the distribution which is due to the attenuation in distance: coherent fading and attenuation are an other source for false alarms. In other words, the left peak is mainly constituted of accumulated loss whereas the overall distribution is constituted of points which are subject to coherent fading. It is particularly visible in Figure 3.7(c), for 50km fibre. However, MIMO estimator allows to decrease the attenuation-related-false alarms peak.

We show in Figure 3.8 that up to 50% of estimated segments for SIMO case yield higher false alarms (lower $\text{SNR}_\varepsilon$) than 75% of MIMO estimated segments over 340m. This comes to 35% for 50km fibre distance (25km being an intermediate case). Also, 15% of the SIMO estimated segments yield higher false alarms than 95% of MIMO estimated segments over 340m as displayed in Figure 3.8, and which comes down to 9% for 50km

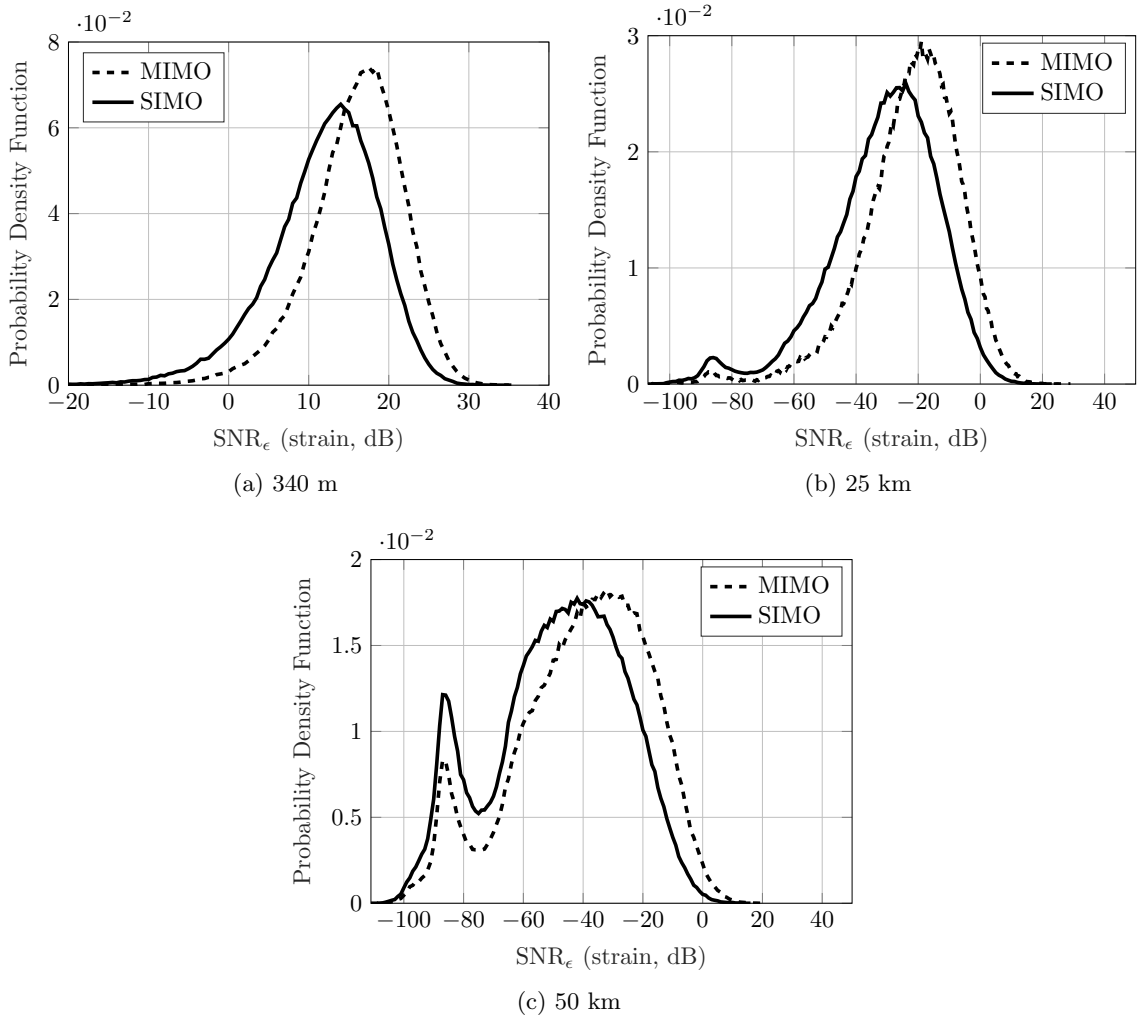


Figure 3.7: Probability density function distribution of $\mathrm{SNR}_\varepsilon$ values, SIMO and MIMO phase estimation methods, fibre simulation with $L_s = 2$m gauge length, $\Delta\nu = 75$Hz, $\mathrm{N} = 10^6$ simulated points

fibre distance.

Moreover, Figure 3.8 displays the difference between the mean values of MIMO and SIMO distributions "$\mu$(MIMO)-$\mu$(SIMO)", which can be seen as the mean strain distinction threshold of $\mathrm{SNR}_\varphi$ in SIMO compared to MIMO method: it is of 3dB at 340m, and grows to 11dB at 25km and 7dB at 50km. We conclude that MIMO enhances the mean achieved SNR and also reduces its fluctuations with respect to SIMO.

From a high number of random simulations, it appears that SIMO phase estimations bring in more variations than MIMO, therefore bringing higher false alarm levels, for the same simulated fibre with same scatterers distribution and birefringence, and for all distance ranges.

| |
|---|
| The performance gap between SIMO and MIMO methods is striking for short distances (below 1km), and remains significant at very long distances (up to 50km here) when coherent fading and attenuation also affect the measurement. Coherent-MIMO sensing appears as a strong, stable phase estimator on short fibre lengths as well as on longer distances. |

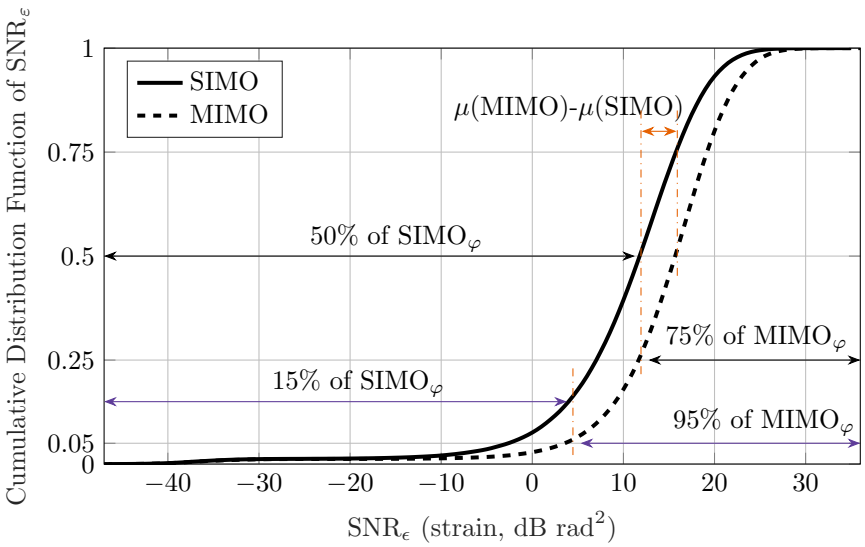


Figure 3.8: Cumulated probability density function distribution of $\text{SNR}_{\varepsilon,\text{dB}}$ values, SIMO and MIMO phase estimation methods, 340m fibre simulation with $L_s = 2$m gauge length, $\Delta\nu = 75$Hz, N = $10^6$ simulated points

### 3.2.3 Discussion on polarization beat length

Regarding undesirable polarization effects, the polarization beat length was also mentioned, as it could play a role in the quality of the received signal when confronted to polarization fading [91].

Polarization beat length, denoted $L_{pb}$, is a fibre-dependent parameter. We remind that for single mode fibres, $L_{pb}$ is of the order of magnitude of 10m [97], and by definition if $L_s \geq L_{pb}$, then the SOP in two successive segments is uncorrelated. In this subsection, we aim at comparing the amplitude and frequency of $\sigma_\varphi$ false alarm peaks as a function of $L_{pb}$, with fixed $L_s$. This should allow to determine if and why there would be a specific $L_{pb}$ range for which the system would encounter more false alarms than usual, in SIMO interrogation (which are the most common systems in the recent research).

Using our simulation tool and SIMO interrogation, $L_{pb}$ varies between the gauge length value $G$, here $G = L_s$ and the fibre length $L_f$, since variations below the gauge length will not impact the algorithm described in chapter 2, and so will the variations of polarization beat length variations beyond the fibre length. Simulations are run for a fibre length $L_f = 10$km and a symbol rate $f_{symb} = 50$MBaud yielding a gauge length (which we define here as the spatial sampling resolution $L_s$) of $L_s = 2$m and $L_{pb}$ is varied between 1m and 10km. The results are displayed in Figure 3.9, with zooms on two locations of the simulated fibre.
Though $\sigma_\varphi$ false alarm peaks are noticed whatever the polarization beat length, on smaller peaks (see between 2.95 and 3.1 km in Figure 3.9(a)) the higher $L_{pb}$ is, the lower $\sigma_\varphi$ is. Indeed in Figure 3.9(a), $L_{pb} = 1$m yields a high number of medium $\sigma_\varphi$ false alarm peaks ($< 10^{-4}$rad), $L_{pb} = 10$m yields less peaks but with higher values, whereas $L_{pb} \geq 100$m display a lot less false alarm peaks as only a few peaks remain at particular fibre distances, yielding several kilometres of fibre free from false alarms, see from 2.95km to 3.25 km in

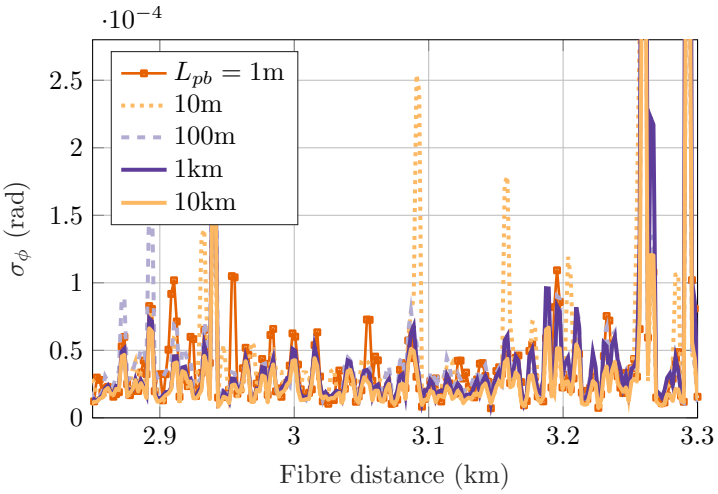


(a) Zoom of a 500m portion around 3km

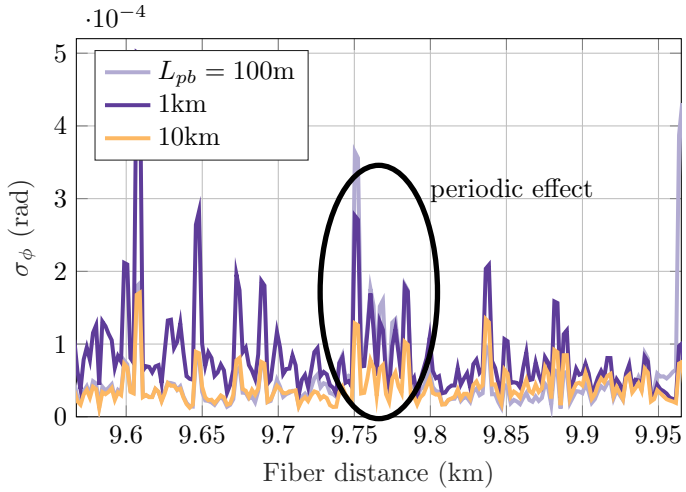


(b) Zoom on common periodic effect for higher $L_{pb}$

Figure 3.9: SIMO simulation for different polarization beat lengths, $\Delta\nu = 0Hz$

Figure 3.9(a). Also, when monitoring $\sigma_\varphi$ over the full fibre length, a periodicity of false alarms is noticed (with a period of about 2m) for $L_{pb} \geq 100$m: it is visible around 3.2km in Figure 3.9(a) and 9.77km in Figure 3.9(b).

Overall, the SOP can take specific values which will degrade the SIMO fading coefficient $c_{mult,\text{SIMO}}$ locally. The intuition here is that if $L_{pb}$ is long enough, such specific values could span several segments and trigger fading zones over several consecutive segments. With a lower sampling resolution[4], the periodic pattern is very well identified in Figure 3.10 for $L_{pb} = 1$km (black thick line): peaks are identified every two kilometres, spreading over almost 1km, with $\sigma_\varphi$ peak values around 0.4rad. No periodic effect is noticed for smaller $L_{pb}$ values though random peaks are present, while for $L_{pb} = 10$km, which is equal to the full fibre length, there are no more $\sigma_\varphi$ peaks.
For a large enough $L_{pb}$, there will be less false alarm peaks, which is in line with [91]. This could also trigger false alarms before $L_{pb}$ becomes longer than the fibre length, on consecutive segments, which is in line with the intuition exposed earlier.

[4]See subsection 3.3.4: "A note on low sampling resolution in the presence of potential artefacts" below. 10-fold lower sampling resolution does not modify the polarization changes for $L_{pb} > 10L_s$.

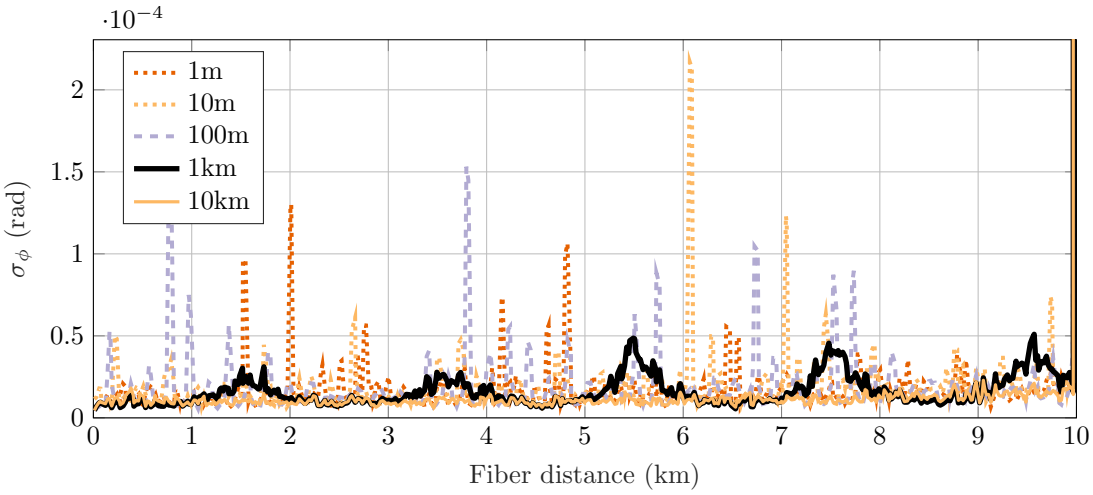


Figure 3.10: SIMO simulation, no laser noise, lowresolution=10

Overall, "large enough $L_{pb}$" in this experiment corresponds to a quasi constant SOP along the full fibre segment. $L_{pb} = L_f$ would mean the fibre ($L_f$ is the fibre length) is a fibre with (very) low birefringence. In such a case, the constant SOP is either a "good" SOP which does not yield polarization induced phase noise (e.g. in Figure 3.10), or a "bad" SOP yielding polarization phase noise. Therefore, $L_{pb}$ does play a role in the quality of the backscattered signal, yet increasing or decreasing $L_{pb}$ will not change the number of degraded segment responses but rather change the spatial distribution of degraded segment responses (the larger $L_{pb}$ is, the more gathered the unstable phase estimations due to polarization induced phase noise).

Finally, in case of usual telecommunication fibre distances (several kilometres at least), it is not realistic to consider $L_{pb}$ close to the full fibre length (we recall $L_{pb} \simeq 20$m in single mode fibres [97]).

In practical cases, we assume $L_s \geq L_{pb}$ by one order of magnitude, which was presented as close enough to yield uncorrelated SOPs from one fibre segment to the next in chapter 2. This also explains why periodic patterns such as in Figure 3.10 are not measured while sensing over single mode fibre: given $L_{pb} > L_f$ in such a case, local occurrences of $c_{mult,\text{SIMO}}$ fading should not exceed one fibre segment.

## 3.3 Optimisation of reliability: defining an intensity estimator

We have seen how polarization fading could be partially avoided [38, 53, 107] or completely mitigated using Coherent-MIMO interrogation. However, several forms of fading still stand in the way towards optimum sensing performance as coherent fading (also known as speckle noise or Rayleigh fading) remains. Indeed, coherent $\Delta\phi$-OTDR relies on the random constructive and destructive intra-impulsion interferences of coherent light inside the fibre sensor [115] such that the sensitivity randomly fluctuates along the fibre sensor and in time.

In order to mitigate Rayleigh fading noise without increasing measurements or processing time, several groups proposed low-cost approaches to either discriminate or remove the false alarm peaks induced by fading effect: in $\Delta\phi$-OTDR, it is possible to identify whether a phase term is an artifact by comparison of successive phase measurements [116] ; one can also select a lower sampling resolution set of backscattered points, chosen on a signal-to-noise ratio basis [99] as addressed further. In these cases, the criterion to decide on the quality of a measurement is based either on the phase alone or on the sole backscattered intensity. Here instead, we aim at introducing a criterion based on the Jones matrices estimates of the fibre sensor (prior to any phase extraction) for early identification of the Rayleigh backscatter fading points from the $\Delta\phi$-OTDR trace.

To do so, we rest on the knowledge brought by MIMO interrogation investigated here above: the retrieval of the full Jones matrices of the fibre segments along the fibre proved itself to give reliable measurements of the phase. Therefore, we wish to push further and come out with reliable measurements of the backscattered intensity.

### 3.3.1 Analytic development of estimators error

Provided that dispersion is negligible, the optical field $\mathbf{E_{out}}$ backscattered in a SSMF can be expressed as the product of transmitted optical sequences $\mathbf{E_{in}}$ with $2 \times 2$ Jones matrix $\mathbf{H}_{d,t}$, which stands for the dual-pass impulse response from the start of the fibre to the $i$th fibre segment at time index $j$ and the injected optical field, as follows:

$$\mathbf{E_{out}} = \mathbf{H_{i,j}}\mathbf{E_{in}} \tag{3.8}$$

The channel response is thus fully characterized in terms of intensity, phase and polarization. One sensing method providing estimations of $\mathbf{H}$ is Coherent MIMO, described in subsubsection 1.2.4.2. It was shown in the above sections that this probing technique fully removes both polarization intensity fading and polarization-induced phase noise effects. We remind that the symbol rate $f_{symb}$ used to inject the probing code of duration $T_{code} = N_{code} \times f_{symb}$ determines the gauge length, or fibre segment length, $L_s = c_{fibre}/(2f_{symb})$. $N_{code}$ is the number of symbols that compose the code. The cumulated phase for segment index $i$ is derived from $\mathbf{H}_i$ as $\frac{1}{2} \times \angle\det(\mathbf{H}_i)$. The local phase per segment is then obtained by spatial differentiation of the cumulated phase. By continuously injecting the probing codes, the system provides periodic estimations $\mathbf{H}_{i,j}$ with a period $T_{code}$ equal to that of the code. Following Nyquist theorem, the achieved mechanical bandwidth is $B_{meca} = 1/(2T_{code})$. In summary, vibrations with a spectral signature below $B_{meca}$ occurring along the fibre can be captured and localized with a spatial accuracy $L_s$.

Now focusing on the Rayleigh fading effect, let us remind the expression of a back-propagated Jones matrix response at segment index $i$:

$$\mathbf{H}_i = A_i p_i \mathbf{U}_i^T \mathbf{M} \mathbf{U}_i \tag{3.9}$$

where $\mathbf{U}_i$ is a unitary Jones matrix describing the state of polarization (SOP) within segment $i$, $T$ is the transpose operator, $\mathbf{M}$ is a reflection matrix, assumed for sake of

simplicity as equal to identity matrix to emulate perfect reflection per polarization axis. $A_i$ and $p_i$ are the attenuation and phase of the Rayleigh-distributed backscattered field at segment index $i$. Consequently, the response comes down to $\mathbf{H}_i = A_i p_i \mathbf{V}_i$ with $\mathbf{V}_i = \mathbf{U}_i^T \mathbf{M} \mathbf{U}_i$ unitary as well. The product $A_i p_i$ results from the sum of all randomly spread elementary scatterers and the fibre segment is subject to Rayleigh fading when its intensity, defined as $|A_i.p_i|^2$, vanishes.

**Intensity expressions in noiseless conditions** The backscattered intensity is derived from the Frobenius norm of $\mathbf{H}_i = \left[\begin{smallmatrix} h_{xx} & h_{xy} \\ h_{yx} & h_{yy} \end{smallmatrix}\right]$ as $|\mathbf{H}_i|^2_{frob} = |h_{xx}|^2 + |h_{xy}|^2 + |h_{yx}|^2 + |h_{yy}|^2$ [99]. Since V is unitary, it is of the form $\left[\begin{smallmatrix} a & b \\ -b^* & a^* \end{smallmatrix}\right]$ where $a$ and $b$ are complex values such that $|a|^2 + |b|^2 = 1$, therefore $|\det(\mathbf{V}_i)| = 1$.

Then $|\mathbf{H}_i|^2_{frob} = |A_i p_i|^2.(|a|^2 + |b|^2 + |-b^*|^2 + |a^*|^2) = 2.|A_i.p_i|^2$. The intensity can alternatively be derived from the determinant of $\mathbf{H}$ by calculating $|\det(\mathbf{H}_i)| = |A_i p_i|^2.(aa^* + bb^*) = |A_i p_i|^2$. Therefore, the two estimators are equivalent and perfectly estimate the intensity of the backscattered optical field in MIMO sensing:

$$\frac{1}{2}.|\mathbf{H}_i|^2_{frob} = |\det(\mathbf{H}_i)| = |A_i p_i|^2 \tag{3.10}$$

Note that in SIMO configuration, the estimated channel comes down to $\hat{\mathbf{H}}_i = \left[\begin{smallmatrix} h_{xx} \\ h_{yx} \end{smallmatrix}\right] = A_i p_i \left[\begin{smallmatrix} V_x \\ V_y \end{smallmatrix}\right]$, where the terms $V_x$ and $V_y$ depict the energy received on the $x$ and $y$ polarization axes of the receiver, respectively. In that case, no determinant can be computed and $|\hat{\mathbf{H}}_i|^2_{frob} = |A_i p_i|^2.(|V_x|^2 + |V_y|^2)$. $|\hat{\mathbf{H}}_i|^2_{frob} = |A_i p_i|^2$ as well as for (3.10) in the absence of noise.

**Intensity expressions in noisy conditions** Given the imperfections of the optical and electronic elements present in a sensing system setup, the estimated matrix $\tilde{\mathbf{H}}$ at the receiver side can be modelled as the $\tilde{\mathbf{H}} = \mathbf{H} + \epsilon$ with $\epsilon = \left[\begin{smallmatrix} \varepsilon_{xx} & \varepsilon_{xy} \\ \varepsilon_{yx} & \varepsilon_{yy} \end{smallmatrix}\right]$ an Additive White Gaussian Noise (AWGN). Under this assumption, the two intensity estimators may diverge. After analytical development, we get the two following expressions for the Frobenius and determinant estimators respectively:

$$\begin{aligned} \frac{1}{2}.|\tilde{\mathbf{H}}_i|^2_{frob} = \frac{1}{2}.|\mathbf{H}_i|^2_{frob} + \frac{1}{2}(|\varepsilon_{xx}|^2 + |\varepsilon_{xy}|^2 + |\varepsilon_{yx}|^2 + |\varepsilon_{yy}|^2) \\ + \Re(a^*.\varepsilon_{xx} + b^*.\varepsilon_{xy} - b.\varepsilon_{yx} + a.\varepsilon_{yy}) \end{aligned} \tag{3.11}$$

$$\begin{aligned} |\det(\tilde{\mathbf{H}}_i)| = ||det(\mathbf{H}_i)| + (\varepsilon_{xx}\varepsilon_{yy} - \varepsilon_{xy}\varepsilon_{yx}) + \\ (a^*.\varepsilon_{xx} + b^*.\varepsilon_{xy} - b.\varepsilon_{yx} + a.\varepsilon_{yy})| \end{aligned} \tag{3.12}$$

where $\Re(X)$ stands for the real part of complex scalar X. Figure 3.11(a) shows, derived from the above model, the module of the error as a function of the signal to noise ratio achieved by simulating AWGN error matrices of various levels whereas the backscattered intensity term $|A_i p_i|^2$ is fixed to unit norm. Though both estimators are equivalent at high SNR values, the $|\det|$ estimator outperforms the Frobenius one below a 10dB SNR with an estimation error module reduction by 2 to 3dB for negative SNR values. This

negative SNR case reflects the situation of low backscatter intensity segments, which may exhibit SNR values far below 0dB with experimental sensing systems. This statement derived from our analytical error model is confirmed by simulations in Figure 3.12 when simulating the interrogation of a 50km fibre and then comparing the Probability Density Function (PDF) of the backscattered intensity estimated with both estimators.

### 3.3.2 Unreliable points on simulated interrogations

The fibre is simulated by means of the static model developed in chapter 2, and probed using Coherent-MIMO interrogation which was described in subsection 1.2.4. We use a symbol rate $f_{symb} = 50$MBaud, binary codes made of $N_{code} = 2^{17}$ symbols, which yields a gauge length $L_s = 2$m, a code length $T_{code} = 2.6$ms and so an analysis bandwidth $B_{meca} = 190$Hz. 500 successive codes of duration $T_{code}$ are injected, that gives a 1.3s overall analysis period of the backscattered channel. The dominant simulated noise is the laser phase noise, set to a linewidth of $\Delta\nu = 75$Hz through a Lorentzian model to emulate the laser source used later in our experimental self-homodyne setup.

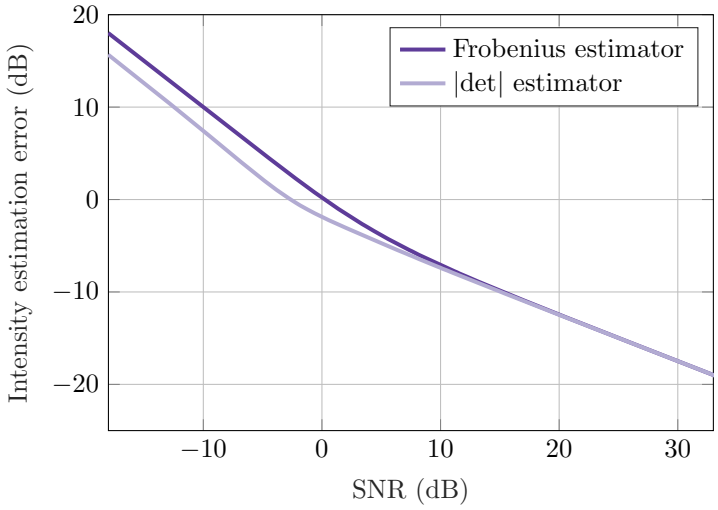


(a) Analytical study

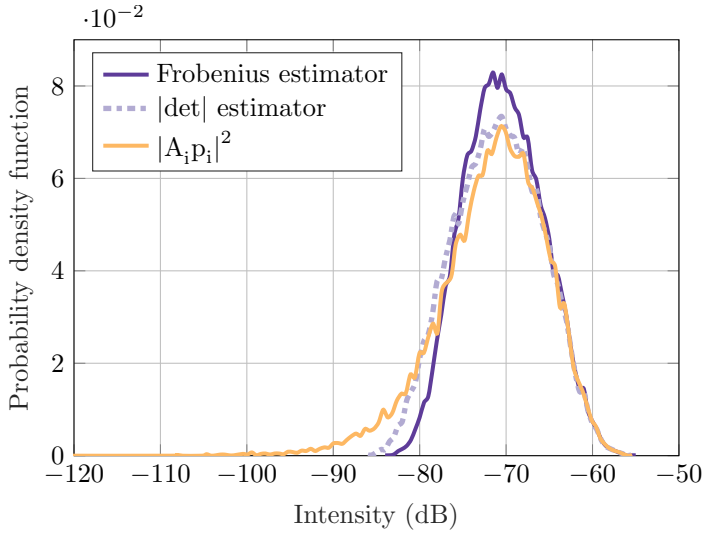


(b) Simulation

Figure 3.11: Comparison of $|\mathbf{H}|^2_{frob}$and $|\det(\mathbf{H})|$ backscattered intensity estimators

The static model used for simulating the fibre generates the set of Jones matrices $\mathbf{H}_i$, one per 2m length fibre segment. So, the estimated intensity, averaged over the 1.3s period by each of the two methods can be compared to the true generated intensity $|A_i p_i|^2$, as displayed in Figure 3.11(b). The PDF of the $|A_i p_i|^2$ reference backscattered intensity follows the expected Rayleigh distribution. Both estimators match the reference intensity distribution for high reflective segments (high SNR), but the estimation is significantly compressed at low reflective ones, with a PDF tending towards a Gaussian shape. This is particularly emphasized with the Frobenius estimator, which hardly allows to discriminate between segments of low ($\text{Intensity}_{dB} = -90$ to $-100$) and even intermediate intensity ($\text{Intensity}_{dB} = -80$) relatively to the intensity distribution. The $|\det|$ estimator PDF much better fits to the reference intensity distribution with low-reflective segments. In other words, it provides a much higher robustness to noise. Therefore, when willing to detect the segments subject to Rayleigh fading and to estimate their intensity, the $|\det|$ estimator is to be preferred in MIMO sensing.

Beyond intensity concerns, we remind that phase variations at segment index $i$ are estimated by periodically calculating $\phi_{MIMO} = 0.5.\angle\det(\mathbf{H}_i)$. Therefore, an estimation error on the matrix intensity also translates into a phase estimation one, giving rise to phase artefacts that degrade the phase sensitivity and which can be wrongly interpreted as mechanical disturbances (false alarms). We reuse the 50km simulated fibre along with the simulation parameters introduced above. The differential phase is calculated from a subset of fibre segments by selecting, according to both estimators, the highest intensity one among every 10 consecutive segments, leading to an average resolution of 20m. This technique brings a distinction threshold gain at the cost of spatial resolution loss [99], see later in subsection 3.3.4.

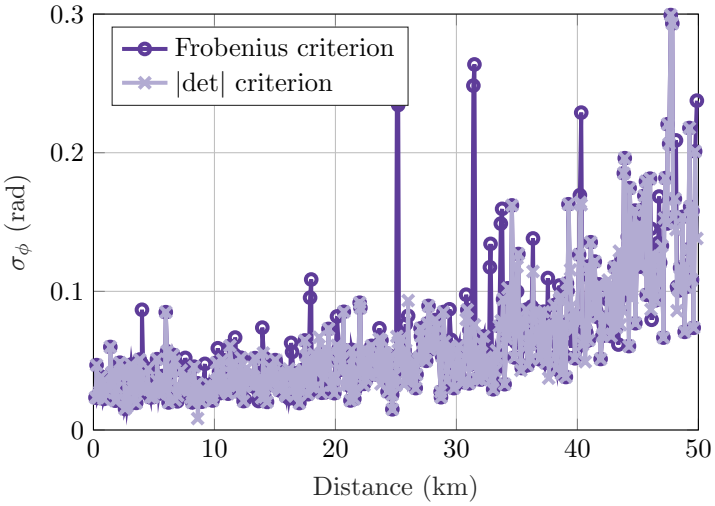


Figure 3.12: Impact on phase distinction threshold of intensity estimator when selecting a highly reflective segments subset (spatial sampling resolution 100m). 50km simulated fibre

Figure 3.12 shows the standard deviation of the phase ($\sigma_\varphi$) during the 130ms simulated period calculated by phase differentiation between the subset of higher intensity segments. In absence of any simulated perturbation, the phase variation is mainly induced by the

Rayleigh fading and by the laser coherence loss, this latter effect being responsible for the constant $\sigma_\varphi$ increase with distance whereas local variations are induced by randomly distributed Rayleigh fading. The higher intensity segment subset selected from the $|\det|$ criterion shows a much lower $\sigma_\varphi$ of their differential phase and so a better distinction threshold along the 50km simulated fibre; and this is a direct consequence of the lower error induced by $|\det|$ intensity estimator relatively to the Frobenius norm.

Therefore, with MIMO sensing that gives access to the Jones matrix estimation $\mathbf{H}_i$ of the backscattered optical field at any fibre segment, the determinant module of $\mathbf{H}$ is, beyond a fair intensity estimator, also a powerful indicator of the ability to numerically extract a reliable phase estimation.

For sensing methods with polarization diversity at the receiver side only (SIMO), we get $h_{xx} + h_{yx} = A_i p_i \times (V_x + V_y) \neq A_i p_i$. Therefore, the intensity estimation, defined as $\hat{\mathrm{I}}_{SIMO} = |h_{xx}|^2 + |h_{yx}|^2$, encloses the Rayleigh fading. Note that this is the only way here to estimate the backscattered intensity level. Nevertheless, $\hat{\mathrm{I}}_{SIMO}$ estimator can also be exploited as an indicator of the ability to extract a reliable phase estimate for SIMO implementations.

### 3.3.3 Observed artefacts mitigation by reliability monitoring

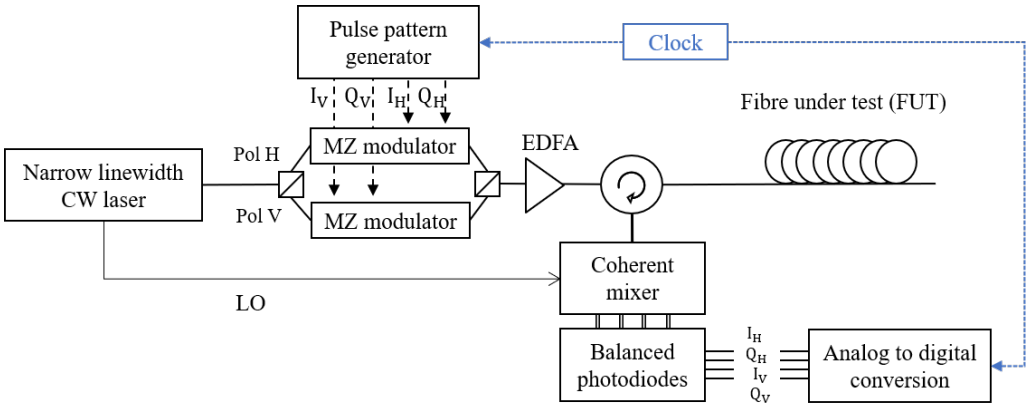


Figure 3.13: Experimental MIMO sensing setup. LO: Local Oscillator, MZ: Mach-Zehnder, CW: Continuous Wave, EDFA: Erbium Doped Fibre Amplifier

The previous section, based on analytical development and simulations, has shown the relevancy of $|\det(\mathbf{H})|$ metric in MIMO sensing to enhance the backscattered intensity estimation at low reflective fibre segments compared to the more usual Frobenius norm. The finer discrimination between low intensity segments was shown to select a more relevant segment subset, thus also improving the estimated phase along the tested fibre thanks to a lower distinction threshold. This section aims to experimentally confirm the benefit on the phase distinction threshold.

Figure 3.13 recalls the overall experimental setup. The Fibre Under Test (FUT) is probed over two orthogonal polarization axes thanks to a Mach Zehnder modulator which modulates a 1536.1nm ultra-narrow linewidth (75Hz for low frequency interrogation [99]) laser source with the same interrogation setup (codes and baud rate) as in the simulation part. In a first experimentation, we probe a 50km length standard telecom fibre

spool placed in a mechanically insulated box to make it less sensitive to environmental noise. The Rayleigh backscattered signal is captured by a coherent mixer, electrically converted and then digitized. After correlation process, a set of Jones matrices estimating the backscattered optical field in both time and distance dimensions is available. The differential phase is finally derived from a subset of highly reflective segments according to both Frobenius and $|\det|$ criteria in the same way and so to achieve the same spatial resolution as in the above simulated case.

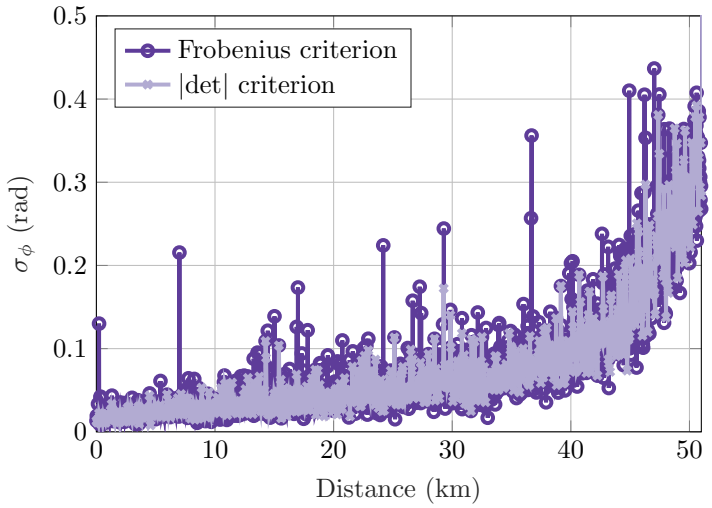


Figure 3.14: Impact on phase distinction threshold of intensity estimator when selecting a highly reflective segments subset (spatial sampling resolution 20m). 51km experimental measurement, no excitation

Figure 3.14 displays, as with Figure 3.12, the temporal $\sigma_\varphi$ of the phase along the 50km FUT. The phase $\sigma_\varphi$ is slightly higher than in the simulation case mainly due to a lack of soundproofing at low mechanical frequencies, the noise floor in the lab being of $60\text{dB}_{\text{SPL}-\text{C}}$ and $49\text{dB}_{\text{SPL}-\text{A}}$[5]. However, we observe the same trend here: the segment selection made with the $|\det|$ intensity criterion brings on a final basis a much lower rate of artefacts than with the Frobenius one (here, 3 false alarms peak $>$ 50mrad above the laser phase noise remain using $|\det|$, compared with 10 to 20 peaks with Frobenius), and so a lowered distinction threshold.

We have until now considered the $\sigma_\varphi$ of the phase per fibre segment in absence of external perturbation. This is based on the statement that, in such a static case, both intensity and phase remain quite stable at any segment during the observation time. Let us now focus on a dynamic case with the FUT mechanically excited at a segment location. A 1km SMF fibre is locally excited by a 15Hz acoustic sine wave at 640m from the fibre start. The sound pressure level reaching the fibre could not be accurately measured at such a low frequency. However, the captured phase variation was sufficiently low to assume that polarization parameters are left unchanged and so that it only affects the fibre length locally.
Figure 3.15 shows the variations in time of the differential phase measured at the excited

[5]Soundmeters are usually fitted with filters to adapt to the human sense of sound, depending on the frequency range. See Appendix A for details on the acoustic sound pressure level (SPL).

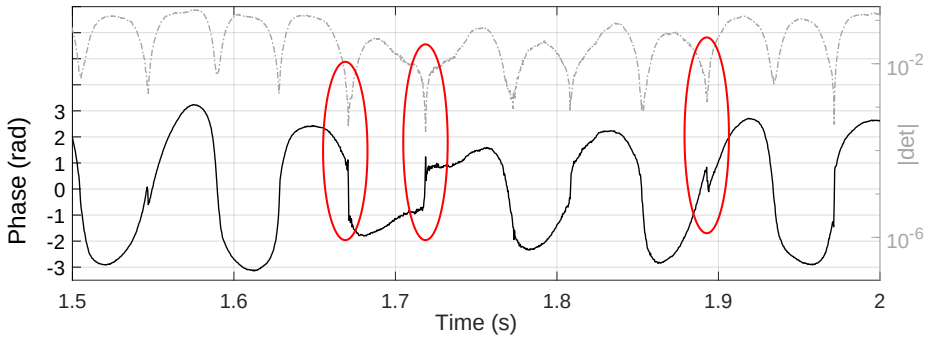


Figure 3.15: Phase variations with fading artefacts observed at a fibre segment perturbed by a 15Hz sine wave (black,bottom) and associated normalized $|\det|$ estimator (grey,top). Correspondence of low $|\det|$ values with distorted phase signal is established with red ellipses.

segment position. The sine wave excitation is quite well captured by the phase though some distortion can be observed, with local artefacts. Superimposed is $\overline{R}_{d,t}$ the intensity estimated by $|\det|$ metric, normalized over all the $\mathbf{H}_{d,t}$ of the measurement within a certain time window (where $d$ is the segment index and $t$ the time index), defined as follows:

$$\overline{R}_{d,t} = \frac{|\det(\mathbf{H}_{d,t})|}{\max\limits_{d,t} |\det(\mathbf{H}_{d,t})|} \tag{3.13}$$

Firstly, we observe that the $|\det|$ metric (namely $\overline{R}_{d,t}$) is modulated by the captured mechanical excitation. This was expected since the applied excitation, when expanding the length of the excited fibre segment, slightly modifies the initial position of the elementary scatterers and so modulates the intensity term $|A_i p_i|^2$. Secondly, there is a correlation between the position of the artefacts observed in the phase response and the local minima of the $|\det|$ metric. This correlation is not perfect since $|\det|$ intensity estimator is slightly biased at low intensity levels and so false positives or negatives cannot be excluded. Nevertheless, it highlights that such artefacts are erroneous phase estimates that occur when the Jones matrix intensity drops.

Therefore, the $|\det|$ metric can be exploited in MIMO sensing not only as a fair intensity estimator but also as a criterion that informs about the ability to extract from any Jones matrix $\mathbf{H}$ a reliable phase information.

The normalized intensity estimator within a certain time window $\overline{R}_{d,t}$ appears in Figure 3.16 superimposed to the phase plot under the form of a colour code to inform about the confidence level of each extracted phase term. The tuning of the quantized metric is in practice set-up dependent and can be updated periodically. This soft-decision metric can be conveniently used in practical situations to distinguish between true mechanical information and artefacts induced by the phase extraction process. Also, it may advantageously feed a further automatic recognition system to enhance the classification process of the captured waveforms.
Note that the SIMO intensity estimator $\hat{\mathrm{I}}_{SIMO}$ could also be used as a first order quality estimator, despite not being immune to coherent fading.

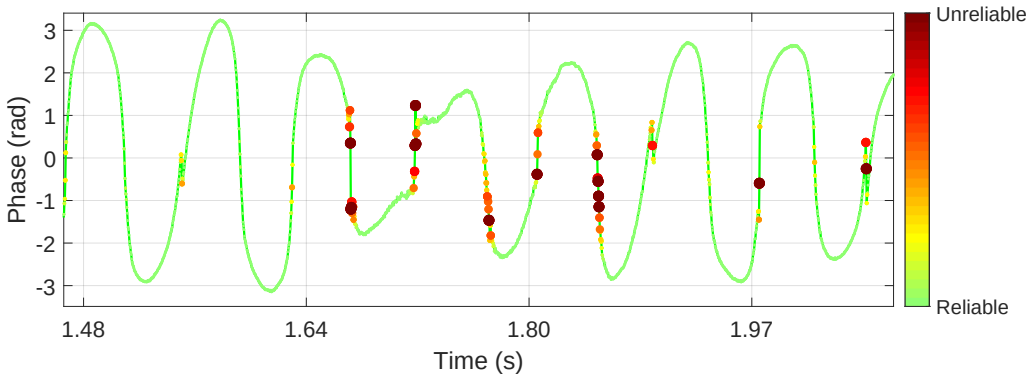


Figure 3.16: Phase variations in time at segment location from Figure 3.15 Superimposed is colour coded $|\det|$ criterion to highlight the artefacts detection

**Blind areas in a sensing system, realistic conditions** Overall, $\overline{R}_{d,t}$ allows to identify blind (distance, time) areas of the $\Delta\phi$-OTDR traces. Over such blind areas, we verify that:

- The presence of an artefact does not indicate the detection of a real vibration or acoustic event
- No event that occurs within this distance and time frame will be detected by the system

Yet, we observed that low-reliability (blind) areas occur over short period of time within a single segment (Figure 3.16), and rarely occur over several successive segments (Figure 3.14). Moreover, dynamic events in deployed fibre environment rarely occur over less than one gauge length (here of the order of the metre) or during less than one code duration (of the order of the microsecond). Therefore, real events such as acoustic disturbances could be retrieved on adjacent segments or adjacent time periods, for example using interpolation between consecutive (distance, time) measurements.

Such a processing method based on the reliability metric, and involving interpolation and pattern recognition would pave the way to the automation of event recognition in distributed sensing systems.

We have highlighted the relevance of a correct estimation of the backscattered intensity in $\Delta\phi$-OTDR applications. MIMO sensing gives access to the Jones matrix of the backscattered optical field and we have demonstrated that the module of its determinant introduces a smaller error than the standard Frobenius norm to estimate the intensity [105]. In a first step, it has allowed to better discriminate between low reflective segments along the sensed fibre, thus lowering the phase distinction threshold.
In a second step, we have shown that this determinant module can be used as a soft-decision reliability metric to detect phase artefacts induced by local intensity drops that potentially superimpose to any detected mechanical signal. This metric is of major interest for further post-processing to help improve the classification of the captured mechanical signals (including artificial intelligence based algorithms, which are out of the scope of this thesis).

### 3.3.4 A note on low sampling resolution in the presence of potential artefacts

The "low sampling resolution factor" has been already mentioned in the previous sections of this chapter, especially when it comes to display sensor results along distance. Indeed, from a native spatial resolution or "gauge length" of the order of magnitude of the metre, several kilometres measurements are often displayed with a resolution around the hundred metres. The motivation for this low-resolution process is twofold:

1. When sensing with a short gauge length with regard to the fibre length, the number of segments to monitor is large, which requires high processing resources and memory storage: in practice, it can be preferred to relax the spatial sampling resolution to save resources ;

2. In the presence of low-reliability segments or points, one straightforward and quick solution would be to remove them from the measurement, at a cost of a coarser spatial sampling resolution.

Low sampling resolution is achieved by selecting a segment subset from the native resolution set: for achieving a downsampling factor $p$, we choose, among every $p$ consecutive segments, the one that provides the highest backscattered intensity on average over the time dimension. The relevance of this intensity-based selection criterion was first justified for dual-polarization interrogation in [117] and is now more convincing following the analysis in section 3.3.

An example on the use of multiple downsampling factors over a 50km measurement is given in Figure 3.17 here after.

The experiment consists in the interrogation of a 50km single mode fibre spool by means of dual-polarization codes (subsubsection 1.2.4.2) of size $N_{code} = 2^{17}$, with symbol rate $f_{symb} = 50$MBaud yielding a code duration $T_{code} = 2.63$ms. A multi-tone perturbation perturbation is introduced by means of a Piezo-Electric Actuator (PEA) at 0.88km from the interrogator[6]. To avoid a permanent monitoring of all fibre segments at $L_s = 2$m corresponding to $f_{symb} = 50$MBaud, we start by processing the differential phases from the highest-intensity segment in each group of adjacent $N = 250$ segments.

On the left part of Figure 3.17(a), we show the selected highest-reflecting segments over the first eight kilometers and the evolution of the corresponding differential phase over one second. The perturbation induced by the actuator is easily detected using an energy criterion, as shown through the power spectral densities of the phases in the insets of Figure 3.17, at an average sampling resolution $L_{coarse} = 250L_s = 500$m. The initial detected position is 1100m. A new selection process is activated locally over the segment preceding the detected alarm using an enhanced sampling resolution $L'_{coarse} = 5L_s = 10$m (random value chosen for illustration). A new localization result at 879m is shown on the right with a better accuracy.

[6]The usage of PEAs for the introduction of localized, low frequency excitations is further developed in the next chapter.

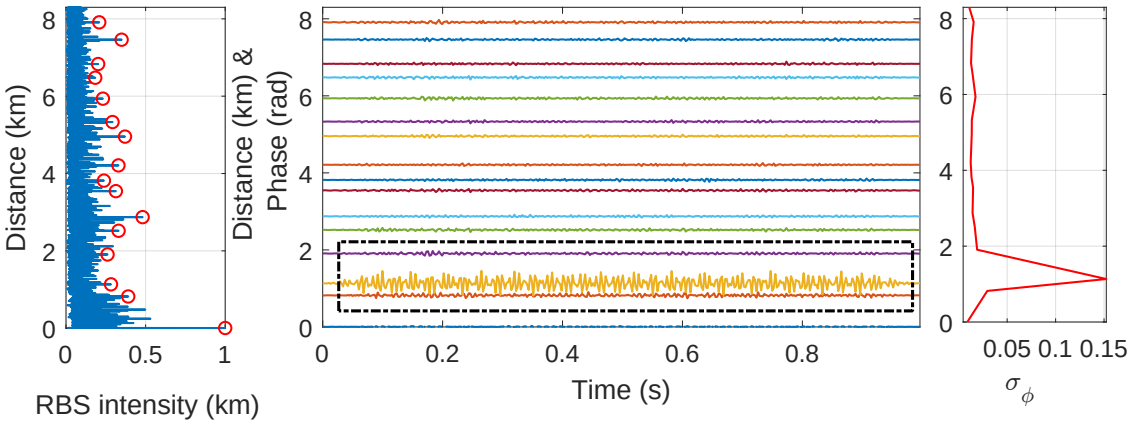


(a) Coarse sampling resolution ($L_{coarse} = 500$m)

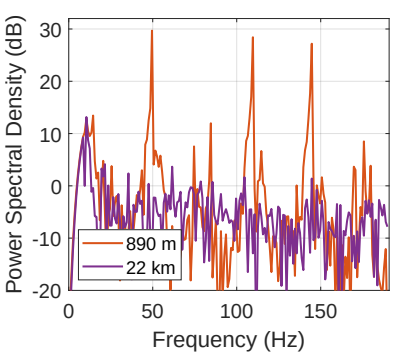


(b) Power spectral density of phases

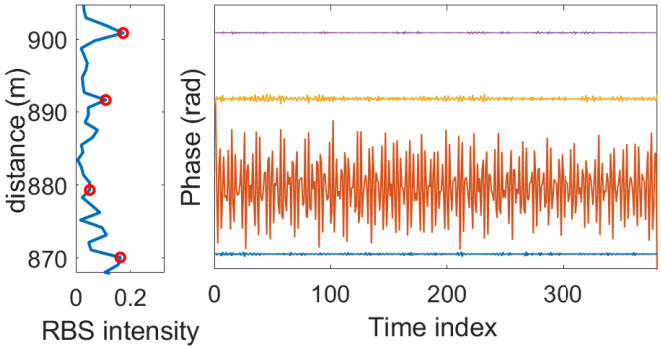


(c) Finer sampling resolution ($L_{coarse} = 10$m)

Figure 3.17: Multi-resolution event localization. **On top**: initial coarse sampling resolution monitoring showing Rayleigh Back-Scattered (RBS) intensity as a function of distance on first 8km & phase evolution at selected best segments each 500m. $\sigma_\varphi$ along distance for event detection. Dash-dotted box: selection of excited zone displayed in (c). **Lower part**: power spectral density of phase for two selected segments, one enclosing an event detection. Second-stage monitoring with a finer selection each 10m over a smaller section bounded by the position of the detected alarm and the preceding alarm-free position.

This multi-resolution approach is capable of handling several alarms in parallel over all the sensed fibre by refining the localization in an iterative way, thus saving computation efforts compared with a permanent monitoring at the native gauge length.

## Summary: On the way to optimize reliability

In this chapter, we were able to explore different fibre sensor interrogation methods, mainly based on polarization diversity: indeed, polarization diversity at the receiver was already considered with interest in the literature as it yields a stable measure of the backscattered signal. Conversely, polarization diversity at the transmitter was not yet precisely studied until now: we demonstrated the advantage of probing a fibre sensor onto two orthogonal polarization axes and finally proposed a probing method which is immune to polarization fading. This method is referred to as "Coherent-MIMO".

Having explored the mechanisms of Coherent-MIMO, we did also define a reliability metric for Coherent-MIMO measurements in this chapter. An analytical and experimental comparison of two intensity estimators was conducted and resulted in the definition of a

soft bit metric which is of major interest for further post-processing of sensing data.

Yet, this chapter's discussions on polarization effects and accuracy assessments enable to go on with some experimental demonstrations and comments on the "Coherent-MIMO" sensing system in chapter 4. Later on in chapter 5, the remaining fading effect – namely coherent fading, will be tackled and possibly mitigated.

# Chapter 4

# Coherent-MIMO sensing in practice: experimental results

Previous sections allowed to determine the performance of the Coherent-MIMO interrogation system, relying on a method which is immune to polarization fading and which allows to assess the reliability of each time-distance-resolved measurement. In the following section, we highlight the system performance, not only by assessing the noise floor levels on static measurements as previously done in simulation, but on real deployed fibres. We evaluate the performance of the Coherent-MIMO sensing system with different types of (realistic) disturbances and environments.

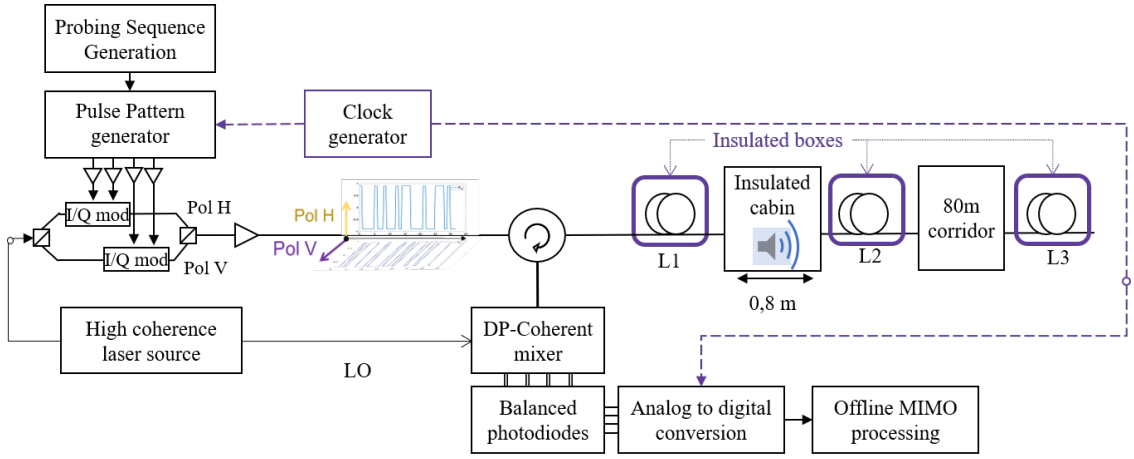


Figure 4.1: Experimental setup for high mechanical bandwidth detection, adapted from [118]. LO: Local Oscillator, I/Q: In-phase/Quadrature, Pol: Polarization, DP: Dual-Polarization, MIMO: Multiple-In, Multiple-Out

**Setup description** Figure 4.1 displays the overall experimental setup for high mechanical bandwidth detection over Standard Single Mode Fibre (SSMF). The highly coherent laser source is an OEWaves OE4030 Whispering Gallery Mode laser operating at $\lambda = 1536.6$nm, the pulse pattern generator is the Arbitrary Waveform Generator AWG5200, 16bits from Tektronix. The AWG provides the stable clock reference. At the receiver side are: a coherent $90^o$ hybrid from Kylia and four Thorlabs PDB480C-

AC Fiber Coupled Balanced Photodetectors with 1.6GHz bandwidth. The acquisition is performed by a 16bits PCIe Gen3 RazorMax Express acquisition board.

The fibre under test is a SSMF made of a first spool of length L1 placed inside a soundproofed box. In this experimental study, soundproofing or "mechanical insulation" of a box means that foam-like materials have been placed on the inside of an home-made box such that the Sound Pressure Level (SPL) of the surroundings is below $42\text{dB}_{\text{SPL,A}}$ and $61\text{dB}_{\text{SPL,C}}$, meaning that external environmental perturbations are sufficiently damped to avoid affecting the fibre. Then, it enters a 0.8m×0.8m×2m also insulated cabin that contains a loudspeaker placed at a 0.5m distance from the fibre, as displayed on the left in Figure 4.2. This 0.8m fibre section is tight between the two walls of the cabin, such as to maximize its sensitivity as described in subsection 4.2.2. A second fibre spool of length L2, still soundproofed, extends the tested fibre section which stays in the laboratory. Then, the fibre continues in the crawl space of an 80m long corridor, see last picture in Figure 4.2, before terminating with a final insulated spool of length L3. The spool sections consist of bare fibre whereas the fibre is covered by a 0.9mm diameter plastic jacket in the insulated cabin and a thicker one (3mm diameter, which is a standard protection as the fibre cable in the corridor was originally meant for communication between two laboratories) in the underground section.

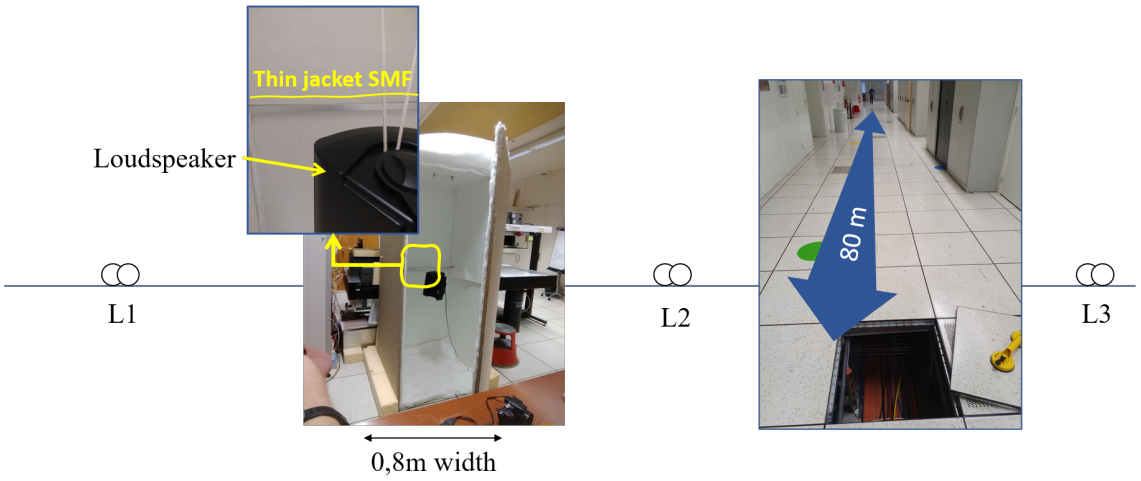


Figure 4.2: Experimental setup for high mechanical bandwidth detection, pictures

The overall length of the fibre span (L1+L2+L3+80.8m) is limited to no more than 2km in this experiment. Indeed, we aim at detecting high bandwidth signals since the round trip time of light $T_{ir}$ in a 1km fibre span is short enough ($T_{ir} \simeq 10\mu$s) to allow a fast repetition rate of the probing signal (below $100\mu$s would allow a mechanical bandwidth $B_{meca} \geq 5$kHz). Also, as stated in the previous sections, the interrogator is assumed to be highly sensitive (distinction threshold of the order of 10 to $1n\varepsilon$ strain within $B_{meca}$) therefore we aim at detecting low energy signals as well as signals with a high dynamic range (a significant ratio between highest and lowest sound level).

## 4.1 Capturing large bandwidth signals

To study the feasibility of recording large mechanical bandwidth signals using a SSMF and a Coherent-MIMO interrogator, a first qualitative study is performed by applying controlled and localized strain to a portion of the fibre under test by mean of a Piezo-Electric Actuator (PEA). This technique is advantageous to handle the exact position where the perturbation reaches the fibre and also to quantitatively relate the optical phase change to the magnitude of the mechanical perturbation [43, 119].

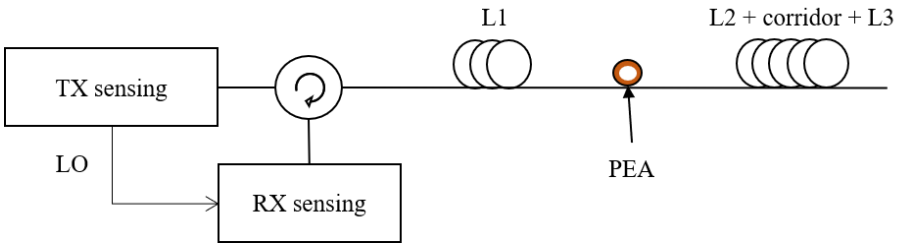


Figure 4.3: Fibre setup for high-bandwidth, mechanical excitations by means of a Piezo-Electric Actuator (PEA)

The simplified setup is displayed in Figure 4.3 where the PEA replaces the soundproofed cabin from Figure 4.1 and $L1 = 871$m and $L2$+corridor+$L3 = 1010$m. The piezoelectric actuator is a cylindrical ($d = 5$cm diameter) element which diameter slightly contracts and dilates according to the voltage $U$ applied to its sides, following $\Delta d = 400\text{pm/V}_{\text{RMS}}$ where $\Delta d$ is the diameter variation, therefore (4.1):

$$\frac{\Delta L}{L} = \frac{\pi \Delta d(U)}{\pi d} = \frac{400}{0.05} U.10^{-12} \tag{4.1}$$

where $\frac{\Delta L}{L}$ is the elongation of the coiled fibre for a given coiled fibre length $L$, in $\varepsilon = \text{m/m}$.

**Linearity of phase response to piezoelectric excitation** As an illustration of equation (4.1), Figure 4.4 gives sensitivity and linearity assessment of a fibre sensor interrogated with dual-polarization binary codes of length $T_{code} = 1.05$ms, subject to 100Hz sinewave piezoelectric excitations at two locations of the fibre sensor. The gauge length for this fibre interrogation is $G = 0.8$m. We notice that at a distance $d = 870$m from the fibre start, the detection threshold is of 10nm extension i.e. $\epsilon = 12.5\text{n}\varepsilon$ in the $B_{meca} = 1/2T_{code} = 476$Hz mechanical bandwidth (strain density $573\text{p}\varepsilon/\sqrt{\text{Hz}}$), whereas after $d = 20.87$km no strain is detected up to 90nm ($\epsilon = 112.5\text{n}\varepsilon$, strain density $5.15\text{p}\varepsilon/\sqrt{\text{Hz}}$). Overall, once the detection threshold is exceeded, the measured amplitude of phase variations $\Delta\phi$ comply with the applied strain following the linear relationship $\Delta\phi = 4\pi n \Delta L \xi/\lambda$.

More generally, the use of PEAs allows to target only a specific portion of the fibre under test, also avoiding multipath acoustic issues.

**High bandwidth piezoelectric excitation** $L = 31$cm of fibre (= 2 fibre loops) are coiled around the actuator. For the interrogation of the fibre sensor, we use dual-polarization codes presented in subsection 1.2.4 with symbol rate $f_{symb} = 50$MBaud and

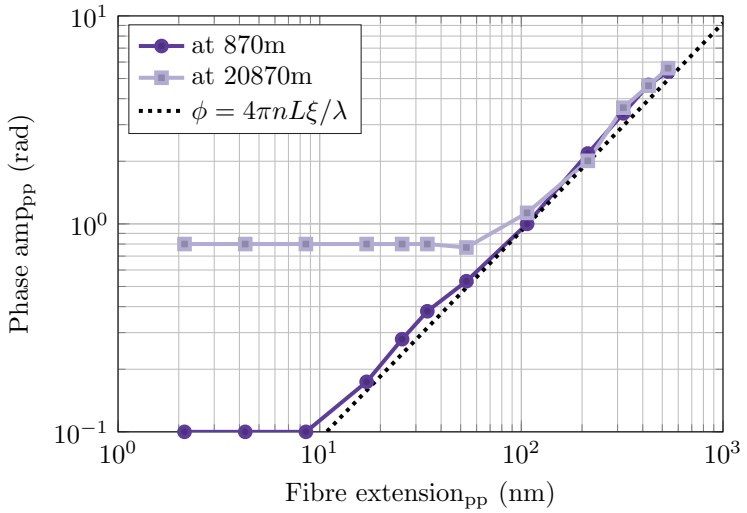


Figure 4.4: Phase amplitude as a function of fibre extension, at two locations on a 25km fibre, from [119]

code duration $T_{code} = 81.9\mu$s, yielding a mechanical bandwidth $B_{meca} = 6$kHz.

To explore the full bandwidth and linearity of the response, we generate a frequency sweep spanning a $[0.1, 6]$kHz range and inject it with constant power level to the PEA. The backscattered phase from the excited segment is measured and its Power Spectral

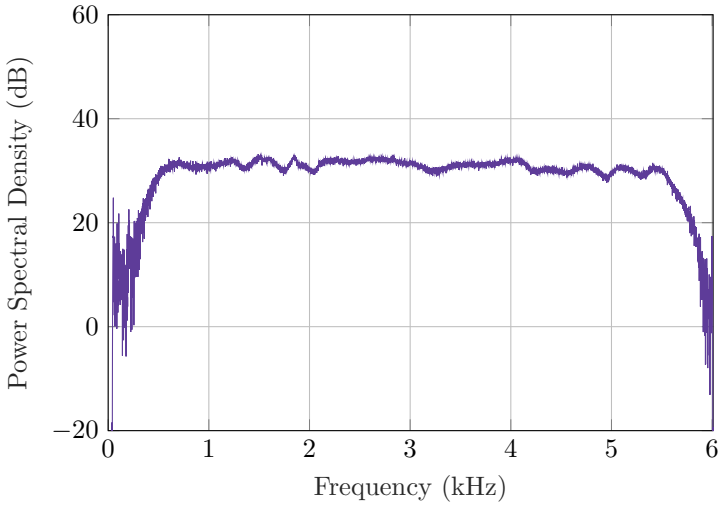


Figure 4.5: Frequency sweep from 100Hz to 6kHz mechanically applied to the fibre by means of a PEA: Power Spectral Density of the measured phase at the excited fibre location

Density (PSD) is displayed in Figure 4.5. The standard deviation of the PSD between $[700, 5300]$Hz is of 0.9dB. This relative flatness of the spectrum illustrates the linearity of the fibre microphone as well as the linearity of the PEA (indeed, there is no simple method to determine whether the small PSD fluctuations are induced by the fibre sensor or the PEA).

Note that even though the human hearing range is $B_{ear} = [0.02, 20]$kHz, the usual bandwidth of the analogue telephony is $B_{phone} = [0.3, 3]$kHz which is acceptable to recognize voice signals. Therefore, now that the flatness of the fibre sensor is assessed up to 6kHz, a 1-second speech signal is recorded and again injected into the PEA at a precise

location along the fibre [120, 121].

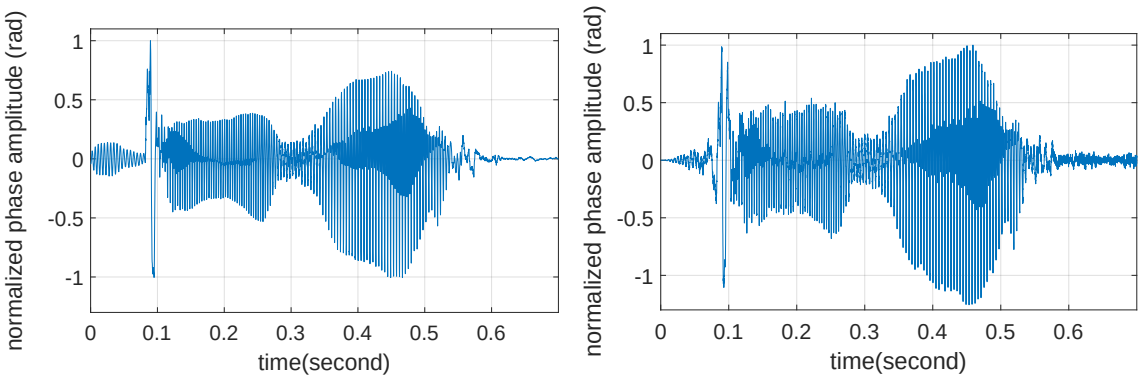


(a) Recorded speech signal

(b) Backscattered phase signal

Figure 4.6: Normalized phase variation of a speech signal "Bonjour", from [120]

Figure 4.6 shows the original recorded speech signal and the backscattered phase signal from the excited segment. The mean square error of Figure 4.6(b) with regards to the reference in Figure 4.6(a) for the first 0.6seconds is 0.098% and the standard deviation of noise after 0.6 seconds is 0.022%. The experiment demonstrates how sensitive the fibre sensor is in a qualitative manner, as the backscattered phase could be listened to, allowing an easy speech recognition [122]. Beyond the low distinction threshold, the high dynamic range of the sensing system contributes to such performance.

## 4.2 Capturing acoustic signals

The above results were achieved with mechanical excitations directly applied to the fibre by means of piezoelectric actuators. For practical situations, the excitation sources (vehicles, machineries, pedestrians...) are rather located a few meters away from the fibre cable deployed by the telecom operator. The fibre is perturbed by vibrations or by acoustic waves over a distance and with an attenuation which is strongly environment-dependent. This situation makes quantitative measurements potentially difficult to achieve in the field and the extrapolation of the results to other environment questionable.

### 4.2.1 Assessment of detection-identification of an acoustic signal

We describe for illustration an experimental study carried out in the building corridor, located after $L1 + L2 + 0.8 = 620$m SMF and placed in a crawl space 0.8m below the floor as pictured in Figure 4.1 and Figure 4.2.

Figure 4.7: Loudspeaker placed in a corridor for acoustic measurements

The setup is tuned to capture perturbations over a 1.53kHz bandwidth and with a 2m

gauge length (coded dual-polarization interrogation, 50MBaud symbol rate, $N_{code} = 16384$ BPSK symbols yielding $T_{code} = 328\mu s$). An acoustic perturbation is generated at 640m from the fibre start by means of a loudspeaker positioned on the floor (see Figure 4.7) that generates a 653Hz pure tone. The tone is emitted from the loudspeaker at various power levels: from 65 to 90dB$_{\text{SPL}}$, and the related Sound Pressure Level (SPL) is measured at the fibre cable closest vertical position in the crawl space by means of a sound level meter. The measured building background noise is of 54dB$_{\text{SPL}}$.

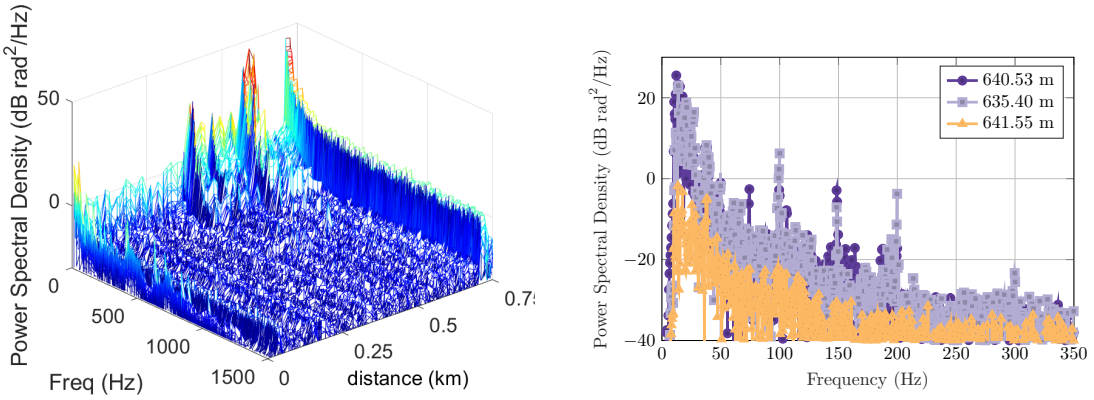


(a) Frequency noise in the frequency/distance plane

(b) Main frequency components (100Hz, 150Hz and harmonics) measured in the corridor

Figure 4.8: Power spectral density (PSD) of unwanted low frequency noises (from 5Hz) present in the building, measured along the fibre sensor

Figure 4.8 displays the power spectral density of acoustic noise in the absence of the loudspeaker excitation. High pressure level acoustic signals components are captured below 300Hz, mainly due to the air conditioning in the building and to specific machinery in the neighbourhood. The common spectral signature of such machinery is a frequency comb, with a low fundamental frequency (25, 50 or 100Hz) and its harmonics (multiples of the fundamental frequency). In Figure 4.8(b), two main perturbations generate 100Hz and 150Hz perturbations, therefore frequency peaks are noticed at 200Hz and 300Hz (second order harmonics).

Then the loudspeaker is switched on, in the corridor. Figures 4.9(a) and (b) display the PSD of the phase variations captured along the fibre within a 2-second period when the sound pressure level at the fibre side is equal to 68 and 88dB$_{SPL}$ respectively. The differential phase is processed over a subset of segments that yields a 15m coarse spatial sampling resolution, and low frequency contributions are filtered out so to keep a proper dynamic (in Figure 4.8, some low-frequency noise contributions reached 50dBrad$^2$/Hz). Figure 4.9(a) highlights that the 68dB$_{SPL}$ pure tone is detected at an estimated position of 646m from the fibre start, roughly 15dB above the phase noise observed in the distance versus frequency plane. When the acoustic waveform reaches the fibre with a sound pressure level of 88dB$_{SPL}$, the pure tone is now detected at 640m and 39dB above the noise. We do not exactly retrieve the 20dB pressure level difference between the 2 measurements, mainly due to the spatial resolution of the analysis.

In addition, it can be observed in Figure 4.9(b) that the 653Hz tone is not simply detected at the fibre position the closest to the loudspeaker (640m from fibre start), but

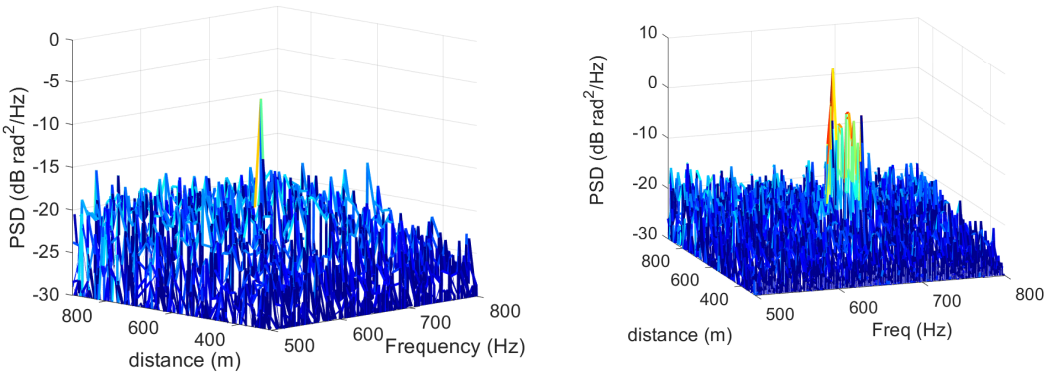


(a) $-7.26\text{dBrad}^2/\text{Hz}$ peak detection for 68dB SPL excitation

(b) $5.77\text{dBrad}^2/\text{Hz}$ peak detection for 88dB SPL excitation

Figure 4.9: Detection of a 653Hz pure tone (close to E5 music note), acoustically generated 0.8m away from the fibre cable at 640m distance

over a wider distance along the fibre: the 653Hz tone is detected about 20dB above the noise 445m and 529m from the fibre start, which is below the 39dB dynamic observed at the peak but still noticeable. The reason is that the high-level excitation of the latter test induces an acoustic radiation in the crawl space below the corridor, thus also affecting fibre cable segments located some tenths of meters away from the loudspeaker position. This contrasts with piezo-electric perturbation for example, which introduces strain at a single location on the fibre sensor. For such a spread event detection, we remind the possible signal spatial interpolation in case of a blind spot along the fibre in the disturbed area (see subsection 3.3.3).

This first acoustic study proves the ability to detect, localize and identify acoustic perturbations of various pressure levels by means of a standard SMF cable deployed in a building.

### 4.2.2 Sensitivity as a function of the fibre settings

Further sensitivity experiments were conducted with regards to the fibre physical settings. At this point, the fibre section of interest is the 0.8m fibre inside the insulated box, located at 420m from the fibre start (Figure 4.1). A single-tone 600Hz acoustic signal is generated with various power levels by a loudspeaker located approximately 50cm from the fibre. The fibre span is interrogated by means of dual-polarization codes. The fibre section under test is attached to different props:

- firstly, the fibre is slightly pulled such as the fibre stays horizontal between the two sides of the insulated box, without any prop
- a second fibre section under test is still pulled tightly but also glued to an aluminium metal plate of thickness 9mm
- the third fibre is glued to a thinner metal plate (1mm thickness) and finally the last tested fibre section is pulled on a Plexiglas plate of thickness 5mm.

The sensitivity of the fibre section in each configuration is assessed in Figure 4.10.

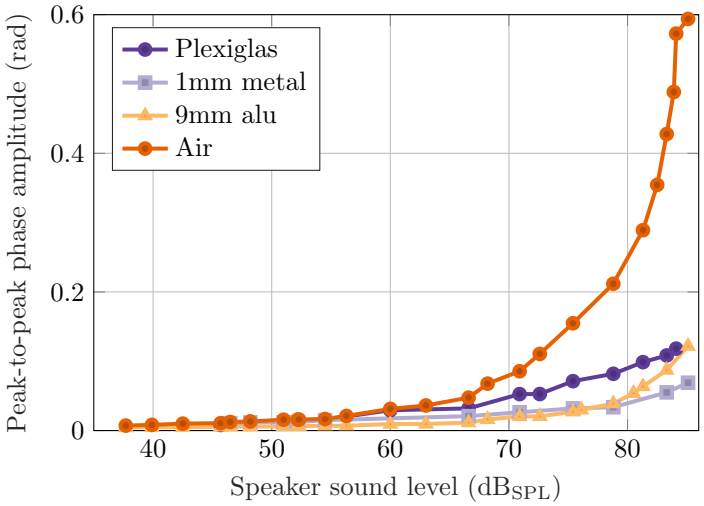


Figure 4.10: Sensitivity of the fibre section depending on its prop, adapted from [120]

For low sound pressure level radiated by the loudspeaker, all configurations are subject to low sensitivity due to the noise floor of the system. From 55dB$_{SPL}$, the free fibre and plexiglas fibre start showing higher sensitivity than those fixed to metal props. Beyond 65dB$_{SPL}$, the sensitivity of the free fibre configuration gets ahead the other ones, while fibres fixed to plexiglas and thick metal reach a comparable sensitivity level after 83dB$_{SPL}$.

The sole excitation signal for this study is an aerial, acoustic signal. Further considerations on the propagation of sound in different materials is out of the scope of this non-exhaustive feasibility study.

Overall, this experiment demonstrated the better sensitivity of aerial fibres to acoustic signals compared to fixed or buried fibres, independently from the interrogator setup configuration (Baud rate, code length...)

## 4.3 Experimental validation of SIMO and MIMO relative performance

In chapter 3, we demonstrated the advantage of MIMO interrogation over SIMO interrogation, in terms of lower distinction threshold and for simulated fibre interrogations.

The experimental setup described in Figure 4.1 is used for the interrogation of a 340m SSMF in the absence of perturbations (static mode), with one polarization channel being switched off at the transmitter side for SIMO interrogation. SIMO and MIMO measurements could not be performed simultaneously, however they are performed successively to ensure close experimental conditions for both methods.

The measured $\sigma_\varphi$ is displayed in Figure 4.11. The $\sigma_\varphi$ for MIMO interrogation presents attenuated peaks that coincide with SIMO interrogation $\sigma_\varphi$ and two independent false alarms. The coincident peaks are likely due to coherent fading, whereas the higher SIMO peaks are mostly a consequence of polarization fading as described in eq.(3.4). Overall, the $\sigma_\varphi$ level is higher with SIMO interrogation compared to MIMO.

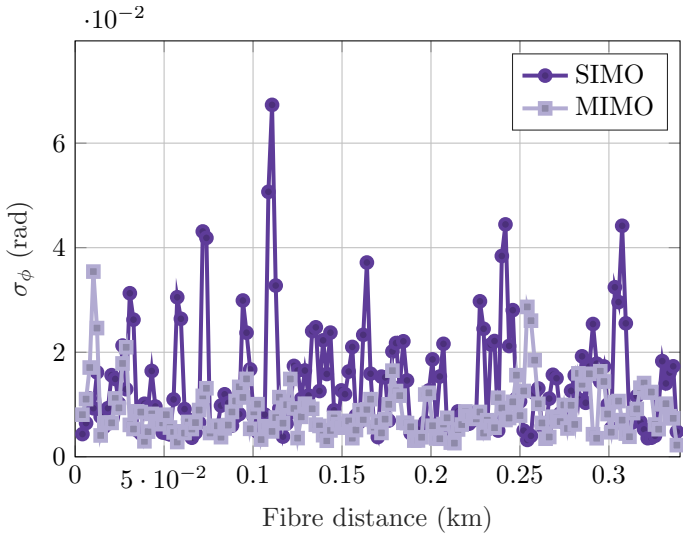


Figure 4.11: Experimental measurement, SIMO and MIMO interrogation of 340m SSMF: $\sigma_\varphi$ along distance

Though Figure 4.11 allows to quantitatively assess the advantage of MIMO interrogation over SIMO, we study the distribution of $\sigma_\varphi$ in Figure 4.12: in Figure 4.12(a), the Probability Density Function (PDF) of $\sigma_\varphi$ values is displayed, which shows how the SIMO $\sigma_\varphi$ values are more spread towards higher phase variations. Figure 4.12(b) displays the cumulative distribution function of $\mathrm{SNR}_\varepsilon = 20\log_{10}\left(\frac{4\pi n\xi G}{\lambda\sigma_\varphi}\right)$ (3.7), similarly to Figure 3.8 which displayed fibre simulations results.

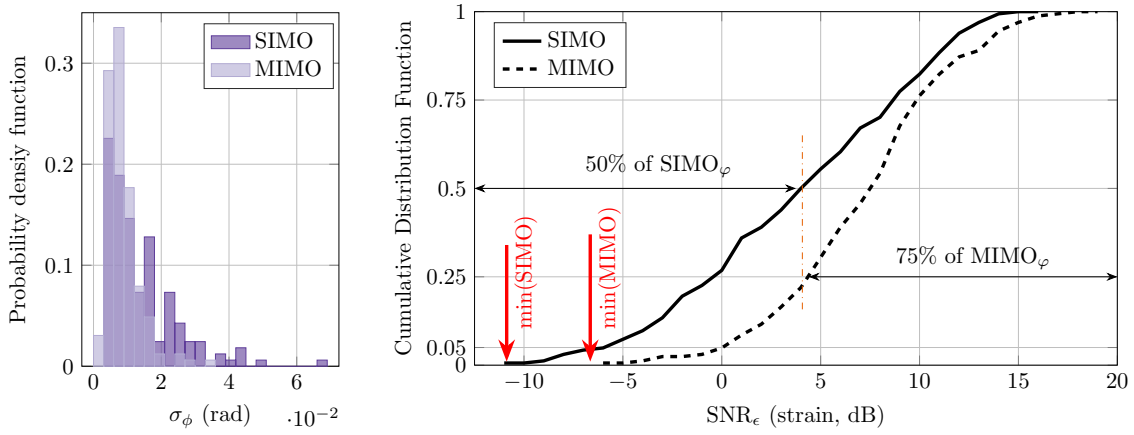


(a) Probability density function

(b) Cumulative distribution function

Figure 4.12: Experimental measurement, SIMO and MIMO interrogation of 340m SSMF: Distribution of $\sigma_\varphi$ values

Figure 4.12(b) validates the simulation results as we show again that up to 50% of the SIMO estimated phases vary more than 75% of MIMO estimated phases over 340m.

In terms of maximal $\sigma_\varphi$ and $\sigma_\varepsilon$ values, i.e. the distinction threshold, we show here a 5dB difference, assessing a distinction threshold in MIMO which is significantly below the SIMO one.

Experimental measurements confirmed the better performance of Coherent-MIMO interrogation over SIMO $\Delta\phi$-OTDR. Among other advantages brought by MIMO probing, the MIMO strain distinction threshold was lowered 5dB below the SIMO strain one on a 340m fibre distance, which is promising regarding the performance of Coherent-MIMO sensing.

## 4.4 Capturing acoustic speech signal on a standard telecom fibre

This final section is to demonstrate the sensitivity of the system, in terms of noise floor, dynamic range as well as mechanical bandwidth. The ability of using the fibre as a microphone array ("multi-microphone") is also demonstrated.

The fibre span in Figure 4.1 with $L1 = 420$m, $L2 = 200$m and $L3 = 300$m is probed over two orthogonal polarization axes with codes of length $T_{code} = 82\mu$s that are repeated with a period equal to the code length (continuous probing), leading to an analysis of mechanical perturbations affecting the fibre over a frequency range from DC up to $B_{meca} = 6.1$kHz. A mechanical bandwidth of 6.1kHz is considered large regarding the capture of speech signals since a $[0.3, 3]$kHz bandwidth is known to mostly enclose sufficient information and so to allow for interpreting any speech message.

The $82\mu$s time length code is composed of 4096 BPSK symbols transmitted at $f_{symb} =$ 50MBaud, which yields a gauge length of 2m. Therefore, the 1km fibre is virtually split into 500 segments, or 500 independent microphones. Calculating the differential phase between consecutive segments allows to locally monitor the fibre, with a 2m native gauge length here. Hence, we continuously monitor the temporal phase changes at different sections of the fibre.

Moreover, we study here the impact of the spatial sampling resolution onto the detection sensitivity by emulating lower spatial sampling resolutions of 4, 8 and 16m respectively. This is achieved by selecting a segment subset from the native resolution set: for achieving a spatial resolution downsampling factor $p$, we choose, among every $p$ consecutive segments, the one that provides the highest backscattered intensity (or reliability metric) on average over the time dimension.

We inject a 5s male voice signal into the loudspeaker placed in the insulated cabin which locally perturbs the fibre at 420m from the start with a Sound Pressure Level (SPL) of 75dB$_{SPL}$, similar to that of a standard conversation volume [123]. In addition, the 80m fibre section in the corridor crawl space is exposed to acoustic and vibratory perturbations present in this part of the building, such as fans in adjacent labs and air conditioning machinery.

Figure 4.13(a) displays the standard deviation of the differential phase, measured along the 5s measurement time, as a function of the fibre distance. On top of the 2m native spatial resolution, we superimpose the standard deviation of the differential phase estimated every 2, 4 and 8 segments on average following the above described lower spatial

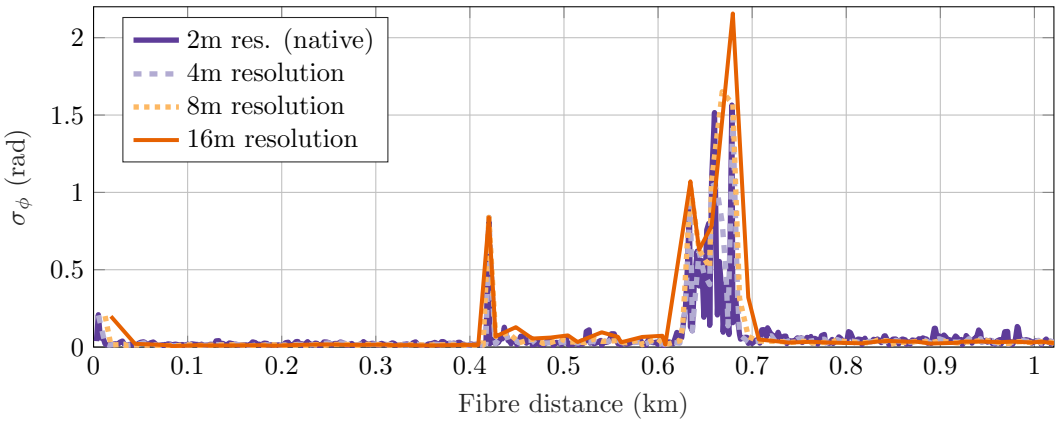


(a)

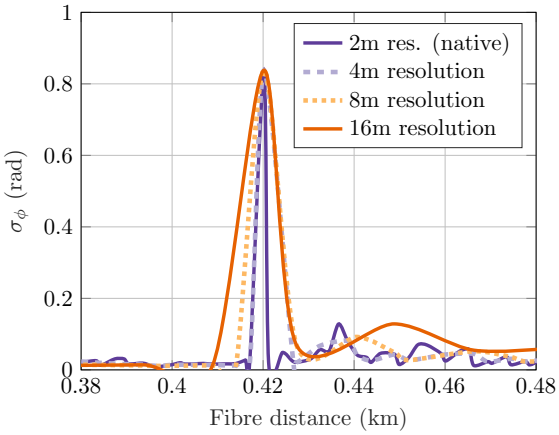


(b) Detection of a speech signal around 420m

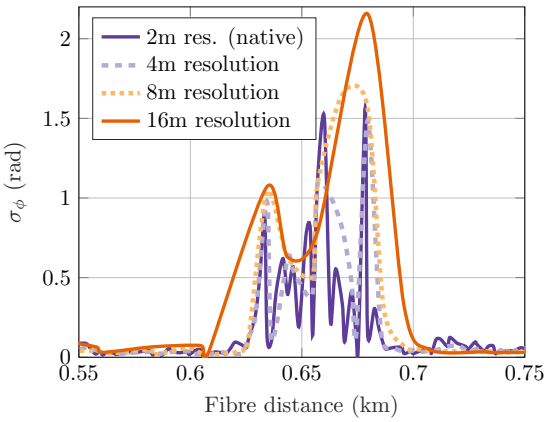


(c) Detection of a low frequency noise around 650m

Figure 4.13: Detection and localization of multiple acoustic signals along a 1km fibre span, mechanical bandwidth: 10Hz high-pass filter

sampling resolution selection procedure. We observe two events at 420m and 660m from the fibre start, which indicates joint detection of two independent mechanical events at the respective locations. These two events are displayed more precisely in Figure 4.13(b) and (c). The former one is accurately localized, with a peak of equal magnitude at 420.2m from the fibre start for all sampling resolutions, meaning that the disturbance spreads over 2m or less. The latter one spreads over 50m, between 640 and 680m, meaning that a perturbation is captured by the fibre over a large area in the corridor. Figure 4.13(c) shows how a more precise spatial sampling resolution allows to determine how the disturbance is spread along the corridor.

Figure 4.14(a) displays the differential phase of the disturbance measured in the corridor as a function of time along with its associated PSD captured at 678m from fibre start (native resolution) in Figure 4.14(b). The second event spectral signature is concentrated in the very low frequencies, with a fundamental component at 18Hz along with its first three harmonics (36, 54, 72Hz) and also a 100Hz component. This detected event is actually caused by a fan machinery installed in a laboratory 10 meters away from the corridor where the fibre is deployed. Such very low frequencies attenuate slowly with the distance, which explains why it is captured by the fibre over 50m around the actual noise source position.

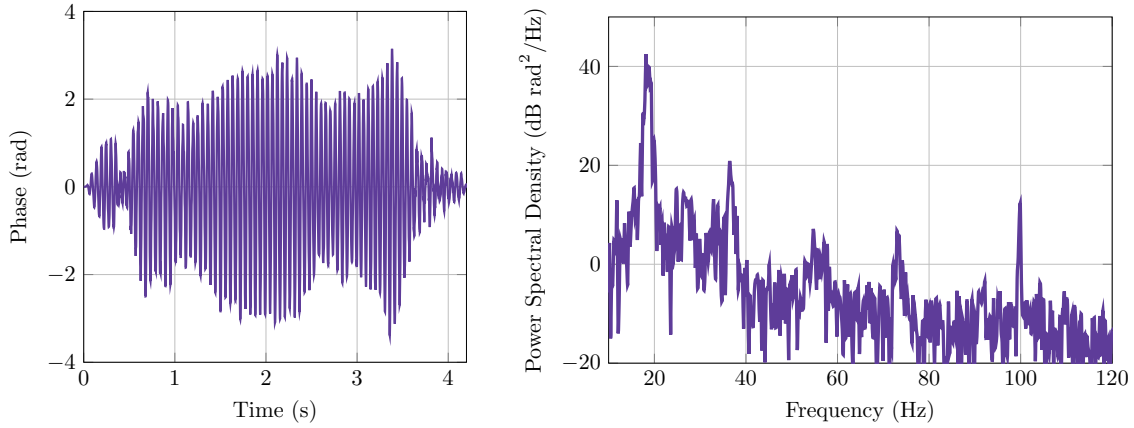


(a) Phase vs time

(b) PSD of phase in low frequencies range

Figure 4.14: Identification of an acoustic low frequency signal located at 678m from fibre start

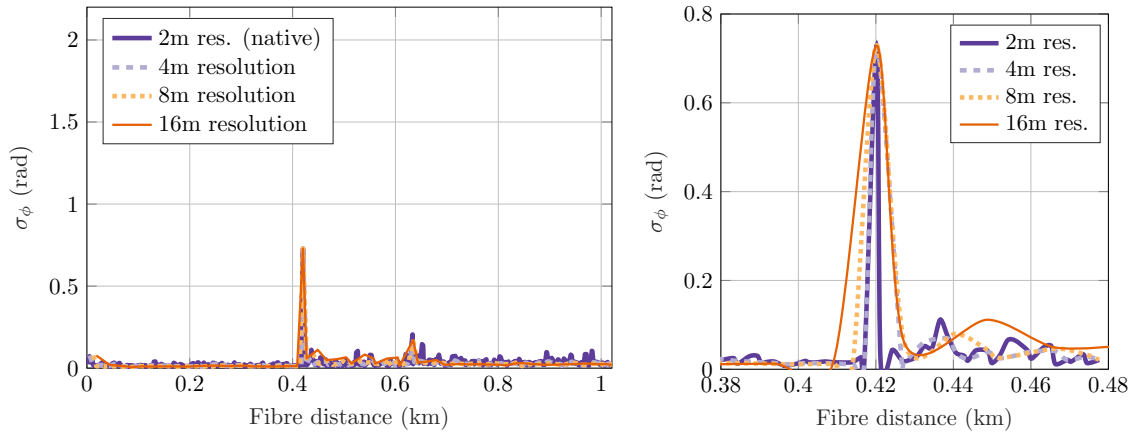


(a) Full distance

(b) Zoom on detection peak

Figure 4.15: Detection and localization of high mechanical frequency event, band-pass filtering between 100Hz and 6.1kHz, for different sampling resolutions

Figure 4.15 shows the same information as in Figure 4.14(a) but including high-pass filtering onto the differential phase time slices to get rid of spectral information below 100Hz: the peak around 650m has vanished, as it could be expected with regard to the spectral signature of the fan machinery Figure 4.14. Conversely, the former one at 420m is left unchanged, with comparable peak magnitude to Figure 4.13(b) and same width, which complies with a speech signature since human voice does not contain any information below 100Hz.

Figure 4.16(a) displays the phase variations measured at the first peak location (420m) for each of the four spatial sampling resolutions. The four signals superimpose with tiny differences only: Figure 4.16(b) zooms on a silent zone of the captured speech signal to magnify differences between the various sampling resolutions. The figure shows lesser phase variations ($\sigma_\varphi$) at lower sampling resolutions (8 and 16m) than at the native one (2m). Finally Figure 4.16(c) displays a zoom on a time slice where some voice signal was detected. Unlike the noisy section, recorded signal sections are very similar whatever the

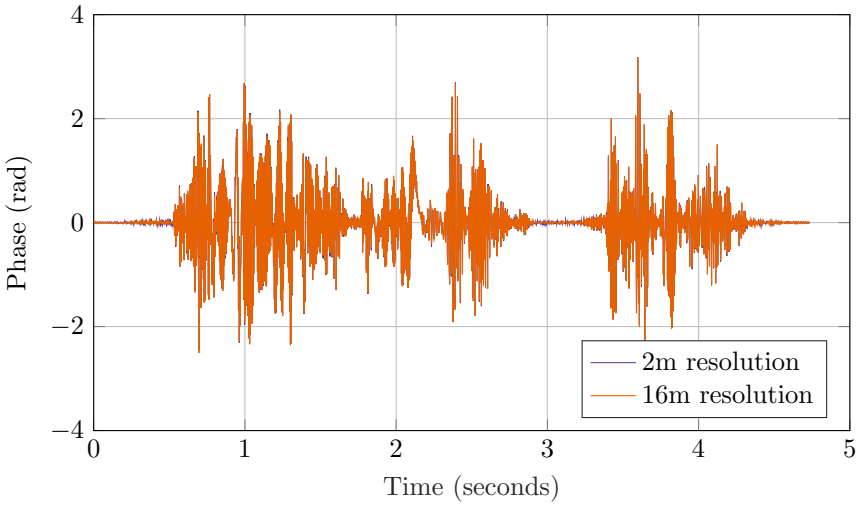


(a) Differential phase in time, for two sampling resolutions. The phases seem to superimpose.

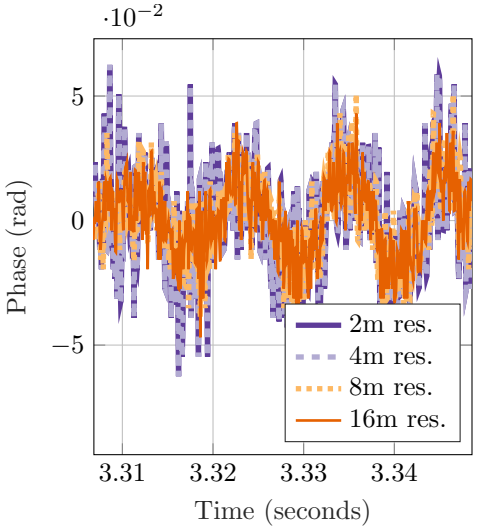


(b) Zoom on silent part

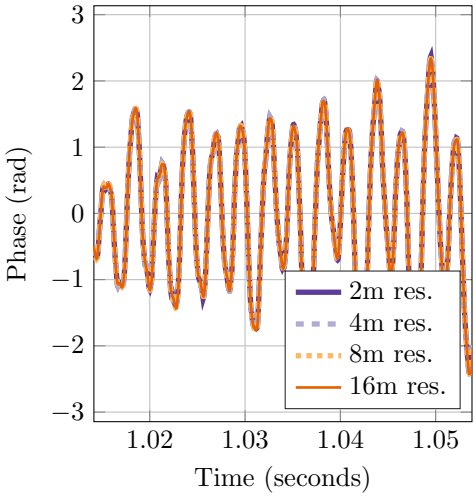


(c) Zoom on signal part

Figure 4.16: Backscattered phase from the fibre segment exposed to the loudspeaker for different spatial sampling resolutions, with close view of the silent part and close view of captured voice

spatial sampling resolution choice.

Coming back to the phase standard deviation in figures Figure 4.13 and 4.15, lower $\sigma_\varphi$ is also observed in the regions where the fibre is not mechanically excited (insulated spools): essentially, coherent fading is mitigated by selecting high intensity peaks at the cost of a reduced spatial sampling resolution.

Listening tests of the speech signal captured at each spatial sampling resolution [122] bring two observations:

Firstly, regardless of the spatial sampling resolution, the voice captured acoustically by the fibre is artefact free, of high audio quality, roughly comparable to that of a mobile phone communication in terms of bandwidth and of dynamic range. They also confirm the capability of the coherent-MIMO phase sensing approach to mitigate Rayleigh backscattering polarization-fading effects and so to accurately capture complex mechanical signals featuring large bandwidth and high dynamic range.
Secondly, the audio background noise brought by the system is slightly reduced when relaxing the spatial sampling resolution, in line with the visual observation from Figure 4.16(b) [118].

Though the fibre is excited over 0.8m only thanks to the insulated box, the differential phase measured over a 16m segment enclosing the box offers a higher sensitivity than the one measured over a 2m segment. It highlights the importance to calculate the differential phase from highly reflective segments to enhance the SNR, at the cost of a loss in accuracy of the event localisation as discussed in section 3.3.

## Summary: On the way towards an ultra-reliable DAS

The present chapter highlighted how the fibre is sensitive to all mechanical disturbances in its surroundings, even the most complex ones such as speech signals (which also extends to musical ones). We especially demonstrated that it is possible to retrieve this information by means of accurate probing of the fibre sensor, in our case using Coherent-MIMO which advantages were demonstrated in chapter 3: the complete mitigation of polarization fading effects allows to gain over twice the distinction threshold achieved with single-polarization interrogation even with polarization diversity detection (namely SISO and SIMO interrogations).

However, we also pointed the presence of coherent sensing in coherent fibre sensors, which lead to unreliable points along the sensor and degrade the spatial resolution as well as the event detection. It was first introduced with a theoretical description before mentioning simple ways to avoid it in section 3.3, and giving examples of that “lower spatial sampling resolution” in action in section 4.4. Now, we aim at a better understanding of this coherent fading effect and potentially mitigate it without (or with a limited) loss of resources.

# Chapter 5

# Diversity through signal processing to mitigate coherent fading

Coherent phase-sensitive OTDR sensors are subject to three main impairments: polarization fading, coherent fading, and laser phase noise. The latter issue was briefly approached in chapter 1. In chapter 3, we demonstrated that Coherent-MIMO is immune to polarization fading, thus allowing to fully focus on coherent fading in this chapter.

Coherent fading is inherent to coherent $\phi$-OTDR and $\Delta\phi$-OTDR since the technique relies on the speckle pattern resulting from the interrogation of the fibre using a highly coherent source [115]. As a main drawback, the distinction threshold randomly fluctuates along the fibre sensor, and in time if the conditions of the fibre sensor change. This impairment is also referred to as Rayleigh fading, interference fading, signal fading, fading noise or speckle noise, as it exists in various fields of application. In the following, we keep the appellation "coherent fading".

The impact of coherent fading cannot be mitigated thanks to trace averaging when using a high coherence laser, since each optical fibre has its own deterministic speckle signature due to how the density fluctuations got frozen in the silica glass. However, it can be limited by the use of coarse and finer frequency-diversity methods which will be addressed in this chapter, *coarse* referring to optical frequency spacings of the order of the GHz, e.g. using different laser sources or sweeping a single source, and *finer* referring to frequency spacings of the order of the MHz e.g. using a same laser source with specific modulation.

In this chapter, we present an interrogation method that relies on fine frequency-diversity but prior to reaching the optical domain of the interrogator: frequency-multiplexed interrogation codes are digitally generated such that we can obtain independent responses from same segments. The interrogation codes generation and the processing of backscattered traces are developed in a specific case where frequency diversity leads to spatial diversity. Different configurations are experienced, in both model and experimental envi-

ronments.

## 5.1 Electrical bandwidth and fading pattern

### 5.1.1 On the necessity of the fading pattern for $\phi$- and $\Delta\phi$- OTDR

We recall the expression of the backscattered optical field from a fibre sensor probed by a signal $E_{in}$, given in chapter 2 as equation (2.1).

$$E_{rx}(t) = \sum_{m=0}^{M} A_m e^{j\phi_m} e^{-2\alpha z_m + j[\omega_0(t-t_m) - 2\beta z_m]} E_0 \mathrm{rect}(\frac{t-t_m}{T_s})$$

Each $A_m e^{j\phi_m}$ term in (2.1) results from the sum of elementary contributions within the $m^{\text{th}}$ segment in (2.2) below:

$$A_m e^{j\phi_m} = \sum_{i=0}^{N_{scat}} a(z_i) e^{j\varphi(z_i)}$$

In chapter 3, we identified the effects of polarization fading and could mitigate this effect using Coherent-MIMO interrogation. Indeed, the general expression of eq.(2.2) is given in eq.(3.4) as reproduced below:

$$I_m = 2(\vec{\mathbf{e}}_1 \cdot \vec{\mathbf{e}}_2)\, \Re\Big( a(z_1)a(z_2) e^{-j(\varphi(z_1)-\varphi(z_2))} \Big)$$

where $\vec{e_i}$ are the polarization orientations of the different backscattered fields. Now that polarization fading is solved, we simply consider the $\vec{e_i}$ are aligned, yielding eq.(2.2). Since all backscattered fields have the same frequency, coherent fading issues remain:

Coherent fading happens when the summations in (2.2) interfere destructively, resulting in $A_m e^{j\phi_m} \to 0$ locally. These interferences result in a speckled intensity trace at the reception [31]. $\phi$-OTDR and $\Delta\phi$-OTDR techniques rely on the change of interference figure $E_{rx}$ when a vibration occurs: this effect allows to precisely retrieve the phase variation induced by the strain or vibration applied to the fibre. If a vibration occurs, the optical path changes and so does the interference figure, allowing for precise phase measurement within a short time and thus over a high bandwidth, hence coherence effects shouldn't be mitigated using low-coherence sources [63, 124]. They are also the reason why intensity variations due to a perturbation have no linear relationship with that perturbation. Such variations are reported as an issue for OTDR techniques that rely on intensity, or that need high spatial resolution [63, 125], since intensity variations affect locally the sensor response.

Hence, coherent fading mitigation without damage to the phase information is needed. The most interesting method yet is to use multiple uncorrelated channels to probe the line: the channels being either frequency channels [126] or different modes of an optical fibre [127], which in both cases will make the most of uncorrelated backscattered amplitudes

and phases per channel. Therefore, we will adapt the Coherent-MIMO probing technique to solve the coherent fading issue.

### 5.1.2 Conditions for independent patterns: what kind of patterns?

Coarse frequency-diversity methods[1] rely on the dependence of the Rayleigh pattern of a given fibre to the interrogation wavelength, therefore on the independence that exists between the Rayleigh patterns of the same optical fibre that is interrogated at different wavelengths e.g. with a 50GHz wavelength spacing [128, pp. 258–260], thus requiring multiplexing and demultiplexing several optical carriers at the transmitter and receiver. Finer frequency-diversity methods operate within smaller spacing, around hundreds of MHz [126, 129, 130].

There are two main types of frequency-diversity interrogation: multiple pulses with different carriers sent to probe the fibre sensor [131]; single pulses with frequency chirping (linear frequency modulation, LFM) [125], from which the channel response of the fibre sensor is recovered by correlation at the receiver side. In $\phi$-OTDR, the introduction of a chirped pulse method can also allow to perform quantitative strain measurement [65] based on the amplitude of $\phi$-OTDR traces, thus avoiding some of the phase-related impairments. Recent works push forward the sensor optimization as they use a series of frequency-shifted interrogation pulses by combining frequency and polarization multiplexing in $\phi$-OTDR [11, 132], thus injecting more individual pulses that would be allowed by the round-trip time of light in the fibre sensor and increasing the spectral occupancy without any impact on the probing duration. The associated optical set-ups may be complex which make them difficult to deploy for field tests outside the laboratories [133].

Instead, we choose here to tackle coherent fading by exploiting the Rayleigh phase pattern diversity. Our approach involves fully digital Orthogonal Frequency Division Multiplexing (OFDM) of probing codes to achieve carrier phase diversity, allowing for coherent fading mitigation while keeping a simple optical setup.

### 5.1.3 Usage of the electrical bandwidth in fibre interrogation

The electrical bandwidth or modulation bandwidth for fibre sensing is not always explicitly mentioned, except in terms of pulse repetition rate or pulse width. Indeed, when the fibre is used only as a sensor, the available fibre bandwidth is several THz wide and therefore is not a concern. However, if we consider co-propagating sensing signals jointly with telecommunication data, the bandwidth is much more constrained and it must be considered. As an example, the DWDM (Dense Wavelength Division Multiplexing) full C-band is constituted of over 80 slots (channels) of 50GHz each, and every GHz is valuable in today's crowded networks. Thus, a (small) multiple of 50GHz modulation bandwidth would be typically allocated to sensing, such as in [13] where 3 slots (= 150GHz) are allocated to a counter-propagating sensing channel. The bandwidth allocation here depends on the symbol rate or pulse repetition rate which defines, along with the pulse shape, the

[1] This can also be referred to as "wavelength diversity"

occupied electrical bandwidth, but also and more importantly on the interrogator peak power which should not induce non-linear interference with data channels. In [13], the sampling rate is of 125MHz ($\ll$ 150GHz) for 40ns probing pulses.

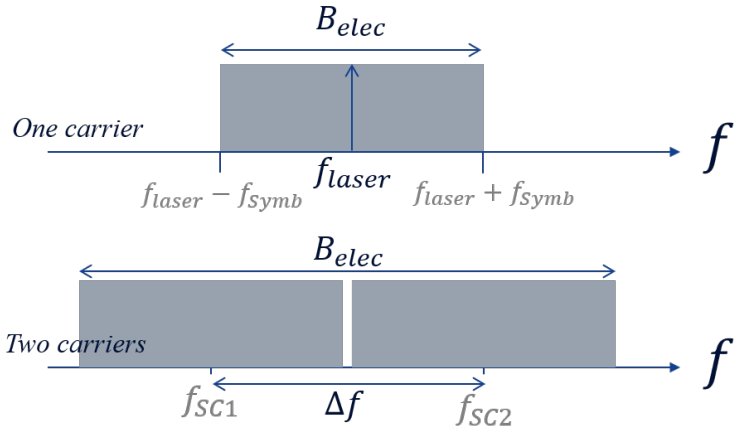


Figure 5.1: Outline schematic of the occupied spectrum in single-carrier and multi-carrier interrogation, with phase independence criteria verified (statistical independence of backscattered patterns)

We observe that an electrical bandwidth $B_{elec}$ around 100MHz, fixed by the symbol rate $f_{Symb}$ and by the pulse shaping[2], is usually enough to sense a fibre with a spatial sampling resolution of the order of the metre. Over such a narrow bandwidth, the elementary scatterers have a flat amplitude spectrum response, and wavelength diversity cannot be achieved. However, to reach statistically independent intensity fading, the fibre should be probed with signals separated by $\Delta f \geq f_{Symb}$ [126, 130, 134] where $f_{Symb} = 1/T_S$. This is illustrated in Figure 5.1 (without consideration for the pulse shape). Therefore, we introduce an OFDM scheme to independently probe the line over several orthogonal subcarriers, verifying $\Delta f = f_{Symb}$ (lower bound for the independence condition) inside the electrical bandwidth $B_{elec}$.

## 5.2 Getting independent responses from the same segment: a digital multi-carrier interrogation scheme

### 5.2.1 Orthogonal Frequency Division Multiplexing

The dual-polarization codes $\mathbf{E}_{in} = \left[\begin{smallmatrix} E_x \\ E_y \end{smallmatrix}\right]$ of length $N_{code}$ symbols, defined in subsection 1.2.4 for single-carrier Coherent-MIMO sensing, are mapped onto $N_{sc}$ subcarriers. The OFDM signal is created by serial-to-parallel, inverse Fast Fourier Transform (iFFT), and parallel-to-serial operations. The iFFT is performed as follows: for a vector $Y$ of length $N$, the elements of vector $X = \text{iFFT}(Y)$ verify, for $i \in [1, N]$:

$$X(i) = \frac{1}{N} \sum_{k=1}^{N} Y(k)\, W_N^{-(i-1)(k-1)} \tag{5.1}$$

[2]In this work, rectangular symbols are sent in the time domain yielding a `sinc` function spectrally, in that case we verify $B_{elec} = 2f_{Symb}$ considering the main lobe of the cardinal sine.

where $W_N = e^{-j2\pi/N}$ are the $N$ roots of unity.

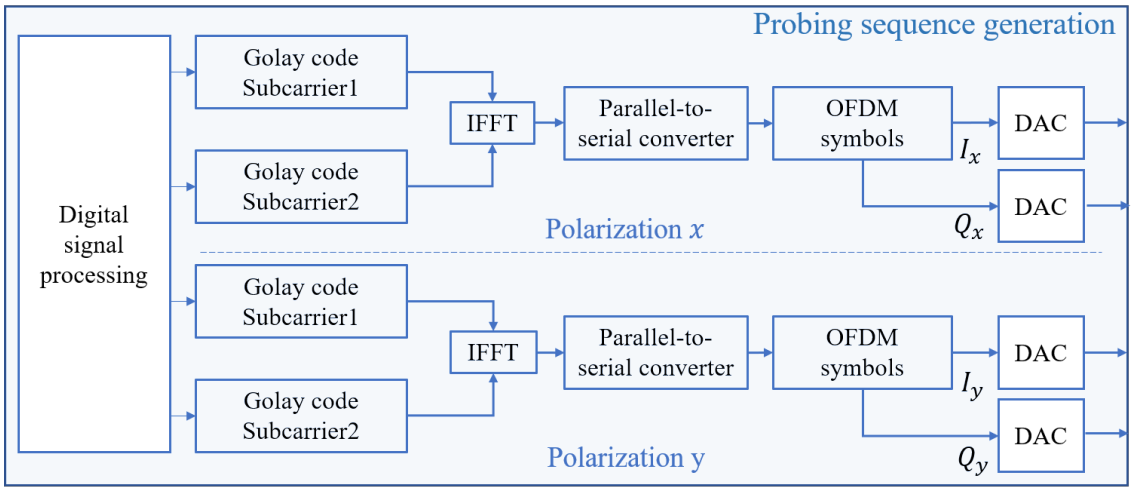


Figure 5.2: MIMO-OFDM signal processing at the transmitter side up to digital-to-analogue conversion (by means of Digital-to-Analogue Converters, DAC) and modulation, two-subcarriers example

Figure 5.2 displays the general block-diagram of the signal processing at the transmitter side, before digital-to-analog conversion through an Arbitrary Waveform Generator (AWG), independent of the optical setup design. The example is given for 2 subcarriers but can be extended to an arbitrary number of subcarriers, as long as $N_{sc} = 2^k$ where $k$ is an integer.

Similarly, Figure 5.3 gives the general block-diagram of the signal processing at the receiver side after coherent detection and analogue-to-digital conversion (by means of Analogue-to-Digital Converters, ADC).

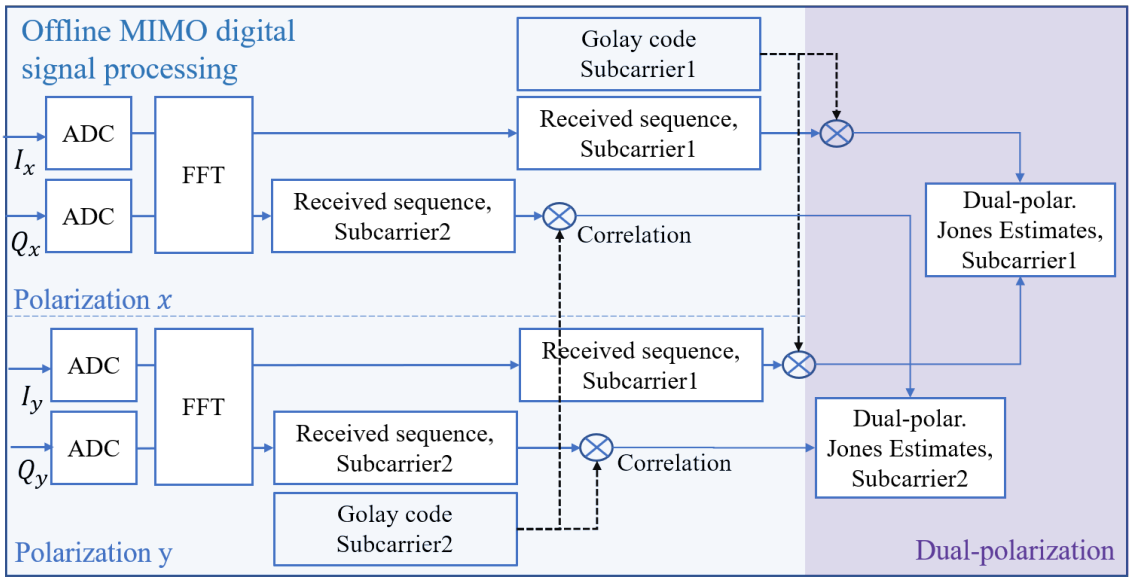


Figure 5.3: MIMO-OFDM signal processing at the receiver, from analogue-to-digital conversion after coherent detection, two-subcarriers example

At the transmitter side, the dual-polarization (MIMO) bipolar codes are generated and duplicated (multiplied up to the desired number of carriers), then combined through iFFT

into a flow of OFDM symbols intended to modulate the probing laser. This step is performed offline as the single-carrier code is determined by its desired length and the iFFT can be tabulated, which is less resource-consuming. At the receiver, the received symbols are redistributed into subcarriers through a Fast Fourier Transform (FFT) step, before correlation with the transmitted probing codes so that the dual-polarization channel estimation by each subcarrier is retrieved (correlation stage is applied to each subcarrier separately) to obtain Jones matrices estimations of the full fibre on each frequency band.

**Considerations on the general case of OFDM interrogation** In the general case, different binary codes could be loaded into each subcarriers. Since the codes have their values in a {-1,1} alphabet, the OFDM alphabet after iFFT is simplified, following the expression (5.1): having $Y(k) = \pm 1$, the $X(i)$ become linear combinations of the $N_{sc}$ roots of unity, divided by $N_{sc}$. Sending several different codes at the transmitter would require a precise tuning of the modulator for fibre sensor interrogation.

In case of dual-polarization coded interrogation, we have seen in subsection 1.2.4 that the codes are sent continuously to probe the fibre sensor. Therefore, it is possible to map codes of different lengths into the presented OFDM multi-carrier scheme. Multiplexing codes with same length would lead to several estimations of same fibre segments on a same mechanical bandwidth, whereas multiplexing codes with different lengths could allow to probe simultaneously on several mechanical bandwidths.

**A special case of OFDM interrogation for channel estimation** For sake of simplicity, we limit ourselves to the case where all $N_{sc}$ subcarriers enclose the same code. Contrary to data transmission, where the purpose is to maximize the fibre capacity, here we aim at channel estimation, so probing a low number (typically 2 or 4 in practice) of sub-carriers with the same codes is not a major concern and makes the implementation easier. Figure 5.4 shows a simple example for one polarization axis and two subcarriers, $N_{sc} = 2$. The subcarriers carry the same code $\{G_{a1}, G_{b1}\}$ for $N_{code} = 8$.

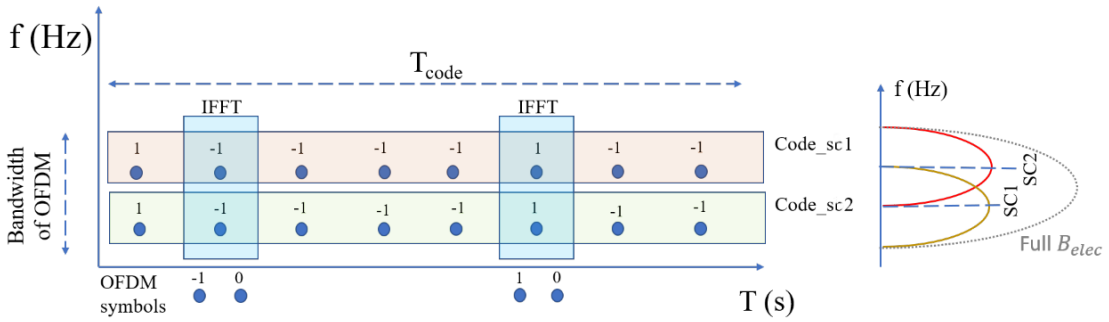


Figure 5.4: OFDM combination for two subcarriers SC1 and SC2, one code duration, one polarization

Following iFFT($\{\pm 1, \pm 1\}$) = $\{\pm 1, 0\}$ and more generally:

$$\text{iFFT}(\{1, \cdots 1\}) = \{1, 0 \cdots 0\} \quad \text{and} \quad \text{iFFT}(\{-1, \cdots -1\}) = \{-1, 0 \cdots 0\}$$

the OFDM code alphabet is now limited to {-1,0,1}. A constant mechanical bandwidth $B_{meca}$ (by keeping the time duration of the probing codes constant) is maintained for fair comparison between the different sensor interrogation methods.

There is an interdependence of the full electrical bandwidth $B_{elec} = 2f_{Symb}$, number of subcarriers $N_{sc}$, and spatial resolution $L_s$ following:

$$L_s = \frac{c_{fibre} N_{sc}}{2 f_{Symb}} \tag{5.2}$$

hence a symbol rate per carrier $f_{Symb,OFDM} = \frac{f_{Symb}}{N_{sc}}$.
Moreover, we define the gauge length $G$ of the interrogation system as a function of the sole full baudrate $f_{Symb}$:

$$G = \frac{c_{fibre}}{2 f_{Symb}} \tag{5.3}$$

- If we choose to maintain a constant $B_{elec}$: the spatial resolution of the sensor is $L_s = \frac{c_{fibre}}{2.f_{Symb,OFDM}}$, resulting in $L_s$ being degraded by $N_{sc}$ times compared to a single-carrier scheme. Constant $B_{elec}$ yields a constant gauge length $G$ .

- Otherwise, keeping a constant electrical bandwidth per subcarrier: $B_{elec}$ increasing by $N_{sc}$ times thus expanding the electrical bandwidth when the symbol rate per subcarrier $f_{Symb,OFDM}$ is left unchanged, to keep a constant spatial resolution.

In the particular configuration using the same code over the $N_{sc}$ subcarriers, the OFDM interrogation amounts to performing an interrogation of the fibre sensor with a $N_{sc}$-fold expanded version of the original code (done by inserting $N_{sc} - 1$ zeros between symbols[3]). Such a configuration maximizes the Peak-to-Average Power Ratio (PAPR)[4] of the interrogation signal compared with other generic OFDM implementations, since the mean input power is kept constant and therefore it will end up being concentrated into the non-zero symbols as displayed in Figure 5.5.

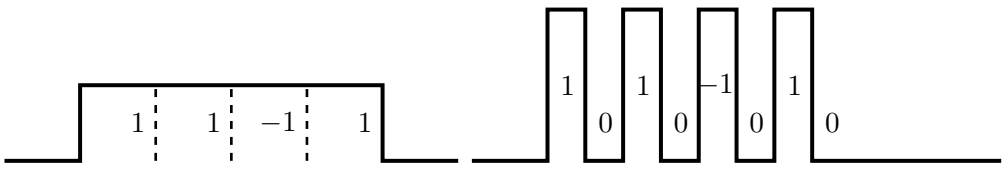


(a) $N_{sc} = 1$ with 4 symbols (b) $N_{sc} = 2$ with 4 OFDM symbols, 8 symbols

Figure 5.5: N-fold expanded BPSK code: $N_{sc} = 1, 2$ examples

Yet, such PAPR is still negligible compared with pulsed interrogation as the power is still spread in time over multiple (OFDM) symbols, thus limiting any nonlinearity-related issues. Furthermore, the OFDM formalism is especially suitable for the linear combination of the backscattered signals at the receiver side through the demultiplexing of the carriers by means of an FFT operation.

[3]The detail of same-code OFDM codes is derived in Appendix B
[4]Or "extinction ratio"

### 5.2.2 Nyquist-shaped digital multicarrier multiplexing

An alternative way to generate multiple frequency interrogation is by means of Frequency Division Multiplexing. Here, we use also dual polarization codes. The first band is generated by duplicating the code such that it occupies $1/N_{sc}$ of the full desired spectrum $B_{elec}$. It is then shaped using a Root Raised Cosine (RRC) filter with desired roll-off factor. Several codes could be generated, yet here we stay in the simplified case where all subcarriers will be loaded with the same code. Therefore, the next subcarriers are simply replications of the first band, then frequency shifted with a multiple of $1/N_{sc}$.

Unlike OFDM for which $N_{sc} = 2^k$ with $k$ integer, here the number of subcarriers can be any integer, provided the frequency shift of each band is enough so that they don't overlap, and at a cost of a possible worse spectral efficiency. At the reception, each spectral band is filtered and then processed separately, similarly to OFDM processing, to obtain Jones matrices estimations of the full fibre on each frequency band.

The implementation of such a method can be complex, what's more the performance of this multicarrier multiplexing technique is slightly worse than OFDM, including because of modulator tuning constraints.

## 5.3 Combination of multiple subcarriers

MIMO-OFDM interrogation yields Jones matrices responses for each time instant $t$, segment at distance $d$ and subcarrier index $n$: $\mathbf{H}_{t,d,n}$. More precisely, we have $N_{sc}$ estimations for $\mathbf{H}_{t,d}$ compared with single-carrier MIMO. The next step is to take advantage of these independent estimations to tackle the coherent fading issue, by either selecting the best estimation per time instant $t$ and fibre distance $d$, or by thoughtfully combining them. Indeed, a simple summation is not a viable option, as depicted in Figure 5.6(a).

The backscattered SOP (b-SOP, evolution of the energy on the four terms of the Jones matrix) is expected to be common to all subcarriers at any time and distance, thus it is not involved in the combination of subcarrier information. The independent phase and amplitude information is therefore enclosed in the sole Jones matrices determinants $\det(\mathbf{H}_{t,d,n})$ from which the local cumulated phase is extracted as $\phi_{t,d,n} = \frac{1}{2}\angle\det(\mathbf{H}_{t,d,n})$, and the reliability metric derived from the backscattered intensity as $R_{t,d,n} = |\det(\mathbf{H}_{t,d,n})|$, as defined in section 3.3. Consequently, we choose to constructively combine the subcarriers responses from their respective Jones matrix determinants $\det(\mathbf{H}_{t,d,n})$.

The rotated-vector-sum combination method is applied to the $D_{t,d,n} = \det(\mathbf{H}_{t,d,n})$ vectors, so as to maximize the combined modulus [125]. For a given segment index $d$, the time-average of phase $\overline{\phi}_{d,n}$ is derived for each subcarrier $n$ and subtracted from the phase of all $D_{t,d,n}$, as depicted in Figure 5.6(b).
The resulting combined determinants are:

$$D_{t,d,combined} = \sum_{n=1}^{N_{sc}} \frac{D_{t,d,n}}{\exp(j\overline{\phi}_{d,n})} \tag{5.4}$$

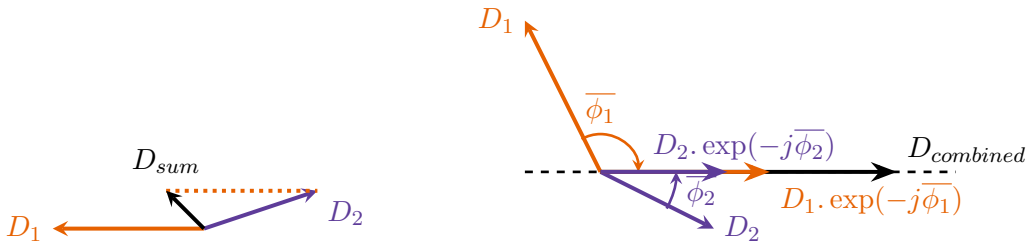


(a) Summation of complex vectors

(b) Rotated-vector-sum method

Figure 5.6: Schematic description of the Rotated Vector-Sum (RVS) operation, $N_{sc} = 2$

The final differential phase between adjacent segments is obtained by subtracting the phases of adjacent $D_{t,d,combined}$, such that $\Delta\varphi_{t,d,combined} = \frac{1}{2}(\angle D_{t,d,combined} - \angle D_{t,d-1,combined})$.

The operation in (5.4) consists in removing the average[5] cumulated phase values $\overline{\phi}_{d,n}$ and keeping the sole variations of the cumulated phase in time, per segment, since the relevant information is enclosed in the differential phases eventually.

- On the one hand, if the fibre segment is static (no mechanical perturbation), then the random variations of phase around the $\overline{\phi}_{d,n}$ are independent and they will fade after combination.
- On the other hand, if the fibre segment is mechanically excited, then all subcarriers are affected the same way such that their oscillations around the phase references $\overline{\phi}_{d,n}$ align, so magnifying the overall captured excitation.

Moreover, section 3.3 did show that $R_{t,d,n} = |D_{t,d,n}|$ is not only the most accurate intensity estimator in MIMO sensing up to our knowledge but also a reliability criterion that informs about the ability to extract a fair phase estimation from any Jones matrix. Therefore, the combination in equation (5.4) is naturally weighted by the reliability metric[6] $R_{t,d,n}$, hence a lower influence of the unreliable estimations on the final result.

### 5.3.1 Individual subcarriers and their combination

To detect mechanical events along the sensor, the differential phase standard deviation (denoted $\sigma_\varphi$, expressed in radians) is monitored along distance: theoretically zero-valued in absence of events, and non-zero positive in case of any detected disturbance.

The $\sigma_\varphi$ from static measurements indicates the distinction threshold below which an event cannot be detected. Also, the reliability metric $R_{t,d,n}$ (or normalized $\overline{R}_{t,d,n}$) gives a priori information on the soundness of the estimation, as defined in section 3.3. Its minimum value in time per segment index $d$ gives an indication on the probability to get local unstable phases estimations giving rise to false alarms.

We simulate a 4-subcarrier OFDM interrogation of a static 1km long Single Mode Fibre (SMF), with laser noise $\Delta\nu = 75$Hz and Additive White Gaussian Noise (AWGN)

[5] Averaged over a certain time window, namely several seconds or tens of seconds. In the following experiments, the time window is the full measurement duration

[6] Or equivalently, by the normalized reliability metric $\overline{R}_{t,d,n} = R_{t,d,n}/\max_{t,d,n}(R_{t,d,n})$.

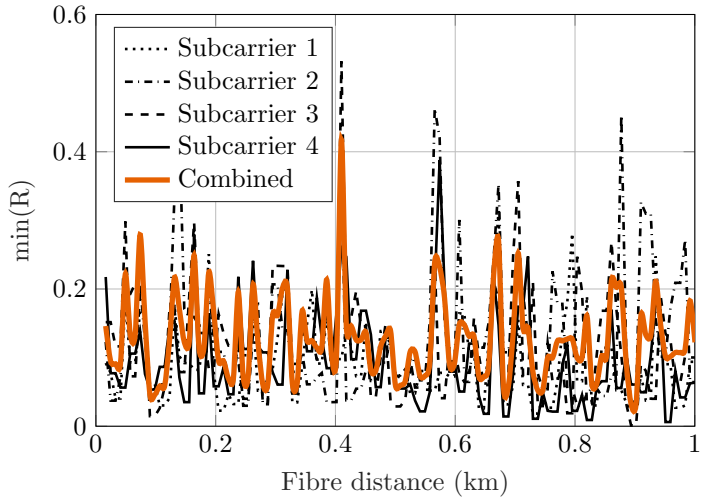


(a) Reliability metric along distance

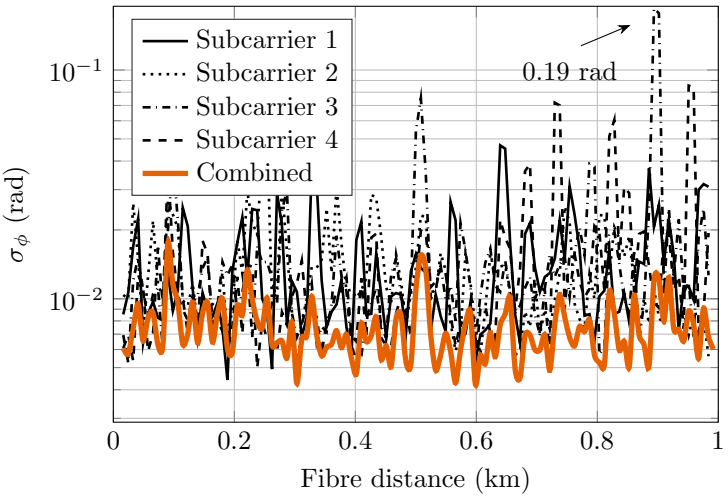


(b) $\sigma_\varphi$ along fibre distance

Figure 5.7: Simulation OFDM4, 1km SMF, $\Delta\nu = 75$Hz, AWGN at the receiver, individual subcarrier responses compared with combined response

at the receiver (shot noise and thermal noise), we set $B_{meca} = 760$Hz and $B_{elec} = 100$MHz ($f_{Symb} = 50$MBaud). The fibre is kept short such that the attenuation with distance does not participate to the fading effect, thus focusing the study on the sole coherent fading effect. Every separate subcarrier is monitored, alongside with the subcarrier combination. Figure 5.7 illustrates the enhancement brought by an OFDM interrogation.

Figure 5.7(a) gives the minimum reliability metric per segment versus distance, and shows that the reliability increases after subcarrier combination compared with individual subcarriers where it locally dives towards 0. In other words, the worst case points are avoided, to the detriment of the best ones. Yet, we remind that the low-reliability (low backscattered intensity) points are statistically the ones that trigger phase artefacts or "false alarms", whereas the distinction between medium reliability and very high reliability points is not relevant when it comes to phase: the estimations remain stable. Therefore, decreasing the level of the highest reliability points has negligible impact on the phase distinction threshold.

Figure 5.7(b) shows $\sigma_\varphi$ along distance, giving the noise floor above which a mechanical event can be detected. The combined measurement presents a noise floor below 0.017rad all along the 1km fibre, which is locally up to 10 times lower than the level given by a single subcarrier (subcarrier 3, around 850m, pointed by the arrow in Figure 5.7(b)).

Notice that the combined $\sigma_\varphi$ in Figure 5.7(b) reaches values that are even lower than the lowest $\sigma_\varphi$ per subcarrier at several locations (300m, 500m, 880m). **This shows that in addition to avoiding the worst-case distinction threshold situations, the OFDM combination scheme performs an averaging on the system noise and thus significantly enhances the overall distinction threshold.**

### 5.3.2 Impact of noises and OFDM contribution

The distinction threshold gain through OFDM is investigated first by simulation: the interrogations of a static, 1km long SMF are simulated. Single-carrier, OFDM with 2 subcarriers and OFDM with 4 subcarriers interrogations are performed. The mechanical bandwidth is fixed to $B_{meca} = 760$Hz for all of the following measurements and simulations. We recall the intensity and sensitivity metrics defined in section 3.2 by equations (3.6) and (3.7) respectively:

$$\text{Intensity}_{dB} = 10\log_{10}(|\det(\mathbf{H})|)$$

$$\text{SNR}_{\varphi,\text{dB}} = 10\log_{10}(1/\sigma_\varphi^2)$$

$$\text{SNR}_{\varepsilon,\text{dB}} = 10\log_{10}(1/\sigma_\varepsilon^2) = 20\log_{10}(\frac{4\pi n\xi G}{\lambda\sigma_\varphi})$$

In the following, the Probability Density Function (PDF) distributions of $\sigma_\varepsilon$ and $\text{Intensity}_{dB}$ will be studied. The relation between $\sigma_\varphi$ along distance and its PDF distribution is displayed in Figure 5.8 below.

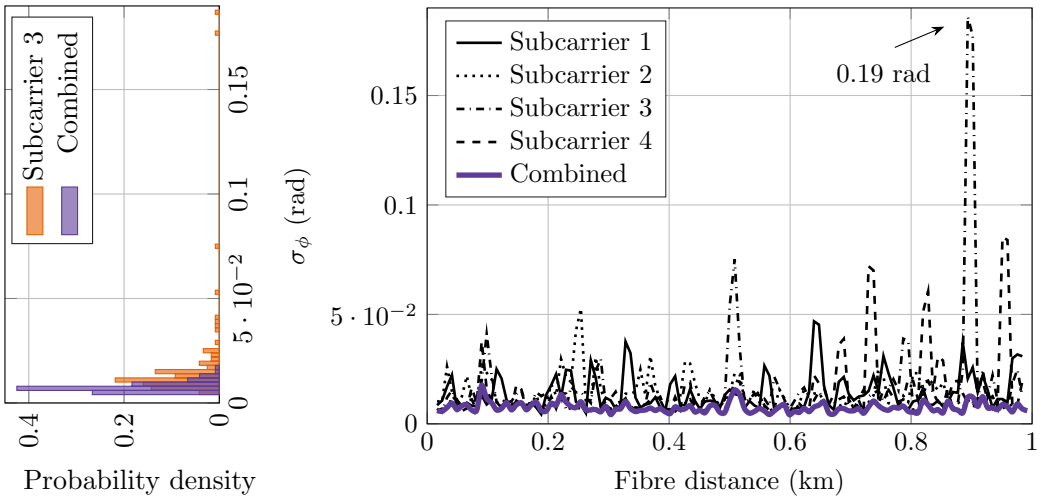


Figure 5.8: Probability density function of $\sigma_\varphi$ values: subcarrier and combination

We notice that the highest values of $\sigma_\varphi$ spread on a wide range, therefore for easier readability, the distribution of $\text{SNR}_{\varphi,\text{dB}}$ and $\text{SNR}_{\varepsilon,\text{dB}}$ will be studied: problematic values

appear on the left side of the distribution.

In this study, two spectral occupation cases are considered and pictured in Figure 5.9:

1. The exploited $B_{elec}$ is kept constant $B_{elec} = 100$MHz in which case the spatial resolution decreases with the number of OFDM carriers according to $L_s = c_{fibre}/(2f_{Symb,carr})$ where $f_{Symb,carr} = f_{Symb}/N_{sc} = B_{elec}/2N_{sc}$
2. The spatial resolution is kept constant with $f_{Symb,OFDM} = 50$MBaud yielding $L_s = 2.05$m, in which case the total interrogation electrical bandwidth changes according to $B_{elec} = 2f_{Symb} = 2f_{Symb,OFDM} \times N_{sc}$

Therefore, we have either $G = 2.05$m for constant $f_{Symb} = 50$MBaud, or $G = 2.05/N_{sc}$ m in constant spatial sampling resolution case following the gauge length definition in (5.3).

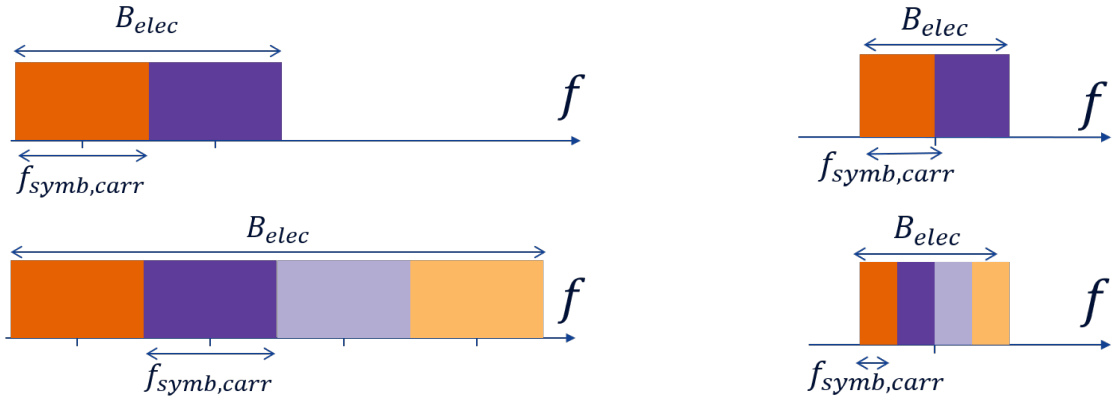


(a) Constant $L_s$ (b) Constant $B_{elec}$

Figure 5.9: Schematic for comparison of the two spectral occupation cases, for two- and four-subcarriers cases

Simulations are conducted on an important number of fibre drawings to quantify the impact of subcarrier combination on the distribution of intensity and phase.

**White noise only, constant $B_{elec}$** Simulation results with AWGN contributions at amplification and detection stages are displayed in Figure 5.10, for constant $B_{elec}$ case.

The observed probability density functions verify a shrinking of the distributions as the number of subcarriers increases, especially the amount of points present in the left part of the distribution which are the most likely to trigger false alarms decreases.

**White noise only, constant $L_s$** In Figure 5.11, the same simulations are conducted but with a varying $B_{elec}$ such that the spatial sampling resolution stays constant.

The observed PDF is similar for the intensity, as we see how the distribution shrinks as the number of subcarriers increases. However, having increased the full $B_{elec}$ and thus decreased the gauge length, a decrease of the $\text{SNR}_\varepsilon$ is noticed in Figure 5.11(b) compared to Figure 5.10(b): though the distributions shrink, their mean value slides towards lower $\text{SNR}_\varepsilon$ values. The reason for that increase is twofold:

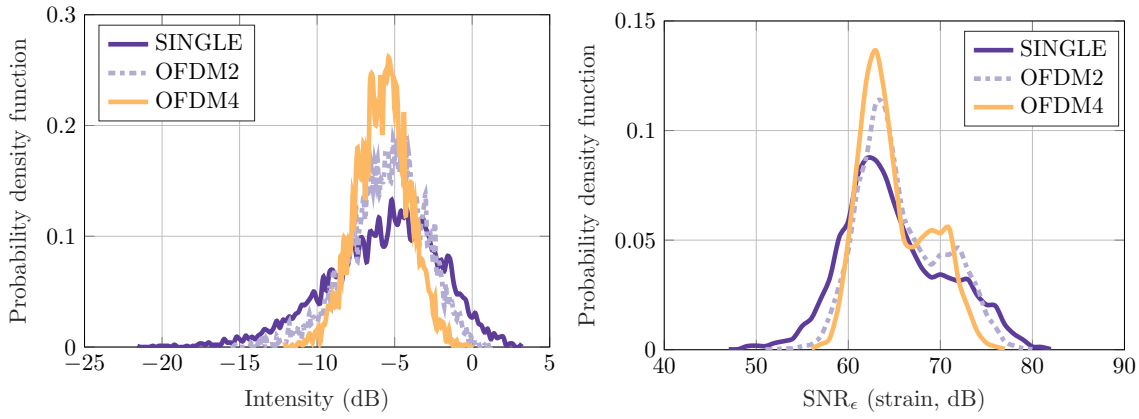


(a) Intensity$_{dB}$ (b) SNR$_\varepsilon$

Figure 5.10: Intensity$_{dB}$ and SNR$_\varepsilon$ probability density functions, constant $B_{elec}$. 1km static simulation, AWGN at the receiver, no phase noise

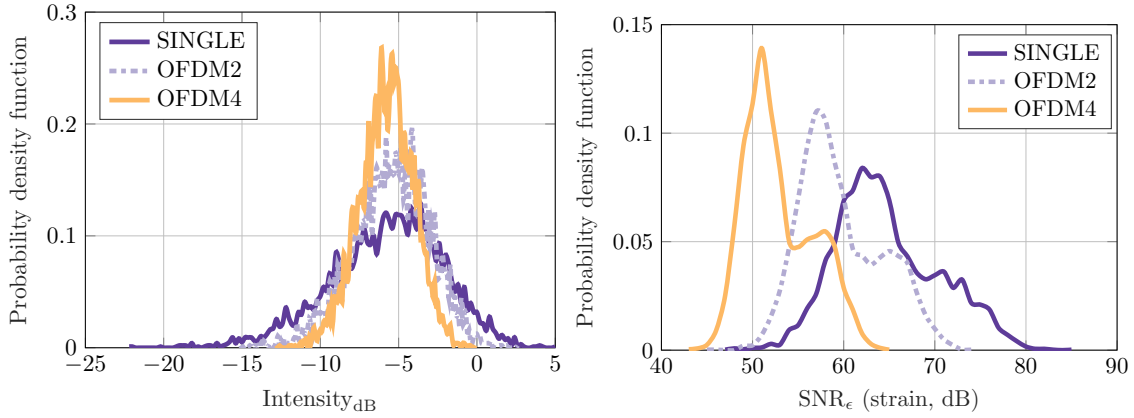


(a) Intensity (b) SNR strain

Figure 5.11: Intensity$_{dB}$ and SNR$_\varepsilon$ probability density functions, constant $L_s$. 1km static simulation, AWGN at the receiver, no phase noise

1. Having a wider overall $B_{elec}$ integrates more AWGN over the interrogation
2. The strain noise floor per subcarrier did not change compared to single-carrier, however the gauge length to which the strain applies got smaller as the fibre is probed by shorter temporal symbols, yielding a stronger noise per distance unit. This is described below:

The SNR$_\varphi$ is obtained per segment, namely the backscattered phase variations per "spatial resolution" $L_s$, which is constant in the present case.
Looking at the SNR$_\varphi$ distribution in Figure 5.12 corresponding to the strain distribution of Figure 5.11(b), the worst phase noise level per gauge length improved as the number of subcarriers increased: +12dB from 1 to 4 carriers (pointed by the arrows in Figure 5.12). Yet, the gauge length of the interrogation system follows $G = 2.05/N_{sc}$ so it was also divided by 4, from $G = 2.05$m to $G = 0.51$m to reach 4-subcarrier interrogation while keeping an overall spatial sampling resolution $L_s = 2.05$m.

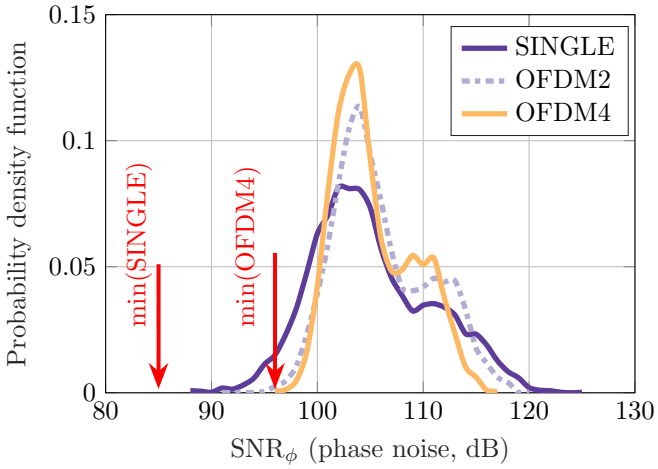


Figure 5.12: SNR$_\varphi$ probability density function distributions, per fibre segment, constant $L_s$ case. 1km static simulation, AWGN at the receiver, no phase noise

Therefore, even though the sensitivity per segment is enhanced, the sensitivity per meter (or per gauge length) did not benefit from the combination with comparable scale.

**White noise and laser phase noise** Secondly, laser phase noise is added. The narrow-linewidth laser used for the following experimental measurements has a linewidth estimated to $\Delta\nu = 75$Hz for low frequencies (see chapter 2). In the simulation, its phase noise is modelled as a Wiener process of variance $\sigma^2 = 2\pi\Delta\nu T_S$ where $\Delta\nu$ is the Lorentzian laser linewidth and $T_S$ the duration of a symbol in the interrogation codes.

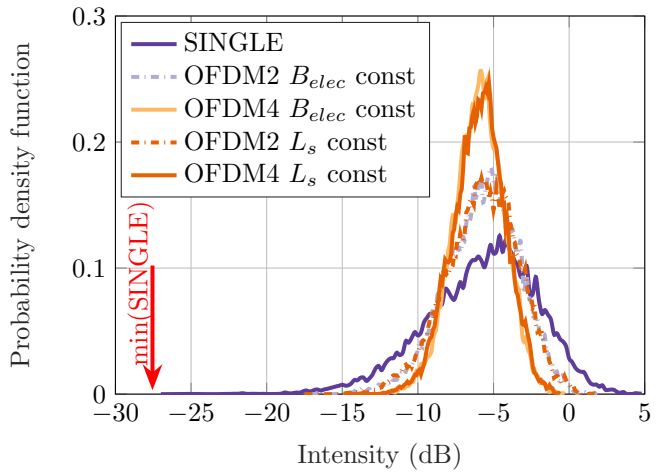


Figure 5.13: Backscattered intensity probability density distributions. 1km static simulation, AWGN at the receiver, laser phase noise $\Delta\nu = 75$Hz

Figure 5.13 shows the Intensity$_{dB}$ distributions in constant $B_{elec}$ and constant $L_s$ cases, for 1 to 4 subcarriers. As for white noise only (above), the electrical bandwidth has no impact on the intensity distributions, since the sole increase of subcarriers and constructive combination shrinks the intensity distributions.

Now, Figure 5.14 displays the SNR$_\varepsilon$ simulation results in presence of white noise and laser phase noise. In Figure 5.14(a), the SNR$_\varepsilon$ behaves as in Figure 5.10(b) (no phase noise case) where the distributions shrink as the number of subcarriers increase, keeping roughly

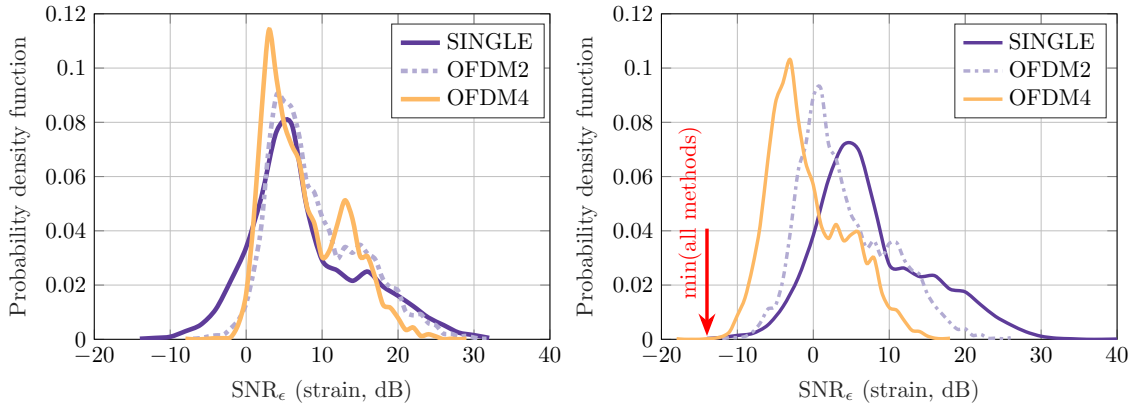


(a) Constant $B_{elec}$ case

(b) Constant $L_s$ case

Figure 5.14: SNR$_\varepsilon$ probability density distributions. 1km static simulation, AWGN at the receiver, laser phase noise $\Delta\nu = 75$Hz

the same mean value while the worst case moves forward ; whereas Figure 5.14(b) shows clearly that the mean value of the SNR$_\varepsilon$ distribution decreases as the number of subcarriers increases. However, if the distributions were shifted of several dB in Figure 5.11(b), here in the presence of laser phase noise the worse case point remains around −10dB strain (as pointed by the arrow in Figure 5.11(b)). Subcarrier interrogation and combination looks more efficient in presence of laser phase noise in the constant $L_s$ case. Yet, the sensitivity increase per segment was still not enough to bring significant improvement per meter.

Simulations demonstrated the interest of using several subcarriers for interrogation in constant $B_{elec}$ case as it results in an improvement of the sensitivity of the interrogator system from 2 subcarriers with an improvement of the worst case sensitivity of almost 8dB with 2 subcarriers and 12dB with 4 subcarriers compared with single-carrier, in the presence of laser noise and AWGN.

In case of constant $L_s$ however, despite the advantage of interrogating on several subcarriers and constructively combining, doubling or quadrupling the electrical bandwidth led to much smaller gauge length. Therefore, the advantage per segment did not turn into an advantage per metre regarding the distinction threshold.

**Is it useful to increase the number of carriers?** Although a higher number of subcarriers can be used for channel interrogation, the sensitivity gain tends to decrease after a certain number of carriers, under the fixed constraints of equivalent electrical and mechanical bandwidths. Figure 5.15 shows the evolution of the SNR$_{\varepsilon,dB}$ PDF when the number of subcarriers increases in the particular case of $B_{elec} = 100$MHz on a 1km simulated distance. After interrogation on 4 subcarriers, an increase of carriers does not bring a significant sensitivity gain (lower mean sensitivity in Figure 5.15(b) with 8 subcarriers); this is due to the use of a decreasing code order (smaller $N_{code}$) when increasing the number of subcarriers, which results in a lower achieved SNR [58].

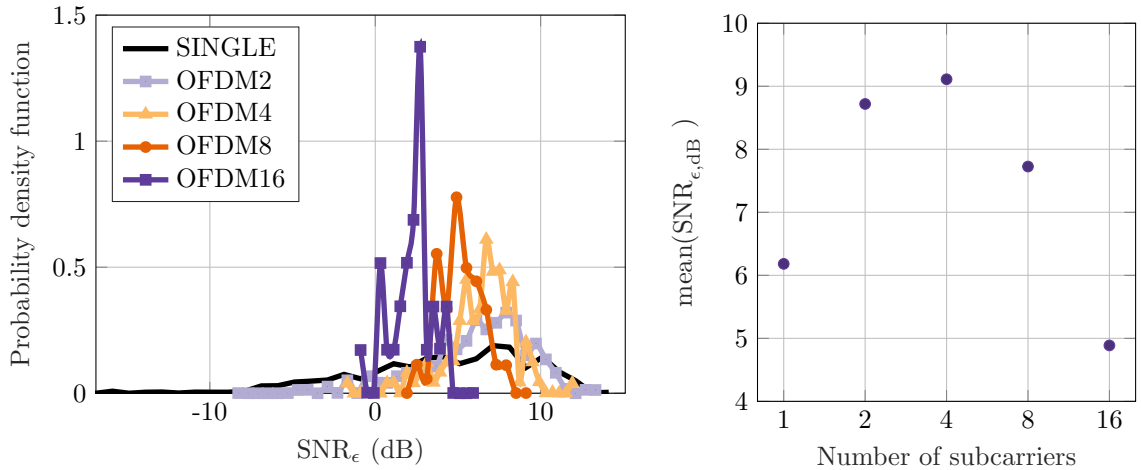


(a) Probability density function

(b) Mean value

Figure 5.15: SNR$_{\epsilon,dB}$ on 1km, for 1 to 16 subcarriers, simulation with 5000 points per interrogation method, $\Delta\nu = 75$Hz and AWGN noise at the receiver

### 5.3.3 Experimental results

The interrogating setup presented in Figure 5.16 is based on our previously introduced Coherent-MIMO interrogation setup: the probing codes are sent onto two orthogonal polarization axis through a dual-polarization 25GHZ electro-optical 3dB bandwidth I/Q Mach-Zehnder modulator to modulate the optical wavelength. Although Figure 5.16 shows the general I/Q configuration, we restrict ourselves to a BPSK or $\{-1, 0, 1\}$ modulation per polarization in this work, as described previously in subsubsection 1.2.4.2.

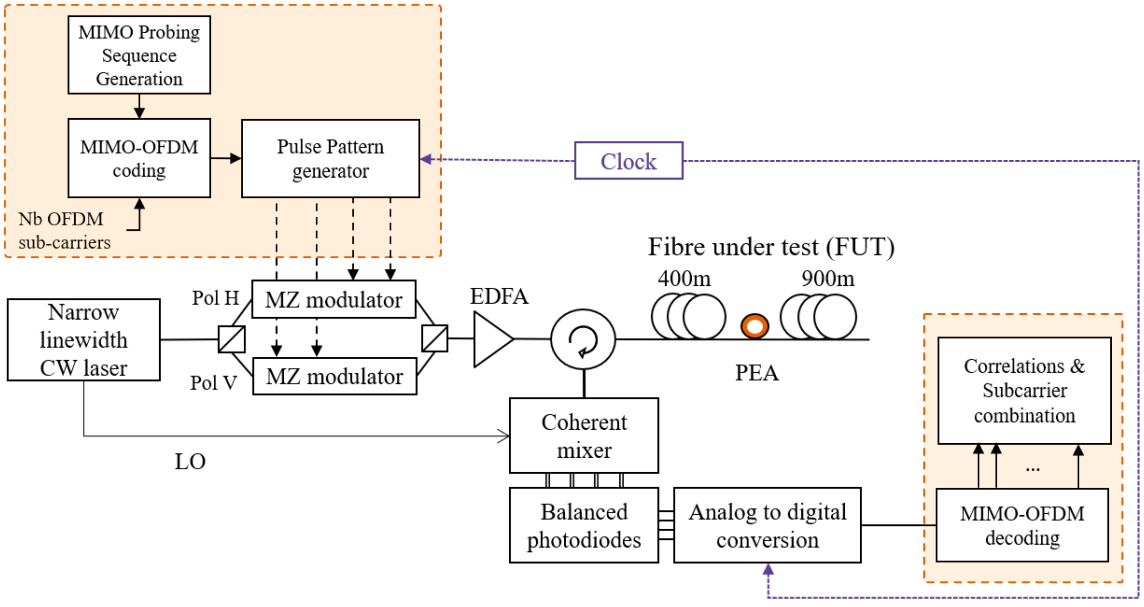


Figure 5.16: OFDM-MIMO interrogation setup. EDFA: Erbium Doped Fibre Amplifier, MZ: Mach-Zehnder, MIMO: Multiple-Input/Multiple-Output, OFDM: Orthogonal Frequency Division Multiplexing, LO: Local Oscillator, PEA: PiezoElectric Actuator, Pol.: Polarization

OFDM sensing is permitted by placing processing blocks before and after the optical setup, namely a MIMO-OFDM coding block at the codes generation stage and a MIMO-OFDM decoding block after coherent reception and analog-to-digital conversion which contents

were previously detailed in Figure 5.3. The core optical setup of the interogator is therefore unchanged.

#### 5.3.3.1 Static experiments: noise floor level

Static experiments are first conducted in laboratory conditions, in a mechanically insulated environment[7]. The Fibre Under Test (FUT) in Figure 5.16 consists in a 1300m long Standard Single Mode Fibre (SSMF) made of the junction of a 400m SSMF spool with an other 900m fibre spool. Similarly to the simulations in subsection 5.3.2, two cases are considered, namely "constant electrical bandwidth" with $B_{elec} = 100$MHz and "constant spatial resolution" with $L_s = 2.05$m. The mechanical bandwidth is also kept at $B_{meca} = 760$Hz, and the frequencies below 60Hz are filtered out to avoid capturing the noise of electrical equipment in the lab.

**Constant $B_{elec}$:** The first measurements are successively single-carrier, OFDM2 and OFDM4 2-seconds interrogations of the same fibre with $f_{Symb} = 50$MBaud, yielding spatial resolutions of 2.05m, 4.10m and 8.20m respectively. The length of the probing code is $N_{code} = 32768$ symbols for single carrier interrogation, $N_{code} = N_{code,single}/N_{sc}$ for OFDM interrogations, such that $T_{code} = 655\mu s$ yielding an overall constant mechanical bandwidth $B_{meca} = 760$Hz.

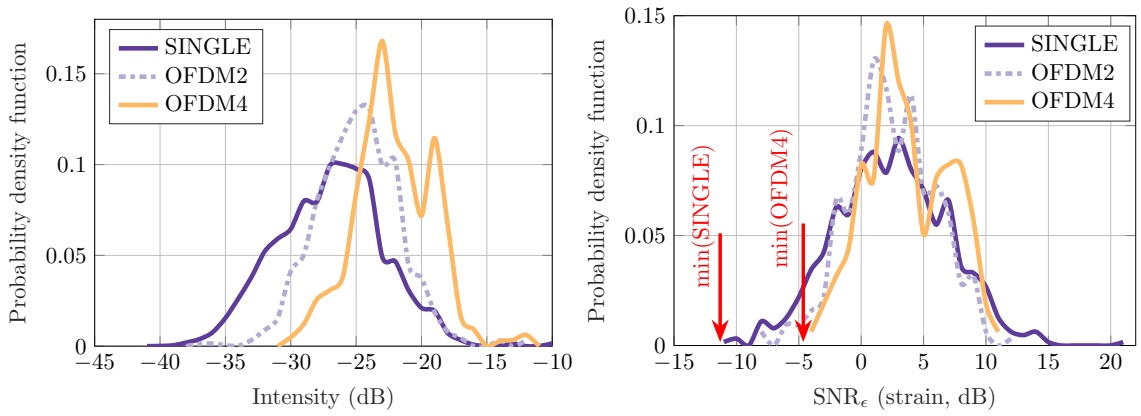


(a) Intensity$_{dB}$ distribution

(b) SNR$_\varepsilon$ distribution

Figure 5.17: Static experimental trace, OFDM interrogation of 1.3km SSMF, constant $B_{elec} = 100$MHz configuration

The performance of these interrogations is displayed in Figure 5.17. As opposed to the simulation, it is noticed that the combination of intensities from several subcarriers leads to a growing overall |det| when the number of subarriers increases, in addition to the shrinking of Intensity$_{dB}$ distributions already observed in Figure 5.14(a). This could be due to the applied normalization at the reception: we normalize each trace with a division by the highest reflected intensity, therefore changing the mean intensity from trace to trace. Meanwhile, the distribution of SNR$_\varepsilon$ values behaves as predicted in Figure 5.14(b)

[7]Soundproofing or "mechanical insulation" of a box means that foam-like materials have been placed on the inside of the box such that external environmental perturbations are sufficiently damped to avoid affecting the fibre.

as the distribution shrinks when increasing the subcarriers number, without any significant change regarding the mean value of the distributions. **The worst case SNR$_\varepsilon$ improves by over 6dB when comparing single-carrier interrogation to OFDM4.**

**Constant $L_s$** Next, successive measurements of 2 seconds each are performed, this time with $B_{elec}$ = 100MHz, 200MHz, 400MHz for single-carrier, OFDM2 and OFDM4 interrogations respectively, therefore $f_{Symb,carr}$ = 50MBaud in all cases yielding a constant spatial resolution $L_s$ = 2.05m. We remind that as a consequence, the gauge length $G$ decreases following $G = \frac{c_{fibre}}{2 f_{Symb,carr} N_{sc}}$. The length of the probing code is $N_{code} = 32768$ symbols for all interrogations such that $T_{code}$ and therefore $B_{meca}$ are kept constant.

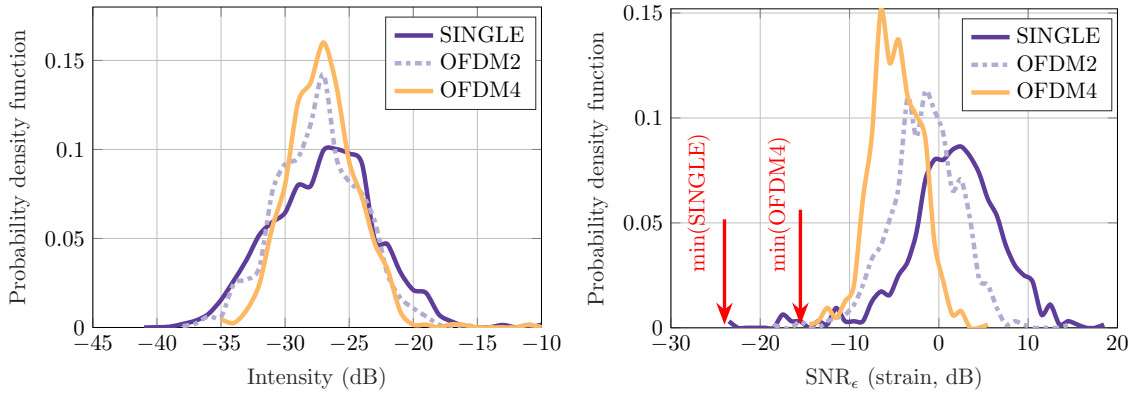


(a) Intensity$_{dB}$ distribution

(b) SNR$_\varepsilon$ distribution

Figure 5.18: Static experimental trace, OFDM interrogation of 1.3km SSMF, constant $L_s$ = 2.05m configuration

Figure 5.18 displays the Intensity$_{dB}$ and SNR$_\varepsilon$ distributions of the measurements.

The Intensity$_{dB}$ distribution here matches the simulation result (Figure 5.14(a)) with shrinking distributions. In Figure 5.18(b), the SNR$_\varepsilon$ distribution shrinks and shifts towards lower SNR values as the number of carriers increases, with a comparable worst-case value. This result in Figure 5.18(b) also matches the simulation result of Figure 5.14(b) well. Note however that despite the apparent same worst case SNR$_\varepsilon$ around −15dB, **the worst case is actually better in OFDM, with a 4.5dB gain from single to 2 carriers and a 8.5dB gain going to OFDM4 as pointed out by the arrows in Figure 5.18(b)**.

Thanks to subcarrier combination, the measured estimations of the fibre segments from Rayleigh-backscattered probing codes are more reliable, thus increasing the overall quality of intensity and phase estimations. At constant gauge length, this decreases the strain noise floor, allowing to detect smaller strain events with several subcarriers than with single-carrier. Such a reduction of the noise floor (minimal SNR$_\varepsilon$ values) is expected to decrease false alarm occurrences, together with an increase of the detection capabilities of the system in dynamic configurations.

#### 5.3.3.2 Dynamic measurements

A piezoelectric actuator is added to the fibre under test in the previously described laboratory configuration: 3.1m of SSMF is wrapped around the actuator and connected between the 400m and the 900m fibre spools (Figure 5.16). The actuator is driven by a 440Hz, 2Vpp sine wave signal. Each measurement lasts for 2 seconds similarly to the previous static interrogations.

**Constant $B_{elec}$** The first series of dynamic measurements is conducted while keeping $B_{elec}$ constant, $B_{elec}$ = 100MHz. Three successive measurements are performed, one for each interrogation method (single carrier, OFDM2 and OFDM4 respectively).

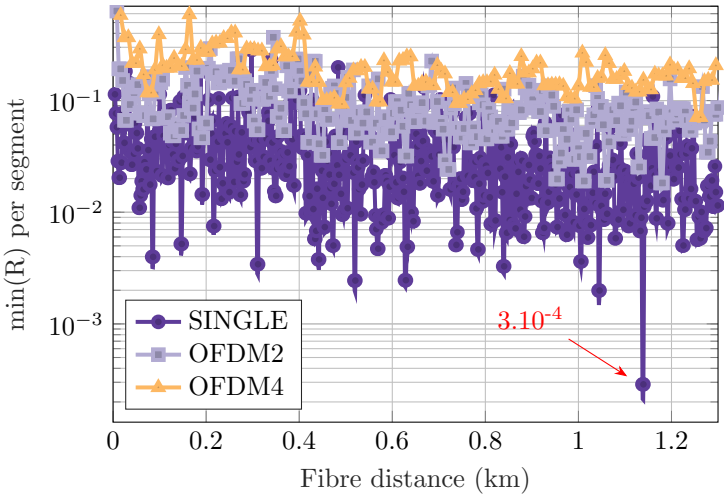


(a) Minimum reliability value in time

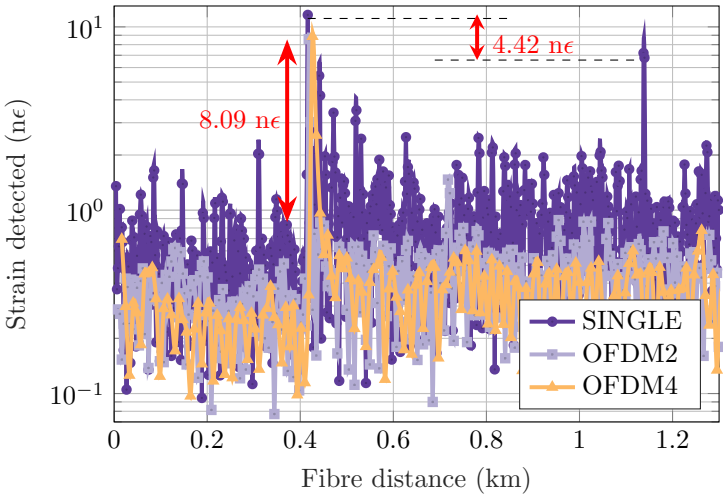


(b) $\sigma_\varepsilon$ along distance

Figure 5.19: Interrogation of 1.3km SSMF excited by 440Hz piezoelectric actuator at 420m, 2 seconds measurement. Constant $B_{elec}$ = 100MHz, detection and localization figures

Figure 5.19 gives the detection data for the constant $B_{elec}$ configuration: reliability versus distance in Figure 5.19(a) and measured strain $\varepsilon$ in nm/m (or n$\epsilon$) versus fibre distance. The reliability in Figure 5.19(a) predicts the quality of the measurement along the fibre: The lower are the minimal reliability values, the higher the false alarm probability

on the detection figure. Indeed, for single-carrier interrogation, the low value at 1.14km on Figure 5.19(a) (pointed by the arrow in the figure) deserves some attention, as it translates into a false alarm on Figure 5.19(b) at the same location. All interrogation methods have a consequent peak where the dynamic strain is applied, as expected. More precisely, since the same strain was applied during all measurements, the same peak amplitude was expected. Both OFDM2 and OFDM4 detection peaks are of 8.87n$\varepsilon$ and the detection peak with single-carrier is slightly higher since we suppose that external noise was also captured.

The dynamic range $DR$ is defined as the difference between false alarm level and detection peak level. Here in Figure 5.19, the detection peak has a better $DR$ when the number of subcarriers increases thanks to the decrease of the phase noise level (false alarms). **Thus we gain $\Delta DR = 3.67\text{n}\epsilon$ between single carrier interrogation and OFDM4 as pictured in Figure 5.19(b)**.

In Figure 5.20 we display the optical phase measurement around the excitation detection, in the frequency domain. Similarly to the detection stage, the identification (of the detected sound or disturbance) gets better when the number of OFDM subcarriers increases: the noise level on Figure 5.20 shrinks by 15dB between single-band interrogation and OFDM4. **Therefore, even though the measured Power Spectral Density decreases in Figure 5.20, its dynamic is 4.3dB higher in OFDM4 than in single-band interrogation, for a similar excitation intensity from the piezoelectric actuator**.

**Constant $L_s$** Secondly, the constant spatial resolution ($L_s$) configuration is investigated. We keep the single-carrier measurement with $B_{elec} = 100$MHz and successively perform new OFDM measurements: OFDM2 with $B_{elec} = 200$MHz and OFDM4 with $B_{elec} = 400$MHz (respectively $f_{Symb} = 100$MBaud and 200MBaud), hence $L_s = 2.05$m for all measurements.

In Figure 5.21, the disturbance is detected with 2.05 meters accuracy for all interrogation methods, with increasing alarm level: from 5.67n$\varepsilon$ for single-carrier to 19.15n$\varepsilon$ with 4 subcarriers as pointed by the arrows in the figure. This is directly related to the increase of the electrical bandwidth for interrogation, and consequently the decrease of the gauge length: the strain is constant, and the strain per gauge length increases.
The average distinction threshold, or noise floor, slightly increases as the number of subcarriers grows. However, false alarms contribute to increase the true distinction threshold for single-carrier and OFDM2 interrogations. **Therefore the detection dynamic, defined as the difference between false alarm level and detection peak level, increases from 2.16n$\epsilon$ for single carrier interrogation to 7.73n$\epsilon$ for OFDM2 and 17.17n$\epsilon$ with OFDM4**.

The Power Spectral Density (PSD) of phase computed at the location of the disturbance (the location is determined thanks to the detection peak in Figure 5.21) is used for further identification of the disturbance. The PSD of phase at disturbance location

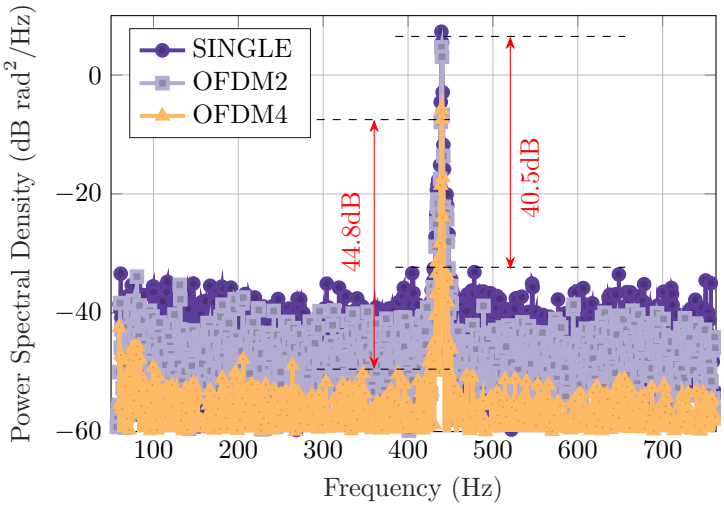


(a) Power spectral density of optical phase

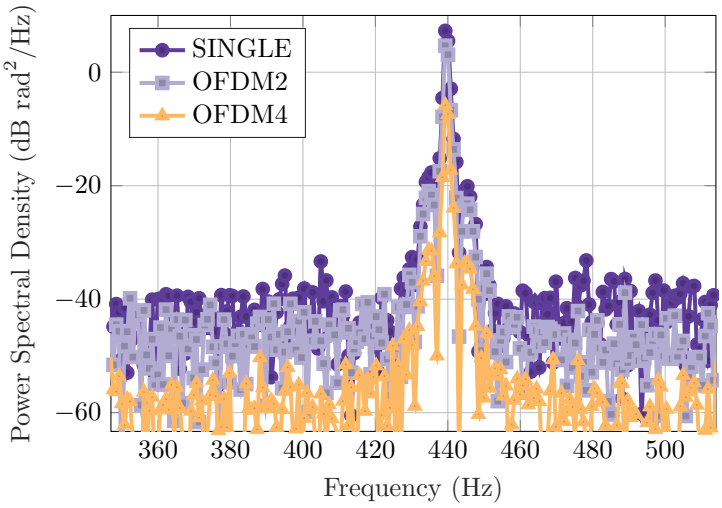


(b) Zoom on peak of Power Spectral Density (PSD). The PSD peaks have roughly the same width, however the overall PSD shifts downwards as the number of subcarriers increases

Figure 5.20: Interrogation of 1.3km SSMF excited by 440Hz piezoelectric actuator, 2 seconds measurement, constant $B_{elec} = 100$MHz. Identification by spectral pattern recognition of the perturbation on the phase measurement at the excitation location

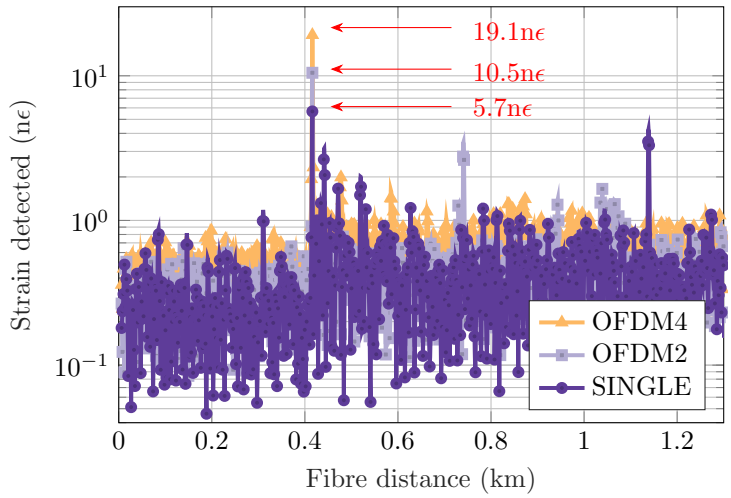


Figure 5.21: $\sigma_\varepsilon$ along distance, measurement on 1.3km SSMF excited by 440Hz piezoelectric actuator, 2 seconds measurement, constant $L_s = 2.05$m.

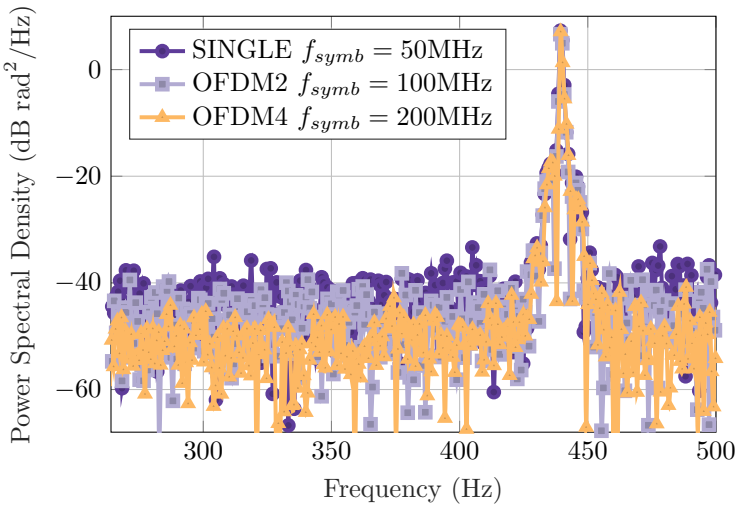


Figure 5.22: Power spectral density of phase at the perturbation location, zoom on identification peak within a 760Hz mechanical bandwidth, measurement on 1.3km SSMF excited by 440Hz piezoelectric actuator, 2 seconds measurement, constant $L_s = 2.05$m.

is displayed in Figure 5.22 for all three interrogation methods. The PSD peak around 440Hz reaches above 7dB rad$^2$/Hz for all methods. The shape and width of the peak is similar to all methods as well, the only difference between methods being the noise floor on both sides of the peak. Here again, the dynamic range increases with the number of subcarriers from 40.6dB rad$^2$/Hz in single-carrier interrogation to 49.9dB rad$^2$/Hz with OFDM4. **This brings in an overall gain of 9.3dB which is better than the one observed in Figure 5.20 for constant $B_{elec}$.**

Figure 5.23 finally shows the minimum reliability min($R$) per segment in constant $L_s$ configuration. Indeed, at a given fibre distance, the reliability $R$ varies in time, and we chose to monitor its minimum value in time as a reliability threshold. An increase of the reliability is observed from single-carrier to multi-carrier interrogation, with no striking difference between OFDM2 and 4 (except for one low value with OFDM2 around 750m). It demonstrates how the decrease of false alarms relies on constructive combination, which

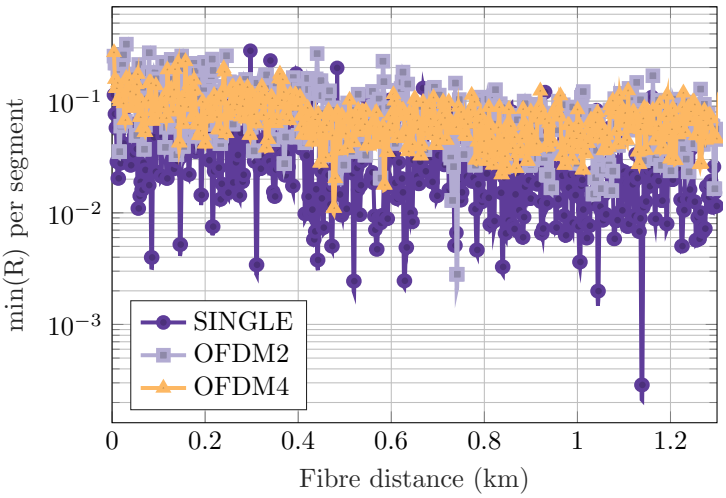


Figure 5.23: Minimum reliability in time along distance, measurement on 1.3km SSMF excited by 440Hz piezoelectric actuator, 2 seconds measurement, constant $L_s = 2.05$m.

is beneficial from the first iteration.

In accordance with previous static simulations and measurements (in subsection 5.3.2 and subsubsection 5.3.3.1 respectively), an improvement of the sensing quality was noticed with the use of OFDM interrogation compared to single-carrier interrogation. Moreover, the detection and identification capabilities are increased when the number of OFDM subcarriers increases (from 2 to 4 carriers here), be it in constant $B_{elec}$ configuration or constant $L_s$ one. Even though constant $L_s$ didn't bring in a better sensitivity floor, we see a better minimum reliability in that case as well. The improvement is brought mainly thanks to the decrease of false alarms, in line with an increase of the reliability of the measurement [135].

### 5.3.4 Lower sampling resolution as an alternative to multi-carrier?

In this chapter, we have been using mainly a simplified version of OFDM interrogation: OFDM with same codes. It is described in further details in Appendix B. Now, as multi-carrier interrogation with same codes leads to lower spatial sampling resolution (constant $B_{elec}$ case) or increased electrical bandwidth (constant $L_s$ case), a legitimate question would be: "why not simply perform lower resolution?"

**Reminders**

- Lower spatial sampling resolution was used in several parts of the manuscript and detailed in subsection 3.3.4: Lower spatial sampling resolution with a downsampling factor $P$ consisted in selecting the most reliable fibre segment among $P$ and every $P$ fibre segments, which reduced the spatial sampling resolution and allowed to get rid of the most annoying $\sigma_\varphi$ false alarms.
- We introduced in section 5.3 a combination method which allows to get rid of false alarms due to unreliable fibre segment estimations as well, which is called "Rotated Vector Sum" (RVS)

**Lower spatial sampling resolution by means of RVS** Using the model from chapter 2, we simulate a 1-km long single-mode fibre. Firstly, only AWGN is added to the interrogation. For a lower spatial sampling resolution of $P$, the fibre is interrogated by single-carrier Coherent MIMO, then every $P$ consecutive fibre segment estimations are combined using RVS. In other words, instead of picking the highest reflecting segment among $P$, the $P$ consecutive ones are combined. It is compared below with OFDM using $P$ subcarriers in constant $B_{elec}$ configuration.

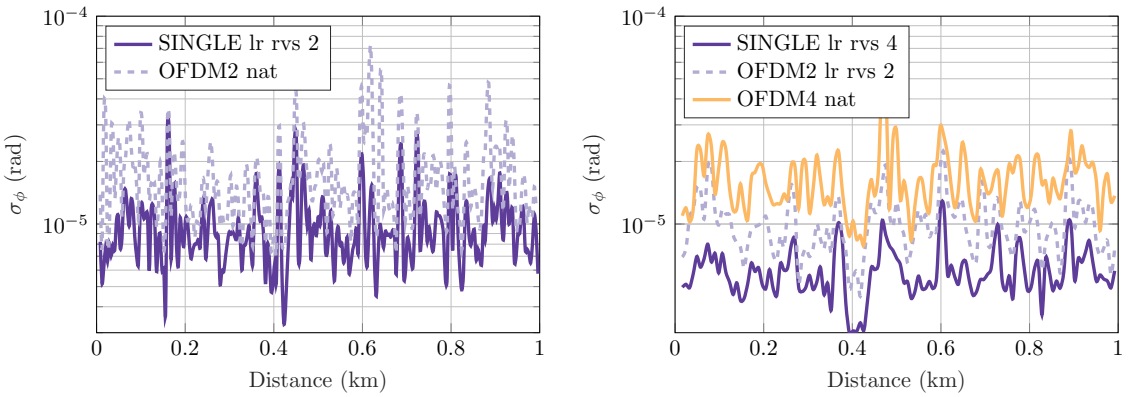


(a) Spatial sampling resolution 4.1m

(b) Spatial sampling resolution 8.2m

Figure 5.24: $\sigma_\varphi$ along distance: comparison of OFDM combination and low resolution combination, AWGN only. "nat": native resolution, "lr rvs": low resolution - rotated vector sum

Figure 5.24(a) shows a comparison of $\sigma_\varphi$ for a low resolution $P = 2$, and Figure 5.24(b) for $P = 4$. For $P = 4$, a lower spatial sampling resolution ($P = 2$) of an OFDM2 interrogation was performed as well as an intermediate case. We can see that performing RVS on consecutive single-carrier segments or on the estimations of a same segment performed in independent subcarriers lead to different results. Moreover, in the presence of white noise only, the RVS on consecutive fibre segments estimations seems to bring in a lower noise floor for static estimation than RVS on multi-carrier interrogation. This would suggest that single-carrier interrogation brings estimations of fibre segments which are more diverse than the estimations of several subcarriers on a same segment, therefore better mitigating coherent fading with consecutive segments combination[8].

Then, laser phase noise with $\Delta\nu = 75$Hz is added and the results are displayed in Figure 5.25. As all noises of the system are simulated, the performance of subcarrier and RVS becomes the same as lower spatial sampling resolution RVS. This would mean that in the presence of laser phase noise and AWGN, single-carrier and multi-carrier interrogations bring comparable diversity in their estimations of segments and subcarriers, leading to a comparable mitigation of coherent fading effects.

[8]Note that the laser output power was the same for all measurements, however the EDFA output power should be double-checked: indeed, a constant output power set-point is a possibility, but not a certainty.

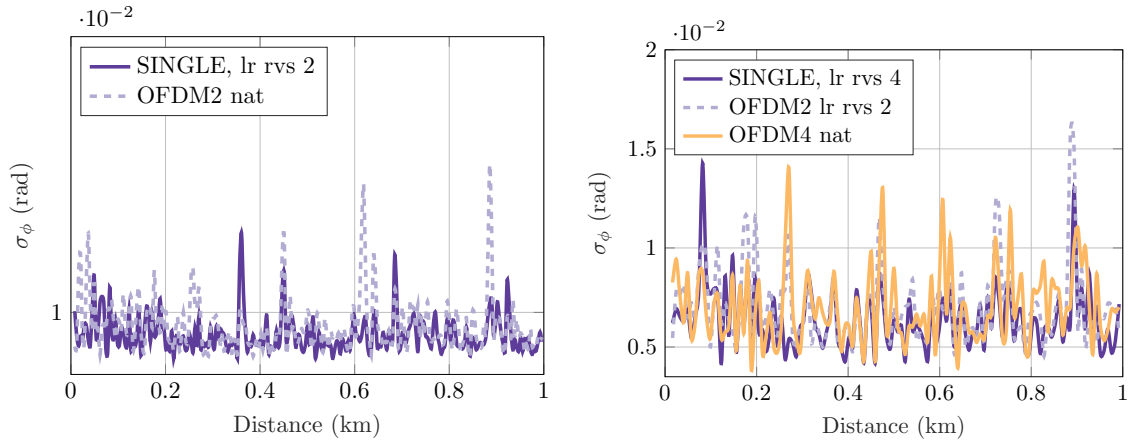


(a) Spatial sampling resolution 4.1m

(b) Spatial sampling resolution 8.2m

Figure 5.25: $\sigma_\varphi$ along distance for OFDM combination compared to lower spatial sampling resolution combination, laser noise $\Delta\nu = 75$Hz and AWGN.

Hence, the use of OFDM with same codes can be considered as an elegant digital signal processing method to perform lower spatial sampling resolution, in addition to paving the way to more complex multi-carrier interrogation techniques which would allow to interrogate the subcarriers with different code lengths and thus to focus on various features of the detected mechanical events.

## 5.4 Identification of a moving target: sensing experiment on deployed fibre cables

The OFDM interrogation scheme will be applied to a deployed cable scenario. A fibre inside a deployed multi-fibres telecom cable, like any other fibre, will experience coherent fading issues. Moreover, the deployed cable is exposed to permanent and moving perturbations and impairments, potentially leading to complex traces where multiple event signatures are present.

In the following, we propose to detect a moving event along a deployed telecom cable, meaning that the energy of the disturbance will be spread in both time and space, making it more difficult to detect and localize than a usual locally applied and monitored disturbance.

For sake of fair comparison between the single-carrier and OFDM cases, we use a common electrical bandwidth $B_e$, determined by the symbol rate. With the multicarrier approach, the rate per subcarrier is $P$ times lower than that of the transmitted OFDM flow, which degrades the initial spatial resolution $L_s = c_{fibre}/2.f_{Symb}$, where $c_{fibre}$ is the speed of light in the fibre, by a P factor compared with the single carrier case. Also, the subcarrier code length is adjusted to provide the same duration $T_{code}$ as for the single carrier case, so preserving the mechanical bandwidth $B_m = 1/T_{code}$.

### 5.4.1 Experimental setup

A 700m-long coated cable enclosing six SSMFs is deployed between two buildings on an enterprise campus. It is buried approximately 0.6m under an asphalt road for most of the

distance, first in a small pipe together with water and electricity lines and then fixed to the wall of a 2m high underground tunnel.

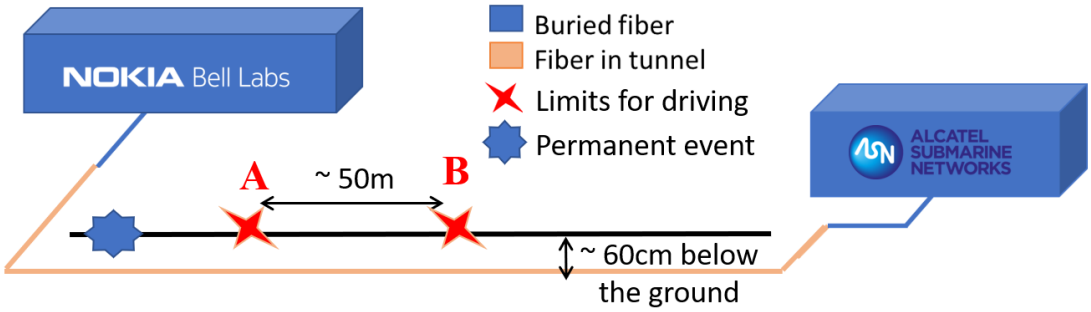


Figure 5.26: Experimental setup: Path of deployed fibre

Figure 5.26 gives an overview of the 700m long fibre cable path deployed between the two buildings. The Coherent-OTDR is installed in a lab in the "Nokia Bell Labs" building, and the cable ends in the "Alcatel Submarine Networks" building. On the cable path, we show the main points of interest for this study, namely a permanent disturbance after 300m from the fibre launching end which is discussed in the next subsection, and the limits between which the vehicle moved for the dynamic part of the study. In Figure 5.27, we show a picture of the road over which the vehicle drove. We notice several manhole covers along the road, which will trigger stronger phase variations at the acquisition.

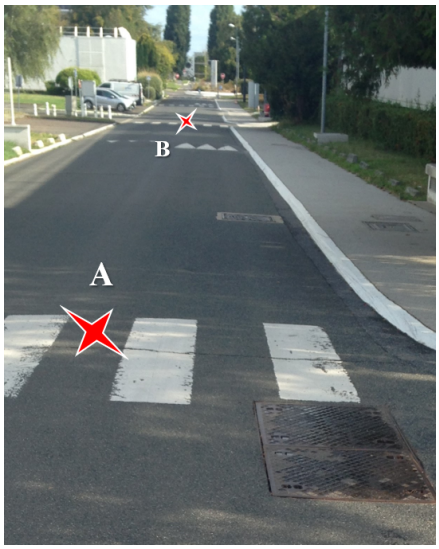


Figure 5.27: Road under which the fibre is deployed

The interrogation setup is depicted in Figure 5.28. The optical part setup is the dual-polarization interrogation coherent (MIMO) phase OTDR with a highly stable laser source at 1536nm mounted in a homodyne configuration and already introduced in chapter 1, subsection 1.2.4.

The novelty here lies on the multi-carrier digital processing blocks introduced in the current chapter. At the transmitter side, the polarization-division-multiplexed OFDM signals are calculated from the selected code length and taking into account the desired number of subcarriers prior to injection into the Mach-Zehnder Modulator (MZM).

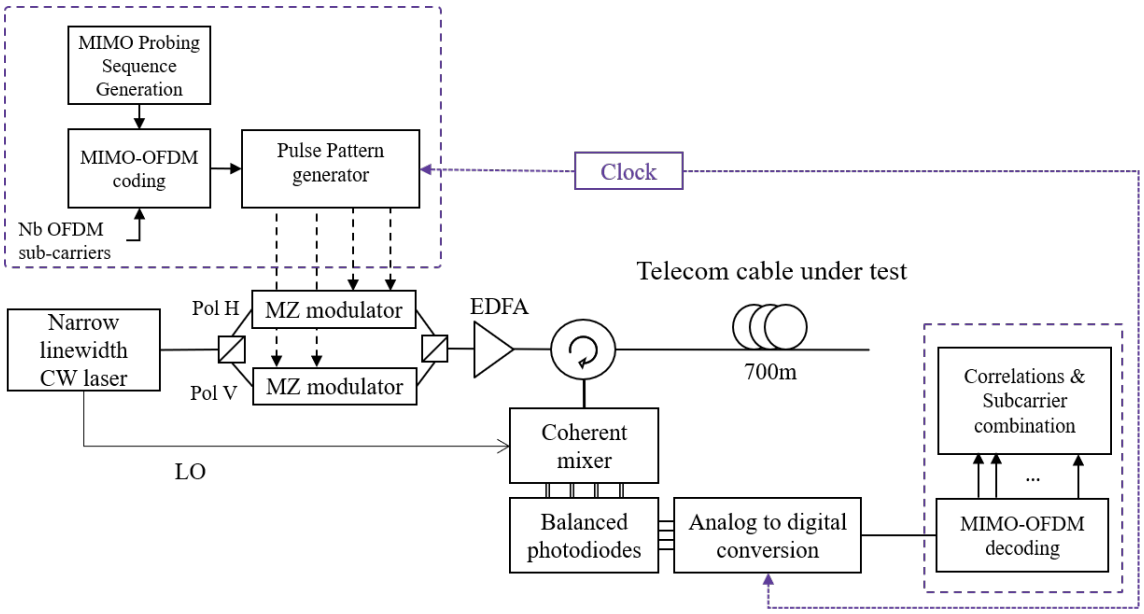


Figure 5.28: Experimental setup: Lab interrogator setup

### 5.4.2 Static measurements

Firstly, one fibre from the cable is interrogated at a symbol rate of 50MBaud without any vehicle in motion on the road, successively through single-carrier, OFDM with 2 subcarriers and OFDM with 4 subcarriers interrogations. At the receiver side, OFDM demodulation is performed through an FFT for both polarization channels. Correlation is then applied per subcarrier and followed by the combination of Jones matrices as previously detailed.

The reliability and sensitivity results are displayed in Figure 5.29 for the $[150-450]$m cable section. Figure 5.29(a) shows the minimum reliability value $R$ in time for each fibre segment[9]. This metric is chosen since phase estimation artefacts occur more likely as $R$ gets close to 0, which affects the detection performance. Here, the overall reliability clearly increases with the number of subcarriers. Figure 5.29(b) shows the system distinction through the standard deviation of the differential phases captured along the same cable section. Beyond the sensitivity, stationary disturbances such as machinery noise, water pipes, echoes in the tunnel locally induce backscattered phase variations. The peak at 300m observed on every measurement in Figure 5.29(b) comes from the noise of a water pipe crossing the fibre path. When $P$ increases, the number and levels of false alarms shrink such that the OFDM4 case, thanks to its higher sensitivity, further highlights the mechanical event and more generally enhances the detection performances.

### 5.4.3 Dynamic measurements and trajectory identification

Secondly, the fibre response is tested while a vehicle moves at a stable speed of 40km/h between A ($t = 0$s, $d = 350$m) and B ($t = 4$s, $d = 390$m) locations.

Figure 5.30(a),(c) and (e) displays the phase response in the time versus distance

[9]The reliability metric was defined in subsection 3.3.3

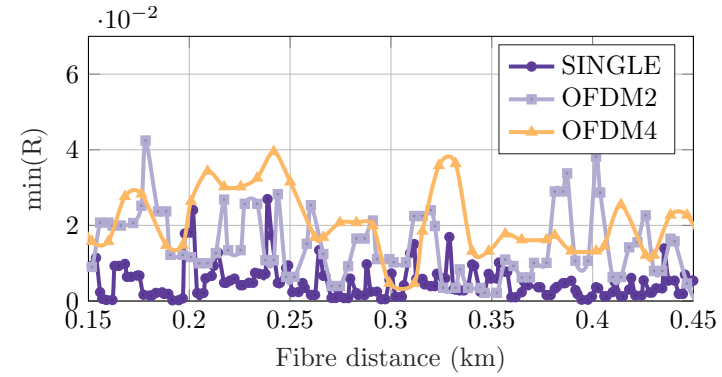


(a) Minimum reliability

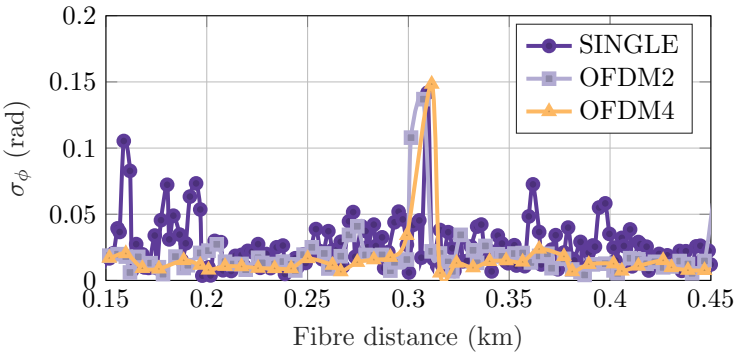


(b) $\sigma_\varphi$ along distance

Figure 5.29: Indicators on reliability and disturbances along distance

plane for the three tested configurations. The false alarms are indicated circled in red in Figure 5.30(a), demonstrating how the single-carrier measurement is disposed to false alarms. With OFDM measurements, the false alarms vanish while the vehicle trajectory is getting more visible with the increase of the number of subcarriers.

Note that raw phase measurements are displayed, however the acquisition encloses backscattered polarization and intensity information in addition to the phase. Moreover, further processing could increase readability of the traces e.g. by substitution of the phase variations by coloured dots as performed for the reliability metric in the following.

We also look at the reliability metric in the time-distance plane in Figure 5.30(b),(d) and (f), in order to validate the behaviour that was observed for static measurements in Figure 5.29. The reliability obviously increases with the number of carriers used for the interrogation, as Figure 5.30(b) looks overall covered in bold, dark points (i.e. low reliability points), especially compared with Figure 5.30(d) and (f). If the differences between ODFM2 and OFDM4 interrogations were not clearly stated in Figure 5.30(c) and (e), Figure 5.30(d) and (f) depicts how they actually differ by their amount of low-reliability points on the reliability maps.

One surprising, yet somehow expected aspect is the remaining low-reliability points in Figure 5.30(b),(d) and (f), especially on OFDM interrogations: they follow the vehicle's trajectory. Unlike low-reliability points outside the trajectory which were eliminated by the first OFDM combinations (from Figure 5.30(b) to (d)), the time-distance points which

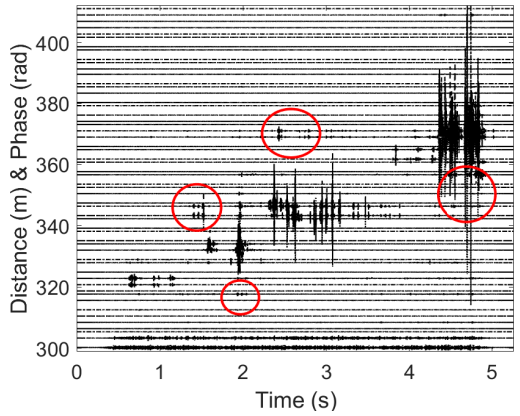


(a) SINGLE

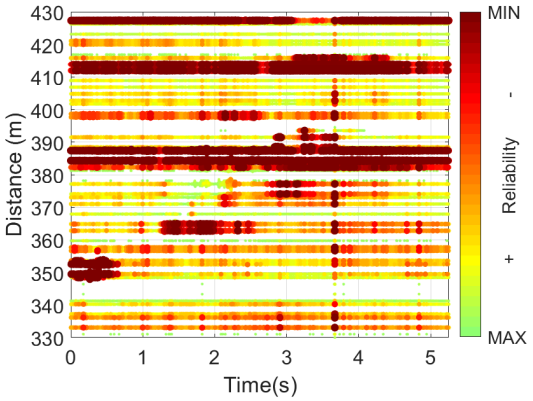


(b) SINGLE

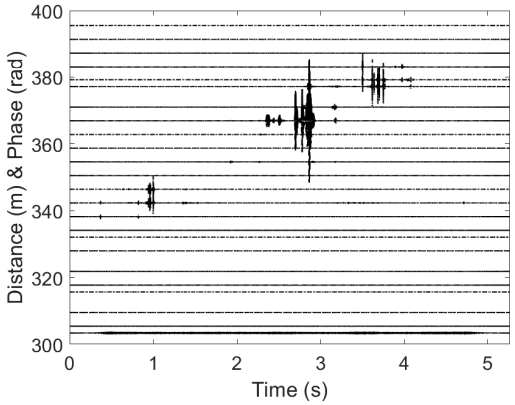


(c) OFDM2

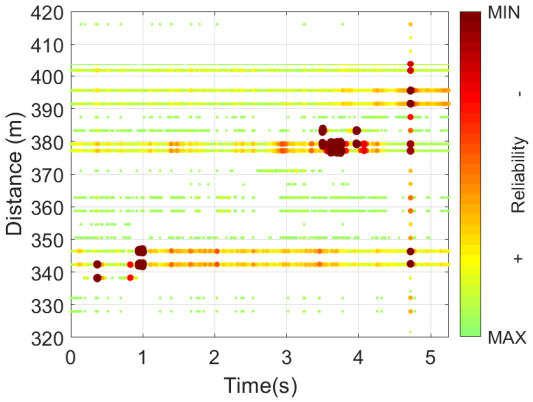


(d) OFDM2

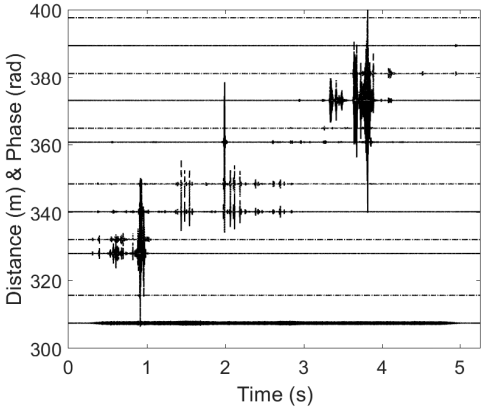


(e) OFDM4

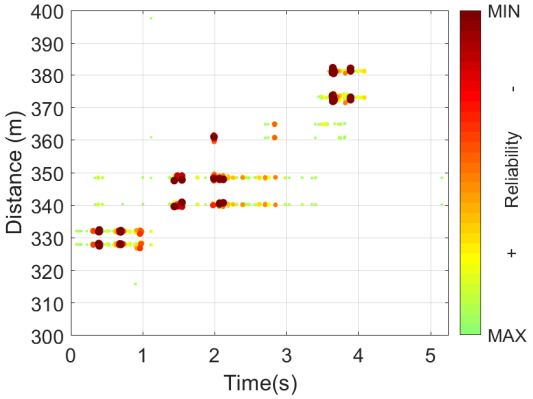


(f) OFDM4

Figure 5.30: Time-Distance phase (left) and reliability (right column) maps. False alarms on phase maps are indicated with red ellipses.

really experienced the vehicle were truly exposed to strong variations, therefore affecting their local state of polarization as the fibre certainly was shaked at some points. As a consequence, the probability to get low reliability at these places did grow, and even OFDM processing was not able to recover enough reliable points.

MIMO-OFDM complements the previously introduced fading free MIMO phase sensing by further enhancing its sensitivity performance, as illustrated here in a deployed scenario [136]. The number of OFDM carriers fixes the trade-off between the targeted coherent fading reduction and spatial resolution (in our case where a common electrical bandwidth $B_e$ is used, yielding 2, 4 and 8m resolution respectively), and must be adjusted according to the application case requirements.

## Summary: Towards an adaptive subcarriers scheme

MIMO-OFDM proved itself to be a flexible solution for fading mitigation as it allows to perform multi-carrier interrogation in a fully digital manner. In Figure 5.15, we've seen that there was a limit to the performance increase brought by multi-carrier interrogation, and more generally throughout this chapter, we were able to show the advantage of multi-carrier interrogation and constructive combination from the first iteration, whatever the configuration in terms of electrical bandwidth or spatial sampling resolution.

Also, long-distance case was not investigated here on purpose in multi-carrier interrogation to avoid involving attenuation effects to the statistics of coherent fading initially, and due to time constraints eventually. However, we believe that this technique, such as every other multi-carrier interrogation technique investigated in the literature, is also suited to longer distances cables, of the order of tens of kilometres.
Among all application cases that Distributed Acoustic Sensing (DAS) can address, multi-carrier interrogation should be an option, yet the performance limit as shown in Figure 5.15 would have to be adapted to the use case (laser linewidth, distance...).

Simulation results are presented in Figure 5.31 below for different fibre distances and in the case where $f_{Symb}$ = 50MBaud (yielding $B_{elec}$ = 100MHz). Due to length constraints on the interrogation codes, the mechanical bandwidths differ as well (see subsubsection 1.2.4.2).
It appears that, similarly to the long distance experiments in subsection 3.2.2, a new low-$\sigma_\varepsilon$ peak appears at the left of the SNR distribution (see Figure 5.31(b) and inset in Figure 5.31(a)): due to attenuation and most importantly laser phase noise in distance, the $\sigma_\varepsilon$ irremediably increases. Yet, Figure 5.31 shows how the use of multi-carrier interrogation and subcarrier combination allows to shift the $\sigma_\varepsilon$ distributions towards higher SNR values. Joint work on laser phase noise reduction and subcarrier combination would allow to increase the distinction threshold for long-distance sensing in the future.

Furthermore, electrical bandwidth was introduced through a discussion of spectral occupancy in telecommunications networks. In such a context, the spectral occupancy is indeed very constrained but it is dynamic as well, as the allocation of spectral resources can evolve in time. A solution such as Coherent-MIMO interrogation which would operate

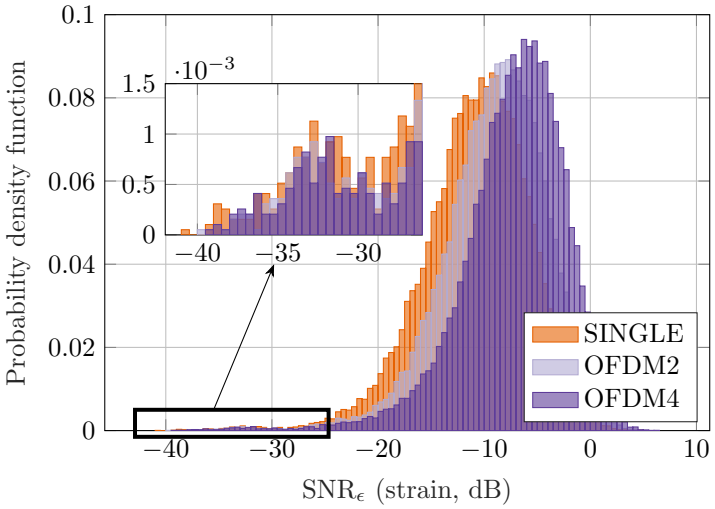


(a) 16km, $B_{meca} = 760$Hz

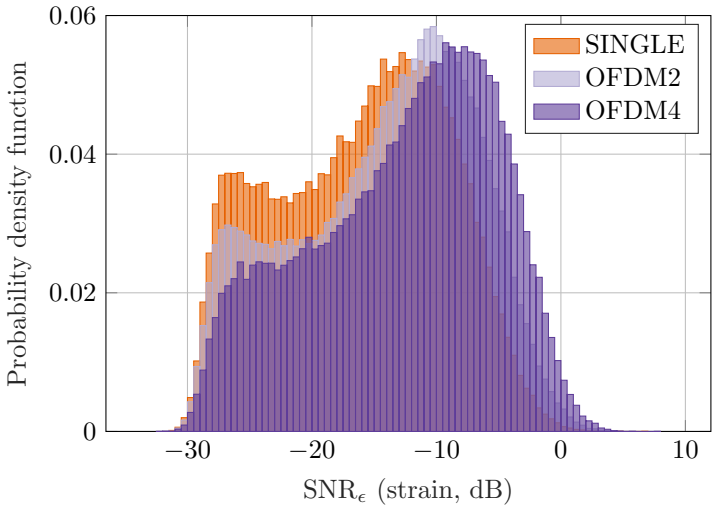


(b) 50km, $B_{meca} = 190$Hz

Figure 5.31: Static fibre simulations: Probability density function of strain distinction threshold for long distances (16 & 50km resp.), with $B_{elec} = 100$MHz, $\Delta\nu = 75$Hz, and AWGN added.

alongside telecommunication data should adapt to such dynamic allocation of resources, and OFDM-MIMO is a solution for adapting the sensing signal to the needs of the operator on given spans.

# Chapter 6

# Increasing the sensing range to network scale: long distance, quasi-distributed, and forward sensing

Having lowered the detection threshold of the interrogation system and process, namely reducing the noise floor in order to detect smaller phase variations, it is now possible to explore the reach of the Coherent-MIMO interrogator. Coherent-MIMO is a distributed fibre interrogator, with digital, low peak power probing signal. The constraints on the distance were discussed in chapter 1 in terms of energy, or signal-to-noise ratio, as well as regarding laser phase noise. In chapter 2, detection thresholds as a function of distance were given and both Figure 2.5 and Figure 3.4 illustrated the constraints in terms of phase noise and interrogation method respectively.

In order to scale with real deployed networks, the distributed sensing system must reach acceptable detection threshold and dynamic range on terrestrial and submarine fibre span distances. It must also coexist with telecommunication data traffic. Moreover, the mechanical conditions of deployed telecommunication cables will lead to distributed sensing systems that are less sensitive than the configurations presented in chapter 4: the thick coating of fibre cables, the mounting or burial of the cables in specific environments... are not engineered so as to get a sensitive fibre sensor, rather the opposite.

Experiments are conducted on Standard Single Mode Fibre (SSMF). Firstly, we assess a complex perturbation identification over 50km fibre in laboratory conditions, by means of synthesized vibrations. Secondly, we prove the possible coexistence of sensing signals and Dense Wavelength Division Multiplexing (DWDM) data transmission over a 82km link comprising deployed fibre as part of an underground 6-fibres telecommunication cable naturally subject to multiple acoustic perturbations which we detect. Eventually, we discuss the use of the distributed sensing interrogator in quasi-distributed mode to span ultra long-haul links such as submarine cables.

## 6.1 Dual-polarization interrogation over a 50km SSMF span

In this section, we use the coherent-MIMO interrogation the way it is described in sub-subsection 1.2.4.2. The detection threshold of the sensing system is enhanced thanks to the elimination of polarization effects as described in chapter 2.

### 6.1.1 Experimental setup

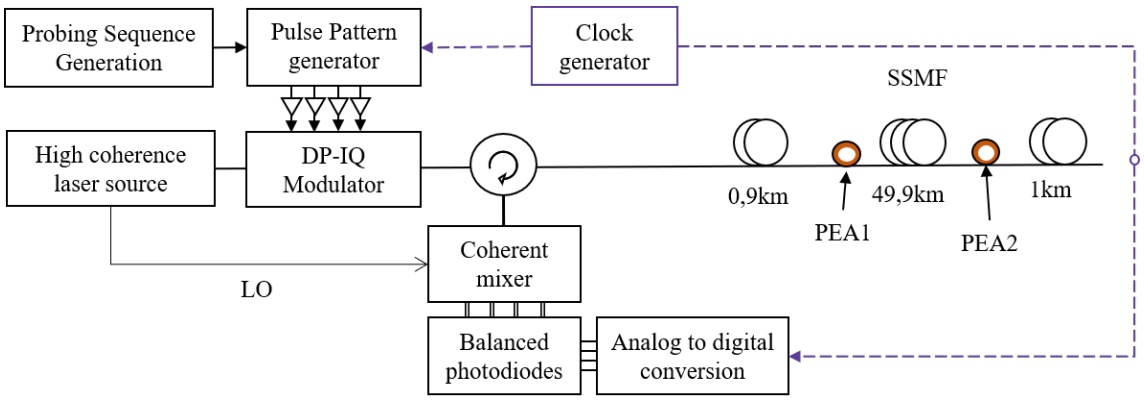


Figure 6.1: Experimental Setup 50km (PEA: PiezoElectric Actuator, LO: Local Oscillator, DP-IQ: Dual Polarization – In-phase and Quadrature, SSMF: Standard Single Mode Fibre)

The setup is presented in Figure 6.1. The probing signals are sent on two orthogonal polarizations through a dual-polarization I/Q Mach-Zehnder modulator ($f_{symb}$ = 50MBaud) to modulate the optical wavelength. The figure refers to the general case of an I/Q modulation, however we restrict ourselves in this work to a BPSK modulation per-polarization. The modulated signal is then amplified to an average power of 5dBm and sent through a circulator into the sensed fibre. The Rayleigh back-scattered signal goes through the circulator to a dual-polarization coherent mixer. The in-phase and quadrature information of the signal projection over two orthogonal polarization states are captured by 1.6GHz 3dB-bandwidth balanced photodiodes. The four captured signals are then sampled at $2f_{symb}$ = 100MSamples/s using a 12-bit resolution scope. Off-line signal processing is carried over the acquired sequences, starting with power normalization, followed by a correlation with the transmitted sequences to periodically extract the fibre response given by a series of $2 \times 2$ Jones matrices separated with a gauge length $G$ = 2m imposed by the symbol rate $f_{symb}$ = 50MBaud. A time synchronization is then applied to detect the periodic responses with a period of $T_{code}$.

An overall 52km-long SSMF link is sensed. Two mechanical perturbations are applied, the first one at approximately 0.9km and the second at approximately 50km from the interrogator. We use cylindrical Piezo-Electric Actuators (PEA) with an outer diameter of 5cm to apply strain on bare fibres (no cable). The first actuator (PEA1) has 55cm of fibre coiled around it while the second one (PEA2) has 133cm. These actuators are fed with electrical signals. The signal generated for the experiment presented in the next section is a combination of tones which emulates an engine noise, used to demonstrate localization of different events as well as identification from spectral analysis.

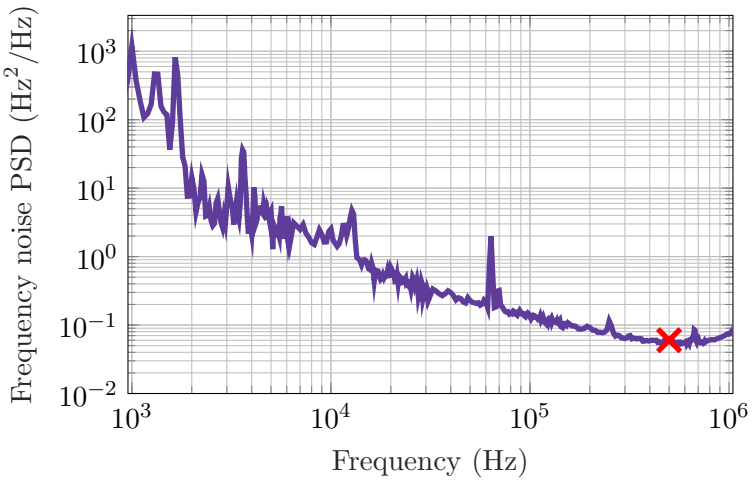


Figure 6.2: Measured frequency noise spectrum of the laser source through a self-heterodyne linewidth measurement setup: Power Spectral Density (PSD) of laser frequency noise vs. frequency. Beginning of white frequency region in the spectrum pointed out by a red cross.

An ultra-low-linewidth laser emitting 10dBm at $\lambda = 1536.6$nm is used as a source at the transmitter and a local oscillator at the receiver, with a given Lorentzian linewidth inferior to 1Hz in a 10$\mu$s time window according to its specifications sheet. We characterized the frequency noise spectrum of the laser through a self-heterodyne linewidth measurement using decorrelation with a delay line with an acousto-optical modulator in one arm of the interferometer.

The obtained frequency noise spectrum is shown in Fig. 6.2. At high frequencies, we can spot the beginning of the white frequency noise region at 0.06Hz$^2$/Hz starting from 500kHz (pointed by red cross in Figure 6.2) from which we measure a Lorentzian linewidth (corresponding to the intrinsic noise of the source) of about $\Delta\nu_{Lorentz} = 0.06\pi \approx 0.2$Hz which agrees well with the specifications. We also emphasize on the increased noise at low frequencies that impacts the quality of the phase measurements at long distances over which the effective linewidth will be higher. The longer the observation time-window is, the more low-frequency phase noise is added [101]. Indeed, as we are computing differential phases, we need a stable phase reference which translates into a high-coherence length requirement for the laser. Ideally, the phase observed by the probing signal at the modulation step and the one that is added by the local oscillator at the coherent mixer on the receiver side should be the same despite of their relative delay.

### 6.1.2 Experimental results

First measurements in static conditions (no disturbances applied through the actuators) with codes of length $T_{code} = 1$ms allowed to get the phase standard deviation $\sigma_\varphi$ measured over an observation window of 1s. It was already shown as a function of distance in Figure 2.5 and is reproduced in Figure 6.3 (bold black line). We notice an exponential growth of phase noise towards 45km and beyond. An exponential growth of the phase $\sigma_\varphi$ is also forecast from the numerical simulation shown for different laser linewidth values,

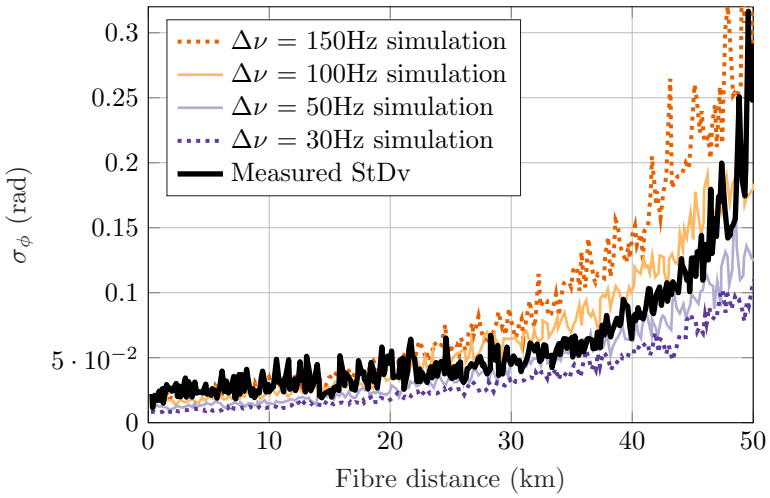


Figure 6.3: Phase standard deviation as a function of distance in static mode (simulations for various laser linewidth values and the experimental result). $\Delta\nu$ of the experimental measurement estimated at 75Hz.

leading to a challenging identification of mechanical events over long distances. Only high-energy perturbations impacting the fibre after tens of kilometres can be detected with a given probing code length, i.e. a fixed targeted mechanical bandwidth.

We observe that the experimental phase $\sigma_\varphi$ over the fibre distance is well fitted by the model when considering a phase noise of a laser with an equivalent Lorentzian linewidth around 75Hz. This is understandable when we look at the non uniform level of the frequency noise that characterizes the used laser source.

### 6.1.3 Recognition of a synthetic engine noise

In this part, we demonstrate the detection of signals that emulate vibrations generated by vehicle engine. Indeed, phase noise limits at several distances were measured in [119] through the recognition of a single tone perturbation, and we wish to verify the performance of the interrogator system for more complex signals. As engine noises can be typically characterized by the association of three main inharmonic frequencies [137], we synthesize a three-tone signal at 50, 105 and 145Hz to simulate an engine noise, and its power spectral density is shown in Figure 6.4(b) (dotted line).

We apply the same signal through the two actuators located around 1 and 51km respectively from the interrogation unit. The probing code length is $T_{code} = 2.62$ms yielding a bandwidth of $B_{meca} = 193$Hz. Figure 6.4(a) shows the measured phase standard deviation $\sigma_\varphi$ as a function of the fibre distance. The two mechanical events appear as two $\sigma_\varphi$ peaks at the expected locations. The phase evolution over the 1s measurement window is also displayed in Figure 6.4(c) and Figure 6.4(d) for each of the two detected peaks locations.

In Figure 6.4(b), we plot the PSD of the differential phase at the locations of the two $\sigma_\varphi$ peaks. The spectral signature of the engine noise at the first location ($\simeq$ 1km) is well preserved, with a Signal-to-Noise Ratio (SNR) of 30dB approximately. After 51km, the

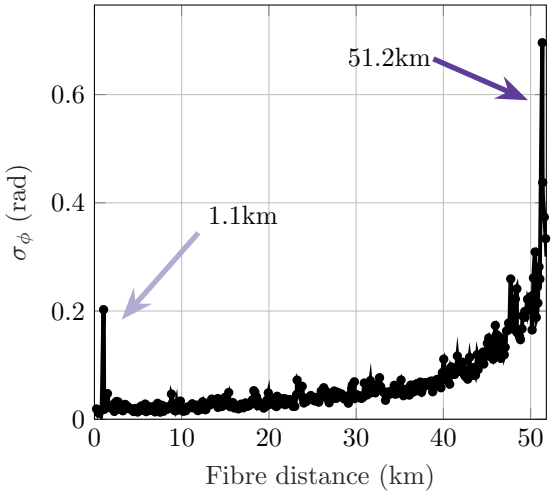


(a) Measured standard deviation of the differential phase along the fibre. Arrow point to the locations where (a) and (b) were measured.

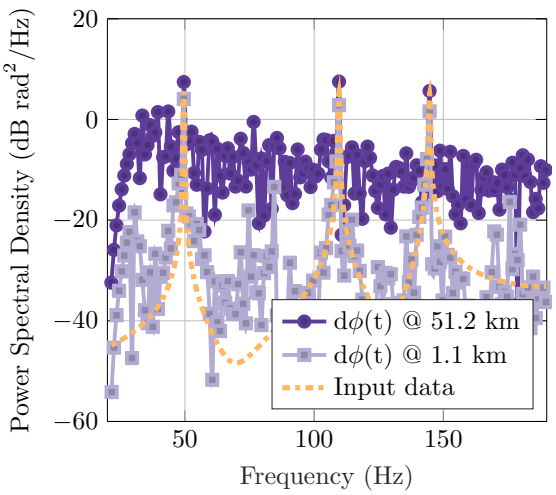


(b) Power spectral densities of phase variations at detected event locations compared to the PSD of the applied vibration signal

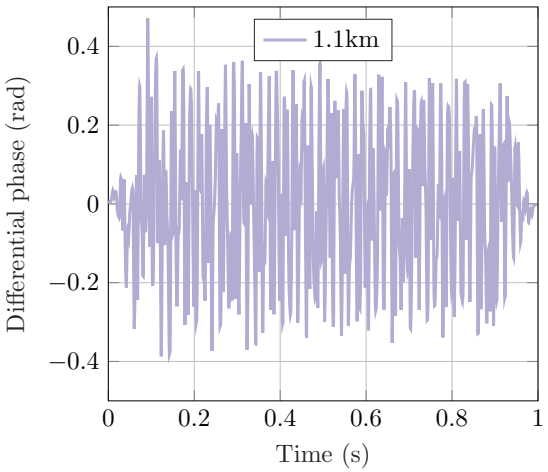


(c) Measured phase versus time at 1km

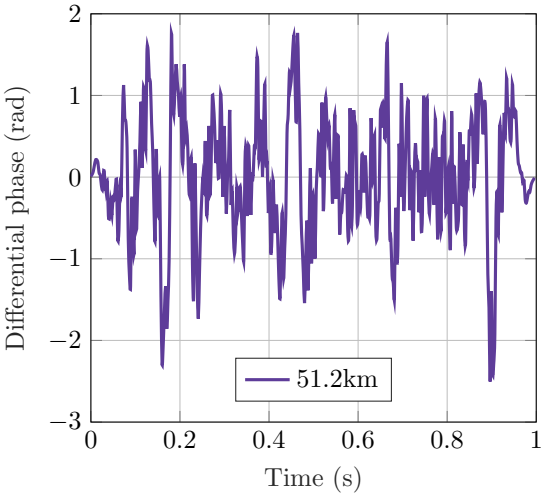


(d) Measured phase versus time at 51.1km

Figure 6.4: Features of the differential phase along the fibre with an engine noise perturbation injected at 0.97 and 51.16km from fibre start

enhanced phase noise resulting from the increased loss of coherence of the laser[1] source reduces the SNR to 10dB roughly, however the recognition of the mechanical event is still possible even after a round-trip propagation over 51km of SSMF. We also notice the higher peak power levels detected at 51.1km, which is consistent with the longer coiled fibre length at this location (133cm coiled fibre at 51.1km versus 55cm at 0.9km).

[1]Following the expression eq.(2.7), our theoretical laser coherence length is $L_{coh} \simeq 890$km

The use of a dual-polarization coherent receiver along with the designed codes in subsection 1.2.4 enabled a mathematically ideal estimation of the fibre response. The modeling of the noise limits associated with the usage of our laser source and interrogation method in chapter 2 allowed to anticipate the detection threshold as a function of fibre distance, giving the maximum reach of this dual-polarization and narrow linewidth configuration for a given detection threshold requirement. Mechanical events, made of a sum of three tones emulating an engine noise, were detected, localized and identified from a spectral analysis over a fibre distance that exceeds 50km.

## 6.2 Long distance sensing along with co-propagating data channels

Now we intend to push the reach further, while keeping the same laser source at the transmitter side. Now, the fibre under test also encloses a deployed fibre cable, and the detected disturbances are real acoustic signals.

In subsubsection 1.2.4.3, we presented an interrogation method by means of digitally generated sweeps which does not manage to give a perfect estimation of the fibre, yet allows to either double the mechanical sensing bandwidth $B_{meca}$ or double the reach (compared to the reach with BPSK Golay-coded sequences) by relaxing the condition on the interrogation sequence length. Indeed, for a round-trip time of light in the fibre $T_{ir}$, the coded sequence condition is $T_{code} > 4.T_{ir}$ while for a digitally generated dual-polarization sweep the condition becomes $T_{sweep} > 2.T_{ir}$ [74]. Moreover, relaxing the detection threshold requirements, it is still possible to trade increased distance and polarization fading by switching to SIMO interrogation and further relaxing the condition to $T_{sweep,SIMO} > T_{ir}$ as briefly developed in chapter 1: Interrogation, estimation, and processing. Adapting to the context.

In the meantime, the following experiment aims at demonstrating the possible coexistence of digital sensing and telecommunication data over a span length. In [13], a first demonstration of fibre sensing based on 40ns optical pulses has been reported with 1 meter resolution for localization. However, since signal pulses in the Distributed Acoustic Sensing (DAS) system exhibit high peak powers, they interfere with data channels if they are co-propagating due to fibre nonlinearity. The DWDM signals and sensing signals were thus counter-propagated and three 50GHz slots were left empty to ensure non-intrusive coexistence between both signals, which is a waste of spectral resources in today's crowded networks [138]. In the following, the possible co-propagation of sensing and DWDM channels with small frequency spacing is demonstrated.

### 6.2.1 Assessing the impact of co-propagating data onto the sensor phase noise

A general overview of the sensing interrogator and transmission setup is given in Figure 6.5.

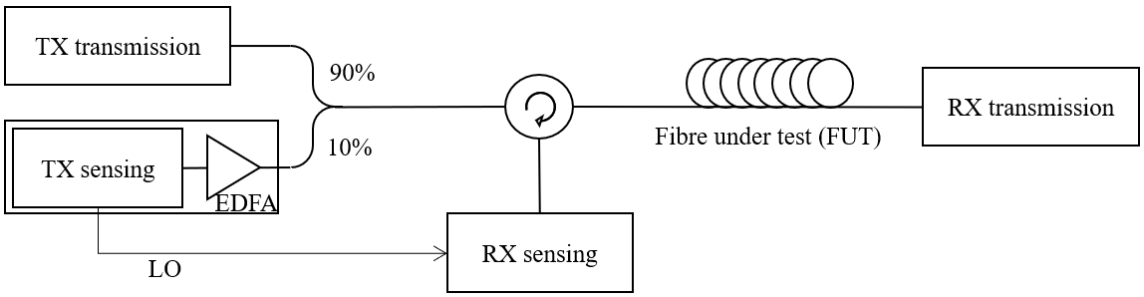


Figure 6.5: Experimental setup for static sensing and data copropagation tests in laboratory conditions

**First coexistence measurements** We compare the interrogator performance for different configurations, first by setting the coupler ratio before the circulator, then by changing the power level of co-propagating telecom data.

After coupling the sensing and data fibres by means of a 90/10 coupler to set the power of the sensing signal similar to other DWDM slots used for transmission, the input power of the sensing transmitter is modified to evaluate its impact on the $\sigma_\varphi$ in Figure 6.6. The input power is measured at the fibre input and is denoted $P_{in}$. For low amplification values

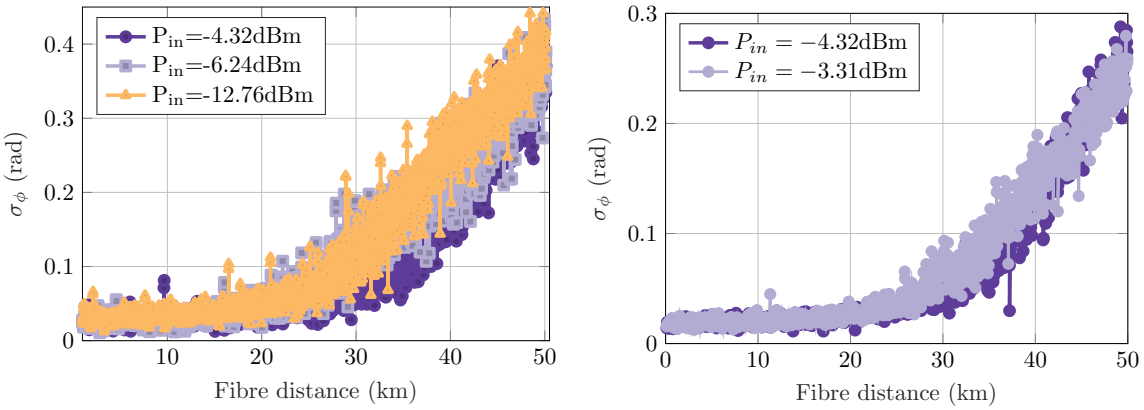


(a) Lower EDFA amplification values

(b) Higher EDFA amplification values

Figure 6.6: Static sensing on 50km SMF, $\sigma_\varphi$ along distance for different input powers (circulator input)

in Figure 6.6(a), the system behaves as it would intuitively: the higher the input power, the more precise the measurement, mostly on long distances. However, Figure 6.6(b) shows that beyond a given current value, no more enhancement is noticed. Therefore, we keep the amplification pump current at $I_{in} = 125$mA yielding $P_{in} = -3.31$dBm in the following.

**Coexistence with full C-band data** The transmission system is now constituted of the full C-band channels, except for the frequency slot around the sensing wavelength. In Figure 6.7, the spacing between sensing channel and data channels is modified, as well as the data input power, initially at 21dBm (for 86 channels, corresponding to an average input power per DWDM channel which is comparable to the power of the sensing channel). The input power of the full C-band signal varies from 19dBm to 11dBm, while the

frequency slot allocated to sensing is 50GHz ("Large Spacing") at first, and then 30GHz ("Small Spacing").

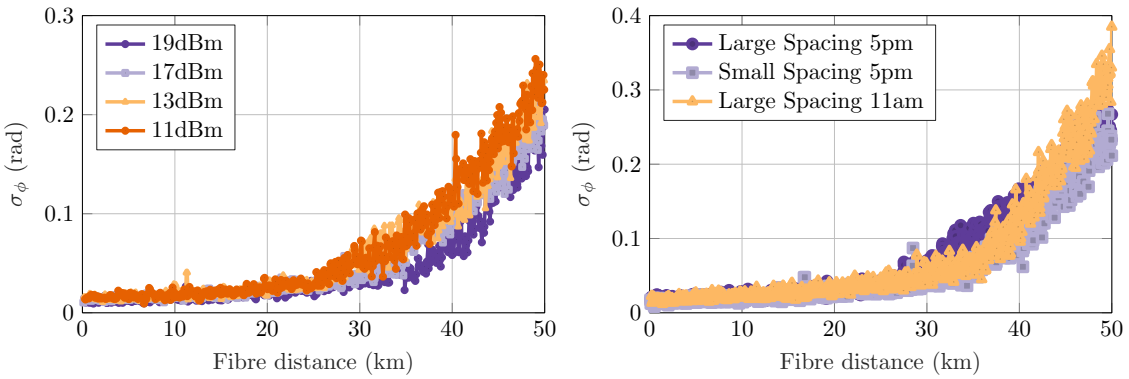


(a) 30Ghz spacing ("small"), adjacent data power change

(b) Spacing change

Figure 6.7: 50km sensing & data interrogation, $\sigma_\varphi$ for different adjacent data input power levels and spacings

The impact of the channel spacing on the transmitted data is discussed in the next subsections. As for the sensing performance, the detection threshold evaluated in terms of $\sigma_\varphi$ seems to stay stable.

Of course, variations are observed in Figure 6.7(a) as a function of the input power of the data, which could lead us to think of a lowered phase noise or detection threshold in the presence of data transmitted with higher input power. Figure 6.7(b) displays $\sigma_\varphi$ measurements for different frequency spacings and at different moments of the day, and the time of the measurement is shown to have a higher impact on the detection threshold than any other parameter: This brings up the concern of system stability, as it appears that the same configuration (here "Large spacing") yields performance fluctuations that are more important than the change of one parameter (namely the channel spacing). The main conclusion from Figure 6.7 would be that **the changes in the transmitted data features has less impact on the sensing performance than the usual fluctuations of the system.**

Therefore, we are confident about the sensing capabilities of the system going into a dynamic study of joint sensing and data transmission in deployed fibre cables over more than 50km which is a long distance with regards to DAS (note that $<$ 100km is short-reach in terms of transmission, 100km being typically a span length).

### 6.2.2 Experimental setup

An 82-km span of SSMF consisting of fibre spools and a 1.4km long deployed fibre cable alternatively placed at different distances from the transmitter is set in three possible configurations as displayed in Figure 6.8.
The deployed fibre in use is part of a coated 6-fibres cable deployed between two buildings. It exits the first building after crossing a datacenter, then it is buried 0.6m under an asphalt road, where various vibration sources are met. The main perturbation is an air

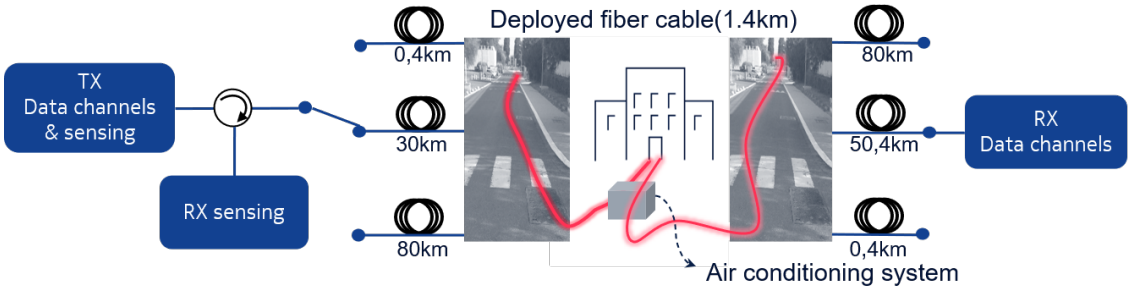


Figure 6.8: Experimental demonstration of co-propagating digital sensing signal and DWDM channels over an 82km-long span, three possible configurations.

(a) Location of the measure & (highlighted) cable

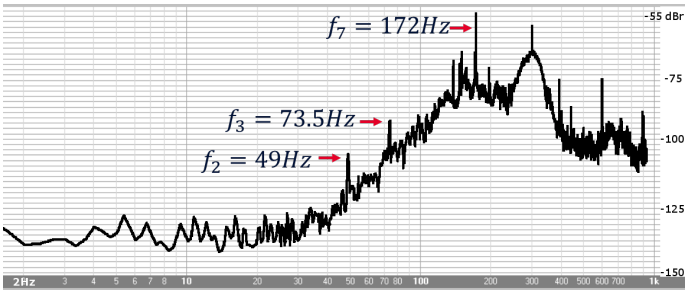


(b) Captured PSD of the perturbation by means of PC microphone

Figure 6.9: Picture of the cable under test and captured spectrum (PSD) of the perturbation near the cable under test

conditioning system 10m distant from the cable and located near the second building. Preliminary acoustic measurements were performed by means of a spectrum analyzer (from a computer microphone): we display the spectrum of the measurement in Figure 6.9(b), however it is performed with a computer microphone, visible in Figure 6.9(a), hence a modest range and quality (spectral response dimmed below 100Hz). The measurements show a spectral signature made of a 24.5Hz fundamental component and harmonics up to the seventh rank (172Hz). Sonometer measurements (not displayed) showed a stable low acoustic pressure of 63dBC/45dBA SPL at the cable.

**Probing channel and coexistence with data channels** The above-described fibre setup is used for the transmission of full C-band data, except for ITU-C51 DWDM slot enclosing the sensing signal, as displayed in the channel set-up in Figure 6.10. The two channels adjacent to the sensing wavelength transport each 600Gb/s telecommunication data and are monitored throughout this study to assess the impact of the sensing channel on data transmission performance.

**Data transmission settings** As shown in Figure 6.11, the sensing signal is coupled to the transmitted C-band channels through a 10/90 optical coupler to set the power of the sensing signal in ITU-C51 slot similar to other DWDM slots used for transmission. In order to keep the overall set-up simple, we monitor the DWDM slots that are adjacent to the sensing signal, and the other DWDM slots are filled with loading channels. The DWDM testbed is composed of 82 loading Distributed FeedBack (DFB) lasers spaced by

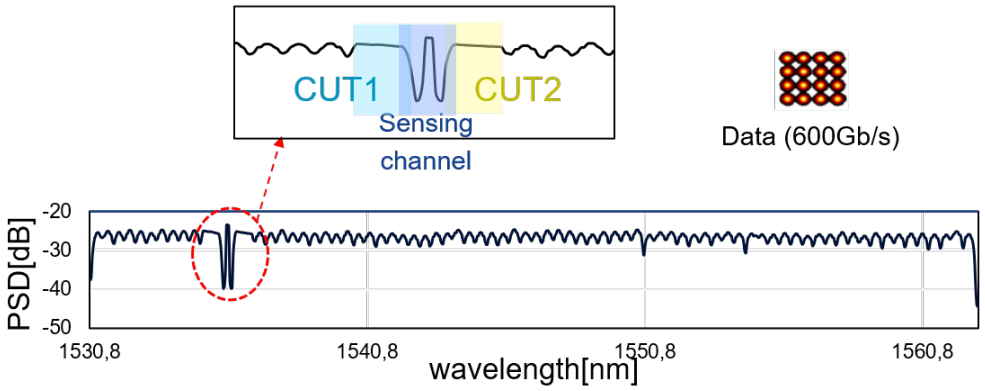


Figure 6.10: Coexistence of sensing and telecom data: Channel arrangement. CUT: Channel under test; PSD: Power Spectral Density

50GHz, plus two Channels Under Test (CUT).

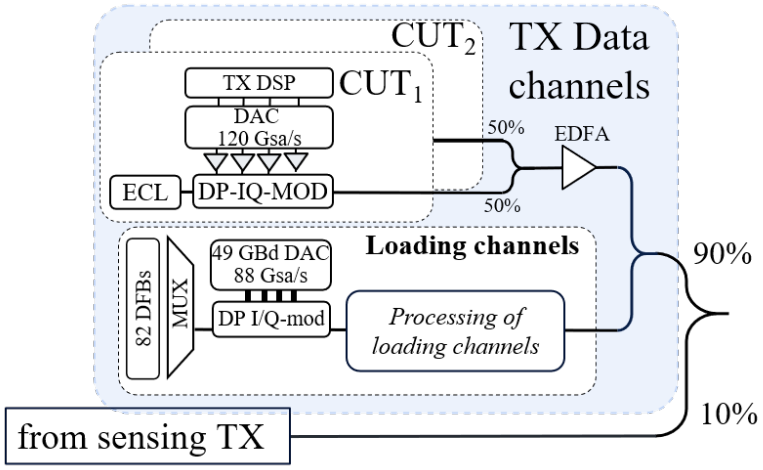


Figure 6.11: Data transmission set-up. CUT: Channel under test; DFB: Distributed FeedBack lasers; ECL: External Cavity Laser

The loading channels are modulated at 49GBd with Dual Polarization (DP) 16QAM modulation and Nyquist pulse shaping using 0.01 roll-off. The specific processing of the loading channels mentioned in Figure 6.11 is not further developed here. The CUTs for data transmission each occupy two consecutive 50GHz slots and are modulated at 90GBd with DP-16QAM, carrying 600Gb/s net bit rate in 100GHz spacing.

**Probing method and set-up** The digital sensing interrogator probes the full span at a rate $f_{symb}$ using digitally generated linear frequency sweep signals covering a $[0 : f_{symb}/2]$ bandwidth over a period $T_{sweep} \geq T_{ir}$, where $T_{ir}$ is the round-trip time of light in the fibre. Though formally less efficient than MIMO codes, sweep probing requires a laser source coherence restricted to the sole fibre round-trip time as described in subsubsection 1.2.4.3, enhancing the sensing range. Moreover, the sweep interrogation is performed on a single polarization, and although the SIMO sweep is subject to polarization fading effects (see chapter 3), it allows to relax again the condition on the length of the probing sequence, therefore relaxing the coherence length constraints of the laser. This probing choice is

justified here to increase as much as possible the distance to sense with the available laser source, at the cost of a higher noise floor.

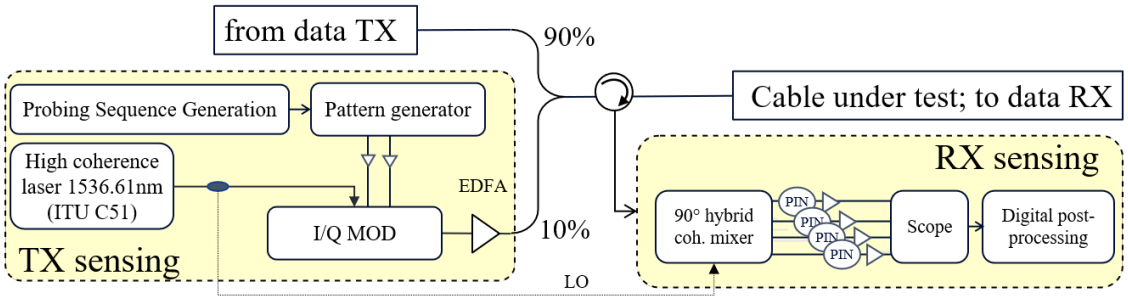


Figure 6.12: Sensing set-up: transmitter and receiver. CUT: Channel under test

A high coherence laser source at 1536.6nm is modulated continuously and periodically at the sweep period $T_{sweep}$. The use of continuous probing reduces the Peak-to-Average Power Ratio (PAPR) with respect to pulsed probing, thus avoiding non-linear induced distortions on surrounding DWDM channels.

**Reception of sensing and transmission signals** The generated full C-band comb is launched into the fibre span at 18dBm, yielding an average channel power of −1dBm per 50GHz slot. At the receiver side, after 82km of SSMF, the CUTs are selected using a WSS (Wavelength Selective Switch) before being sent to the coherent receiver as depicted in Figure 6.13. A high-speed sampling scope operating at 256GS/s is used to store waveforms and digital signal processing [72] is performed offline to measure the output SNR of each 600Gb/s channel under test.

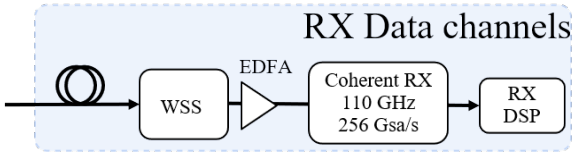


Figure 6.13: Co-propagating sensing and DWDM channels: Data channels receiver set-up

The backscattered light is captured at the launching end of the fibre span by another coherent receiver in Figure 6.12. As illustrated in the figure, self-homodyne configuration of the coherent receiver captures the signal backscattered from the sole sensing slot. After correlation with the transmitted signals, the coherent sensing system recovers the backscattered optical field and extracts a segmented representation of the probed fibre where the differential phase is characterized at each segment along the fibre path.

### 6.2.3 Sensor performance results

The fibre span is interrogated continuously with $f_{symb}$ = 50MBaud, covering a 600Hz sensing bandwidth. The standard deviation of the backscattered phase denoted $\sigma_\varphi$ is given in Figure 6.14 and Figure 6.15 for the three different scenarios depicted in Figure 6.8. First, the deployed fibre cable is placed at the start of the span, and its phase variations signature is captured in Figure 6.14(a). After such short distance (0.4km before reaching

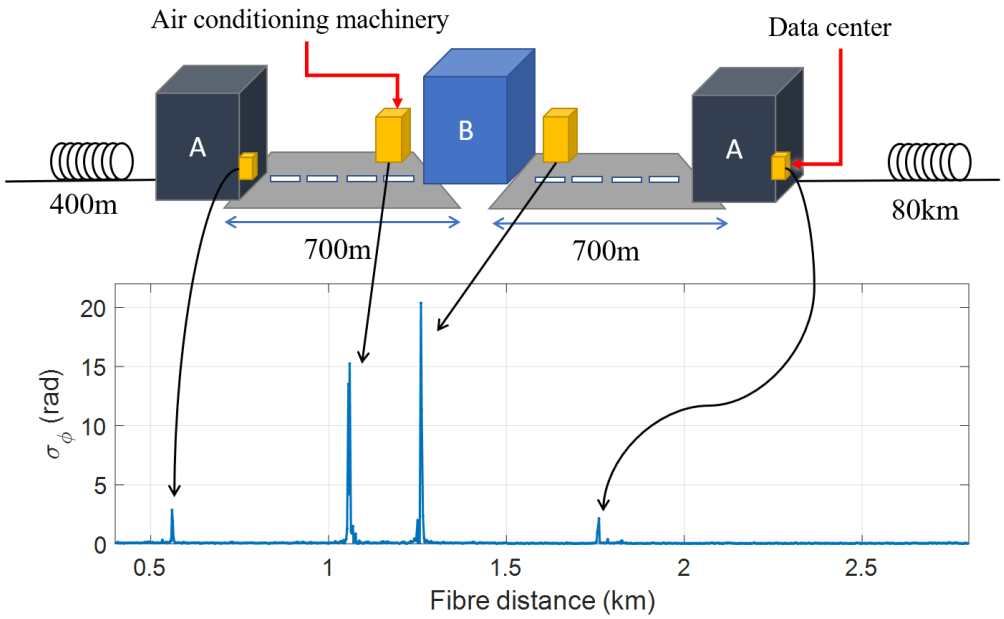


(a) Deployed cable after 400m fibre: air conditioning system detected at 1.1km and 1.3km, data center machinery triggers smaller alarms

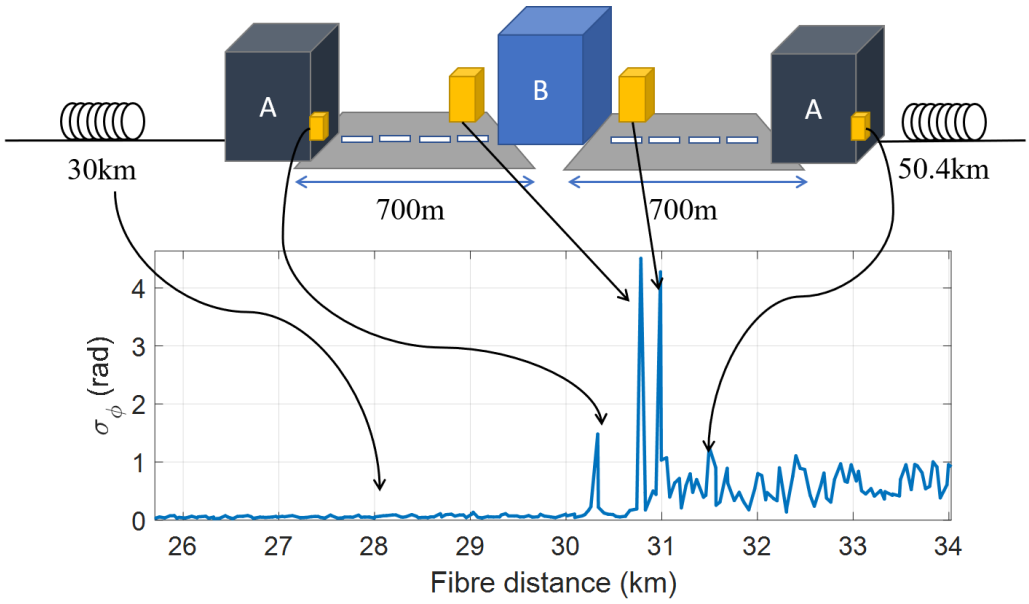


(b) Deployed cable after 30km fibre

Figure 6.14: Phase variations induced by two main external vibration sources, deployed cable placed after different fibre lengths

the deployed cable), the $\sigma_\varphi$ along distance is given at the native resolution of the system ($L_s = 2.05$m), therefore the phase variations due to both the crossing of a datacenter at the beginning of the fibre cable and the presence of an air conditioning system halfway-through the cable path are detected as different peaks. Moreover, as described in Figure 6.8, the deployed fibre cable experiences the external vibrations twice as it performs a round trip between two buildings, leading to the 4 distinct peaks in Figure 6.14(a).

Note that the round-trip is not needed for either detection or localization purposes, and it is set this way because of the experimental setup configuration where the transmitter and receivers are located in the same building. Yet, this round-trip of the fibre allows to double-check the location of the perturbations: the two highest $\sigma_\varphi$ peaks in Figure 6.14(a) are distant of 200.4m meaning that the air conditioning system is located approximately 100m away from the fibre turnaround (where the fibre cable loops). It is approximative since the noisy system is located several metres from the fibre paths as described earlier. Then, a 30km fibre span is inserted between the TX and the cable (Figure 6.14(b)). The datacenter and air conditioning systems are still correctly localized and identified with a spatial sampling resolution finer than 10m, allowing to differentiate between the different detection peaks.

An increase of the detected $\sigma_\varphi$ is observed at the right side of Figure 6.14(b), therefore of the detection threshold. This is a consequence of the strong disturbance induced by the air conditioning system vibrations: when disturbances giving rise to phase variations over $2\pi$, unwrapping issued can occur, which in turns degrade the computation of differential phase for the following fibre segments. In the presence of noise or attenuation (due to the increased distance from the probing source), such as here in Figure 6.14(b) after 31km fibre, the issue is somehow amplified. This issue has to be addressed through digital signal processing. Yet, we do not address it here. In such conditions, multi-event detection could be compromised at long distances: in Figure 6.14(b), the second $\sigma_\varphi$ due to the data-center machinery noise is only slightly above the increased detection threshold.

**Acoustic event detection after 80km SSMF** Finally, the fibre cable is connected after 80km SSMF and the full evolution of $\sigma_\varphi$ along the fibre span is given in Figure 6.15. In Figure 6.15(a), the $\sigma_\varphi$ is displayed with a coarse spatial sampling resolution of 51m. Strong variations due to laser phase noise are noticed along the fibre. After 81km, $\sigma_\varphi$ peaks are noticed on the trace, as displayed in the inset of Figure 6.15(a). To make sure the peaks are an alarm and not another noise peak at the coherence length limit of the laser source, further spatial averaging was needed, thus decreasing the spatial sampling resolution to $L_{coarse} = 102$m. Therefore, the peaks are not differentiated any more and appear as one single event, yielding a single $\sigma_\varphi$ detection peak at 81km in Figure 6.15(b).

Nevertheless, successful identification of the disturbance induced by the air conditioning machinery is observed at such distance as shown by the PSD of the phase in Figure 6.16(a). The PSD of phase at the $\sigma_\varphi$ peaks locations gives the spectral signature of the machinery, in line with the acoustic measurement performed near the cable displayed

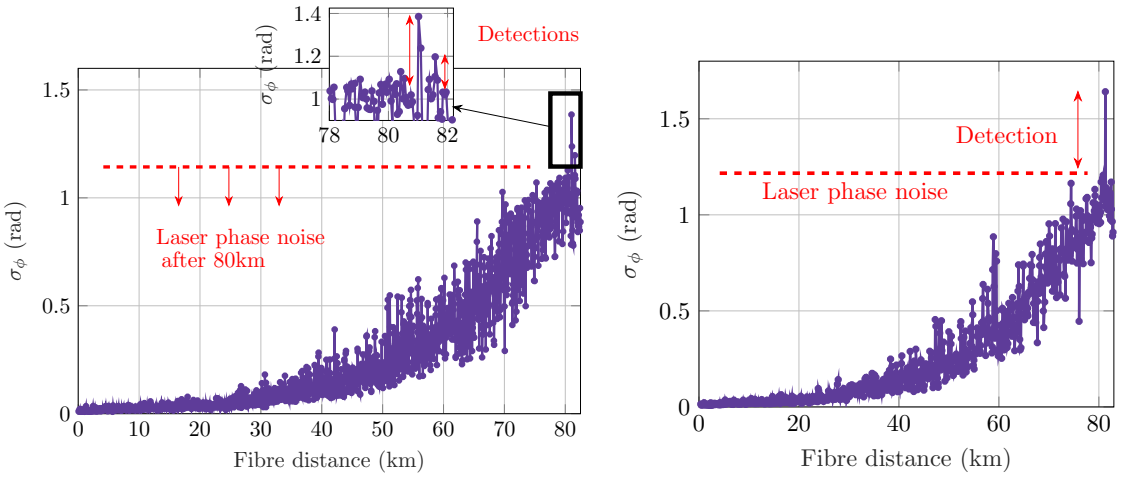


(a) Lower spatial sampling resolution 51m, zoom on detection peaks

(b) Lower spatial sampling resolution 102m, one detection peak

Figure 6.15: Phase variations induced by two main external vibration sources (200m spacing): deployed cable after 80km fibre

in Figure 6.9 (harmonic spectrum with 24.5Hz fundamental frequency). After 81km, the fundamental and third order harmonic are visible on the spectrum, exceeding the noise level by nearly 10dB. We display the time evolution of the phase in Figure 6.16(b), illustrating how the fundamental frequency went weaker at 81km compared to 31km, whereas some harmonics remain which bring a periodic shape to the phase at 81km despite the noise floor.

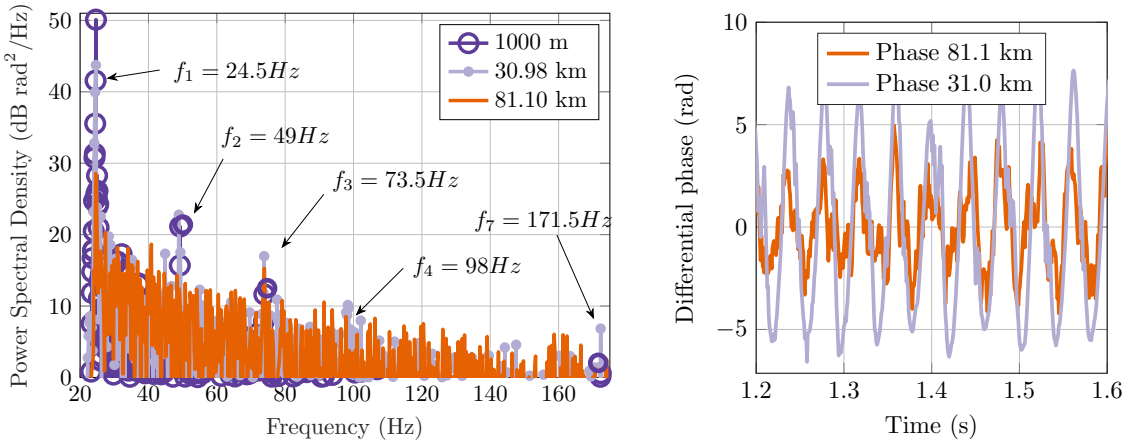


(a) Power spectral density (PSD)

(b) Differential phase in time

Figure 6.16: Differential phase and its power spectral density at $\sigma_\varphi$ detection peak location: identification of the disturbance for different distances from the fibre start

### 6.2.4 Transmission performance results

Finally, we analyze the performance of the adjacent coherent channels carrying 600Gb/s data. The experiment will be considered as successful if the presence of a sensing channel doesn't impact the data.

The SNR of the detected 16QAM constellations is measured at the receiver side. First,

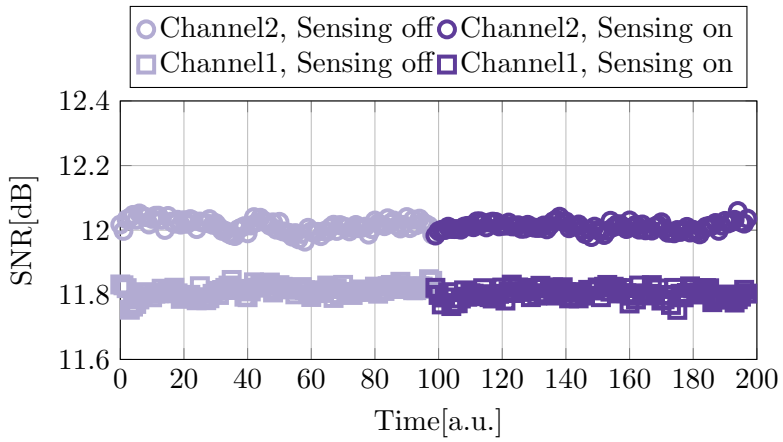


Figure 6.17: Measured SNR of CUTs with and without sensing signal

the sole loading data and channels under test are switched on, and the SNR is given in Figure 6.17, for the 100 first time units, and for both channels under test. The SNR for CUT1 is about 0.2dB below CUT2. Then the sensing channel is switched on: it operates in a 50GHz spacing in ITU grid 51. The SNR is measured for 100 more time units in Figure 6.17. Overall, the measured SNR after 82km transmission is left unchanged while switching on and off the sensing signal.

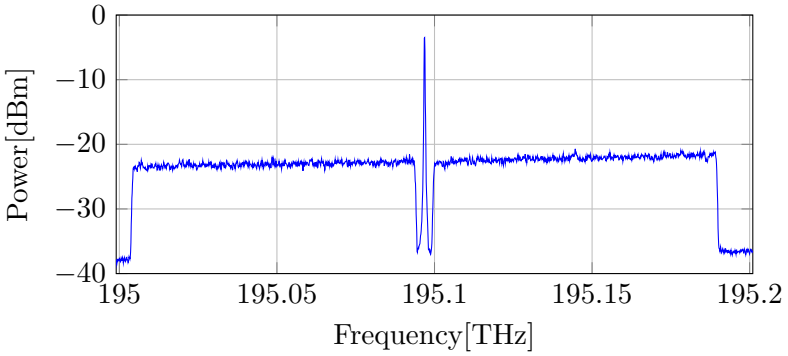


Figure 6.18: Optical spectrum of CUTs spaced 2GHz apart from the sensing signal

The next experiment is about channel spacing. The set-up that was used during the sensing experiments above was realized with a 25GHz frequency spacing between the sensing spectrum and the data on channels under test 1&2. Now the CUTs are brought closer and closer to the sensing signal, up to a 2GHz spacing in Figure 6.18. It was not possible to perform smaller spacing due to the coarse granularity of the WSS used in the experiment.

Finally, we measure the impact of setting the CUTs closer and closer to the sensing signal in Figure 6.19. The results are displayed for CUT2, although the conclusions are similar for CUT1 and 2. The SNR performance of the channel 2 (centered around $f = 195.15$THz in Figure 6.18) remains stable as we approach the sensing signal down to 2GHz. This result further demonstrates the non-intrusive coexistence of our digital sensing system with high speed transmission data.

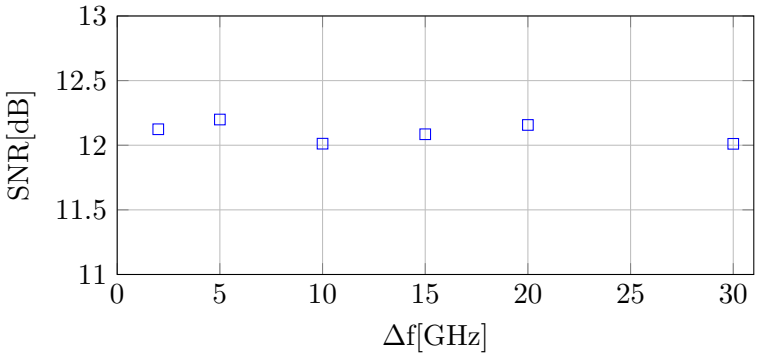


Figure 6.19: Measured performance of CUT 2 vs frequency spacing

Detection, localization, and identification of a true vibration event was performed over a deployed fibre cable after 82km fibre distance, together with co-propagating 600Gb/s DWDM data transmission. We observed not only a lack of impact on the transmitted DWDM data with a standard spacing as a 50GHz ITU slot is allocated to the sensing signal, we also noticed no impact of the digital coherent sensing system over the transmitted data down to 2GHz band spacing. This result is paving the way for a per span high sensitivity-high bandwidth vibration monitoring of in use telecom networks seamless to the transmitted data traffic.

## 6.3 Quasi-distributed forward scheme for long range sensing

In this section, a technique addressing long-distance sensing (namely far beyond 100km fibres) is presented.

We were able to perform sensing of an acoustic vibration over 82km SSMF in the previous section. The current distance records in dynamic, $\phi$-OTDR are, to the writers' knowledge: 131km ultra-long $\phi$-OTDR with high sensitivity [88] on dedicated fibres with Raman amplification, 150km hybrid BOTDA-$\phi$-OTDR [139], 226.3km bi-directional amplification $\phi$-OTDR system [140], 160km without in-line amplifiers [141]. All these systems need either a special fibre coating or specific amplification somewhere on the line, and sometimes use secondary techniques such as Raman amplification that could disturb the co-propagating signals in the case where the used line is not a dedicated fibre (but, say, a dedicated linewidth). Indeed, although Raman amplification can be used for both data and sensing channels, the required configuration (bi-directional amplifiers, filtering...) might differ [140]. In addition, the noise source detected in these references were likely to have a much higher pressure level at the cable side than the one in our experimentation (we work with acoustic disturbances of normal conversation level which are obviously far less energetic than earthquakes of hammer strokes on utility poles).

In order to increase the reach of distributed fibre sensors, the principle of forward sensing or phase sensing was investigated by several groups of researchers. In section 1.3, we mentioned [8] where phase sensing was performed over 535km deployed fibre: the issue with phase sensing however is the absence of straightforward localization data. Localization for phase sensing was proposed in [47] where the fibre sensor still performs a

round-trip in the environment to be monitored. An outline schematic of the sensor is given in Figure 6.20. At the turnaround, a loop with a delay line and an AOM is added,

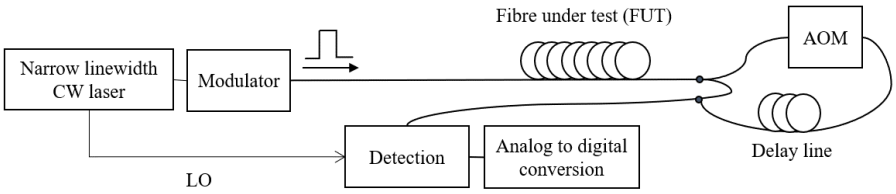


Figure 6.20: Outline schematic of a phase sensing set-up with possible localization, with coupled delay line and Acousto-Optic Modulator (AOM), adapted from [47]

such that one fraction of the sensing signal is delayed and shifted in frequency: assuming a mechanical event occurred and was detected on both ways, the shifted and delayed signal will allow to deduce the localization of the event. However, the localization is computed under certain conditions which restrain the possible frequency range in which an event is detected, and the gauge length of the system is rather large. What we retain from [47] is that localization in phase sensing is obtained under the condition of changing the design of the fibre sensor, from a simple fibre loop to something more complex.

Other possible methods for localization for forward phase sensing rely on the synchronization of fibre-optic communication networks. Relying on commercial transponders synchronization, a localization accuracy of 7km over 380km bidirectional WDM link was demonstrated [142] for the detection of strong disturbances (hammer on utility poles). In the future, such mechanisms are expected to allow for localization in $10,000$km long fibre cables for geophysical measurements [48], this time using the polarization information (SOP) gathered from the commercial transponders.

**Taking advantage of the submarine cable topology** Currently deployed submarine cables enclose bidirectional fibre links, where both forward and backward directions are amplified. The backwards direction is referred to as the "supervision channel", into which a fraction of the forward channel power is coupled after each amplifier. An outline schematic of the fibre link is presented in Figure 6.21. Such a fibre configuration is called "ladder

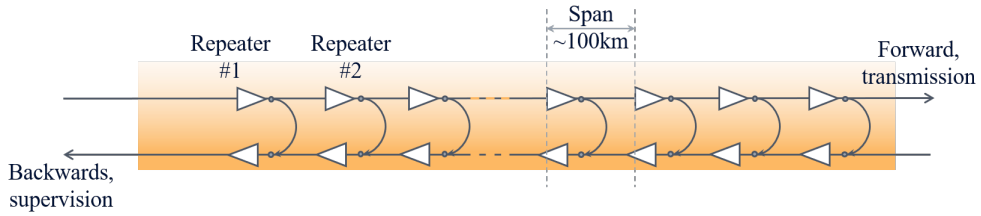


Figure 6.21: Outline schematic of a possible bidirectional fibre link configuration in a submarine cable

topology". Different types of information travel down the supervision channel, in some cases including an intensity-OTDR for detection and localization of major losses and breaks [45].

Leveraging the recent advances on (forward) phase-sensing and phase-OTDR, we propose a distributed forward sensing method adapted to the submarine cables configuration [143]. The principle is similar to the $\Delta\phi$-OTDR, using a narrow linewidth laser source and modulated probing sequences, only it relies on the optical signal returning from the supervision channel instead of backscattered light. The main reasons are:

- Backscattered signal does not cross the amplifiers, which would limit a traditional $\Delta\phi$-OTDR to the first span of the fibre link
- Attenuation is too important after 100km, therefore almost no backscattered signal would be recovered. The supervision channel allows to retrieve direct transmitted light that is far more intense than backscattered one

As a consequence, the system is not fully distributed any more, as the feedback loops (coupling from forward, transmission channel to supervision channel) now act as the reflectors in the fibre. Similarly to FBG-based fibre sensors, we call this configuration "quasi-distributed".

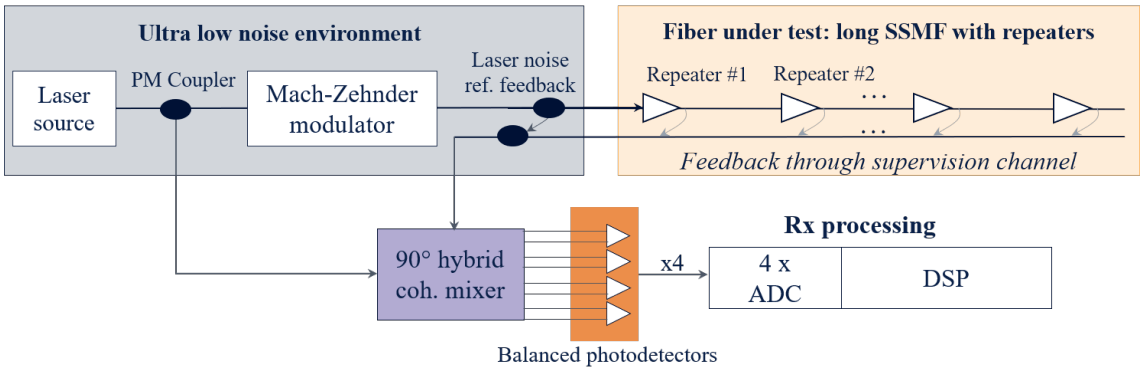


Figure 6.22: Interrogation system and fibre cable sensor design

Figure 6.22 displays the general set-up of such an interrogator that probes a submarine cable. In the proposed setup, a specific reference feedback is added to the interrogator before connecting to the cable under test. This allows to have an estimation of the noise contributions which are inherent to the interrogator set-up: white noises and most importantly laser phase noise. This reference noise will be subtracted to the other incoming signals such that the sole environmental noises are retrieved.

Figure 6.23 shows the difference between our sensor architecture (quasi distributed sensor) and the usual distributed sensor architecture using reflectometry, together with their intensity responses.

- On the left of Figure 6.23, the sensor is an optical fibre with silica impurities responsible for Rayleigh backscattering effect. We call them "scatterers". The number of scatterers is huge compared to the length of the fibre, and so the number of estimates extracted from the fibre will depend on the interrogation frequency (one estimate per group of scatterers). The interrogation baud rate $f_{Symb}$ defines the resolvable length or spatial sampling resolution of the sensing system. Such a response spreads on twice the length of the probed line, leading to a spreading time $T_{IR} = 2.L_{fibre}.c_{fibre}$,

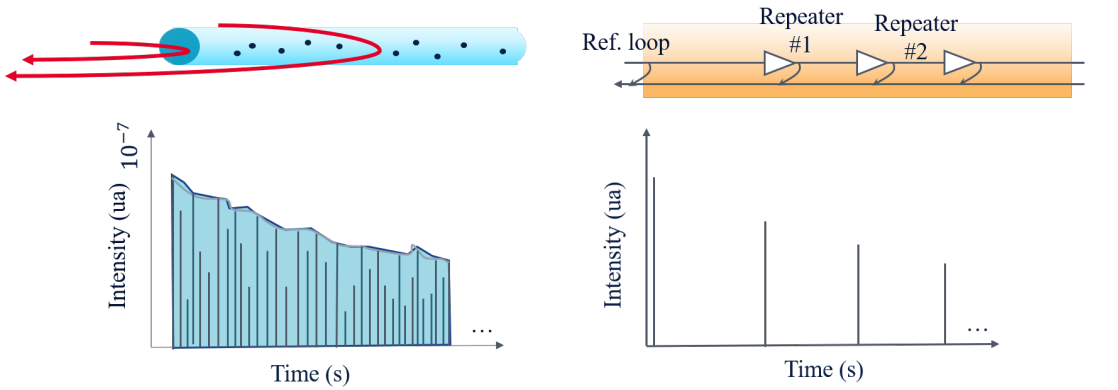


Rayleigh backscatter intensity response

Forward sensing intensity response of a multi-spans cable

Figure 6.23: Comparison of distributed and quasi-distributed sensor outputs

with $c_{fibre}$ the speed of light in the optical fibre.

- On the right of Figure 6.23 is the architecture of a long-distance optical cable with repeaters, which is our sensor. We call that architecture "ladder topology". A part of the signal is coupled back to the feedback channel after each repeater: the measured signal is the integral of the dynamic strain over the entire fibre propagation path (up to the coupler). Since there are several spans, several impulse signals are received. In that case, the length of the spans defines the spatial resolution and gauge length of the system.

Using a Coherent-MIMO interrogator, it is possible to retrieve full Jones matrices from each rung on the ladder, which are forward Jones matrices of the full span followed by the full supervision span (on the way back). The retrieved information will be reliable under the condition of laser coherence, similarly to Rayleigh backscatter sensing.

Overall, such a set-up allows to combine the advantages of phase-sensing (long reach) and distributed acoustic sensing (distance-resolved measurements) for sensing on submarine cables provided the availability of a highly coherent laser source, in line with the long distance to sense.

# Conclusion and perspectives

In a world crisscrossed over and over by telecommunications fibres at increasing rate, where quality of service, automation, and infrastructure safety are primary concerns, the need for various types of sensors is a primary concern. Distributed fibre sensors are suited for a wide range of applications, due to their large presence in the ground of cities, roads and oceans, due also to their light weight, low carbon footprint, and moreover because of the ability to sense over tens of kilometres using a single interrogator.

In this thesis, we explored the potential of distributed acoustic sensing on single mode telecommunication fibres, using $\Delta\phi$-OTDR. This Distributed Acoustic and Vibration Sensing technique relies on a narrow linewidth laser for the sensor interrogation and on coherent detection for phase retrieval at the receiver.

First, a review of the different methods for optical fibre sensing interrogation was performed. Several techniques for dual-polarization probing were mentioned and described, including Golay-based probing codes in subsection 1.2.4 (further referred to as "Coherent MIMO") which demonstrate perfect autocorrelation properties, allowing for an enhancement of the backscattered channel estimation process.

Then, a numerical model was developed to explore the limits of $\Delta\phi$-OTDR interrogation of single-mode fibre taking the polarization dimension into account. From this model, we were able to demonstrate that Coherent-MIMO sensor interrogation is immune to polarization fading, which is one of the major impairments in distributed fibre sensors. Beyond the advantage of polarization diversity reception, dual-polarization probing of the fibre sensor allowed to remove input polarization induced phase noise. Once immune to polarization fading, the sensors features a lower distinction threshold, making the detection of low power disturbances possible.

Experimental results of acoustic sensing over a 6kHz mechanical bandwidth onto few kilometres of single mode fibre were displayed, and the gain brought by Coherent-MIMO interrogation for high bandwidth acoustic sensing over standard single mode fibre was quantified compared with more standard sensing approaches (i.e. methods which do not fully exploit polarization diversity).

Another major result of this thesis is the investigation for mitigating coherent fading effects by means of digital signal processing techniques. We proposed a digital frequency diversity scheme which allows to interrogate the fibre sensor on multiple subcarriers carved in the electrical interrogation bandwidth, based on Orthogonal Frequency Division Multi-

plexing (OFDM). By a combination of the different subcarrier estimations using rotated vector sum, this method did effectively mitigate the worst intensity minima induced by coherent fading, thus further lowering the distinction threshold of the sensing system.

Finally, experimental measurements were conducted on long distance, assessing the interest of Coherent-MIMO and other related interrogation methods to detect acoustic disturbances up to 80km telecom fibre. Also, thanks to the low PAPR of Coherent-MIMO interrogation sequences, we were able to demonstrate how sensing signals and telecommunications signals can coexist in a DWDM communication system, without interfering with each other.

All of the works conducted within this thesis, from theoretical studies on the polarization-related fading effects to the experimental demonstration of sensing and telecommunications coexistence in the same fibre, are an invitation to push Distributed Acoustic Sensing (DAS) further thanks to the knowledge acquired throughout the development of high speed optical communications. The encounter of phase-OTDR and digital signal processing is a promising matter.

In the trail of this work, more open questions are to be explored: on the techniques to increase the reach of the $\Delta\phi$-OTDR interrogation system, enhancements could be brought to the laser source, both by refining the laser model for simulations and by stabilizing the laser phase noise in the set-up. On the system noises and distortions that can impact the dynamic range of the captured backscattered signals, digital signal processing could be added to learn from transmitter and receiver noises and thus perform channel deconvolution. In deployed systems, spatial and temporal signal interpolation should be developed to overcome blind-spot related issues for the capture of events. Also in case of strong energy vibrations, specific processing should be developed to overcome unwrapping and slew rate issues. Of course, due to the huge amount of captured data, the development of machine learning techniques to identify and classify specific patterns would accelerate the process of $\Delta\phi$-OTDR traces analysis.

The joint development of interrogator accuracy and pattern recognition, together with the already proven compatibility of Coherent-MIMO and data transmission, presents Coherent-MIMO sensing as a promising technique to capture a wide range of disturbances from already-deployed telecommunication networks. The integration of Coherent-MIMO to the network nodes as a basis for all sorts of sensing is a realistic “next step” towards smart optical networks automation and telemetry.

# Appendix A

# Sound Pressure Level measurements

Sound pressure level measurements were reported throughout this manuscript to quantify either the noise floor in the laboratory or the level of acoustic excitations during the experiments.

Sound pressure is the average variation in atmospheric pressure caused by the sound. The unit of pressure measurement is pascal (Pa, or $N/m^2$). The Sound Pressure Level (SPL) of a sound is measured in decibels (dB). It is equal to

$$20 \log_{10} \left( \frac{P_{sound}}{P_{ref}} \right) \tag{A.1}$$

where $P_{ref}$ is the reference of sound pressure, and $P_{sound}$ is the root mean square (RMS) of the measured sound contributions. In air, $P_{ref} = 2.10^{-5}$Pa (20 $\mu$Pa), which is an approximate of the lowest sound pressure possible to hear for human ear at 1kHz reference frequency.

## Sound pressure filters: dB(A), dB(B) and dB(C)

The human ear has a non uniform sensitivity level along the acoustic frequency range. To adapt to the ear, sound meters are usually fitted with filters. The standard A and C filters are displayed in Figure A.1.

**A-contour filter** To quantify the perceived sound by the ear, the A-contour weighting filters out the lower frequencies, therefore eliminating the Pressure Level of inaudible frequencies. As a consequence, all audible frequencies are not treated equally. Thus, the measured sound power level is given in $dB_{SPL}$ or more precisely $dB_{SPL-A}$.

The A-contour filter is the most commonly used filter for practical assessments of loudness, be it in music concerts or to usually measure ambient sound levels.

**B-contour filter** The B-contour filter will approximate the ear for lower frequencies, thus taking loud bass sounds into account (more weight for low audible frequencies compared with the A-contour filter). It is an intermediate filter between A and C filters that is rarely used.

**C-contour filter** Finally, the C-contour filter will almost not filter out low frequencies. It approximates the ear only at very high sound levels where even low frequencies can cause discomfort.

C-contour filter is used for sound pressure level measurements of traffic noise near highways or plane noise near airports.

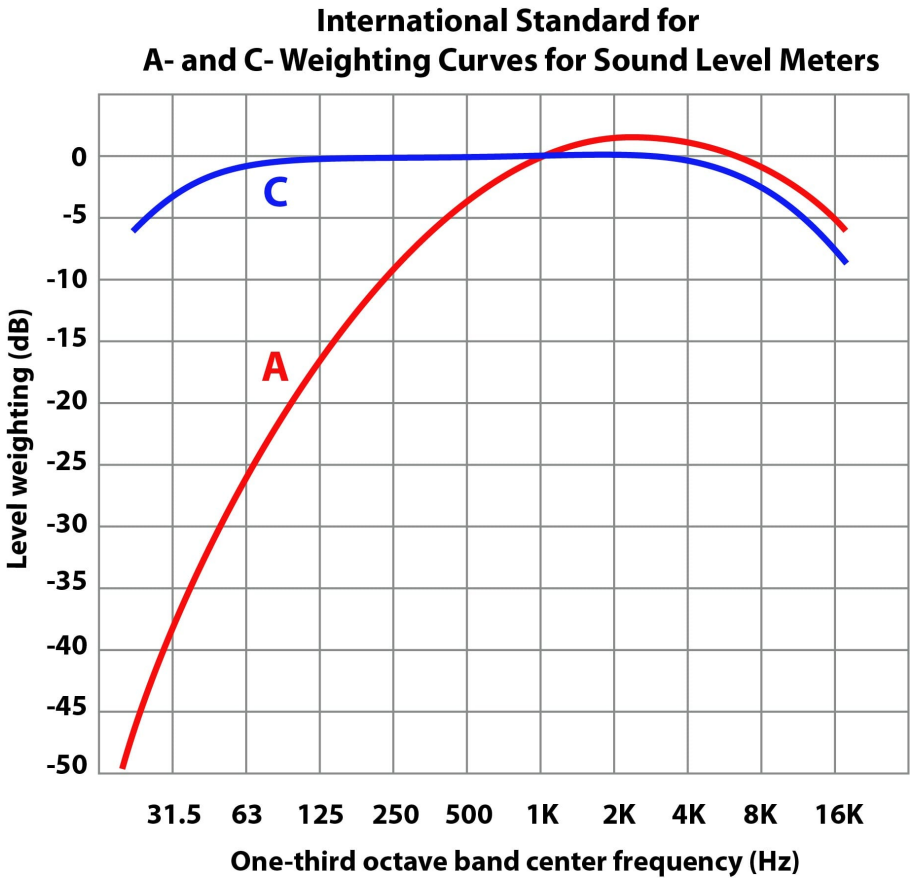


Figure A.1: Comparison of A-contour filter and C-contour filter for sound pressure level measurements [144]

# Appendix B

# Simple OFDM case: frequency or space?

In chapter 5, we have been using a specific case of multi-carrier interrogation: OFDM with same codes to probe each OFDM sub-carrier, which allows to get different phase estimations for the same fibre segments. This appendix aims to go more in-depth in this topic.

## Rayleigh diversity emulation with identically modulated OFDM subcarriers

The fibre sensor is probed by a single laser wavelength (with narrow linewidth), hence the acquisition of a stable, unique Rayleigh backscattered pattern in the context of single-carrier probing. Using Coherent-MIMO sensing, the backscattered pattern is obtained in the form of $2 \times 2$ Jones matrices. The $2 \times 2$ Jones matrices single-carrier estimations are denoted $\mathbf{h}_q$, as depicted in Figure B.1(a), $q$ is the segment index, with a spatial resolution step $L_s$ determined by the symbol rate $f_{Symb} = 1/T_s$ as follows: $L_s = c_{fibre}/2f_{Symb}$.

We have seen that using a digital frequency diversity scheme for the probing codes leads to different backscattering patterns from each subcarrier, see subsection 5.1.3. Now, we will see how the interrogation with OFDM multiplexed interrogation codes runs, in the case where $B_{elec}$ is constant.

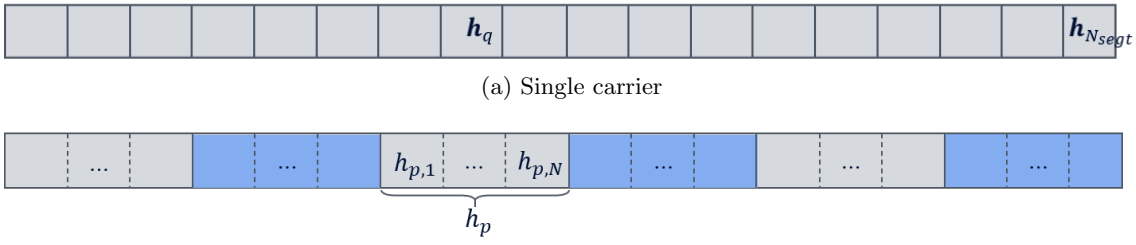


(a) Single carrier

(b) Multi-carrier

Figure B.1: Optical fibre model : spatial segmentation for an interrogation at same bandwidth occupation, $p, q$ are segment indices, $N_{sc}$ is the number of OFDM subcarriers

Figure B.1(b) depicts the probing sequence for a fibre interrogation using OFDM with $N_{sc}$ subcarriers. Following the bandwidth against spatial resolution trade-off with constant $B_{elec}$, the OFDM spatial resolution verifies $L_{s,OFDM} = N_{sc}L_s$. Each OFDM symbol comprises $N_{sc}$ symbols at $f_{Symb}$.

Let's consider a dual-polarization interrogation and detection. The fibre channel is expressed under the form of 2×2 Jones matrices. The following assumptions and definitions are made:

- $N_{sc}$ the number of OFDM subcarriers:
- $\mathbf{h}_n$ the channel response of the sensed fibre with a step determined by the symbol rate $f_{Symb} = 1/T_s$ and a channel length of $L_h$ coefficients or taps (we call them "fibre segments")
- We are sending the same code on all the subcarriers, each code has $N_{code}$ symbols
- We consider an OFDM sequence with duration $T_{seq,OFDM}$ and length $N_{code}$ OFDM symbols, hence $N_{seq,OFDM} = N_{sc}N_{code}$ and therefore $T_{seq,OFDM} = N_{code}N_{sc}T_s$.

During $T_{seq,OFDM}$, we are sending $N_{sc}N_{code}$ symbols. At the iFFT input on the transmitter side, we send:

$$X^1_{in,1}, X^1_{in,2}, \cdots, X^1_{in,N_{sc}}, \cdots, X^{N_{code}}_{in,1}, X^{N_{code}}_{in,2}, \cdots, X^{N_{code}}_{in,N_{sc}} \tag{B.1}$$

When sending the same codes on all subcarriers: $x^k_{out,m} = 0$ for $m > 1$ ($k$: OFDM segment index). Only the first term is non-zero for $m = 1$ for each iFFT. Hence, we are sending an upsampled version of the code (symbols in the Golay code are now separated by $N_{sc} - 1$ zeros. The transmitter sends:

$$x^1_{out,1}, 0, \cdots, 0, x^2_{out,1}, 0, \cdots, 0, x^{N_{code}}_{out,1}, 0, \cdots, 0 \tag{B.2}$$

The receiver will get a convolution of the sent sequence with the channel

$$y_k = y(k) = (\mathbf{h} * x)(k) = \sum_{n=1:N_{sc}:+\infty} x_n \mathbf{h}_{k-n+1} \tag{B.3}$$

This form of the convolution takes into account the upsampling in $x_n$ (meaning that the step here is $N_{sc}$ and not 1 which is the general case for a convolution as there are $N_{sc} - 1$ zero value between two non-null symbols).
The receiver will perform an FFT followed by a correlation with a code to extract the channel response estimate. The discrete form of the FFT is: $Y_l = \sum_{m=1}^{N_{sc}} y_m e^{\frac{-2\pi i l m}{N_{sc}}}$.

For $N_{sc} = 2$ and assuming a channel with 4 segments with respective coefficients $h_1, h_2, h_3, h_4$, up to $y_k$ are:

$$\begin{aligned} y_1 &= h_1 x_1 \\ y_2 &= h_2 x_1 \\ y_3 &= h_3 x_1 + h_1 x_3 \\ y_4 &= h_4 x_1 + h_2 x_3 \\ y_5 &= h_3 x_3 + h_1 x_5 \\ y_6 &= h_4 x_3 + h_2 x_5 \\ &\dots \end{aligned} \tag{B.4}$$

For $N_{sc} = 2$, the FFT operation defined above becomes $Y_{2l-1} = -y_{2l-1} + y_{2l}$ and $Y_{2l} = y_{2l-1} + y_{2l}$ for $l > 0$. In the general case, the estimated channel coefficients are given by:

$$\mathbf{H}_l^k = \sum_{m=1}^{N_{sc}} \mathbf{h}_m e^{-\frac{2\pi i l m}{N_{sc}}} \quad l : 1 \to N_{sc},\ k : 1 \to \lfloor \frac{L_h}{N_{sc}} \rfloor \tag{B.5}$$

where we have $N_{sc}$ versions of each channel response with a spatial resolution corresponding to $N_{sc}T_s$.

As the $N_{sc}$ versions are different channel estimations, the probability to get coherent fading at the same location for all $N_{sc}$ subcarriers decreases with the number of subcarriers, thus bring a mitigation of coherent fading at the sensor output when the outputs of each subcarrier are carefully combined.

# Bibliography


[1] A. H. Hartog, *An Introduction to Distributed Optical Fibre Sensors*. CRC Press, 2017. DOI: 10.1201/9781315119014.

[2] B. Lu *et al.*, "High spatial resolution phase-sensitive optical time domain reflectometer with a frequency-swept pulse," *Opt. Lett.*, vol. 42, no. 3, pp. 391–394, Feb. 2017. DOI: 10.1364/OL.42.000391.

[3] J. Zhang *et al.*, "80 km fading free phase-sensitive reflectometry based on multicarrier NLFM pulse without distributed amplification," *Journal of Lightwave Technology*, vol. 37, no. 18, pp. 4748–4754, Sep. 15, 2019, ISSN: 0733-8724, 1558-2213. DOI: 10.1109/JLT.2019.2919671.

[4] Z. Yang, M. A. Soto, and L. Thévenaz, "200 km fiber-loop brillouin distributed fiber sensor using bipolar golay codes and a three-tone probe," in *International Conference on Optical Fibre Sensors (OFS24)*, H. J. Kalinowski, J. L. Fabris, and W. J. Bock, Eds., Curitiba, Brazil, Sep. 28, 2015, p. 96 340. DOI: 10.1117/12.2195256.

[5] Y. Chen, A. H. Hartog, R. J. Marsh, I. M. Hilton, M. R. Hadley, and P. A. Ross, "A fast high-spatial-resolution Raman distributed temperature sensor," in *23rd International Conference on Optical Fibre Sensors*, J. M. López-Higuera, J. D. C. Jones, M. López-Amo, and J. L. Santos, Eds., International Society for Optics and Photonics, vol. 9157, SPIE, 2014, pp. 797–800. DOI: 10.1117/12.2058109.

[6] J. Park *et al.*, "Raman-based distributed temperature sensor with simplex coding and link optimization," *IEEE Photonics Technology Letters*, vol. 18, no. 17, pp. 1879–1881, 2006. DOI: 10.1109/LPT.2006.881239.

[7] S. Li and Z. Wu, "Development of distributed long-gage fiber optic sensing system for structural health monitoring," *Structural Health Monitoring*, vol. 6, no. 2, pp. 133–143, 2007. DOI: 10.1177/1475921706072078.

[8] G. Marra *et al.*, "Ultrastable laser interferometry for earthquake detection with terrestrial and submarine cables," *Science*, eaat4458, Jun. 14, 2018, ISSN: 0036-8075, 1095-9203. DOI: 10.1126/science.aat4458.

[9] A. Mecozzi, M. Cantono, J. C. Castellanos, V. Kamalov, R. Muller, and Z. Zhan, "Polarization sensing using submarine optical cables," *Optica*, vol. 8, no. 6, p. 788, Jun. 20, 2021, ISSN: 2334-2536. DOI: 10.1364/OPTICA.424307.

[10] O. H. Waagaard *et al.*, "Real-time low noise distributed acoustic sensing in 171 km low loss fiber," *OSA Continuum*, vol. 4, no. 2, p. 688, Feb. 15, 2021, ISSN: 2578-7519. DOI: 10.1364/OSAC.408761.

[11] M. J. Murray and B. Redding, "Quantitative amplitude-measuring $\phi$-OTDR with $p\varepsilon/\sqrt{Hz}$ sensitivity using a multi-frequency pulse train," *Optics Letters*, vol. 45, no. 18, p. 5226, Sep. 15, 2020, ISSN: 0146-9592, 1539-4794. DOI: 10.1364/OL.400159.

[12] I. D. Luch, P. Boffi, M. Ferrario, G. Rizzelli, R. Gaudino, and M. Martinelli, "Vibration sensing for deployed metropolitan fiber infrastructure," *Journal of Lightwave Technology*, vol. 39, no. 4, pp. 1204–1211, Feb. 2021, ISSN: 1558-2213. DOI: 10.1109/JLT.2021.3051732.

[13] M.-F. Huang *et al.*, "First field trial of distributed fiber optical sensing and high-speed communication over an operational telecom network," *Journal of Lightwave Technology*, vol. 38, no. 1, pp. 75–81, 2020, ISSN: 1558-2213. DOI: 10.1109/JLT.2019.2935422.

[14] J. C. G. M, *Evaluation of measurement data — guide to the expression of uncertainty in measurement*, Sep. 2008.

[15] A. Chrysochoos and Y. Surrel, "Basics of metrology and introduction to techniques," in *Full-Field Measurements and Identification in Solid Mechanics*, M. Grédiac, F. Hild, and A. Pineau, Eds., Hoboken, NJ USA: John Wiley & Sons, Inc., Dec. 25, 2012, pp. 1–30, ISBN: 978-1-118-57846-9. DOI: 10.1002/9781118578469.ch1.

[16] SEAFOM. "DAS parameter definitions and tests." (2018), [Online]. Available: http://seafom.com.

[17] A. H. Hartog, "Propagation in optical fibres," in *An Introduction to Distributed Optical Fibre Sensors*, CRC Press, 2017, ch. 2.1. DOI: 10.1201/9781315119014.

[18] S. Shimada, *Coherent lightwave communications technology*. Springer Science & Business Media, 2012.

[19] D. R. Paschotta. "Polarization beat length." (), [Online]. Available: https://www.rp-photonics.com/polarization_beat_length.html (visited on 10/08/2021).

[20] S. D. Personick, "Photon probe — an optical-fiber time-domain reflectometer," *The Bell System Technical Journal*, vol. 56, no. 3, pp. 355–366, Mar. 1977, ISSN: 0005-8580. DOI: 10.1002/j.1538-7305.1977.tb00513.x.

[21] T. Giallorenzi *et al.*, "Optical fiber sensor technology," *IEEE Transactions on Microwave Theory and Techniques*, vol. 30, no. 4, pp. 472–511, Apr. 1982, ISSN: 0018-9480, 1557-9670. DOI: 10.1109/TMTT.1982.1131089.

[22] A. D. Kersey, A. Dandridge, and A. B. Tveten, "Dependence of visibility on input polarization in interferometric fiber-optic sensors," *Opt. Lett.*, vol. 13, no. 4, pp. 288–290, Apr. 1988. DOI: 10.1364/OL.13.000288.

[23] A. D. Kersey, "Recent progress in interferometric fiber sensor technology," in *Microlithography '91, San Jose,CA*, R. P. DePaula and E. Udd, Eds., San Jose, CA, Feb. 1, 1991, p. 2. DOI: 10.1117/12.24724.

[24] M. K. Barnoski and S. M. Jensen, "Fiber waveguides: A novel technique for investigating attenuation characteristics," *Appl. Opt.*, vol. 15, no. 9, pp. 2112–2115, Sep. 1976. DOI: 10.1364/AO.15.002112.

[25] A. J. Rogers, "Polarization-optical time domain reflectometry: A technique for the measurement of field distributions," *Appl. Opt.*, vol. 20, no. 6, pp. 1060–1074, Mar. 1981. DOI: 10.1364/AO.20.001060.

[26] J. N. Ross, "Birefringence measurement in optical fibers by polarization-optical time-domain reflectometry," *Applied Optics*, vol. 21, no. 19, p. 3489, Oct. 1, 1982, ISSN: 0003-6935, 1539-4522. DOI: 10.1364/AO.21.003489.

[27] J. G. Ellison and A. S. Siddiqui, "A fully polarimetric optical time-domain reflectometer," *IEEE Photonics Technology Letters*, vol. 10, no. 2, pp. 246–248, Feb. 1998, ISSN: 1041-1135. DOI: 10.1109/68.655373.

[28] P. Ferdinand, "État de l'art du domaine des capteurs à fibres optiques et réseaux associés : Capteurs répartis par analyse de la polarisation de la lumière rétrodiffusée," Thèse de doctorat dirigée par Ostrowsky, Dan B. Physique Nice 1990, Ph.D. dissertation, Université de Nice, 1990, 1 vol. (740 f.)

[29] A. Rogers, S. Shatalin, and S. Kannellopoulos, "Optical-fibre backscatter polarimetry for the distributed measurement of full strain fields," in *Fiber Optic Sensor Technology and Applications IV*, International Society for Optics and Photonics, vol. 6004, 2005, p. 600 404.

[30] H. Izumita, Y. Koyamada, S. Furukawa, and I. Sankawa, "Stochastic amplitude fluctuation in coherent OTDR and a new technique for its reduction by stimulating synchronous optical frequency hopping," *Journal of Lightwave Technology*, vol. 15, no. 2, pp. 267–278, Feb. 1997, ISSN: 1558-2213. DOI: 10.1109/50.554377.

[31] J. W. Goodman, "Some fundamental properties of speckle," *Journal of the Optical Society of America*, vol. 66, no. 11, p. 1145, Nov. 1, 1976, ISSN: 0030-3941. DOI: 10.1364/JOSA.66.001145.

[32] P. Healey, "Fading in heterodyne OTDR," *Electronics Letters*, vol. 20, no. 1, pp. 30–32, Jan. 1984, ISSN: 0013-5194. DOI: 10.1049/el:19840022.

[33] Y. Muanenda, C. J. Oton, S. Faralli, and F. Di Pasquale, "A cost-effective distributed acoustic sensor using a commercial off-the-shelf DFB laser and direct detection phase-OTDR," *IEEE Photonics Journal*, vol. 8, no. 1, pp. 1–10, Feb. 2016, ISSN: 1943-0655. DOI: 10.1109/JPHOT.2015.2508427.

[34] J. Juarez, E. Maier, K. N. Choi, and H. Taylor, "Distributed fiber-optic intrusion sensor system," *Journal of Lightwave Technology*, vol. 23, no. 6, pp. 2081–2087, Jun. 2005, ISSN: 1558-2213. DOI: 10.1109/JLT.2005.849924.

[35] P. Healey and D. Malyon, "Otdr in single-mode fibre at 1.5 $\mu$m using heterodyne detection," *Electronics Letters*, vol. 18, no. 20, pp. 862–863, 1982.

[36] Lu, Yuelan, Tao Zhu, Liang Chen, and Xiaoyi Bao, "Distributed vibration sensor based on coherent detection of phase-OTDR," *Journal of Lightwave Technology*, p. 5 585 644, Nov. 2010, ISSN: 0733-8724, 1558-2213. DOI: 10.1109/JLT.2010.2078798.

[37] M. Chen, A. Masoudi, and G. Brambilla, "Performance analysis of distributed optical fiber acoustic sensors based on $\varphi$-OTDR," *Optics Express*, vol. 27, no. 7, p. 9684, Apr. 1, 2019, ISSN: 1094-4087. DOI: 10.1364/OE.27.009684.

[38] J. J. Mompó, L. Shiloh, N. Arbel, N. Levanon, A. Loayssa, and A. Eyal, "Distributed dynamic strain sensing via perfect periodic coherent codes and a polarization diversity receiver," *Journal of Lightwave Technology*, vol. 37, no. 18, pp. 4597–4602, Sep. 2019, ISSN: 1558-2213. DOI: 10.1109/JLT.2019.2913464.

[39] G. A. Cranch and P. J. Nash, "High-responsivity fiber-optic flexural disk accelerometers," *J. Lightwave Technol.*, vol. 18, no. 9, p. 1233, Sep. 2000.

[40] Y. Tong, Z. Li, J. Wang, H. Wang, and H. Yu, "High-speed mach-zehnder-otdr distributed optical fiber vibration sensor using medium-coherence laser," *Photonic Sensors*, vol. 8, no. 3, pp. 203–212, 2018.

[41] J. Jiang *et al.*, "Quasi-distributed fiber-optic acoustic sensing with MIMO technology," *IEEE Internet of Things Journal*, pp. 1–1, 2021, ISSN: 2327-4662. DOI: 10.1109/JIOT.2021.3050924.

[42] S. J. Mihailov *et al.*, "Extreme environment sensing using femtosecond laser-inscribed fiber bragg gratings," *Sensors*, vol. 17, no. 12, p. 2909, 2017.

[43] E. Awwad, C. Dorize, P. Brindel, U. Bertuzzi, J. Renaudier, and G. Charlet, "Large bandwidth phase-sensitive DAS with novel polarization-multiplexed probing technique," in *26th International Conference on Optical Fiber Sensors*, Optical Society of America, 2018, ThE63. DOI: 10.1364/OFS.2018.ThE63.

[44] T. Saitoh, K. Nakamura, Y. Takahashi, H. Iida, Y. Iki, and K. Miyagi, "Ultra-long-distance fiber bragg grating sensor system," *IEEE Photonics Technology Letters*, vol. 19, no. 20, pp. 1616–1618, 2007. DOI: 10.1109/LPT.2007.904918.

[45] A. Leroy and O. A. Sab, "14 - submarine line terminal," in *Undersea Fiber Communication Systems (Second Edition)*, J. Chesnoy, Ed., Second Edition, Academic Press, 2016, pp. 509–549, ISBN: 978-0-12-804269-4. DOI: https://doi.org/10.1016/B978-0-12-804269-4.00014-3.

[46] M. R. Fernández-Ruiz, H. F. Martins, S. Martin-Lopez, and M. Gonzalez-Herraez, "Submarine seismic tomography using optical fibres," *Europhysics News*, vol. 51, no. 3, pp. 22–24, May 2020, ISSN: 0531-7479, 1432-1092. DOI: 10.1051/epn/2020304.

[47] Y. Yan, F. N. Khan, B. Zhou, A. P. T. Lau, C. Lu, and C. Guo, "Forward transmission based ultra-long distributed vibration sensing with wide frequency response," *Journal of Lightwave Technology*, pp. 1–1, 2020, ISSN: 1558-2213. DOI: 10.1109/JLT.2020.3044676.

[48] Z. Zhan *et al.*, "Optical polarization–based seismic and water wave sensing on transoceanic cables," *Science*, vol. 371, no. 6532, pp. 931–936, Feb. 26, 2021, ISSN: 0036-8075, 1095-9203. DOI: 10.1126/science.abe6648.

[49] H. F. Martins, S. Martin-Lopez, P. Corredera, P. Salgado, O. Frazão, and M. González-Herráez, "Modulation instability-induced visibility fading in phase-sensitive OTDR," in *Fifth European Workshop on Optical Fibre Sensors*, L. R. Jaroszewicz, Ed., Krakow, Poland: The International Society for Optical Engineering, May 20, 2013, 87943E. DOI: 10.1117/12.2026062.

[50] Y. Tang, X. Yi, and W. Shieh, "Chapter 13 - optical performance monitoring for coherent optical systems," in *Optical Performance Monitoring*, C. C. Chan, Ed.,

Oxford: Academic Press, 2010, pp. 351–383, ISBN: 978-0-12-374950-5. DOI: https://doi.org/10.1016/B978-0-12-374950-5.00013-4.

[51] G. Charlet *et al.*, "Transmission of 16.4-bit/s capacity over 2550 km using pdm qpsk modulation format and coherent receiver," *J. Lightwave Technol.*, vol. 27, no. 3, pp. 153–157, Feb. 2009.

[52] Q. Liu, L. Liu, X. Fan, J. Du, L. Ma, and Z. He, "A novel optical fiber reflectometry technique with high spatial resolution and long distance," in *Asia Communications and Photonics Conference 2014*, Shanghai: OSA, 2014, AW3I.2, ISBN: 978-1-55752-852-0. DOI: 10.1364/ACPC.2014.AW3I.2.

[53] M. Ren, P. Lu, L. Chen, and X. Bao, "Theoretical and experimental analysis of Φ-OTDR based on polarization diversity detection," *IEEE Photonics Technology Letters*, vol. 28, no. 6, pp. 697–700, Mar. 2016, ISSN: 1941-0174. DOI: 10.1109/LPT.2015.2504968.

[54] G. Yang, X. Fan, B. Wang, Q. Liu, and Z. He, "Polarization fading elimination in phase-extracted OTDR for distributed fiber-optic vibration sensing," in *2016 21st OptoElectronics and Communications Conference (OECC) held jointly with 2016 International Conference on Photonics in Switching (PS)*, Jul. 2016, pp. 1–3.

[55] A. Arnould, "Ultra-wideband and high symbol rate transmission systems for next-generation optical fiber communications," Ph.D. dissertation, Institut polytechnique de Paris, 2021.

[56] K. Kikuchi, "Fundamentals of coherent optical fiber communications," *Journal of Lightwave Technology*, vol. 34, no. 1, pp. 157–179, 2015.

[57] H. F. Martins, K. Shi, B. C. Thomsen, S. Martin-Lopez, M. Gonzalez-Herraez, and S. J. Savory, "Real time dynamic strain monitoring of optical links using the backreflection of live PSK data," *Optics Express*, vol. 24, no. 19, p. 22 303, Sep. 19, 2016, ISSN: 1094-4087. DOI: 10.1364/OE.24.022303.

[58] C. Dorize and E. Awwad, "Enhancing the performance of coherent OTDR systems with polarization diversity complementary codes," *Opt. Express*, vol. 26, no. 10, pp. 12 878–12 890, May 2018. DOI: 10.1364/OE.26.012878.

[59] S. Wang, X. Fan, Q. Liu, and Z. He, "Distributed fiber-optic vibration sensing based on phase extraction from time-gated digital ofdr," *Opt. Express*, vol. 23, no. 26, pp. 33 301–33 309, Dec. 2015. DOI: 10.1364/OE.23.033301.

[60] Z. Zhao *et al.*, "Interference fading suppression in $\phi$-OTDR using space-division multiplexed probes," *Optics Express*, vol. 29, no. 10, pp. 15 452–15 462, May 10, 2021, Publisher: Optical Society of America, ISSN: 1094-4087. DOI: 10.1364/OE.422608.

[61] R. Zhao *et al.*, "Frequency drift mitigation of $\phi$-OTDR using difference-fitting method," *Applied Optics*, vol. 60, no. 2, p. 459, Jan. 10, 2021, ISSN: 1559-128X, 2155-3165. DOI: 10.1364/AO.410938.

[62] K. Tsuji, K. Shimizu, T. Horiguchi, and Y. Koyamada, "Coherent optical frequency domain reflectometry using phase-decorrelated reflected and reference lightwaves," *Journal of Lightwave Technology*, vol. 15, no. 7, pp. 1102–1109, 1997. DOI: 10.1109/50.596955.

[63] R. Goldman, A. Agmon, and M. Nazarathy, "Direct detection and coherent optical time-domain reflectometry with golay complementary codes," *Journal of Lightwave Technology*, vol. 31, no. 13, pp. 2207–2222, Jul. 2013, ISSN: 0733-8724, 1558-2213. DOI: 10.1109/JLT.2013.2264273.

[64] J. Geng, C. Spiegelberg, and S. Jiang, "Narrow linewidth fiber laser for 100-km optical frequency domain reflectometry," *IEEE Photonics Technology Letters*, vol. 17, no. 9, pp. 1827–1829, 2005. DOI: 10.1109/LPT.2005.853258.

[65] J. Pastor-Graells, H. Martins, A. Garcia-Ruiz, S. Martin-Lopez, and M. Gonzalez-Herraez, "Single-shot distributed temperature and strain tracking using direct detection phase-sensitive OTDR with chirped pulses," *Optics express*, vol. 24, no. 12, pp. 13 121–13 133, 2016.

[66] J. Bernard, J. Ducate, Y. Gausson, J. Guillon, and G. Le Blevennec, "Field portable reflectometer for single-mode fiber cables," in *Proc. 10th Eur. Conf. Opt. Commun.*, 1984.

[67] M. Nazarathy *et al.*, "Real-time long range complementary correlation optical time domain reflectometer," *Journal of Lightwave Technology*, vol. 7, no. 1, pp. 24–38, Jan. 1989, ISSN: 0733-8724. DOI: 10.1109/50.17729.

[68] M. Jones, "Using simplex codes to improve OTDR sensitivity," *IEEE Photonics Technology Letters*, vol. 5, no. 7, pp. 822–824, Jul. 1993, ISSN: 1941-0174. DOI: 10.1109/68.229819.

[69] Y. Wu, Z. Wang, J. Xiong, J. Jiang, and Y.-J. Rao, "Bipolar-coding $\phi$-OTDR with interference fading elimination and frequency drift compensation," *Journal of Lightwave Technology*, pp. 1–1, 2020, ISSN: 1558-2213. DOI: 10.1109/JLT.2020.3003440.

[70] R. C. Jones, "A new calculus for the treatment of optical systems i. description and discussion of the calculus," *J. Opt. Soc. Am.*, vol. 31, no. 7, pp. 488–493, Jul. 1941. DOI: 10.1364/JOSA.31.000488.

[71] G. A. Wellbrock *et al.*, "First field trial of sensing vehicle speed, density, and road conditions by using fiber carrying high speed data," in *2019 Optical Fiber Communications Conference and Exhibition (OFC)*, Mar. 2019, pp. 1–3.

[72] A. Arnould *et al.*, "Field trial demonstration over live traffic network of 400 Gb/s ultra-long haul and 600 Gb/s regional transmission," in *46th European Conference on Optical Communication (ECOC 2020)*, Dec. 2020.

[73] F. Pittalà, A. Mezghani, F. N. Hauske, Y. Ye, I. T. Monroy, and J. A. Nossek, "Efficient training-based channel estimation for coherent optical communication systems," in *Advanced Photonics Congress*, Optical Society of America, 2012, SpTu3A.4. DOI: 10.1364/SPPCOM.2012.SpTu3A.4.

[74] C. Dorize, E. Awwad, S. Guerrier, and J. Renaudier, "Optimal probing sequences for polarization-multiplexed coherent phase OTDR," in *Optical Fiber Sensors Conference 2020 Special Edition*, Washington, DC: OSA, 2021, T3.23, ISBN: 978-1-55752-307-5. DOI: 10.1364/OFS.2020.T3.23.

[75] S. Guerrier, C. Dorize, E. Awwad, and J. Renaudier, "A dual-polarization rayleigh backscatter model for phase-sensitive OTDR applications," in *Optical Sensors and*

*Sensing Congress*, San Jose, California: OSA, 2019, ETu3A.4, ISBN: 978-1-943580-61-3. DOI: 10.1364/ES.2019.ETu3A.4.

[76] J. Peterson and G. Vurek, "Fiber-optic sensors for biomedical applications," *Science*, vol. 224, no. 4645, pp. 123–127, 1984, Publisher: American Association for the Advancement of Science, ISSN: 0036-8075. DOI: 10.1126/science.6422554.

[77] D. Tosi, S. Poeggel, I. Iordachita, and E. Schena, "11 - fiber optic sensors for biomedical applications," in *Opto-Mechanical Fiber Optic Sensors*, H. Alemohammad, Ed., Butterworth-Heinemann, 2018, pp. 301–333, ISBN: 978-0-12-803131-5. DOI: https://doi.org/10.1016/B978-0-12-803131-5.00011-8.

[78] A. Beisenova, A. Issatayeva, S. Korganbayev, C. Molardi, W. Blanc, and D. Tosi, "Simultaneous distributed sensing on multiple MgO-doped high scattering fibers by means of scattering-level multiplexing," *Journal of Lightwave Technology*, vol. 37, no. 13, pp. 3413–3421, 2019, ISSN: 0733-8724. DOI: 10.1109/JLT.2019.2916991.

[79] P. Clément, R. Gabet, V. Lanticq, and Y. Jaouën, "B-OTDR solution for independent temperature and strain measurement in a single acquisition," *Journal of Lightwave Technology*, vol. 39, no. 18, pp. 6013–6020, Sep. 2021, ISSN: 1558-2213. DOI: 10.1109/JLT.2021.3088956.

[80] "Structural health monitoring — febus-optics." (), [Online]. Available: https://www.febus-optics.com/en/page/structural (visited on 11/16/2021).

[81] "Structural health monitoring — luna inc.," Luna. (), [Online]. Available: https://lunainc.com/solution/structural-health-monitoring (visited on 11/16/2021).

[82] P. Ferdinand, S. Magne, and G. Laffont, "Enhancing safety in nuclear power plant with optical fiber sensors," in *Int. Conf. on Fast Reactors ans Related Fuel Cycles, Safe Techn. and Sustainable Scenarios (FR13), Paris*, 2013, pp. 4–7.

[83] E. F. Williams *et al.*, "Distributed sensing of microseisms and teleseisms with submarine dark fibers," *Nature Communications*, vol. 10, no. 1, p. 5778, Dec. 18, 2019, ISSN: 2041-1723. DOI: 10.1038/s41467-019-13262-7.

[84] A. Sladen *et al.*, "Distributed sensing of earthquakes and ocean-solid earth interactions on seafloor telecom cables," *Nature Communications*, vol. 10, no. 1, p. 5777, Dec. 2019, ISSN: 2041-1723. DOI: 10.1038/s41467-019-13793-z.

[85] T. Brugière *et al.*, "Polarization activity monitoring of an aerial fiber link in a live network," in *Optical Fiber Communication Conference*, Optical Society of America, 2016, Tu3G–3.

[86] S. Ozharar, Y. Ding, Y. Tian, T. Wang, Y. Yoda, and Y. Aono, "Static weight detection and localization on aerial fiber cables using distributed acoustic sensing," in *Optical Fiber Communication Conference (OFC) 2021*, Optical Society of America, 2021, Tu6F.3.

[87] H. F. Taylor and C. E. Lee, "APPARATUS AND METHOD FOR FIBER OPTIC INTRUSION SENSING," 1993.

[88] F. Peng, H. Wu, X.-H. Jia, Y.-J. Rao, Z.-N. Wang, and Z.-P. Peng, "Ultra-long high-sensitivity Φ-OTDR for high spatial resolution intrusion detection of pipelines," *Optics express*, vol. 22, no. 11, pp. 13 804–13 810, 2014.

[89] Fotech.com. "Advanced DAS border and perimeter security — fotech." (), [Online]. Available: https://www.fotech.com/solutions/security/livedetect/ (visited on 11/16/2021).

[90] L. B. Liokumovich, N. A. Ushakov, O. I. Kotov, M. A. Bisyarin, and A. H. Hartog, "Fundamentals of optical fiber sensing schemes based on coherent optical time domain reflectometry: Signal model under static fiber conditions," *Journal of Lightwave Technology*, vol. 33, no. 17, pp. 3660–3671, Sep. 2015, ISSN: 0733-8724. DOI: 10.1109/JLT.2015.2449085.

[91] A. Masoudi and T. P. Newson, "Analysis of distributed optical fibre acoustic sensors through numerical modelling," *Optics Express*, vol. 25, no. 25, p. 32 021, Dec. 11, 2017, ISSN: 1094-4087. DOI: 10.1364/OE.25.032021.

[92] S. Guerrier, C. Dorize, E. Awwad, and J. Renaudier, "Introducing coherent MIMO sensing, a fading-resilient, polarization-independent approach to $\phi$-OTDR," *Optics Express*, vol. 28, no. 14, p. 21 081, Jul. 6, 2020, ISSN: 1094-4087. DOI: 10.1364/OE.396460.

[93] J. N. Damask, *Polarization optics in telecommunications*. Springer Science & Business Media, 2004, vol. 101.

[94] L. J. Boya, E. Sudarshan, and T. Tilma, "Volumes of compact manifolds," *Reports on Mathematical Physics*, vol. 52, no. 3, pp. 401–422, 2003, ISSN: 0034-4877. DOI: https://doi.org/10.1016/S0034-4877(03)80038-1.

[95] J. N. Damask, "Construction of general unitary matrix," in *Polarization optics in telecommunications*, vol. 101, Springer Science & Business Media, 2004, ch. The spin-vector calculus of polarization, pp. 50–71.

[96] R. B. Sosman, *The Properties of Silica: An introduction to the properties of substances in the solid non-conducting state*. Book Department, The Chemical Catalog Company, Incorporated, 1927, vol. 37.

[97] F. Corsi, A. Galtarossa, and L. Palmieri, "Beat length characterization based on backscattering analysis in randomly perturbed single-mode fibers," *Journal of Lightwave Technology*, vol. 17, no. 7, pp. 1172–1178, Jul. 1999, ISSN: 0733-8724. DOI: 10.1109/50.774250.

[98] M. Fleyer, J. P. Cahill, M. Horowitz, C. R. Menyuk, and O. Okusaga, "Comprehensive model for studying noise induced by self-homodyne detection of backward rayleigh scattering in optical fibers," *Opt. Express*, vol. 23, no. 20, pp. 25 635–25 652, Oct. 2015. DOI: 10.1364/OE.23.025635.

[99] E. Awwad, C. Dorize, S. Guerrier, and J. Renaudier, "Detection-localization-identification of vibrations over long distance SSMF with coherent delta-phi-OTDR," *Journal of Lightwave Technology*, vol. 38, no. 12, pp. 3089–3095, 2020, ISSN: 1558-2213. DOI: 10.1109/JLT.2020.2993167.

[100] M. Fleyer, S. Heerschap, G. A. Cranch, and M. Horowitz, "Noise induced in optical fibers by double rayleigh scattering of a laser with a $1/f^{\nu}$ frequency noise," *Opt. Lett.*, vol. 41, no. 6, pp. 1265–1268, Mar. 2016. DOI: 10.1364/OL.41.001265.

[101] G. D. Domenico, S. Schilt, and P. Thomann, "Simple approach to the relation between laser frequency noise and laser line shape," *Appl. Opt.*, vol. 49, no. 25, pp. 4801–4807, Sep. 2010. DOI: 10.1364/AO.49.004801.

[102] N. Bucalovic, V. Dolgovskiy, C. Schori, P. Thomann, G. D. Domenico, and S. Schilt, "Experimental validation of a simple approximation to determine the linewidth of a laser from its frequency noise spectrum," *Appl. Opt.*, vol. 51, no. 20, pp. 4582–4588, Jul. 2012. DOI: 10.1364/AO.51.004582.

[103] M. R. Fernández-Ruiz, J. Pastor-Graells, H. F. Martins, A. Garcia-Ruiz, S. Martin-Lopez, and M. Gonzalez-Herraez, "Laser phase-noise cancellation in chirped-pulse distributed acoustic sensors," *Journal of Lightwave Technology*, vol. 36, no. 4, pp. 979–985, Feb. 2018, ISSN: 0733-8724. DOI: 10.1109/JLT.2017.2766688.

[104] Y. Shao *et al.*, "Enhancing laser phase-noise immunity of distributed vibration sensor by phase-extraction $\varphi$-OTDR," in *2018 Asia Communications and Photonics Conference (ACP)*, Oct. 2018, pp. 1–3. DOI: 10.1109/ACP.2018.8595805.

[105] C. Dorize, S. Guerrier, E. Awwad, and J. Renaudier, "Identification of rayleigh fading induced phase artifacts in coherent differential $\phi$-OTDR," *Optics Letters*, vol. 46, no. 11, pp. 2754–2757, Jun. 1, 2021, ISSN: 1539-4794. DOI: 10.1364/OL.427944.

[106] M. O. V. Deventer, "Polarization properties of rayleigh backscattering in single-mode fibers," *Journal of Lightwave Technology*, vol. 11, no. 12, pp. 1895–1899, Dec. 1993, ISSN: 0733-8724. DOI: 10.1109/50.257947.

[107] Q. Yan, M. Tian, X. Li, Q. Yang, and Y. Xu, "Coherent $\phi$-OTDR based on polarization-diversity integrated coherent receiver and heterodyne detection," in *2017 25th Optical Fiber Sensors Conference (OFS)*, Apr. 2017, pp. 1–4. DOI: 10.1117/12.2265463.

[108] D. W. Stowe, D. R. Moore, and R. G. Priest, "Polarization fading in fiber interferometric sensors," *IEEE Transactions on Microwave Theory and Techniques*, vol. 30, no. 10, pp. 1632–1635, Oct. 1982, ISSN: 0018-9480. DOI: 10.1109/TMTT.1982.1131301.

[109] J. C. Juarez and H. F. Taylor, "Polarization discrimination in a phase-sensitive optical time-domain reflectometer intrusion-sensor system," *Optics Letters*, vol. 30, no. 24, p. 3284, Dec. 15, 2005, ISSN: 0146-9592, 1539-4794. DOI: 10.1364/OL.30.003284.

[110] F. Gu, Y. Li, L. Liang, and M. Zhang, "Comparison of three combining methods for polarization-diversity receiving in $\varphi$ -OTDR," in *2018 23rd Opto-Electronics and Communications Conference (OECC)*, Jul. 2018, pp. 1–2. DOI: 10.1109/OECC.2018.8729943.

[111] A. D. Kersey, M. J. Marrone, and A. Dandridge, "Observation of input-polarization-induced phase noise in interferometric fiber-optic sensors," *Opt. Lett.*, vol. 13, no. 10, pp. 847–849, Oct. 1988. DOI: 10.1364/OL.13.000847.

[112] A. D. Kersey, M. J. Marrone, and A. Dandridge, "Analysis of input-polarization-induced phase noise in interferometric fiber-optic sensors and its reduction using

polarization scrambling," *Journal of Lightwave Technology*, vol. 8, no. 6, pp. 838–845, Jun. 1990. DOI: 10.1109/50.54500.

[113] S. Lin *et al.*, "Rayleigh fading suppression in one-dimensional optical scatters," *IEEE Access*, vol. 7, pp. 17 125–17 132, 2019, ISSN: 2169-3536. DOI: 10.1109/ACCESS.2019.2895126.

[114] N. Frigo, A. Dandridge, and A. Tveten, "Technique for elimination of polarisation fading in fibre interferometers," *Electronics Letters*, vol. 20, no. 8, pp. 319–320, Apr. 1984, ISSN: 0013-5194. DOI: 10.1049/el:19840216.

[115] H. Gabai and A. Eyal, "On the sensitivity of distributed acoustic sensing," *Optics Letters*, vol. 41, no. 24, p. 5648, Dec. 15, 2016, ISSN: 0146-9592, 1539-4794. DOI: 10.1364/OL.41.005648.

[116] F. Pang *et al.*, "A fading-discrimination method for distributed vibration sensor using coherent detection of $\varphi$-OTDR," *IEEE Photonics Technology Letters*, vol. 28, no. 23, pp. 2752–2755, Dec. 2016, ISSN: 1941-0174. DOI: 10.1109/LPT.2016.2616023.

[117] E. Awwad, C. Dorize, and J. Renaudier, "Efficient multi-event localization from rayleigh backscattering in phase-sensitive OTDR systems," in *Optics and Photonics for Sensing the Environment*, Optical Society of America, 2019, EW6A–2.

[118] C. Dorize, S. Guerrier, E. Awwad, and J. Renaudier, "Capturing acoustic speech signals with coherent MIMO phase-OTDR," in *2020 European Conference on Optical Communications (ECOC)*, Dec. 2020, pp. 1–4. DOI: 10.1109/ECOC48923.2020.9333283.

[119] C. Dorize, E. Awwad, and J. Renaudier, "High sensitivity $\varphi$-OTDR over long distance with polarization multiplexed codes," *IEEE Photonics Technology Letters*, vol. 31, no. 20, pp. 1654–1657, Oct. 2019, ISSN: 1041-1135, 1941-0174. DOI: 10.1109/LPT.2019.2942083.

[120] W. Tomboza, "Characterization of optical fiber for distributed acoustic sensing," M.S. thesis, Institut d'optique Graduate School, Paris Saclay University, 2019.

[121] W. Tomboza, S. Guerrier, E. Awwad, and C. Dorize, "High sensitivity differential phase OTDR for acoustic signals detection," *IEEE Photonics Technology Letters*, vol. 33, no. 13, pp. 645–648, Jul. 1, 2021, ISSN: 1941-0174. DOI: 10.1109/LPT.2021.3084557.

[122] C. Dorize, S. Guerrier, E. Awwad, and J. Renaudier. "Capturing acoustic speech signals." Audio resources. (2020), [Online]. Available: https://bit.ly/soundresourceECOC20.

[123] J. Horáček, V. Radolf, V. Bula, J. Veselỳ, and A. Laukkanen, "Experimental investigation of air pressure and acoustic characteristics of human voice. part 1: Measurement in vivo," *Engineering Mechanics*, vol. 129, 2012.

[124] L. Palmieri and L. Schenato, "Distributed optical fiber sensing based on rayleigh scattering," *The Open Optics Journal*, vol. 7, no. 1, 2013.

[125] D. Chen, Q. Liu, and Z. He, "Phase-detection distributed fiber-optic vibration sensor without fading-noise based on time-gated digital OFDR," *Optics Express*, vol. 25, no. 7, p. 8315, Apr. 3, 2017, ISSN: 1094-4087. DOI: 10.1364/OE.25.008315.

[126] A. H. Hartog *et al.*, "The use of multi-frequency acquisition to significantly improve the quality of fibre-optic-distributed vibration sensing," *Geophysical Prospecting*, vol. 66, pp. 192–202, S1 2018, ISSN: 1365-2478. DOI: 10.1111/1365-2478.12612.

[127] M. J. Murray, A. Davis, C. Kirkendall, and B. Redding, "Speckle-based strain sensing in multimode fiber," *Optics Express*, vol. 27, no. 20, p. 28 494, Sep. 30, 2019, ISSN: 1094-4087. DOI: 10.1364/OE.27.028494.

[128] A. H. Hartog, "Rayleigh backscatter, issues and solutions," in *An Introduction to Distributed Optical Fibre Sensors*, CRC Press, 2017, ch. 6.5.1. DOI: 10.1201/9781315119014.

[129] J. Zhou, Z. Pan, Q. Ye, H. Cai, R. Qu, and Z. Fang, "Characteristics and explanations of interference fading of a $\phi$ -OTDR with a multi-frequency source," *Journal of Lightwave Technology*, vol. 31, no. 17, pp. 2947–2954, Sep. 2013, ISSN: 1558-2213. DOI: 10.1109/JLT.2013.2275179.

[130] M. D. Mermelstein, R. Posey, G. A. Johnson, and S. T. Vohra, "Rayleigh scattering optical frequency correlation in a single-mode optical fiber," *Optics Letters*, vol. 26, no. 2, p. 58, Jan. 15, 2001, ISSN: 0146-9592, 1539-4794. DOI: 10.1364/OL.26.000058.

[131] M. Zabihi *et al.*, "Continuous fading suppression method for $\phi$-OTDR systems using optimum tracking over multiple probe frequencies," *Journal of Lightwave Technology*, vol. 37, no. 14, pp. 3602–3610, Jul. 15, 2019, ISSN: 0733-8724, 1558-2213. DOI: 10.1109/JLT.2019.2918353.

[132] B. Redding, M. J. Murray, A. Davis, and C. Kirkendall, "Quantitative amplitude measuring $\varphi$-OTDR using multiple uncorrelated rayleigh backscattering realizations," *Optics Express*, vol. 27, no. 24, p. 34 952, Nov. 25, 2019, ISSN: 1094-4087. DOI: 10.1364/OE.27.034952.

[133] H. He *et al.*, "Suppression of the interference fading in phase-sensitive OTDR with phase-shift transform," *Journal of Lightwave Technology*, vol. 39, no. 1, pp. 295–302, Jan. 2021, ISSN: 1558-2213. DOI: 10.1109/JLT.2020.3023699.

[134] K. Shimizu, T. Horiguchi, and Y. Koyamada, "Characteristics and reduction of coherent fading noise in rayleigh backscattering measurement for optical fibers and components," *Journal of Lightwave Technology*, vol. 10, no. 7, pp. 982–987, Jul. 1992, ISSN: 1558-2213. DOI: 10.1109/50.144923.

[135] S. Guerrier, C. Dorize, E. Awwad, and J. Renaudier, "A fully digital MIMO-OFDM scheme for fading mitigation in coherent $\Delta\phi$-OTDR," *Optics Express*, Oct. 6, 2021, Publisher: Optical Society of America, ISSN: 1094-4087. DOI: 10.1364/OE.436146.

[136] C. Dorize, S. Guerrier, E. Awwad, P. A. Nwakamma, H. Mardoyan, and J. Renaudier, "An OFDM-MIMO distributed acoustic sensing over deployed telecom fibers," in *2021 Optical Fiber Communication Conference (OFC)*, 2021, p. 3.

[137] J.-F. Sciabica, M.-C. Bézat, V. Roussarie, R. Kronland-Martinet, and S. Ystad, "Caractérisation des variations de timbre du bruit moteur dans l'habitacle d'une automobile par application d'un modèle auditif," in *10ème Congrès Français d'Acoustique*, 2010, p. 6. DOI: hal-00551173.

[138] Z. Jia *et al.*, "Experimental coexistence investigation of distributed acoustic sensing and coherent communication systems," *Optical Fiber Communication Conference*, p. 3, 2021.

[139] Y. Fu *et al.*, "Ultra-long-distance hybrid botda Φ-OTDR," *Sensors*, vol. 18, no. 4, p. 976, 2018.

[140] M. Lai *et al.*, "Ultra-long distance distributed intrusion detecting system assisted with in-line amplification," *IEEE Photonics Journal*, vol. 9, no. 2, pp. 1–10, 2017.

[141] Z. Ye, C. Li, and C. Wang, "Ultra-long-distance (> 160 km) distributed optic fiber vibration sensing system without an in-line repeater," *Applied optics*, vol. 58, no. 13, pp. 3426–3431, 2019.

[142] G. A. Wellbrock *et al.*, "Field trial of vibration detection and localization using coherent telecom transponders over 380-km link," in *2021 Optical Fiber Communications Conference and Exhibition (OFC)*, Jun. 2021, pp. 1–3.

[143] E. Awwad, C. Dorize, and S. Guerrier, "Fiber phase sensing using a ladder topology," US20210231467A1, US Patent App. 17/150,916, Jul. 2021.

[144] "Frequency-weighting sound level measurements: dB(a) vs. dB(c)," HGC Engineering. (Oct. 18, 2011), [Online]. Available: `https://acoustical-consultants.com/built-environment/noise-investigations/frequency-weighting-sound-level-measurements-a-weighting-dba-vs-c-weighting-dbc/` (visited on 12/03/2021).

[145] C. Dorize, E. Awwad, S. Guerrier, and J. Renaudier, "Vibration identification over 50km SSMF with pol-mux coded phase-OTDR," in *45th European Conference on Optical Communication (ECOC 2019)*, IEEE, Sep. 2019, pp. 1–4. DOI: `10.1049/cp.2019.0898`.

[146] S. Guerrier, C. Dorize, E. Awwad, and J. Renaudier, "Towards polarization-insensitive coherent coded phase OTDR," in *Optical Fiber Sensors Conference 2020 Special Edition*, Optical Society of America, Washington, DC: OSA, 2021, T3.20, ISBN: 978-1-55752-307-5. DOI: `10.1364/OFS.2020.T3.20`.

[147] S. Guerrier, C. Dorize, E. Awwad, and J. Renaudier, "Captation de vibrations par fibre optique: une approche télécom," presented at the Journées Nationales de l'Optique Guidée (JNOG) - Optique Dijon 2021, Jul. 5, 2021.

[148] C. Dorize and S. Guerrier, "Fiber event detection using reliability metrics," European pat. 3896409A1, Oct. 20, 2021.

[149] C. Dorize and S. Guerrier, "A spectral diversity combiner for MIMO sensing," European pat., Dec. 2021.

# Publications and patents

## Conference papers

[74] C. Dorize, E. Awwad, S. Guerrier, and J. Renaudier, "Optimal probing sequences for polarization-multiplexed coherent phase OTDR," in *Optical Fiber Sensors Conference 2020 Special Edition*, Washington, DC: OSA, 2021, T3.23, ISBN: 978-1-55752-307-5. DOI: 10.1364/OFS.2020.T3.23.

[75] S. Guerrier, C. Dorize, E. Awwad, and J. Renaudier, "A dual-polarization rayleigh backscatter model for phase-sensitive OTDR applications," in *Optical Sensors and Sensing Congress*, San Jose, California: OSA, 2019, ETu3A.4, ISBN: 978-1-943580-61-3. DOI: 10.1364/ES.2019.ETu3A.4.

[118] C. Dorize, S. Guerrier, E. Awwad, and J. Renaudier, "Capturing acoustic speech signals with coherent MIMO phase-OTDR," in *2020 European Conference on Optical Communications (ECOC)*, Dec. 2020, pp. 1–4. DOI: 10.1109/ECOC48923.2020.9333283.

[136] C. Dorize, S. Guerrier, E. Awwad, P. A. Nwakamma, H. Mardoyan, and J. Renaudier, "An OFDM-MIMO distributed acoustic sensing over deployed telecom fibers," in *2021 Optical Fiber Communication Conference (OFC)*, 2021, p. 3.

[145] C. Dorize, E. Awwad, S. Guerrier, and J. Renaudier, "Vibration identification over 50km SSMF with pol-mux coded phase-OTDR," in *45th European Conference on Optical Communication (ECOC 2019)*, IEEE, Sep. 2019, pp. 1–4. DOI: 10.1049/cp.2019.0898.

[146] S. Guerrier, C. Dorize, E. Awwad, and J. Renaudier, "Towards polarization-insensitive coherent coded phase OTDR," in *Optical Fiber Sensors Conference 2020 Special Edition*, Optical Society of America, Washington, DC: OSA, 2021, T3.20, ISBN: 978-1-55752-307-5. DOI: 10.1364/OFS.2020.T3.20.

[147] S. Guerrier, C. Dorize, E. Awwad, and J. Renaudier, "Captation de vibrations par fibre optique: une approche télécom," presented at the Journées Nationales de l'Optique Guidée (JNOG) - Optique Dijon 2021, Jul. 5, 2021.

## Journal publications

[92] S. Guerrier, C. Dorize, E. Awwad, and J. Renaudier, "Introducing coherent MIMO sensing, a fading-resilient, polarization-independent approach to $\phi$-OTDR," *Optics*

*Express*, vol. 28, no. 14, p. 21 081, Jul. 6, 2020, ISSN: 1094-4087. DOI: 10.1364/OE.396460.

[99] E. Awwad, C. Dorize, S. Guerrier, and J. Renaudier, "Detection-localization-identification of vibrations over long distance SSMF with coherent delta-phi-OTDR," *Journal of Lightwave Technology*, vol. 38, no. 12, pp. 3089–3095, 2020, ISSN: 1558-2213. DOI: 10.1109/JLT.2020.2993167.

[105] C. Dorize, S. Guerrier, E. Awwad, and J. Renaudier, "Identification of rayleigh fading induced phase artifacts in coherent differential $\phi$-OTDR," *Optics Letters*, vol. 46, no. 11, pp. 2754–2757, Jun. 1, 2021, ISSN: 1539-4794. DOI: 10.1364/OL.427944.

[121] W. Tomboza, S. Guerrier, E. Awwad, and C. Dorize, "High sensitivity differential phase OTDR for acoustic signals detection," *IEEE Photonics Technology Letters*, vol. 33, no. 13, pp. 645–648, Jul. 1, 2021, ISSN: 1941-0174. DOI: 10.1109/LPT.2021.3084557.

[135] S. Guerrier, C. Dorize, E. Awwad, and J. Renaudier, "A fully digital MIMO-OFDM scheme for fading mitigation in coherent $\Delta\phi$-OTDR," *Optics Express*, Oct. 6, 2021, Publisher: Optical Society of America, ISSN: 1094-4087. DOI: 10.1364/OE.436146.

## Patents

[143] E. Awwad, C. Dorize, and S. Guerrier, "Fiber phase sensing using a ladder topology," US20210231467A1, US Patent App. 17/150,916, Jul. 2021.

[148] C. Dorize and S. Guerrier, "Fiber event detection using reliability metrics," European pat. 3896409A1, Oct. 20, 2021.

[149] C. Dorize and S. Guerrier, "A spectral diversity combiner for MIMO sensing," European pat., Dec. 2021.

ECOLE
DOCTORALE

**Titre :** Captation de perturbations mécaniques large bande par détection cohérente de la rétrodiffusion Rayleigh dans les fibres optiques

**Mots clés :** rétrodiffusion Rayleigh, détection cohérente, fibre optique, capteur distribué

**Résumé :** Répondant à une demande croissante de connectivité entre les individus, entre les pays et par conséquent entre les continents, les fibres optiques de télécommunications sont déployées dans le monde entier. Les continents comme les océans sont désormais quadrillés par ces réseaux dont l'importance stratégique n'est plus à démontrer. De manière plus générale, les fibres optiques sont une alternative aux capteurs électrodynamiques de vibrations, avec un atout majeur : la possibilité de détecter et localiser des phénomènes indépendants tout au long de la fibre, bien au-delà de la simple détection de ruptures de fibres et allant jusqu'à la reconnaissance de multiples signatures audio voire de la parole.
Cette thèse a pour but d'étudier finement la rétrodiffusion Rayleigh dans les fibres optiques, qui permet de capter de l'information induite par des perturbations mécaniques tout le long d'une fibre. Nous étudions le potentiel des fibres optiques en tant que microphones distribués, en terme de bande passante mécanique et de sensibilité. Nous décrivons le système d'interrogation des capteurs à fibre distribués, et proposons la modélisation d'un tel interrogateur en tenant compte du multiplexage des signaux sur deux axes orthogonaux de polarisation lors de la propagation dans la fibre. Nous étudions la problématique de l'évanouissement dans la fibre : à la fois l'évanouissement de polarisation que nous parvenons à annuler grâce à la méthode d'interrogation *Coherent-MIMO*, et l'évanouissement cohérent que nous proposons de diminuer en recourant à une interrogation multi-porteuses électronique. Différents résultats de mesure sont également présentés dans cette thèse : nous validons le seuil de distinction du système d'interrogation sur quelques kilomètres de fibre monomodes de télécommunications, puis, sur des dizaines de kilomètres de fibres incluant des câbles déployés, nous validons la pertinence d'un système de captation par segment de fibres dans les réseaux télécom à haut débit, ouvrant ainsi la voie à des systèmes de télémétrie évoluée dédiés aux réseaux optiques de demain.

**Title :** High bandwidth detection of mechanical stress in optical fibre using coherent detection of Rayleigh scattering

**Keywords :** Rayleigh backscattering, coherent detection, optical fibre, distributed sensor

**Abstract :**
Telecommunication fibres are being deployed all over the world, connecting distant people, institutions, companies with an outstanding quality of service in terms of data rate and latency. Their strategic value in terms of global economy and daily life is now undeniable. Monitoring such an infrastructure has become mandatory, and that far beyond the standard case of breaks localization. From a broader standpoint, optical fibres are an alternative to electro-dynamic point sensors, with a strong asset: the capability to detect and localize multiple independent phenomena all along a fibre. Thus, the millions of kilometers of currently deployed optical fibre around the world constitute a huge potential base of sensors. Distributed vibration sensors have a huge potential regarding sensing of dynamic events, detecting of multiple acoustic signatures up to speech signals.
In this thesis, we show how distributed optical fibre sensors can be designed on top of telecommunication fibres, namely standard single mode fibres, and we explore their potential in terms of reach, detection threshold, and sensing bandwidth. We present the interrogator systems for distributed fibre sensing and build a dual-polarization numerical model of such an interrogation system and fibre sensor. Secondly, we tackle the coherent fading issue by means of frequency diversity in the digital domain, i.e. directly applicable at the modulation of the interrogation sequences, before entering the optical domain. We developed MIMO-OFDM which retrieves independent channel estimations from a single fibre segment; the estimations are further combined, and the obtained estimations are assessed with regards to the reliability metric. Throughout this thesis, many experimental measurements were conducted, assessing the capabilities of the Coherent-MIMO interrogator on single-mode-fibre sensors in terms of reach, bandwidth, and detection threshold. We also demonstrate the co-propagation of a sensing signal along with high data rate channels, without any impact on the transmitted data, paving the way to the enhanced monitoring and telemetry in deployed telecommunication networks.

**Institut Polytechnique de Paris**
91120 Palaiseau, France